Construction and Characterization of a Single Stage Dual Diaphragm Gas Gun

Nathaniel Steven Helminiak
Marquette University

CONSTRUCTION AND CHARACTERIZATION OF A SINGLE STAGE DUAL DIAPHRAGM GAS GUN

by

Nathaniel Steven Helminiak, B.S., E.I.T.

A Thesis submitted to the Faculty of the Graduate School,
Marquette University,
in Partial Fulfillment of the Requirements for
the Degree of Master of Science

Milwaukee, Wisconsin

December 2017

ABSTRACT

CONSTRUCTION AND CHARACTERIZATION OF

A SINGLE STAGE DUAL DIAPHRAGM GAS GUN

Nathaniel Steven Helminiak, B.S., E.I.T.

Marquette University, 2017

In the interest of studying the propagation of shock waves, this work sets out to design, construct, and characterize a pneumatic accelerator that performs high-velocity flyer plate impact tests. A single stage gas gun with a dual diaphragm breach allows for a non-volatile, reliable experimental testing platform for shock phenomena. This remotely operated gas gun utilizes compressed nitrogen to launch projectiles down a 14 foot long, 2 inch diameter bore barrel, which subsequently impacts a target material of interest. A dual diaphragm firing mechanism allows the 4.5 liter breech to reach a total pressure differential of 10ksi before accelerating projectiles to velocities as high as 1,000 m/s (1570-2240 mph). The projectile's velocity is measured using a series of break pin circuits. The target response can be measured with Photon Doppler Velocimetry (PDV) and/or stress gauge system. A vacuum system eliminates the need for pressure relief in front of the projectile, while additionally allowing the system to remain closed over the entire firing cycle. Characterization of the system will allow for projectile speed to be estimated prior to launching based on initial breach pressure.

ACKNOWLEDGMENTS

I submit this thesis to the public for review with the utmost thanks to God, my family, mentors, friends, and sponsors for their help and support throughout the process of generating this work. I am truly grateful for the unconditional love of my family, as there is no way that I would have made it this far without their support. Further, Dr. John Borg, my advisor for the majority of my higher academic career has provided an education that extends beyond pure scholasticism and has informed some of the greatest choices in my life to date. I can think of few thesis topics quite as extraordinary as the construction and characterization of a gas gun. My thanks are also extended to the members of my committee: Dr. Casey Allen, Dr. Anthony Bowman, Dr. Johnathan Fleischmann, and Dr. Hyunjae Park, for their mentorship and commitment to my education since my arrival in the undergraduate program at Marquette University. They, in addition to the other professors and professionals, working within the Opus College of Engineering have each provided innumerable opportunities to grow and develop. My gratitude goes out to the members of the shock physics lab, especially Jeff Lajeunesse, Merit Schumaker, Peter Sable, Chris Johnson, Logan Beaver, Ashley Hatzenbihler, and Emilie Teitz. Finally, I thank the Defense Threat Reduction Agency and by extension the United States of America for providing the means and freedoms to pursue my education. From Proverbs 25:2, “It is the glory of God to conceal a matter; to search out a matter is the glory of kings.” My opportunity to pursue the glory of kings has been provided in hours of expertise and patience on the part of many people. I continue to pray that I someday might be able to provide to others the same gifts others have shared with myself.

-Nathaniel ϟteven Helminiak

TABLE OF CONTENTS

LIST OF TABLES

LIST OF FIGURES

1. INTRODUCTION

1.1 Motivation

The objective of this work is three fold:

First, a usable platform is created from which to conduct shock experiments. The current work platform includes 1D Planar Shock, Shock Compaction of Materials, Pressure Shear, Granular Material Compaction and Conical Shots. However, the gun capability could be adjusted to include work on penetration studies and damage modeling.

Second, this work seeks to demonstrate the operational safety of the 2 inch gas gun with a manual giving clear record of parts, their selection and operation. It is expected that with time the gun will adapt and improve; however, the basics will likely remain the same.

Third, it is desired to provide the new shock physics researcher with a suite of tools with which to conduct research. By simplifying gun operation and optimizing performance, more focus is placed on novel research. To this end, explicit scripts have been included within this works' appendices, which should allow the researcher to quickly create operational parameters to suit experiments and ensure the 2 inch gas gun will operate both correctly and consistently. Sections within this thesis should be consulted as first reference for use of the Gas Gun, then if there are questions, feel free to contact the author.

1.2 History and Review

1.2.1 Ballistics in History: A Path to Gas Gun Technology and Shock Physics

It is unknown when the human race first began experimenting with projectiles. One would have to imagine it happened somewhat like this: Early humans through observation or by happenstance did cause to effect or did witness a significant change in the velocity of a local object apart from the effecter resulting in an impact a distance from the point of origin. This use of projectiles was eventually utilized by an individual as a tool/weapon and this tool was later passed to other individuals through history.

A selection of some of the projectile tools/weapons found earliest in human history is compiled below in Figure 1.1. Though the exact use of some of the artifacts complied is sometimes questioned as humans of that time left no clear messages or recording of use [1], it is clear that developments in projectile technology were well underway. Spears such the Schöningen spear [2] (378,000 and 398,000 BC) could be utilized as both a short range and a long-range weapon. Bows and arrows found in Kenya (9400 – 10500 BC) [3], improved mechanical advantage as well as creating an ability to store potential energy in the form of string tension. Rock slings and stones found in Turkey (7000 BC) [4] [5] increased the acceleration felt by projectiles through use of longer moment arms.

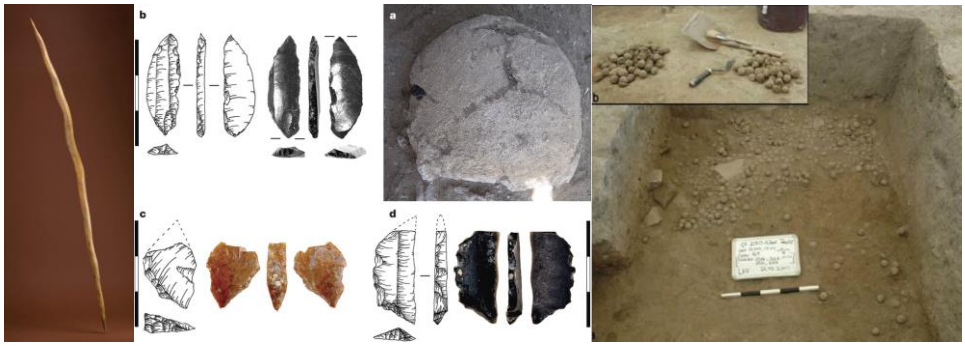

Figure 1.1 Early ballistics technologies: spear [6], arrows [3], and slings [4].

From this point in history, others would improve upon the craft through various methods of improving the peak velocity, accuracy and flight paths of these projectiles. Continuing in time, one of the earliest known recording of projectile use is found on the Stele of the Vultures (2500 – 2340 BC) found in modern day Iraq [7] where early man recorded the usage of arrows in war (see Figure 1.2).

"They fought each other,
and towards Enanatum
a man shot an arrow.
He was penetrated by the arrow,
but he broke it off."
-Stele of Vultures

Figure 1.2 Stele of Vultures [8] and quote from the translation [9].

Stone and wooden tools became upgraded with stronger bronze enhancements. The Bronze Age (3000 BC – 1000 BC) [10] tools were being used in more challenging scenarios, hunting ever larger animals and using armor. With new challenges came a continued demand for innovation and improvement. Metallurgical proficiency in the Iron Age (1200 BC – 1200 AD) [11] would continue a trend searching for improvements through material selection, which continues the present day. During the Iron Age, the technologies of the spear sling and bow were enlarged. The Roman Mangonel (catapult) is thought to have been developed around the same time 400 BC [12] in which the Greek historian Diodorus Siculus documented the mechanical ballista as a weapon of war [13]. Just 100 years later in 300 BC the Chinese would develop the Trebuchet [13].

By this point, there was clear military and scholastic consideration undertaken by people in history. Scientists such as Aristotle (364 – 322 BC) would begin to ponder the nature of motion. Theories in his work, “Physics” [14], considered the natural motion of materials to be governed by the amount of certain fundamental elements within an object: earth, air, water, fire, and ether. Each object would attempt to move towards other elements of certain types, which encircled the earth in layers: water surrounding earth, air rising through water, and fire rising through air. When an object like a stone, which was made of the earth element, was placed in water or flung through the air, it tended to seek out its natural place falling through other elements attempting to reach its natural place on the lowest plane of the elements. For projectile motion, an object would first use up violent motion, traveling in a straight line and then follow natural motion, moving directly to its natural place.

About this time, it is supposed that Archimedes of Syracuse (287 – 212 BC) developed the first gas gun [15]. While the original work and perhaps publications of Archimedes have not yet been found, his work on the "Architronito" [16] (see Figure 1.3), the first single stage light gas gun, was drawn by Leonardo da Vinci, who cited Archimedes as its inventor. From notes, it appears that the system utilized steam to propel targets at the enemy. It is likely that the cannon, while impressive for its time, took both a long time to load as well as pressurize and was not yet practical for use on a moving battlefield. Tests done by MIT showed that given optimal implementation of the design, the "Architronito" was likely capable of firing a 0.5 kg projectile at a muzzle velocity of 280 m/s [17].

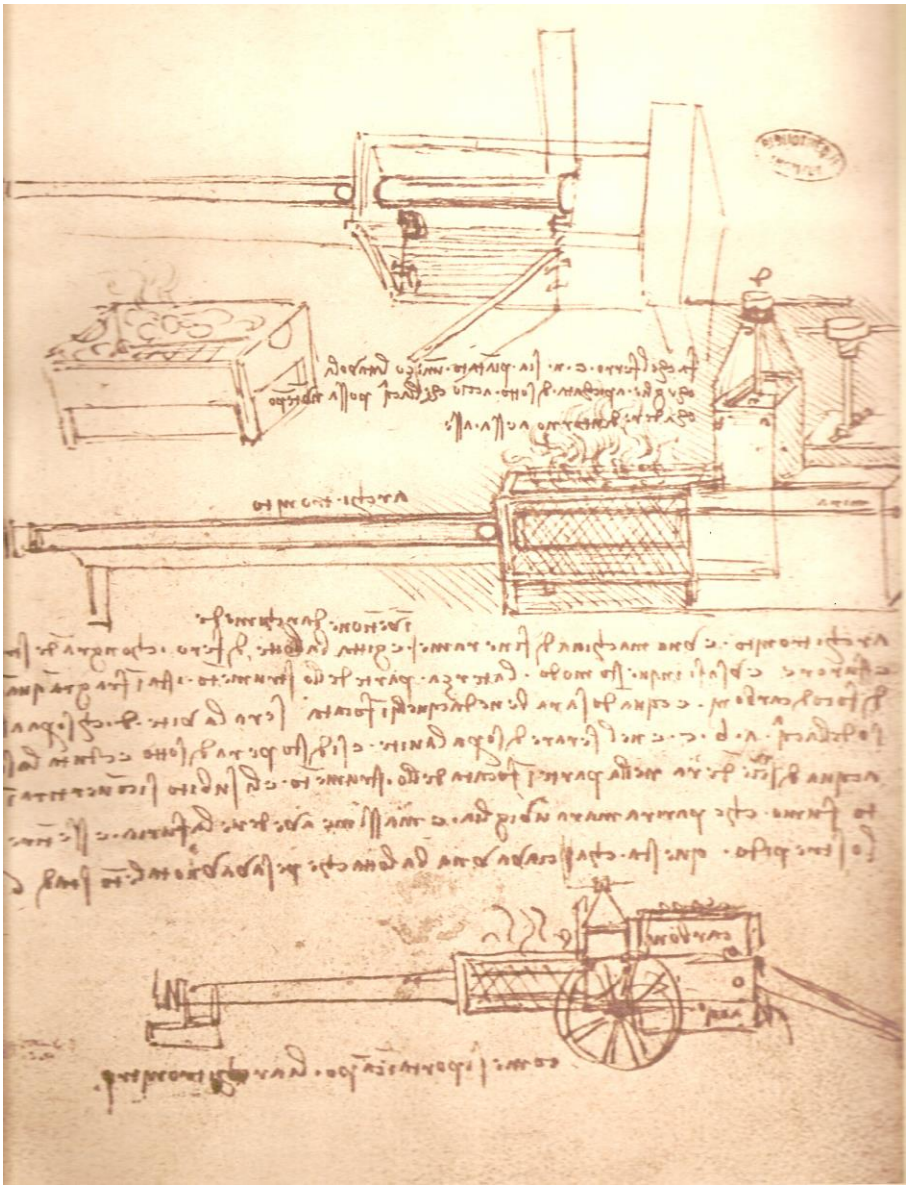

Figure 1.3 The "Architronito" drawn by Leonardo Da Vinci.

A solution to the problem of rapid power and quick loading would later be solved by the Chinese between 948 and 951 AD [18]. An ancient Daoist text, the Zhenyuan Miiaodao Yaolue, seems to refer to an ancient form of propellant. A military text appearing a little later, Wujing Zongyao, gives careful instructions and recipe for gun

powder [19]. Historian Kenneth Chase points out evidence of primitive firearms in the forms of fire lances, which could be loaded with small projectiles and expelled during flaming. These are followed by cave temple painting in Sichuan dating from the 1100's AD, which include an early cannon and bomb. Hand canons, or early firearms, would first appear in the Middle East battle of Ayn Jalut between the Egyptian Mamluks and the Mongols, playing a part in stopping the Mongol goal of western expansion [20].

Firearm technology would be of great military importance as energy could be stored in a form that was easy for the common man to apply, lowering the barriers of strength and skill. From about 1100 AD onwards, the powdered gun would make its way around the rest of Asia, Europe (see Figure 1.4), and Africa, where the firearm and cannon would serve alongside the sword, spear, bow, horse, trebuchet, and catapult. Indeed the historian Niccolo Machiavelli wrote in his 1519 *The Art of War*, "There is no wall, whatever its thickness that artillery will not destroy in only a few days" [21].

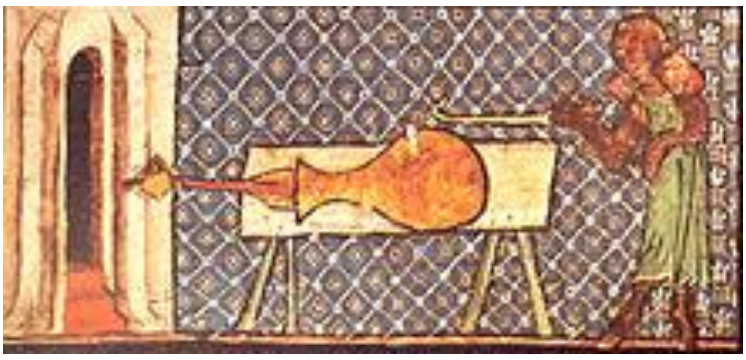

Figure 1.4 The earliest pictogram found of a european cannon [22].

Eventually, the rifling of the barrel, invented by August Kotter in Germany during 1498, would improve the accuracy of these projectiles [23]. Once projectiles could be propelled in a manner that was repeatable, scholars returned to the problem of predicting projectile motion. Most gun operators at this time would use Tartaglia's 1537 mixed motion projectile model, which presumed that objects would initially start with all violent motion and decay in a mixed state to natural motion (explaining an object's more curved trajectory) [24]. Galileo's theory of parabolic motion was first published in Speccio Ustoria [25] by means of a former Jesuit student, Bonaventrua Cavaleri. Later, Galileo in 1636 would expound upon this theory in his own work, "Discourses Concerning Two New Sciences" [26], stating that an object would fall with constant acceleration during its travel to earth, meaning that a projectile's motion was chiefly parabolic. Issac Newton in 1656 would add air resistance showing that drag at low velocities was proportional to the density of the fluid through which the projectile travels, cross sectional area, and shot weight [27]. Johann Bernoulli in 1695 would formulate, by assuming uniform density, a relation between the pressure energy contributing to drag and the velocity of a projectile, which is known today as the Bernoulli equation [28].

Manufacturers during this period also did a great deal to improve the firearms of the day. Cannons that were scaled down in size could be carried in one's hand; hence, they were given the name "hand cannon". These cannons were improved with the addition of an ergonomic body and matchlock system, like the one seen in the French Blunderbuss (handgun) shown in Figure 1.5. Finally, ball shot was replaced with a conical bullet and spiral cut (rifled) barrel creating a rifle much akin to a modern weapon.

Figure 1.5 1760 French Blunderbuss [29] and a 1803 British Baker Rifle [30].

As manufacturing improved and guns reached a new plateau in terms of working principle, scientists again began to make significant progress. Benjamin Robins invented the ballistic pendulum, which allowed for the measurement of projectile and muzzle velocities. In his 1805 book "New Principles of Gunnery" [31], Robins utilized the principles of numerical integration by Euler [32] to determine projectile motion, which Euler himself would later translate to German with added contributions.

Inspired by John Locke's Electro-Chronograph created in 1848, with its ability to record events in time [33], Francis Bashforth improved upon Robins' method to measure ballistic velocity with the creation of the Electro-ballistic ChronoGraph (Figure 1.6) [34]. With this electro-chronograph, Bashforth and others tested a variety of projectiles shapes, angles, charge strength, and environmental conditions.

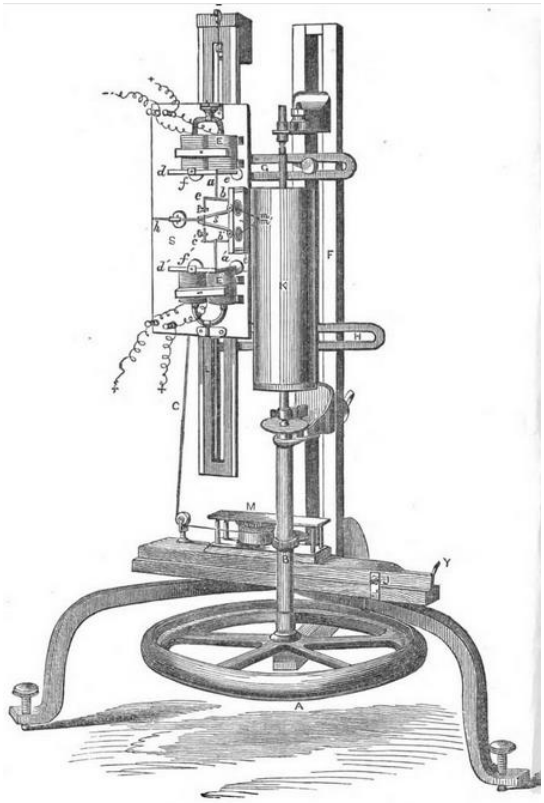

Figure 1.6 Francis Bashforth's Electro-ballistic ChronoGraph [35].

Armed with increasingly accurate experimental data, numerical models of calculating projectile motion also became quite accurate. Though these model methods were very precise, calculations required a long time to work out and were only valid for standard projectile shapes. Solutions needed to be quickly determined for a given set of battlefield conditions, so ballistic tables were developed using both experimental and analytical solutions to provide accuracy in hitting a target [36] [37]. Ballistic tables by Bashforth were later adapted by Russian General Mayevski [38] with additional experimental data collected by M. Krupp [39]. In 1880, Italian Colonel Francesco

Siacci published his work, “Balistica” [40]. Works from “Balistica” provide the basis for several modern ballistic works, including those by James Ingalls [41] and R.H. Kent [42], who along with F.B. Pidduck [43] formed the analytical calculation for modern light gas gun projectile velocities. Their work compiled in a comprehensive document by Sigel [44] is referenced and utilized in section 4.5.

With the new projectile motion developments, countries fought with increasingly sophisticated weaponry, culminating in World War 1 (1914-1918) with guns such as the rifle, machine gun and artillery (Figure 1.7). Aided by the aforementioned advancements in ballistic calculations, the deadliest war the world had yet seen occurred with the advent of new military phenomena such as trench warfare and airborne assault [45].

Figure 1.7 French cannon used in the Franco Prussian War 1870 [46] and the M1903 World War 1 rifle [47].

During World War 2 (1939-1945), continued developments in technology were made [48]. While perhaps the ballistics technology with the greatest impact came from the German ballistic and rocket projects, the Germans also invested time and effort into enormous cannons. Powder guns such as the Dora and Gustav Rail Cannons (Figure 1.8)

launched projectiles of high mass, 4,800 kg-7,100 kg (10,600-15,700 pounds), up to 38-48km (24-30 miles) away [49]. Multi-charge powder “accelerating-guns”, like the V3 (Figure 1.8) developed by Haskell, R. and Lyman, A.S. [50], attempted to increase the range of the single stage powder gun. Experiments carried out at the Sandy Hook Proving Ground by the U.S. Army Ordinance Department found a multistage 6-inch gun had the ability to shoot a 69 kg (152 pounds) projectile a velocity of 548.9m/s (1801 feet/second), which was comparable in ability to that of single barrel guns of this same period [51].

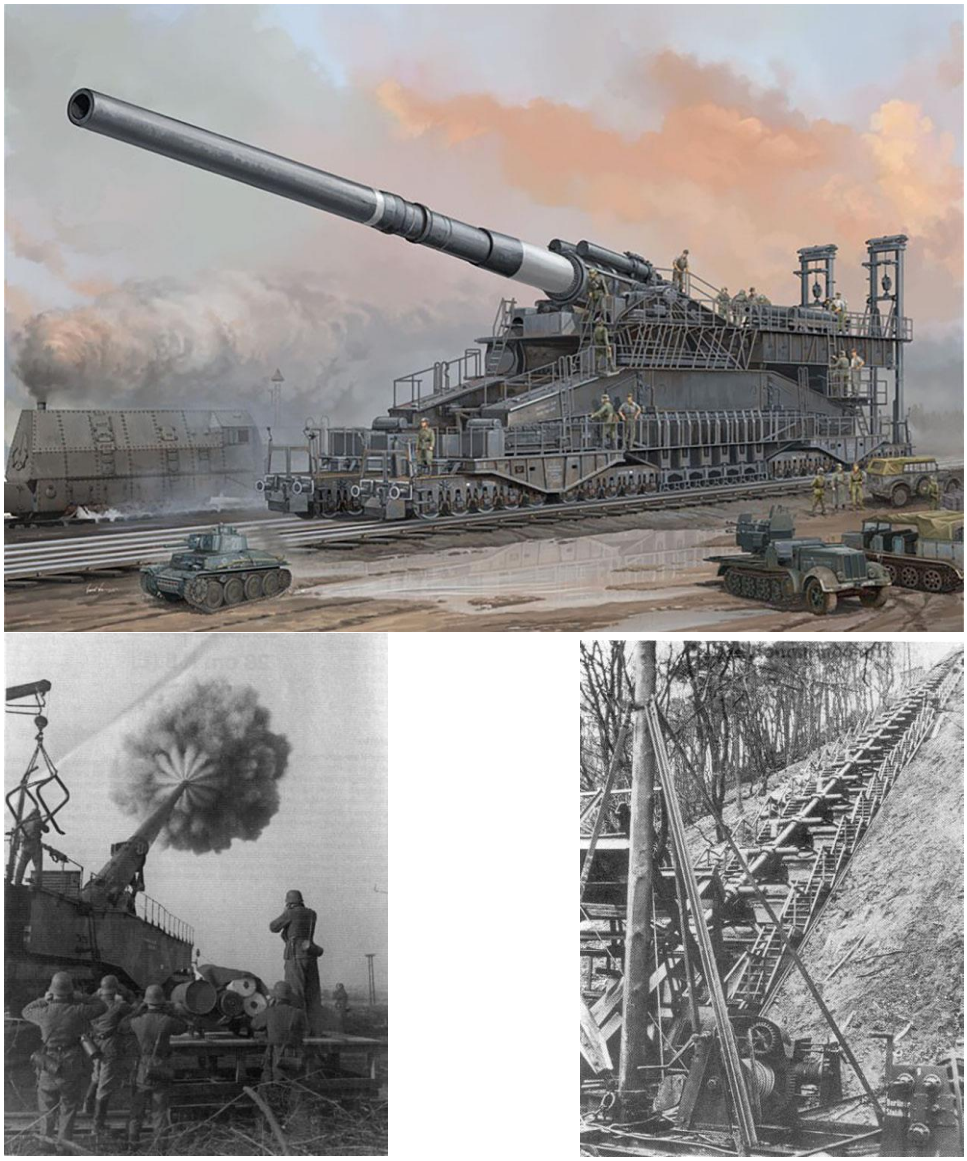

Figure 1.8 German rail cannons “Gustov” (top), “Dora” (left) [52] and V3 (right) [53].

In order to calculate the vast number of projectile path solutions during World War 2, a number of men and predominantly women were employed as equivalent computers to calculate ballistics trajectories. After the end of the second World War, the United States would unveil their newest tool the ENIAC (Figure 1.9), the first turing-complete programmable electronic computer used for ballistic calculations in 1945 [54].

Trajectories of the standard projectile, as well as projectile paths of non-standard types, could be calculated in a fraction of the time.

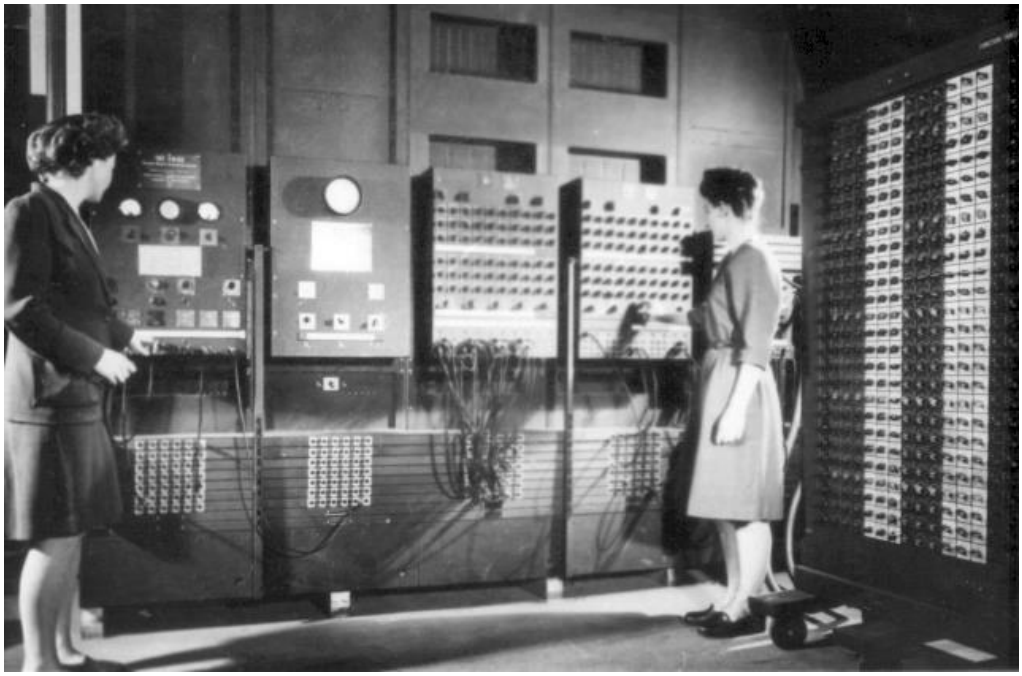

Figure 1.9 ENIAC and a pair of computer operators [55].

From World War 2 onwards computers ran and still run the majority of ballistic calculations as well as the design and simulation of projectile impacts. No longer would designs for ballistics solely remain with guns. Modern designs for missiles, armor, spacecraft, and satellites, speeding up to velocities of 73km/s (45 miles/second) [56], all rely on shock physics and related fields for designs. To engineer projectiles suited for operation at these speeds, numerical hydrocodes are the tool used for simulations and shock guns (such as powder and gas) that provide valuable experimental data with which to inform models.

The advent of German rockets and missiles traveling at 6.0 km/s and the new capability of the computer marked a continuation of change in warfare and industry towards faster capable vehicles carrying weapons, satellites and personnel [57]. From the time the U.S. left World War 2 and entered the Cold War to the present day, tools for testing the behavior of materials under these extreme conditions have been needed.

1.2.2 A Brief History of Shock Physics and Numerical Tools

While not the chief focus of this paper, a quick primer mention of shock physics is required as light gas guns primarily function within the shock regime. Shock physics and simulations of shock events are often informed by experimental data captured within light gas gun experiments.

Shock Physics is the study of materials under explosive or impact loading conditions. Typically, these materials interact at high speeds and strain rates that create a shock through a material. Shocks are first proposed in a work by Euler, who suggested the existence of a discontinuous function that changes value instantaneously without a gradient [58]. Poisson would later take this idea and apply it to sound waves [59]. A historical review of shock phenomenon becomes muddy at this point, but a good summary of the enfolding events can be found within Manuel D Salas' article, "The curious events leading to the theory of shock waves" [60]; indeed, this work corroborated much of the previous histories found. In short, Sir William Tomson, Lord Rayleigh, and Sir George Stokes would then argue over the applicability of the derived equations of mass and momentum, as they seemed in violation of the conservation of energy [61].

Though it was initially thought that these equations would violate conservation of energy, Rankine would discover the adiabatic nature of shock waves, allowing for the conservation of energy [62]. Hugoniot would then close the loop relating kinetic energy to internal energy [63], leaving the shock physics community with three equations for the conservation of: mass, momentum, and energy. These could be closed with a material equation of state and, if applicable, a material strength model. Models predating hydrocodes would use jump equations (1.1)-(1.4) [64] to model the interactions of wave fronts moving through a given material:

$$\rho_0 U_s = \rho(U_s - U_p) \tag{1.1}$$

$$P - P_0 = \rho_0 U_s U_p \tag{1.2}$$

$$PU_p = \frac{1}{2}\rho_0 U_s {U_p}^2 + \rho_0 U_s (E - E_0) \tag{1.3}$$

$$U_s = U_p S + C_0 \tag{1.4}$$

where ρ is density, U_s is the shock speed, U_p is the particle speed, P is pressure, E is internal energy, S is the Hugoniot slope and C_0 is the material bulk sound speed. These jump equations, while not able to capture the full behavior of the Navier-Stokes equation, provide researchers a quick way to anticipate general wave behavior between material interfaces, through a method known as impedance matching. For those interested in a

complete outline of hydrocode equations and computational methods the author recommends M.L. Wilkins' "Computer simulation of dynamic phenomena" [66].

Hydrocodes, which include the Navier-Stokes equation and closure models, give engineers and scientists the tools needed to simulate shock physics events. Two major methods of computing impacts and shock mechanics were methods based in Eularian (named by Dirchlet) and Lagrangian (named by D'Alembert) grid based mechanics [65] (see Figure 1.10). In Eularian mechanics, mass would move through a fixed set of cells, which proved most useful for large deformation and mixed material mechanics, but struggled with fracture and material boundaries. Lagrangian codes, while excellent for defining material boundaries (as the cells were mapped to the material), required that material be re-meshed. This was problematic in instances where material fractured into small pieces computationally expensive to re-mesh each step. Both types of codes are still available today with the most modern codes, such as CTH, using mixed Eularian-Lagrangian models. Marquette University's own KO 1D hydrocode is a formulation of the Lagraingian HEMP Hydrocode [66].

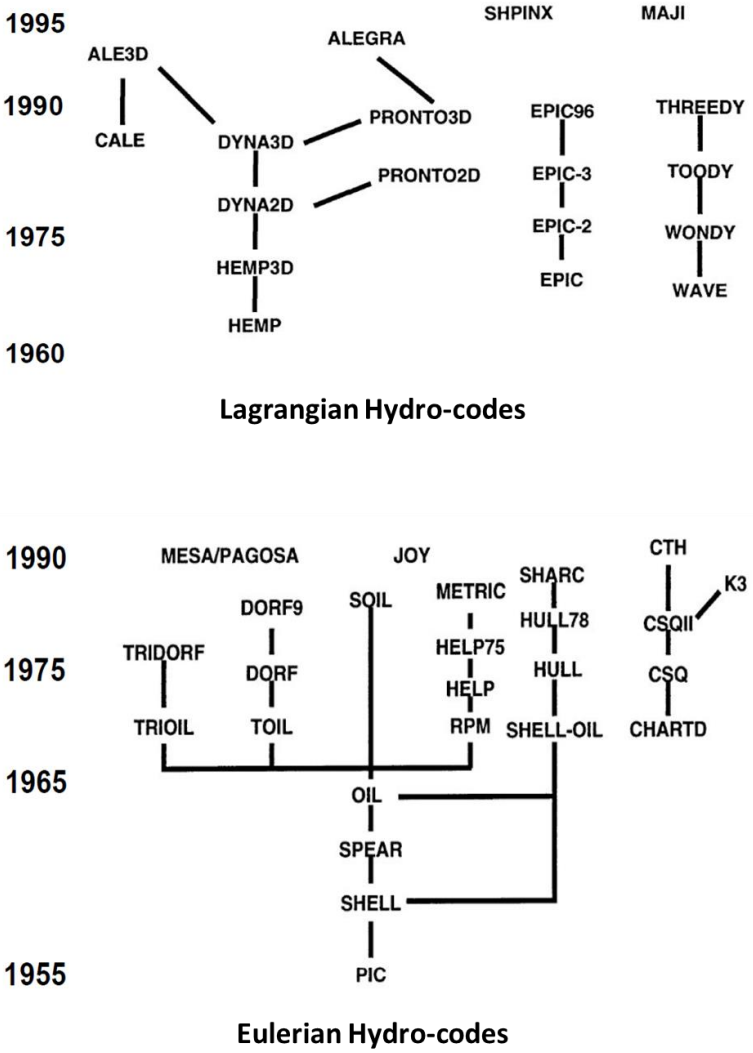

Figure 1.10 Progression of Hydrocodes [67].

1.2.3 The Gas Gun

The development of the rocket engine traveling in the range of one to tens of kilometers per second spurred the development of test platforms capable of reproducing high velocity and high strain rate events within repeatable laboratory conditions. The U.S. would become an international hub from which shock physics experimentation and

development stemmed. While experiments could be and were conducted using rocket sled facilities like those shown in Figure 1.11, these experiments can be quite costly and time-consuming to setup.

Figure 1.11 Rocket sled track at Sandia National Laboratories [68].

Conversely, gas guns are around the world are used for their consistency and ease of use in testing penetrations and impacts, creating new material types and expanding our knowledge of material properties at high strain rates. While a system level test like a rocket sled impact might provide the behavior of an entire system, its accuracy is tied to the many specific variables of the particular experiment. A gas gun provides a tool to precisely measure the responses and material properties of individual components. Compiling results of multiple gas gun shots enables simulation to better understand the underlining phenomena of a full-scale test. In short, gas guns afford experimental studies a platform providing relatively cheap, clean, reliable and repeatable studies, which can be used as building blocks to understand more complex systems and behaviors. The first fully operational, documented, single stage light gas gun was developed by Professor E.J.

Workman at New Mexico Institute of Mining and Technology in 1948. His proposal outlines a method for launching projectiles above 2.75 km/s, the limit of powder gas guns at the time [70]. In Figure 1.12 below, a generalized schematic of a single stage gas gun is shown. During the development of light gas gun technology, several technological discoveries were made, such as gas molecular size and temperature being found to have an effect on peak projectile velocities in addition to the initial pressure of the gas and mass of the projectile [69].

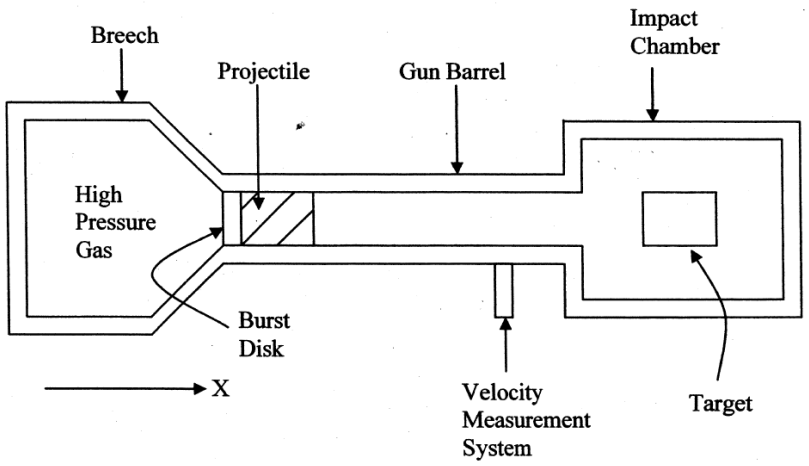

Figure 1.12 Components of a typical single stage light gas gun [71].

As is shown in the above figure, a single stage light gas gun consists of a breach that contains pressurized gases, often nitrogen, helium or hydrogen. This use of "light" gases (low molecular weight) provides an increase in gas gun performance. In general, light gases, having higher sound speeds and lower molecular weight, boost projectiles to higher speeds for a given breach pressurization. Once the breach pressure is released into the barrel by means of a fast acting valve, wrap-around breach or diaphragm system, the

projectile (composed of a sabot and sample) is propelled down the barrel and collides with a target or other experimental setup. Eventually, researchers would add a second barrel [72], compressing the gas used as the propellant for another barrel and boosting experimental velocities even higher.

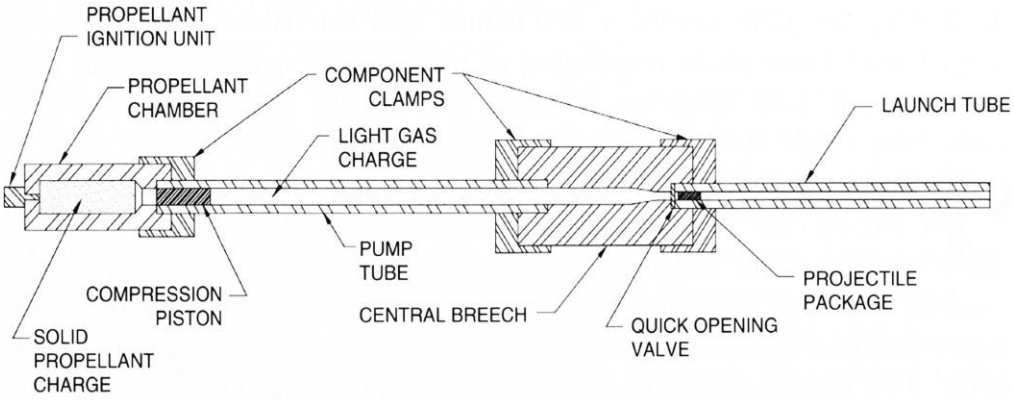

Figure 1.13 Typical components within a two stage light gas gun [73].

In 1950, the initial work done by Professor Workman was classified and the gun was lost to public research. Within the US government, work was continued at NASA Ames and slowly spread to other branches of the government. Eventually light gas gun development returned to public research institutions. Figure 1.14 below plots the progress of velocities attained by light gas gun technology.

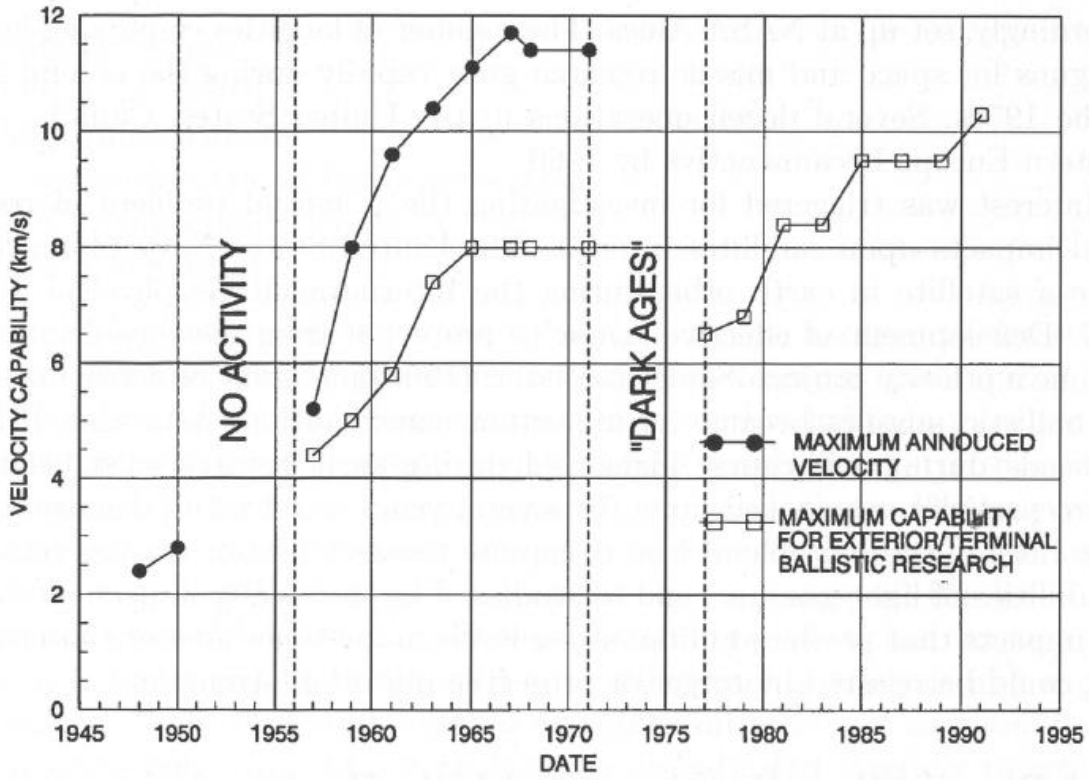

Figure 1.14 Historical view of peak gas gun velocity over the years 1945-1995 [73].

The 1970's were a period of economic, and in turn research, struggle within the United States. The period between 1970-1977, coined the gas gun "dark ages" by Hallock Swift [73], saw reduction in research funding and a step backwards in progress. After the recession, work was renewed in earnest. The shock community would receive renewed initiative as the United States and Russia continued the Cold War, thus increasing the importance of shock and nuclear physics as can be seen in Figure 1.15.

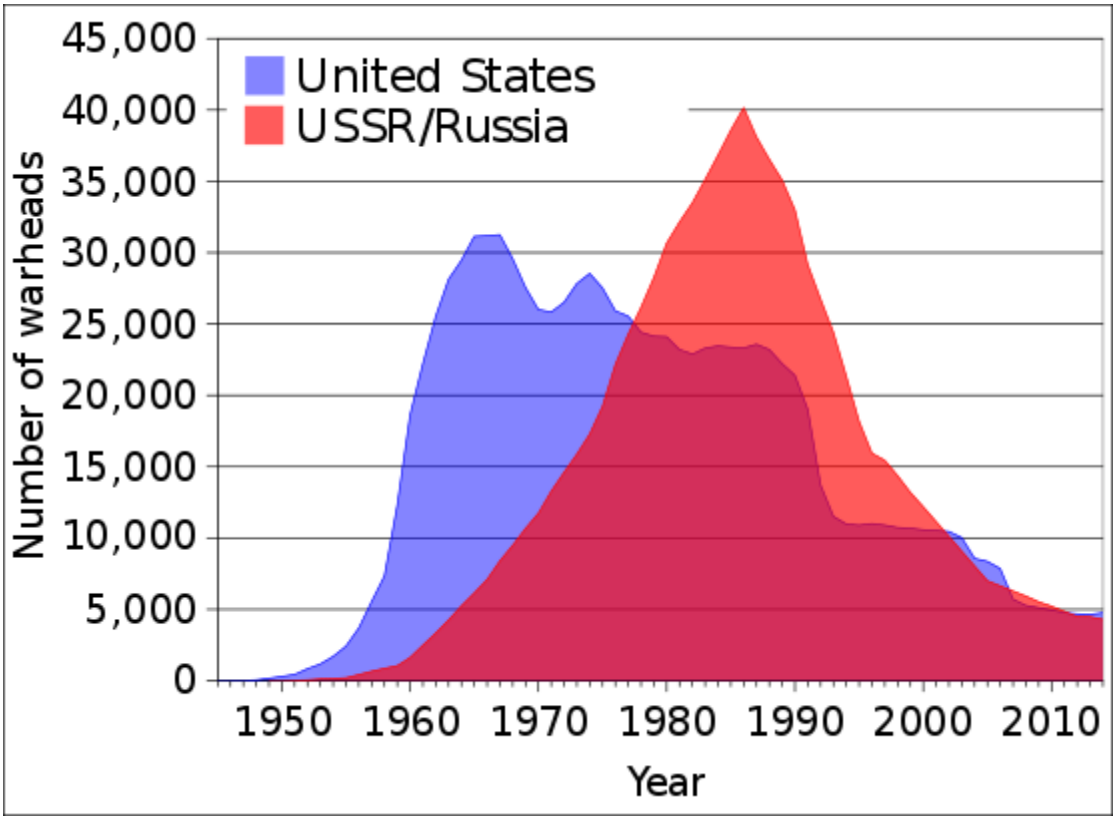

Figure 1.15 Nuclear stockpiles of the United States and Russia [74].

Support for the shock community would hit a new peak when the Reagan administration began a new national program known as the Strategic Defense Initiative, dubbed "Star Wars" by the public media of the time, which sought to intercept nuclear warheads before impact with the United States [78]. Development of these light gas guns was initially spearheaded by government, with scientific communities dedicated to the field such as the Triservice Hypervelocity Impact Committee 1956 [73]. Others, including the Aeroballistics Range Association (ARA) 1959 [75], HyperVelocity Impact Society (HVIS) 1985 [76], and APS topical group, Shock Consolidation of Condensed Matter (SCCM) [77], are still around today with vibrant communities.

From this point onward a variety of research institutions maintain over 50 gas guns around the world, some of which are included and referenced in

Figure 1.16 below.

[80]

A: New Mexico Institute of Mining and Technology, New Mexico, USA, [79] [81]
B: Washington State University, Washington, USA, [82]
C: Ames Research Center, California, USA, [83]
D: Lawrence Livermore National Laboratory, California, USA, [84]
E: California Institute of Technology, California, USA, [85]
F: Los Alamos National Laboratory, New Mexico, USA, [86]
G: Shock Thermodynamics Applied Research (STAR) Facility, New Mexico, USA, [87]
H: Oklahoma State University–Stillwater, Oklahoma, USA, [88]
I: Rice University, Texas, USA, [89]
J: Argonne National Lab, Illinois, USA, [90]
K: Marquette Shock Physics Laboritory, Wisconsin, USA, [71]
L: Arnold Engineering Development Complex, Tennesse, USA, [91]
M: University of Dayton, Ohio, USA, [92]
N: University of New Brunswick, New Brunswick, Canada, [93]
O: Harvard, Massachusetts USA → Now University of California, Davis, California, USA, [95]
P: Naval Ordnance Laboratory, Maryland, USA, [96]
Q: Naval Surface Weapons Center. Virginia, USA, [99]

R: Georgia Tech, Georgia, USA, [100]
S: Eglin Air Force Base, Florida, USA, [101]
T: Cavendish Laboratory, Cambridge, United Kingdom, [102], [103]
U: Imperial College, London, United Kingdom, [104]
V: University of Kent, Canterbury, United Kingdom, [105]
W: French-German Research Institute of Saint-Louis, Saint-Louis, France, [106]
X: Fraunhofer Institute for High-Speed Dynamics, Freiburg, Germany, [107]
Y: Zababakhin All-Russian Scientific Research Institute for Technical Physics, Chelyabinck Oblast, Russia, [108]
Z: University of Tel-Aviv, Tel-Aviv, Israel, [109]
AA: Bhabha Atomic Research Center, Bombay, India, [110]
BB: *China Academy of Space Technology* (*CAST*), Beijing, China, [111]
CC: Japan Aerospace Exploration Agency (JAXA), Kanagawa, Japan, [112]
DD: Kyushu Institute of Technology, Kitakyushu, Japan, [113]
EE: Hypervelocity Impact Research Center, Mianyang, China, [114]
FF: Southwest Institute of Fluids Physics, Sichuan, China, [115]
GG: University of New South Wales, Sydney, Australia, [116]
HH: Materials Research Laboratory, DSTO Melbourne, Australia, [117]
II: DSTO Aeronautical and Maritime Research Laboratory, Salisbury South Australia, Australia, [118]

Figure 1.16 Locations of a few academic and national gas gun facilities.

Within the shock physics community, there are generally three types of guns utilized for projectiles of large mass (less than.1 kg), which are: powder guns, single stage gas guns and two stage light gas guns. Velocities for these guns depend largely on the mass of the projectile and the driving pressures; however, for the general scale projectile (0.01 grams to 1000 grams), velocities and general uses are cited from Gun's Manufacturer Physics Applications Inc. [119].

Powder guns are most often the first facilities the uninitiated imagine when thinking of shock physics gun research. In general, these facilities are harder to maintain as the handling of explosives generally requires licensing. Residual powder and products of the explosive reaction must also be cleaned after every experiment. Explosives, having

high energy concentration, are often the propellant of choice for the military, so these guns serve to test behaviors of materials under similar loading conditions. Even though explosives provide powder guns fast acceleration, they are not the fastest of the three typical gun types, with powder guns typically operating between 0.3-2.7 km/s. Powder guns are known for their use in armor penetration studies and testing of new projectile shapes and materials. Single stage gas guns, like Marquette University's, have a large range of projectile velocities ranging from muzzle velocities less than 150 m/s to well over 1000 km/s. These types of guns are used for equation of state research, high strain rate testing of materials, creating new composite materials, testing the damage to air planes from bird strikes and low velocity impact of space debris. Two stage gas guns test in velocities in excess of powder or single stage gas guns. Space debris, ultra-high strain rates, fusion reactions [120] and EOS testing as well as modern weaponry are all tested with two stage gas guns. From this point, development may spread to even higher velocities with three stage gas guns [92] or guns with multiple pressurized chamber layers to overcome material strength limitations.

When thinking about gas guns it its useful to think in terms of strain rate. While the civil engineers amongst the population work under the isothermal range of material deformation, gas gun research moves far beyond the ranges of intermediate and high strain rates. Gas guns approach ranges of material deformations where even solid materials might instantaneously yield and flow in hydrodynamic fluid like flow.

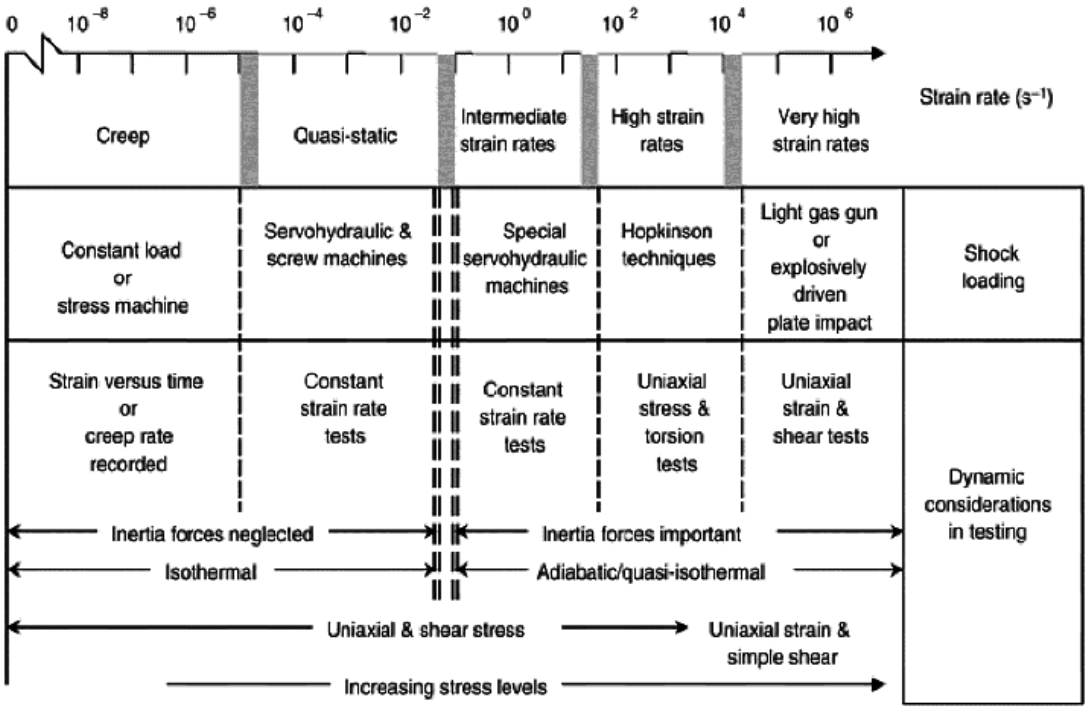

Figure 1.17 Typical testing setups and testing methods [121].

Light gas guns are also used to test the largest of the small sized projectiles. For small projectiles, light gas guns generally can produce experiments of meterorite and micro meterorite impact. Perfromance at even lower mass is often completed by plasma and electrostatic accelerators (Figure 1.18). With lower projectile mass projectile, speed can be increased, with the smallest of projectiles on the order of atoms in size being accelerated to over 99% the speed of light (296,794,533 m/s or 663,910,463 mph) at CERN [122]

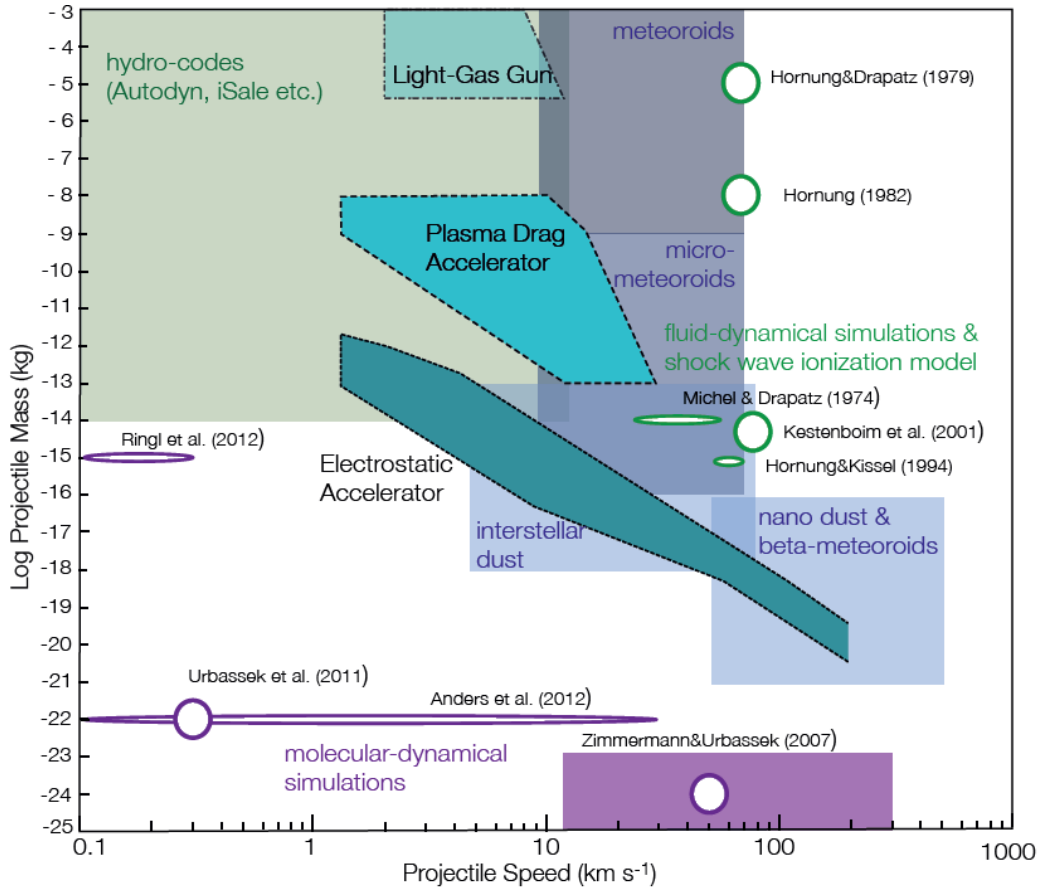

Figure 1.18 Projectile mass as a function of speed for three low mass accelerator types [123].

A plot comparing the muzzle velocities of some well-known gas gun facilities shooting projectiles at or above mesoscale is shown in Figure 1.19 below.

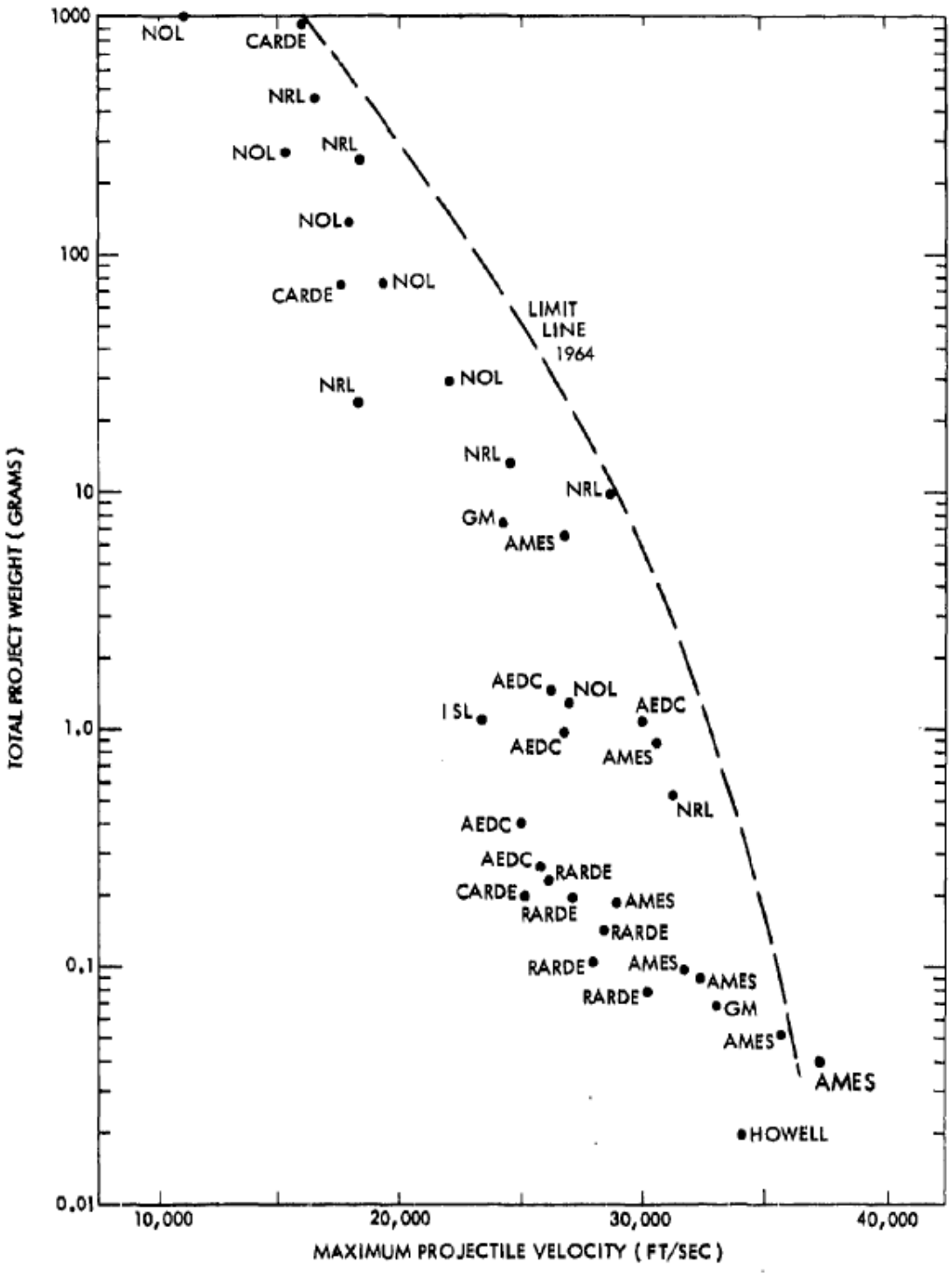

Figure 1.19 Plot of mass vs. speed of some well-known gas guns [150].

During the course of this research, this author had several opportunities to visit a variety of shock physics facilities both in the United States and abroad as shown below in Figure 1.20. While each facility functions using the same core principles guns are customized to suit experiment: using slotted barrels to maintain the aliment of the sabot with a target, manufacturing target tanks with additional hardware for using in cooling a sample, or the addition of new diagnostic equipment such as a high speed pyrometer. The author again wishes to thank the owners of these facilities, in which he was allowed to absorb knowledge offered freely by these research groups. Facilities visited included Harvard's single stage gas gun facility, which is now moving to UC Davis. This research group, headed by Sarah Stewart, researches geophysics and is well known for their research into the phases of water. STAR is a US Department of Energy facility at Sandia National Laboratories with several types of gas and powder guns. Their research covers a wide variety of studies ranging from defense to research. Georgia Tech's Facility does similar work to Marquette with a single stage light gas gun research in flyer plate experiments and granular material interactions. Finally, the University of Kent has a small two stage gas and powder gun, with a shotgun cartridge providing the first stage with power and compressed gas propelling the projectile. Kent utilizes their gas gun to model astrophysics events including their most recent publication on the viability of organisms reentering earth's atmosphere.

Harvard [95]

Shock Thermodynamics Applied Research [87]

Georgia Tech [100]

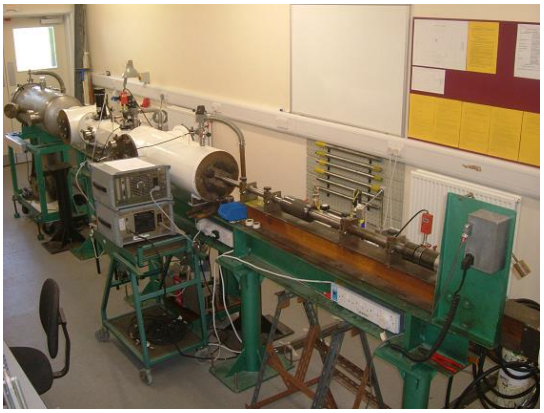

University of Kent [105]

Figure 1.20 Gas gun facilities visited by the author.

This literature review is by no means comprehensive, though it does provide a good overview of gas gun history and prehistory. For those seeking more detail, both A.C. Charters “Development of the high-velocity gas-dynamics gun,” [124] as well as H. F. Swifts “Light-Gas Gun Technology: A Historical Perspective” [73] are recommended.

After viewing other sources, these two articles admirably highlight historically relevant events, from a perspective closer to the field in detail greater than in the text above.

1.2.4 Marquette's History of Shock and Gas Guns

Marquette's Shock facility has a long-standing pedigree stemming from its inception with Dr. John Borg. By this time already, it seemed to the author that there was a fair bit of history developed. While this history is partially outside of the scope of this paper, it helps to both contextualize and provide reasoning for the newest gas gun's construction. It also provides a future historian with names, research developments and reasons to include Marquette University as an institute of interest within the field of shock research. The author apologizes in advanced for any missing or misinterpreted information, specifically with regards to past researchers in the years before 2015, as the researcher was involved in middle school to undergraduate academic teaching exercises during this period. For those that wish to skip the brief summary of past Marquette Shock Physics Research that follows a timeline is presented below in Figure 1.21.

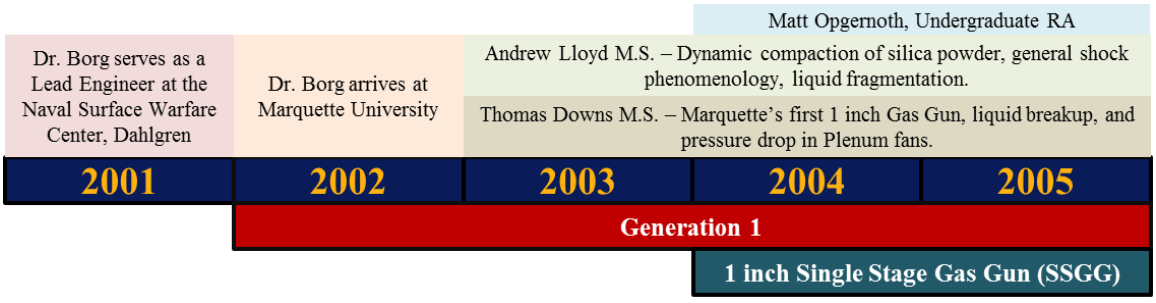

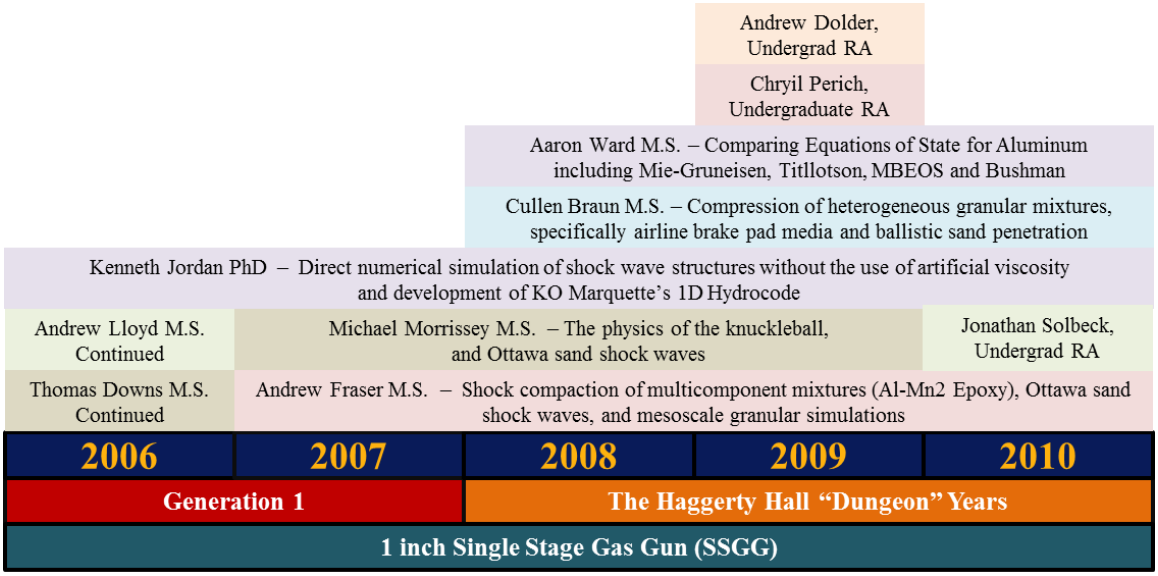
Andrew Dolder, Undergrad RA
Chryil Perich, Undergraduate RA
Aaron Ward M.S. – Comparing Equations of State for Aluminum including Mie-Gruneisen, Titllotson, MBEOS and Bushman
Cullen Braun M.S. – Compression of heterogeneous granular mixtures, specifically airline brake pad media and ballistic sand penetration
Kenneth Jordan PhD – Direct numerical simulation of shock wave structures without the use of artificial viscosity and development of KO Marquette's 1D Hydrocode
Andrew Lloyd M.S. Continued
Michael Morrissey M.S. – The physics of the knuckleball, and Ottawa sand shock waves
Jonathan Solbeck, Undergrad RA
Thomas Downs M.S. Continued
Andrew Fraser M.S. – Shock compaction of multicomponent mixtures (Al-Mn2 Epoxy), Ottawa sand shock waves, and mesoscale granular simulations
2006
2007
2008
2009
2010
Generation 1
The Haggerty Hall "Dungeon" Years
1 inch Single Stage Gas Gun (SSGG)

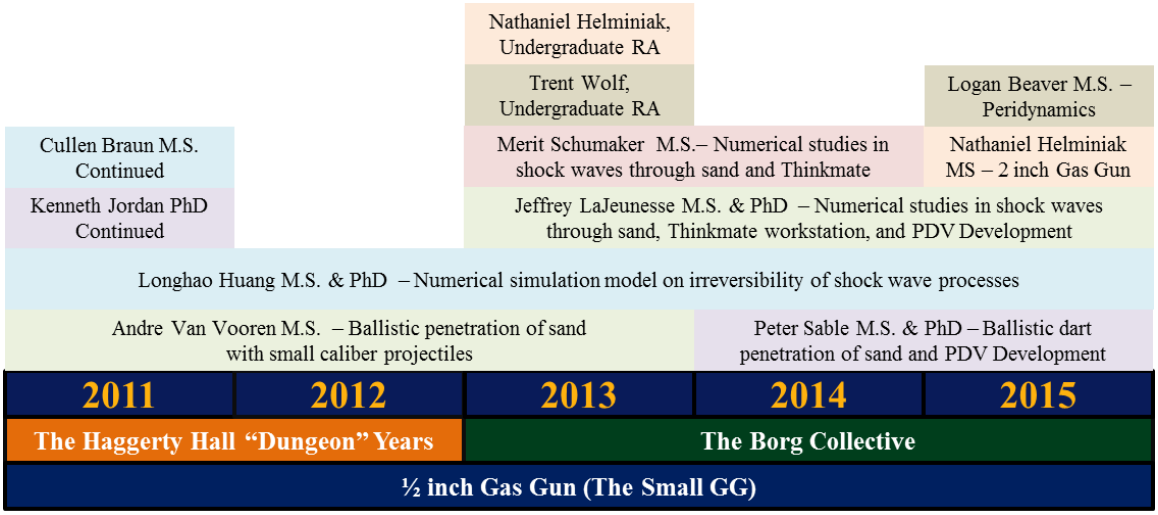
Nathaniel Helminiak, Undergraduate RA
Trent Wolf, Undergraduate RA
Logan Beaver M.S. – Peridynamics
Cullen Braun M.S. Continued
Merit Schumaker M.S.– Numerical studies in shock waves through sand and Thinkmate
Nathaniel Helminiak MS – 2 inch Gas Gun
Kenneth Jordan PhD Continued
Jeffrey LaJeunesse M.S. & PhD – Numerical studies in shock waves through sand, Thinkmate workstation, and PDV Development
Longhao Huang M.S. & PhD – Numerical simulation model on irreversibility of shock wave processes
Andre Van Vooren M.S. – Ballistic penetration of sand with small caliber projectiles
Peter Sable M.S. & PhD – Ballistic dart penetration of sand and PDV Development
2011
2012
2013
2014
2015
The Haggerty Hall "Dungeon" Years
The Borg Collective
½ inch Gas Gun (The Small GG)

Figure 1.21 The history of Marquette's Shock Physics Laboratory, 2001-2017.

Marquette's shock physics history begins with Dr. John Borg; a doctorate, full professor and recent Mechanical Engineering Department Chair with initial academic background in the areas of Fluids and Turbulence. From here Dr. Borg would become lead engineer at the Naval Surface Warfare Center Computational Physics Group (1997-2002) with shock physics related projects, including work involving the experimental fracture of steel liquid filled cans (shown in Figure 1.22 below).

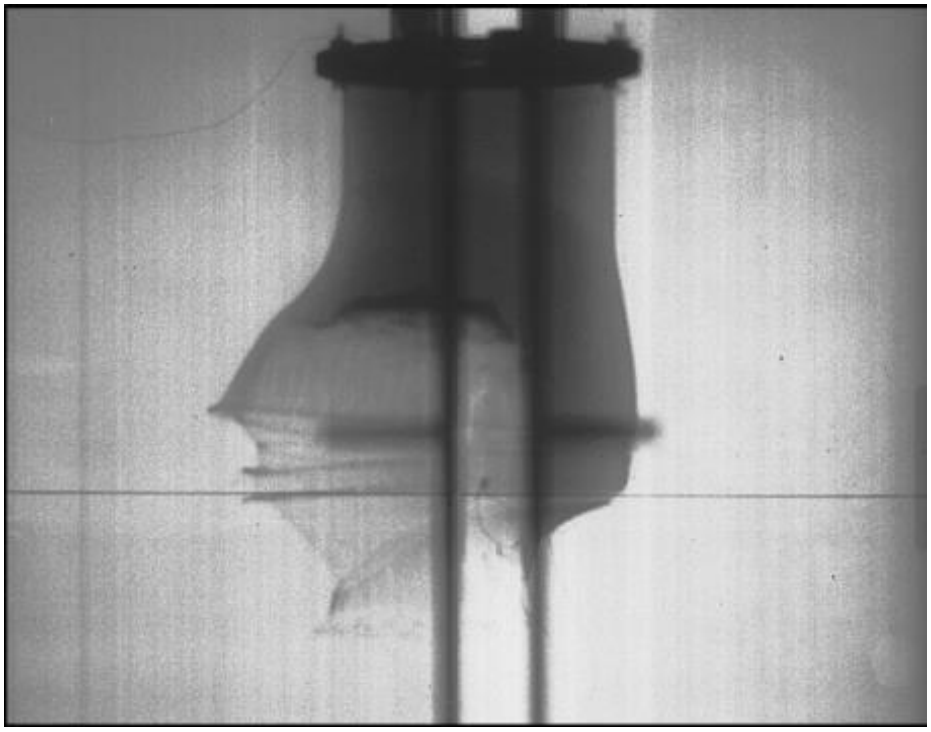

Figure 1.22 Liquid filled steel cylinder fragmentation experiment [125].

The first generation of shock students at Marquette University spanning the years between Dr. Borg's arrival at Marquette University in 2002 and 2006, consisted of two graduate students, Andrew Llyod and Thomas Downs, and an undergraduate student, Matt Openorth. This trend of graduate student pairs would continue with new sets of graduate students every 2 to 3 years and undergraduate assistants.

From the literature, Tom Downs [126] was the main force behind the creation of Marquette's first experimental 1 inch dual diaphragm single stage light gas gbun Figure 1.23. After the creation of this light gas gun, T. Downs used the experimental setup to conduct shock experiments for liquids and porous media. Within his thesis T. Downs mentions undergraduate M. Opgenorth in to Marquette faculty and employees for their assistance in building the gas gun.

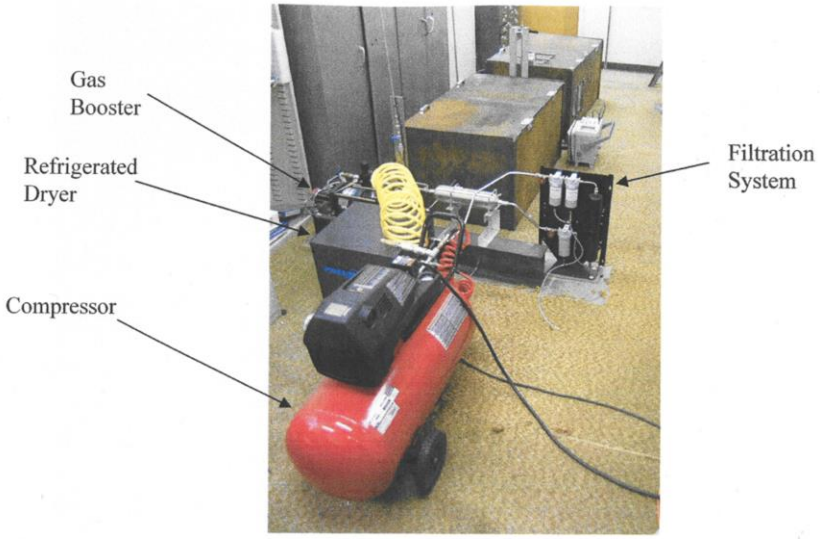

Figure 1.23 Marquette's original 1 inch single stage light gas gun.

During this same period, Andrew Llyod [127] would begin the use of CTH as well KO hydro-codes, still in use by the Marquette physics lab, comparing the numerical compaction of silica powder within CTH and KO against experimental data obtained at Marquette Figure 1.24.

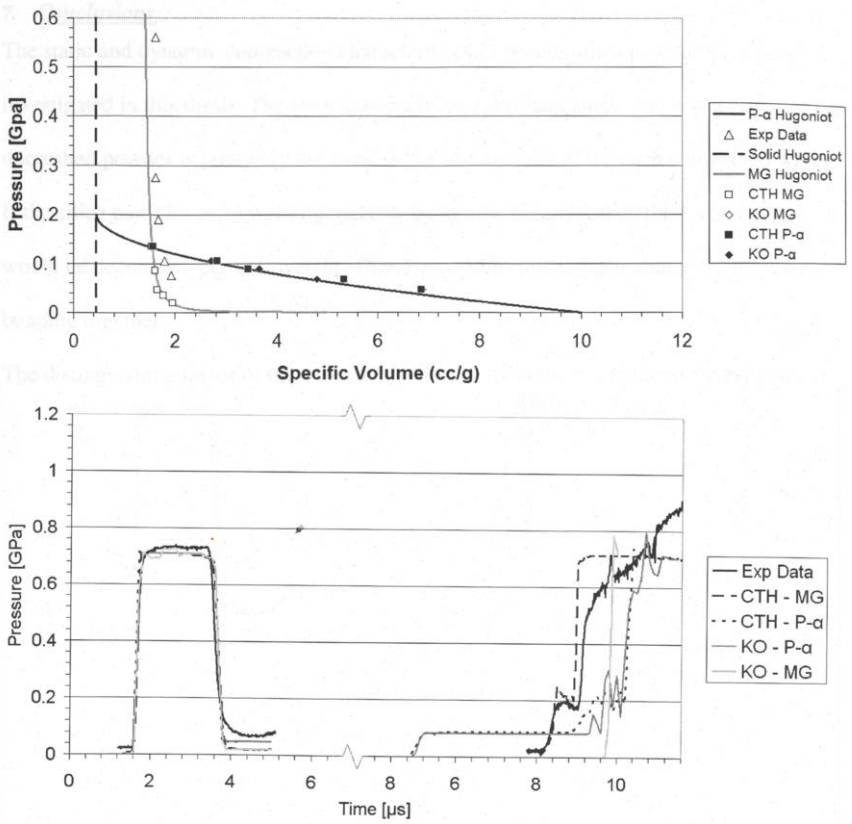

Figure 1.24 P-v plot (above) of Hugoniot curves and P-t diagram (below) for a flyer impacting a 0.1 g/cc silica sample at 405 m/s.

After the graduation of these three, student publications slow until the second generation of Marquette shock physics students, referenced in Andrew Fraser's Master thesis as the "Dungeon" graduate students. This moniker was so coined as the shock physics lab at that point in history was kept in the basement of Haggerty Hall.

The first set within the Haggerty "Dungeon" consisted of the following Graduate groups: (1) Andrew Fraser, Kenneth Jordan and Michael Morrissey; (2) Aaron Ward and Cullen Braun; and (3) Andrew Van Vooren and Longhao Huang. Undergraduate students within this group consisted of Andrew Dolder, Chyril Perich, Johnathan Solbeck, and Jeff Midday.

Beginning with Andrew Fraser [128], research was conducted on shock compaction of multiple component mixtures with numerical simulations of Al-MnO2-Expoxy, shown in Figure 1.25, matching well with experiments conducted at the NSWC-Indian Head 4in Gun Range. Amongst those mentioned in his thesis, A. Ward thanks Jeff Midday and Michael Morrissey.

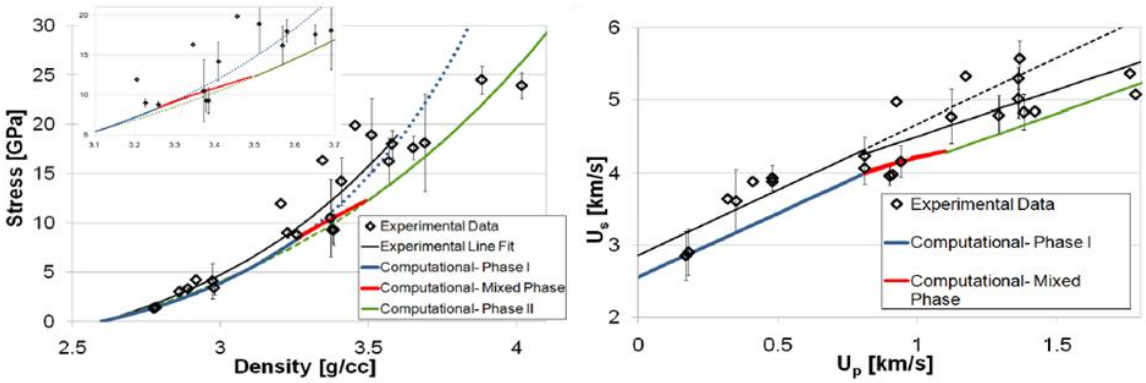

Figure 1.25 Stress, density, and Us Up relations for Al-MnO2-expoxy.

Michael Morrissey's [129] thesis, not on shock, but rather the aerodynamics of the knuckleball (Figure 1.26), showcased how the seams and initial throwing conditions affect the evolution of ball trajectory and behavior, which brought much recognition to the Mechanical Engineering Department. While not playing baseball, M. Morrissey also conducted work on waveforms within Ottowa sand with graduate Andrew Fraser and undergraduate Chyril Perich. Within his acknowledgements M. Morrissey thanks fellow graduate student Aaron Ward as well as undergraduate Andrew Dolder.

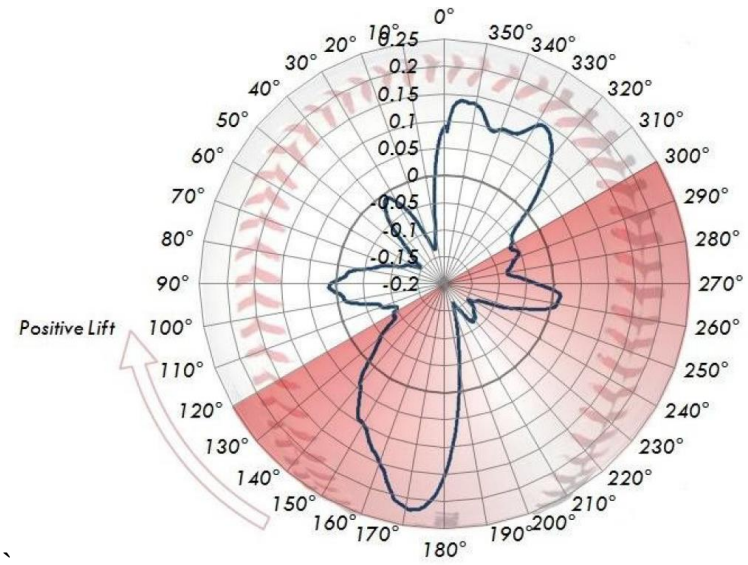

Figure 1.26 Lift in lbs experienced by a baseball traveling at 70 mph rotating at 50 rpm, red is indicative of behavior experienced by a knuckle ball.

Aaron Ward [130] performed his thesis work on the examination of different types of equations of state, comparing the well know Mie-Gruneisen with Titllotson, MBEOS and Bushman, shown below in Figure 1.27. Results of this thesis found that the Bushman EOS performed better than other EOS under strong shock at pressures greater than 1.5 Mbar.

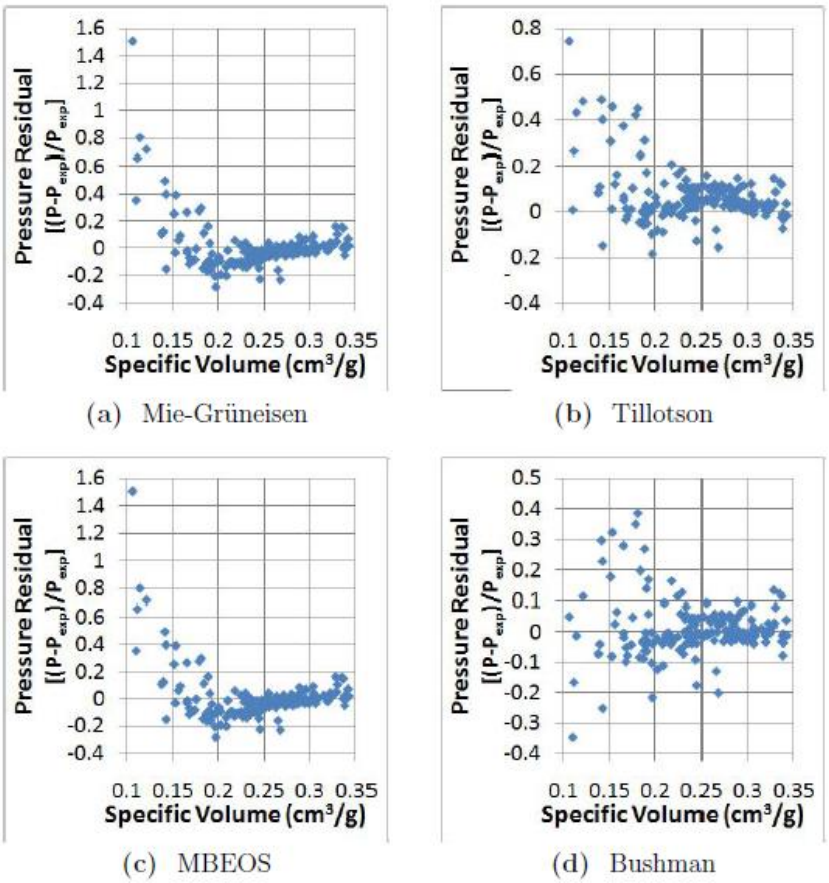

Figure 1.27 Pressure residuals taken from various equations of state for varying specific volume.

Cullen Braun [131] researched the rapid compression of heterogeneous granular mixtures for use in aviation brake pads (below in Figure 1.28). From his work with the 1 inch single stage gas gun, he was able to develop an equation of state and bulk sound speeds for this specific material. Cullen Braun mentions Andrew Fraser and Ken Jordan as helpful fellow graduate students.

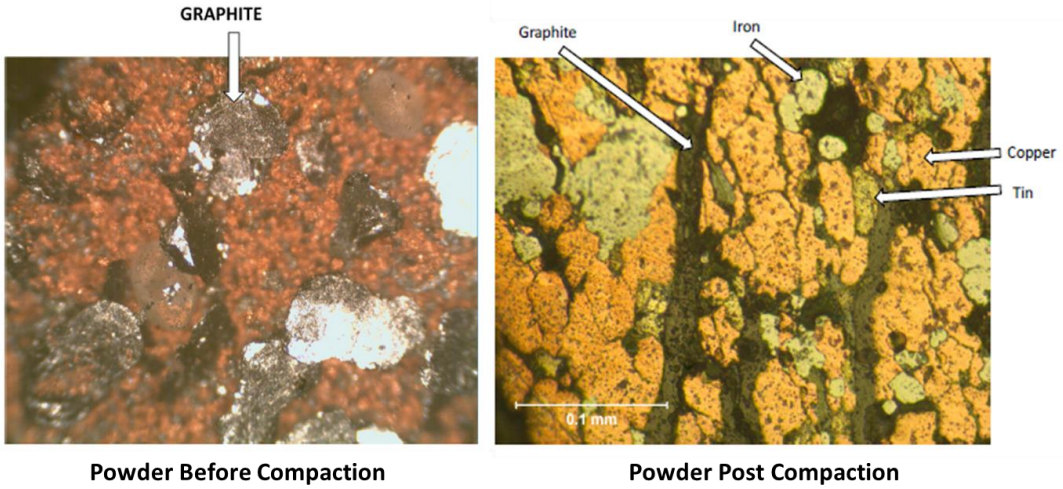

Figure 1.28 Dynamically compacted aviation brake powder at 0.203 GPa.

Kenneth Jordan's thesis [132] developed Marquette's one dimensional hydrocode KO based on Wilkins One Dimensional HEMP Formulation [66]. His work successfully simulated shock wave with an irreversibility model, shown in Figure 1.29, rather than artificial viscosity, reducing numerical error with the Mie-Gruneisen Equation of State.

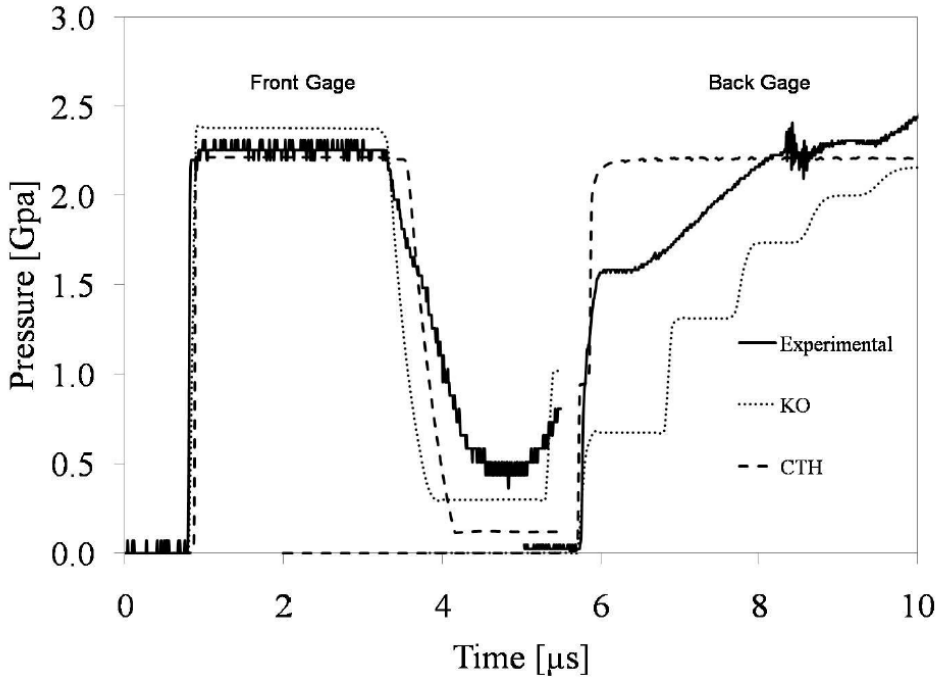

Figure 1.29 Comparison of shock pressure measured for 0.1g/cc porous silica at 1100 m/s.

Longhao Huang's research [134] focused on numerically simulating the irreversibility of shock waves within gases and water focusing on the Mie-Gruneisen Equation of State. In addition to parameter evaluation of water, his work also found that the shock wave thickness did not seem to be a function of specific heat, heat conductivity, viscosity nor length scale (see Figure 1.30). Longhao decided to continue past his Masters and still continues towards his PhD.

Parameters Evaluation, Water

Mach#	Up	S	C0	γ_0	uv	h_x	*Nodes*
1.323	277.867	1.920	1650	4.984	3.100	1/8	4800

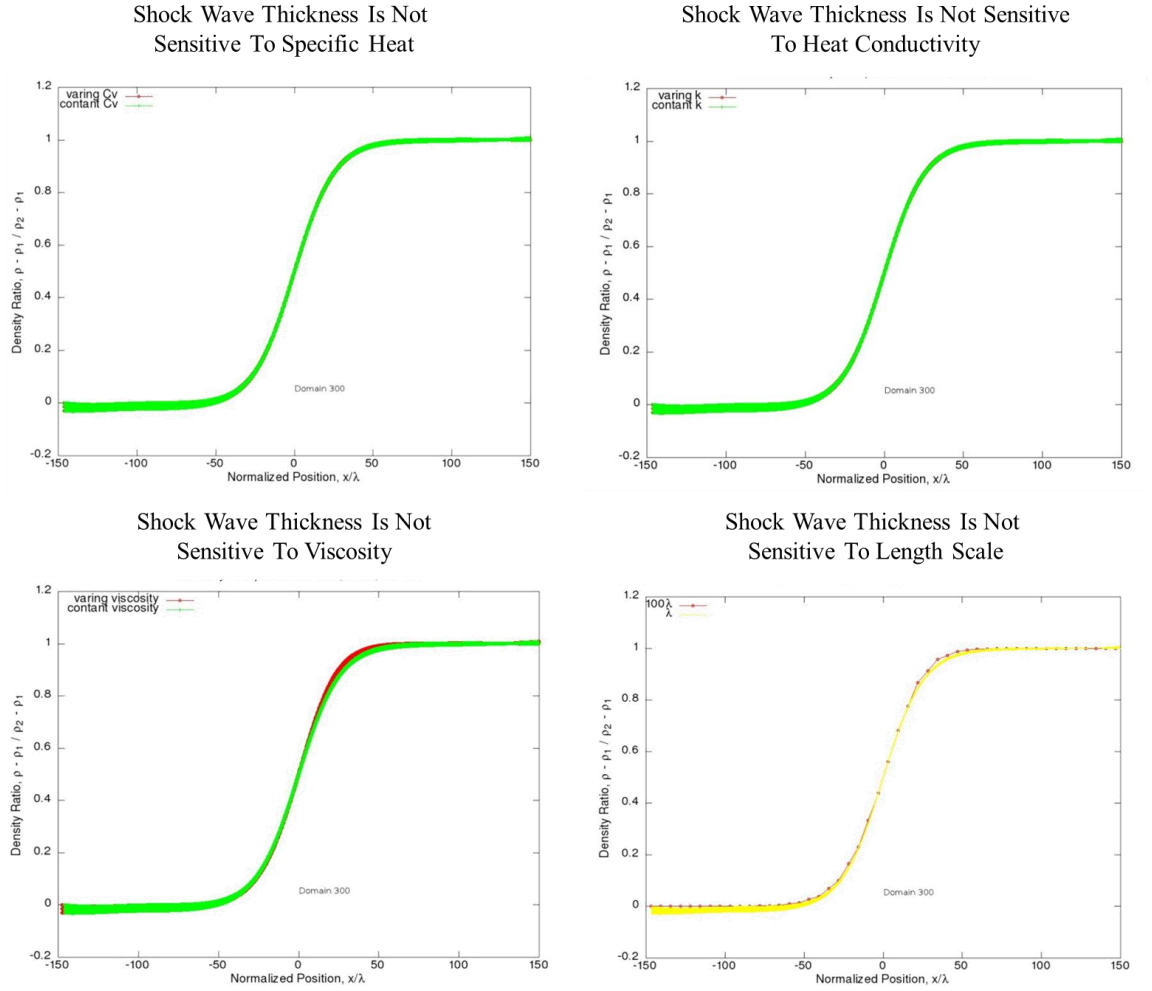

Figure 1.30 Sensitivity analysis of water equation of state.

Finally Andrew Van Vooren [133] researched the behavior of heterogeneous materials under dynamic loading, dart penetration into sand, both experimentally with Marquette's ½ in gas gun and numerically within EMU peridynamics. His results found longitudinal and shear wave sound speeds as 263 m/s and 209 m/s respectively and improved penetration with conical and hemispherical dart tips.

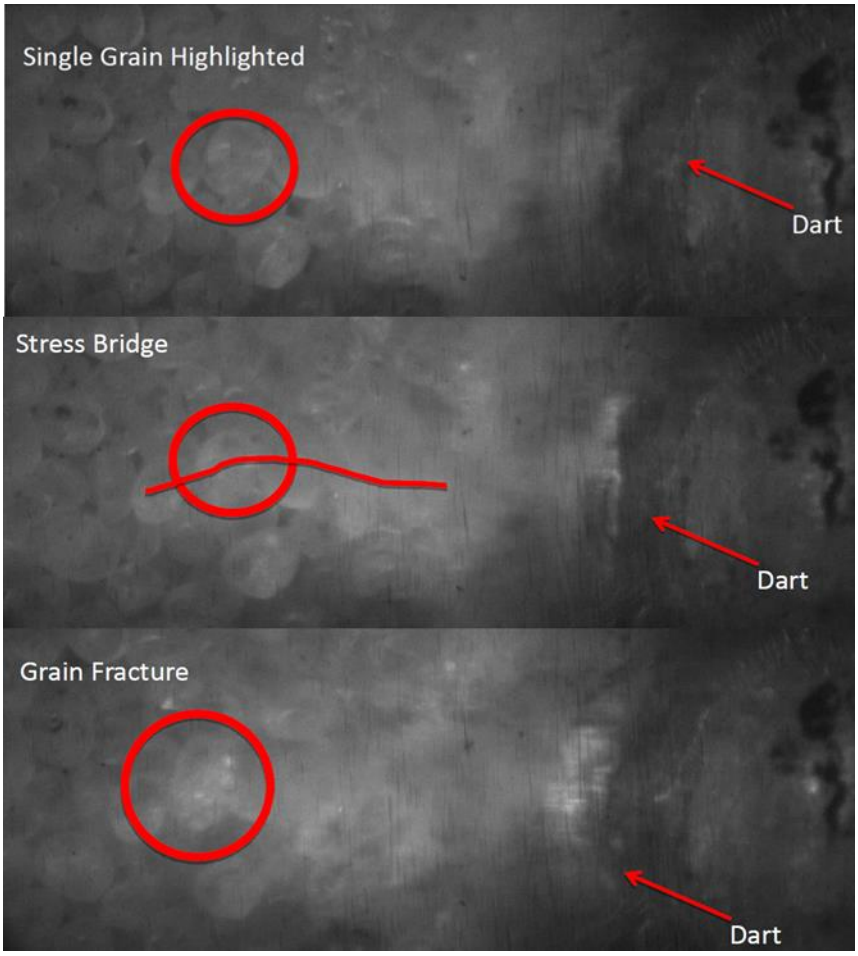

Figure 1.31 Progression of fracture within a single grain of sand.

Of significant note for this report, it was during this period that the development of Marquette's ½ inch gas gun (Figure 1.32) was constructed by Cullen Braun and Andrew Fraser. Of this second generation, the author was able to meet Andrew Van Vooren, an end user of the developed ½ inch gas gun, during his final days of work with the ½ in sand penetration gun after its relocation to Engineering Hall. After A. Van Vooren left in the Fall of 2013, the lab was empty for a short week until the arrival of the third generation of shock physics students.

Figure 1.32 Marquette's 1/4 inch single stage light gas gun.

This latest group, of which the author considers himself a part, consists of the following individuals known as the Borg Collective (shown in Figure 1.33 below).

Figure 1.33 Marquette Shock Physics Borg Collective.
(left to right): Emilie Teitz, Logan Beaver, Nathaniel Helminiak, Dr. John Borg, Longhao Huang, Jeff LaJeunesse, Peter Sable and Janaka Kosgolla.

The convention of naming labs seems to have grown either from the original Haggerty Dungeon Dwellers or the ever-present Wede Lab run by Dr. Philip Voglewede's Dynamics Group (designated by a dandelion). On this brief tangent, the Borg Collective has noticed other named laboratories appearing at Marquette: the Allen Wrench Engine Research lab (also sometimes referred to as the tadpoles) run by Dr. Casey Allen, and the Singer Nation run By Dr. Simcha Singer, which simulates particle combustion. Perhaps this is a trend will continue…?

Returning to the current generation, new groups of graduate students (Jeffery LaJeunesse, Merit Schumaker, Peter Sable, Nathaniel Helminiak, Logan Beaver, Emilie Teitz and Christopher Johnson with undergraduates Trent Wolf and Ashley Hatzenbihler) continue at present from prior group efforts. Janaka Kosgolla, shown in Figure 1.33, was a post-doctoral student, who work closely with Dr. Borg and would frequently interact as a coworker and friend.

Both Merit Schumaker and Jeffery LaJeunesse worked closely together on the shock wave propagation within heterogeneous materials and together built the lab's 64 core workstation "Thinkmate" presumably named after the company supplying the hardware. The undergraduates, Trent Wolf and Nathaniel Helminiak, during the summer of 2013, worked on parts of the ½ in gas gun and would observe and organize some mysterious objects taking up space within the shock physics lab (Figure 1.34). The author obviously decided to become a graduate student and continue work on those mysterious objects.

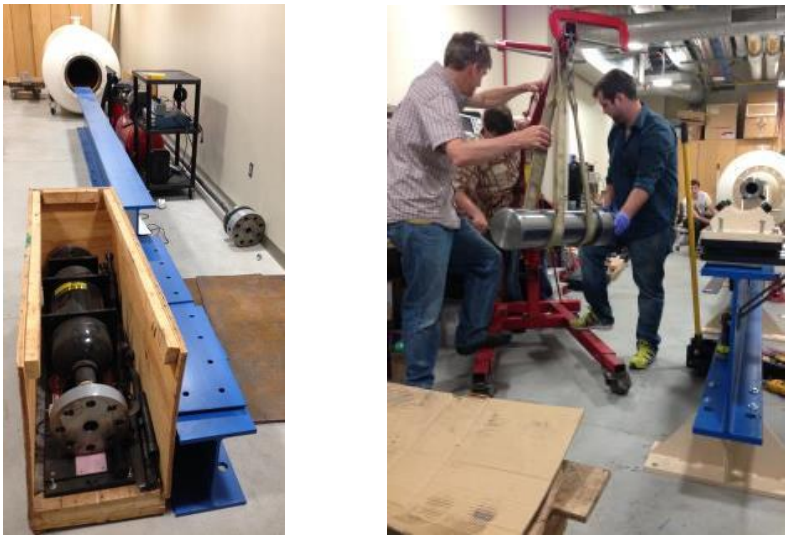

Figure 1.34 Mysterious components within the Shock Physics Lab, and later installation of completed design.

Merit Schumaker's thesis [136] focused on the numerical simulation of heterogeneous brake pad media undergoing dynamic compaction within CTH. By use of this numeric technique, one could examine grain interaction (shown in Figure 1.35) in a way which could not otherwise be seen with current experimental measurement methods. Noted was CTH's model of internal energy not directly capturing frictional heat and irreversibility.

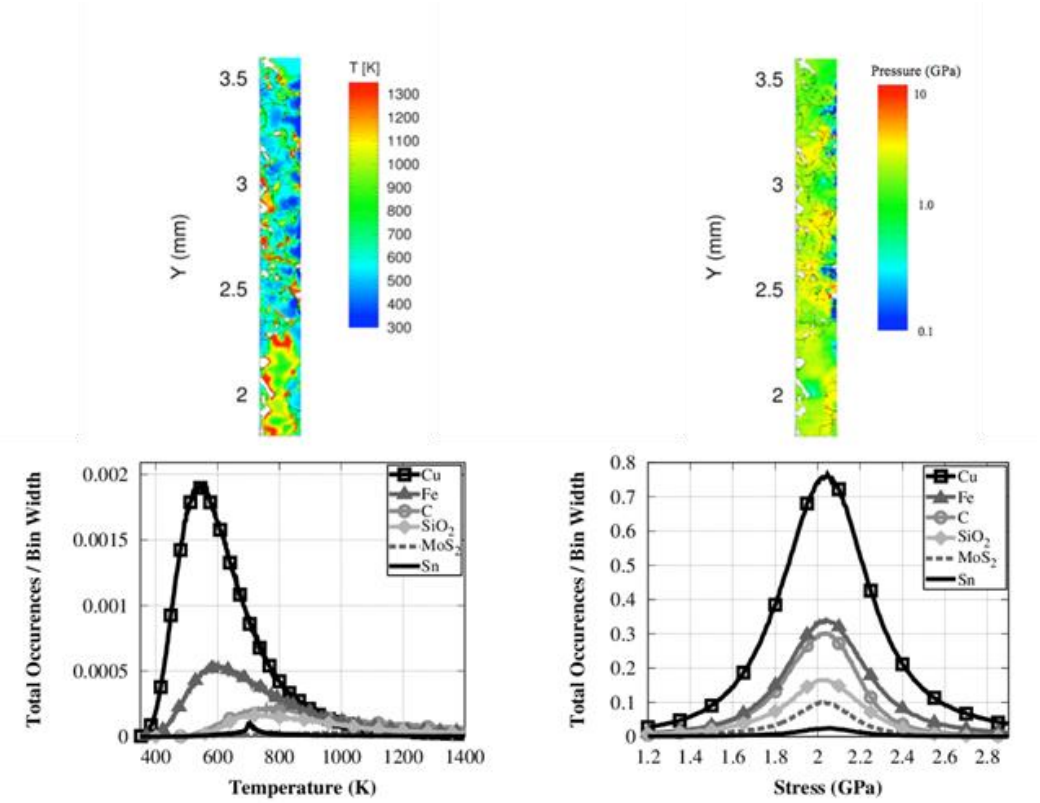

Figure 1.35 Two dimensional sections of temperature and stress paired with distributions of temperature and stress experienced during the simulation of airline break powder from an impact of 800m/s.

Jeffery LaJeunesse [135] in his thesis conducted similar work modeling velocity profiles of shocks within sand of various grain diameters. Within his work, findings indicated that a single simulation over a small sampling of experimental domain might roughly capture the shock rise and steady state behavior on the rear of a sample. Of importance, as shown in Figure 1.36, was a need to examine and average the behavior of multiple tracers within the simulation for bulk behavior.

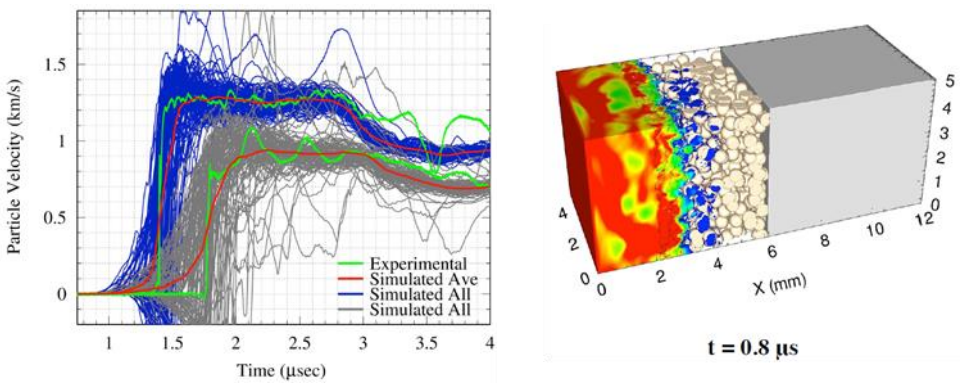

Figure 1.36 Particle velocity profiles and domain for 425-500 µm diameter sand grains.

Joining M. Schumaker and J. LaJeunesse one year later, Peter Sable [137] finished work on sand penetration with Marquette's ½ inch gas gun. His work, shown in Figure 1.37 below, utilized a digital image correlation (DIC) technique to better characterize sand interation with a kinetic pentrator. Through this, a better understanding was of the mechanisms by which the kinetic energy of the projectile transferred irreversibly into heat, grain motion, compaction and grain fracture. In addition, the diffusion of momentum was found to have a positive relation with projectile velocity.

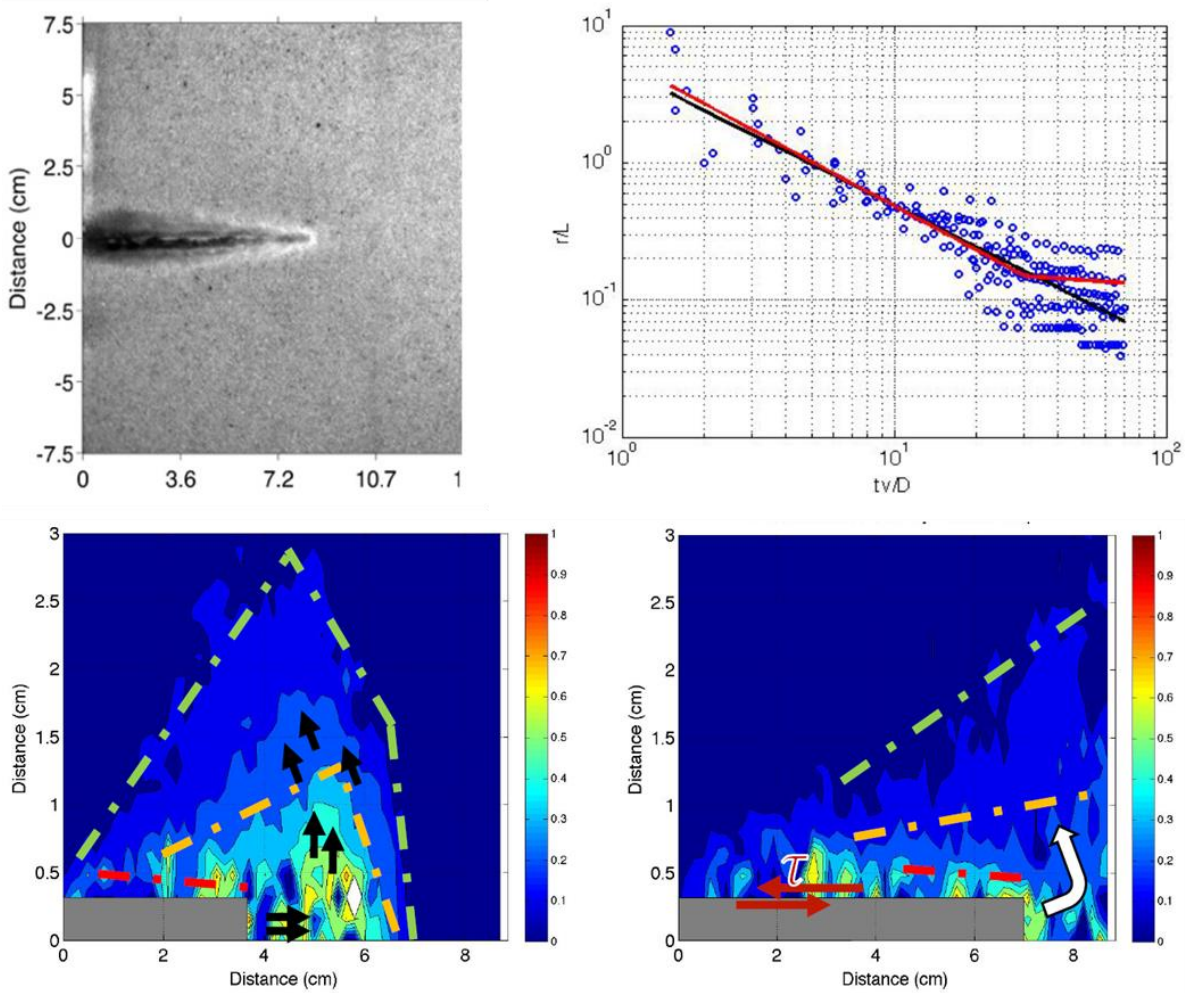

Figure 1.37 Normalized view of experimental velocity data taken from PIV (data clearly shows the shear effects near the projectile wall in addition to the location of the compaction wave created by the projectile). A non-dimensional plot of momentum diffusion with non-dimensional time shows a linear relationship between momentum, diffusion and projectile velocity.

Of these last three graduate students, both J. LaJeunesse and P. Sable decided to continue their research at Marquette University as PhD students where they continued work on shock compaction, pressure shear numerical simulations within CTH and experimental data capture.

Logan Beaver [138] worked on two major projects. While his initial project experimented with peridynamic simulation of granular mechanics, this study was eventually shelved in favor of explosive simulations. His work utilized Marquette's KO model alongside CTH to model the effects of changing the ratio between explosive's radius and liner radius within exploding cylinders (see Figure 1.38). In addition, this work compared the computational results of several parametric optimization studies comparing genetic, gradient descent, and dividing rectangles algorithms.

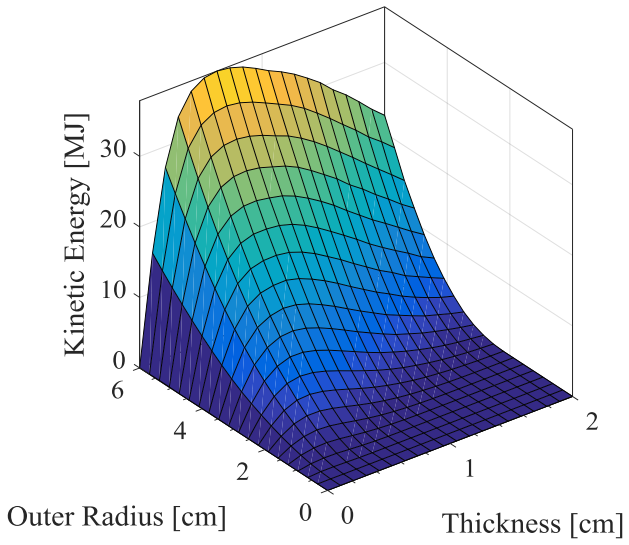

Figure 1.38 The kinetic energy output of an aluminum cylinder driven by an explosive TNT charge as a function of outer radius and wall thickness. The materials used were aluminum for the wall and TNT for the explosive.

Emilie Teitz [139] worked as a one year master's student and conducted shock experiments within water shown in Figure 1.39. Her work continued to utilize the ½ inch

gas gun and tested some of the new remote firing systems added to the gas gun for increased researcher safety.

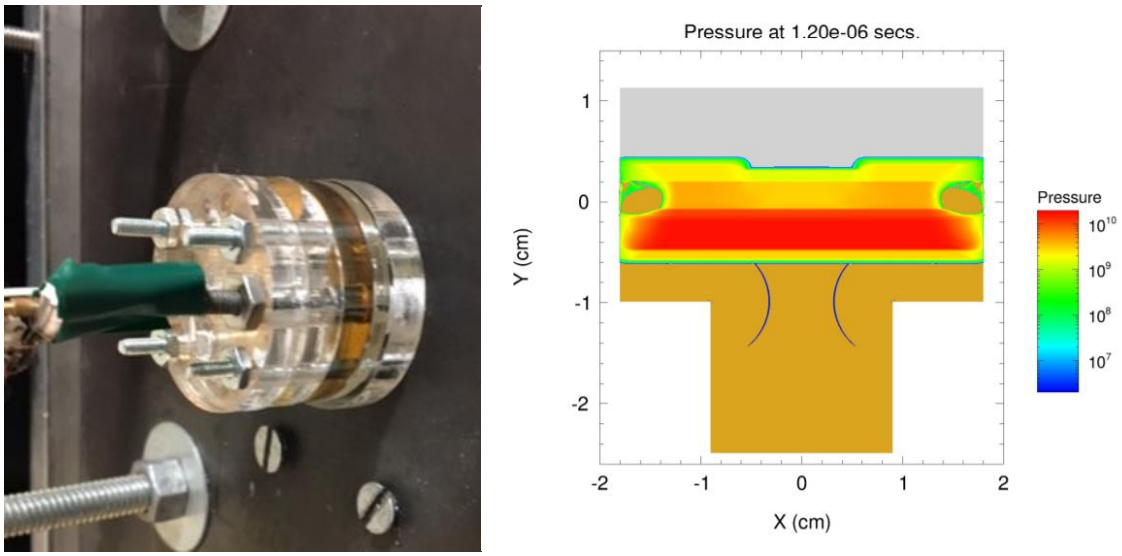

Figure 1.39 Experimental Setup and numerical simulations of shock waves through water.

Christopher Johnson, the most recent member of the Marquette Shock physics community has continued development of the PDV System. His stationary work and that using a rotating Dremel wheel has given the group added confidence that the PDV system can accurately resolve the normal and transverse surface velocity components. The experimental setup is presented in Figure 1.40 below. Developments from this work will include the best material surface treatment and best practices to resolve velocity components from pressure shear experiments.

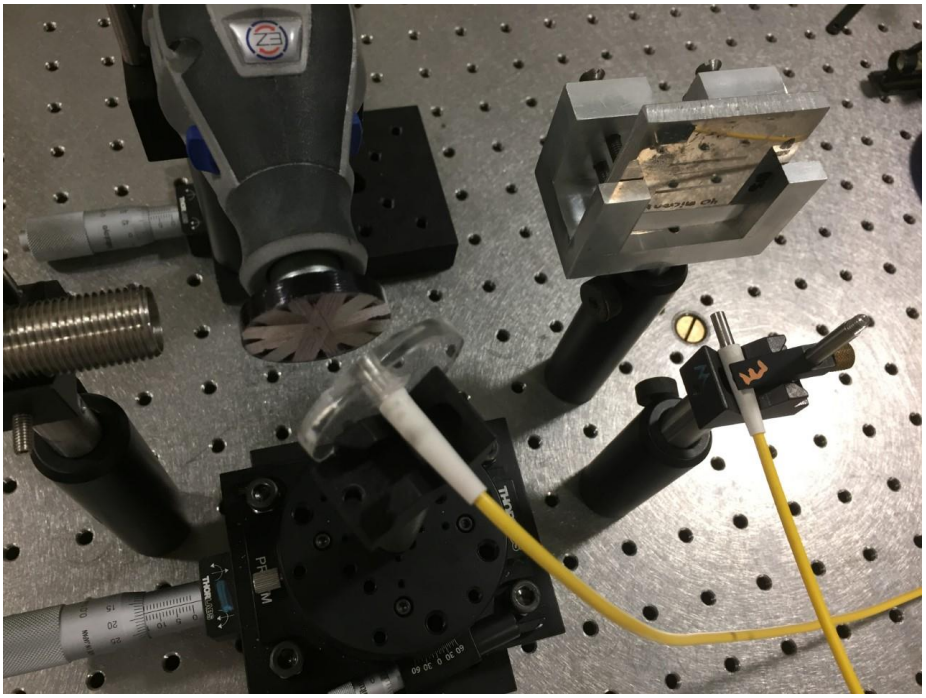

Figure 1.40 Optical PDV setup with yellow collimators testing moving targets (spun on the Dremel) and stationary targets such as the rectangular clamped sample.

The author would like to take this opportunity to thank the members of the Shock Physics Group and other members of the community for laying a foundation upon which this researcher could build and contribute. The review above is by no means comprehensive but it is hoped that a concise history of the field might push readers to explore more sections of history in depth. Thus ends the historical review of shock physics research and gas gun history presented by this researcher. Topics appearing within the text include references to other related fields relevant to the section in which they reside.

2. CONSTRUCTION

This section comprises the design aspect behind Marquette's new 2 inch dual diaphragm single stage gas gun shown below in Figure 2.1. Designed to run on either a cylinder of nitrogen or building supplied pressurized air, this system is meant to be a long term experimental test bed for use by future shock researchers at Marquette University. Care has been taken to ensure that safety of researchers is maintained through the preparation and firing process in both construction, covered here, and policy, covered later. This section attempts to both verify the safety of the gun from a design standpoint as well as provide a complete listing of components necessary for replacement and day to day operations. This will not cover specific diagnostic equipment such as particular oscilloscope and only a brief overview of systems such as the PDV or Dynasen pin setup which are out of the scope of this paper. Suggested resources for this information include papers written by previous member of the Marquette shock physics community, which are referenced in the previous historical section 1.2.4.

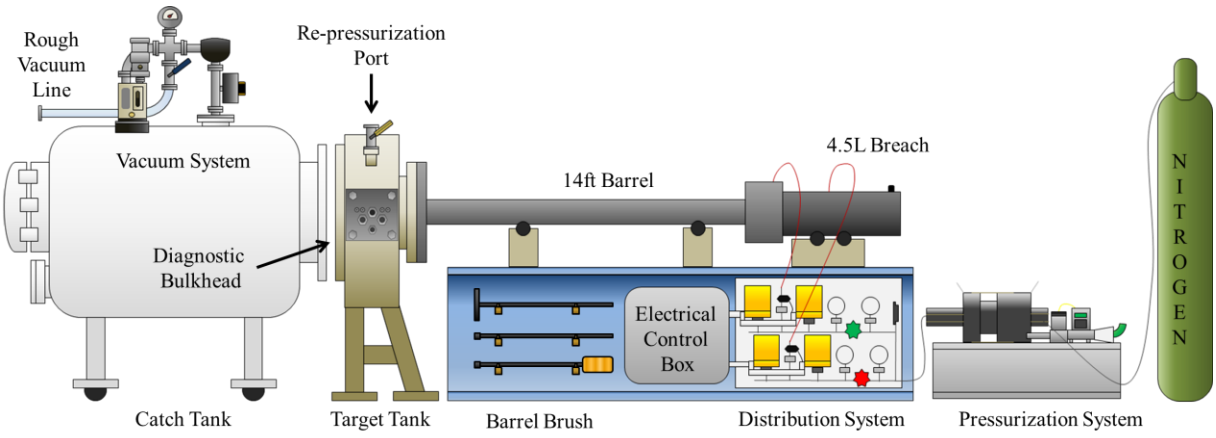

Figure 2.1 Preliminary concept showcasing the gun system overview.

2.1 Static Gun Components

2.1.1 Breach

The Marquette gas gun begins with an air source, supplied by either the 120 psig building line or a 3,000 psig nitrogen tank from Airgas. Utilizing a Haskel pneumatic piston compressor, the pressurization system can charge the breach and trigger cavity up to the operational pressure of 10 ksi. Flow into and out of the breach and burst disk cavity is remotely controlled by a set of four independently actuated valves, while a safety valve ensures that the system remains at safe operating pressure. These will be covered in greater depth in the active systems section.

The breach of the gas gun is the storage reservoir where the system's future kinetic energy reserves are stored as potential energy in the form of a pressurized gas. While the breach can be thought of in loose terms as a gas tank, it is important to note that it also serves as the structure of the dual diaphragm launch system, allowing for the placement of burst disks within the breach assembly.

Upon receiving the breach and barrel assembly from Physics Applications Inc. both the barrel and breach were rinsed in oil and tailings from the manufacturing process were recovered in large quantity from both breach and barrel which were used to identify the material utilized.

Figure 2.2 Discovery and removal of tailings.

While the tailings were too small to test in a hardness tester, the availability of Marquette's Scanning Electron Microscope allowed for an elemental breakdown of the metal. The metal based on the presences of both Chromium and Molybdenum (shown in Figure 2.3 below) in addition to Magnesium, Iron, and Carbon, fit the composition of the 41xx series of steel [140]. Reviewing the metal compositions, it is assumed that both the barrel and breach were formed from 4135 or 4140 Steel commonly referred to as ordnance or gun steel [141].

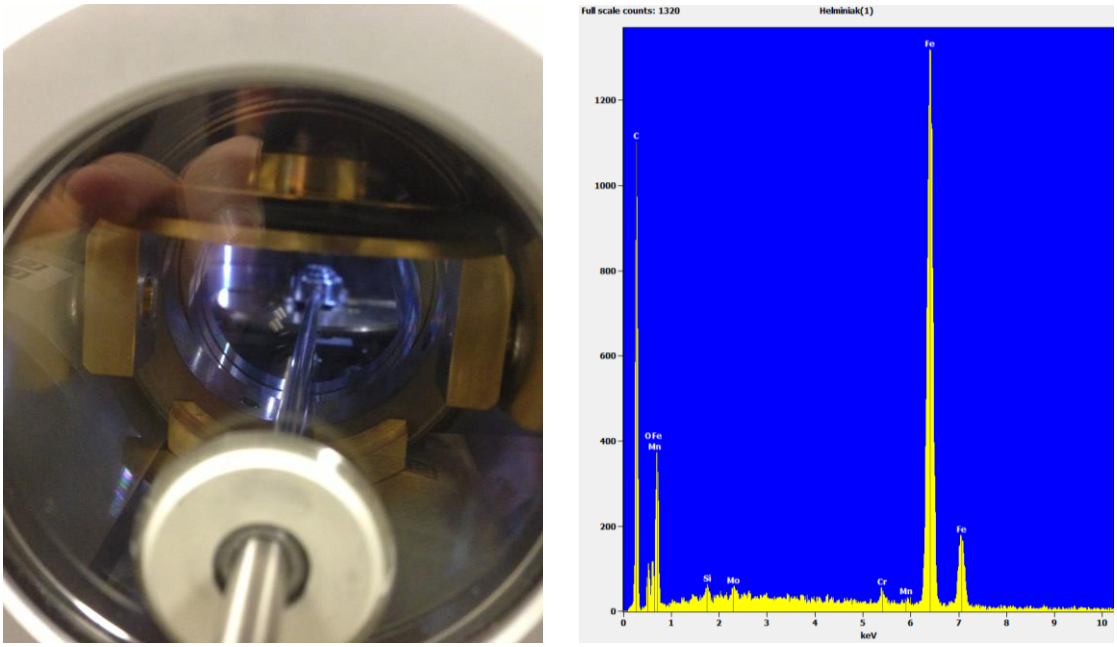

Figure 2.3 Scanning electron microscope and sampled material composition.

In order to verify the ability of the received breach and assess the pressurization safety factor, CES Edupack's data on AISI 4135 Steel (The lower carbon conservative estimate) was utilized summarized below in Table 2.1 and Figure 2.4.

Table 2.1 Mechanical Properties of AISI 4135 Steel [142]

Mechanical Properties	Value	Units
Young's Modulus	29-30.5	10^6 psi
Yield Strength	70.1-85	ksi
Tensile Strength	90.1-100	ksi

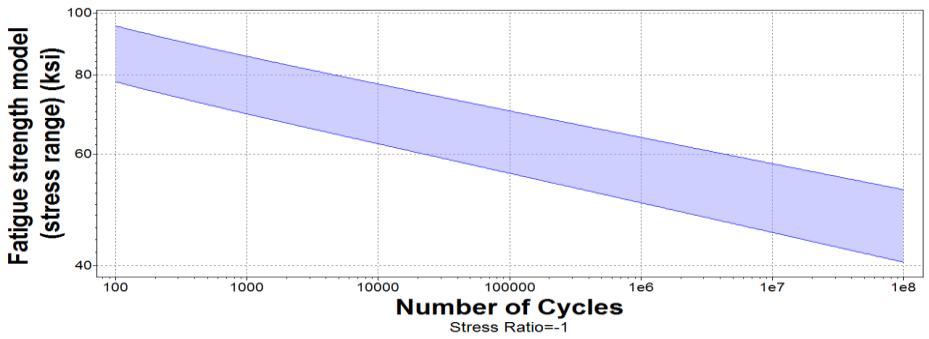

Figure 2.4 Fatigue strength of AISI 4135 steel [142].

Having identified the breach material, one can now verify the engineering and safety of the delivered parts. In order to evaluate the safety of the breach it is necessary to examine both the shell and cap head. Breach dimensions are given below in Figure 2.5.

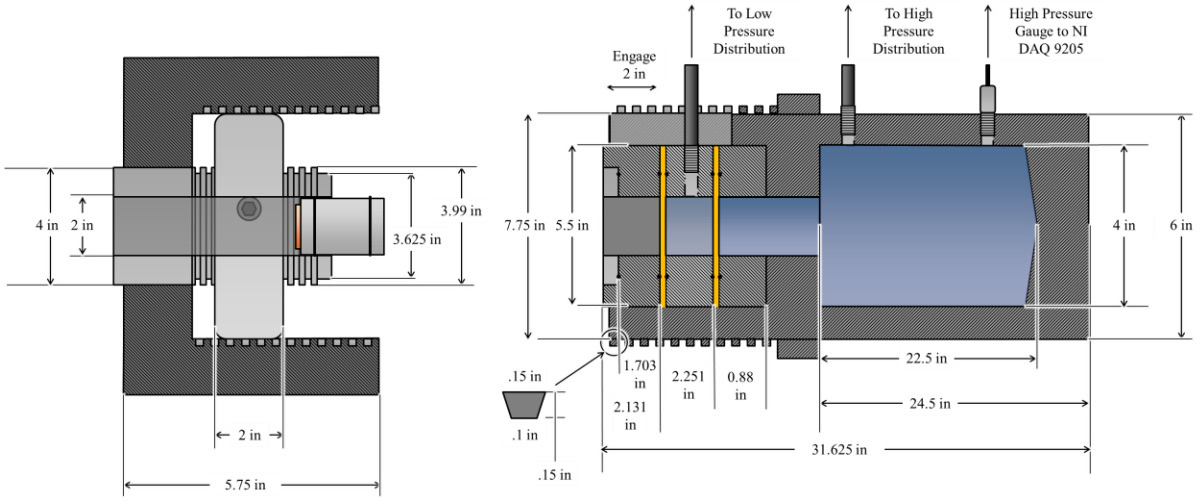

Figure 2.5 Breach assembly and dimensions (taken by caliper).

Starting with the design of the breach's shell examining both the hoop and longitudinal stress given by the equations below:

$$\sigma_\theta = \frac{PR}{t} \tag{2.1}$$

$$\sigma_{long} = \frac{PR}{2t} \tag{2.2}$$

While these equations represent the ideal stress experienced in the circumferential and longitudinal direction a number of safety factors (Corrosion, Tolerance, Weld Efficiency) have been added by the ASME Boiler and Pressure Vessel Code [143] in order to ensure safe operating standards. Table 2.2 below contains dimensions and constants relevant to the breach, in addition to suggested constants given within the ASME literature.

Table 2.2 Properties of the Marquette Breach Relevant for its Shell

Variable	Symbol	MU Breach	Units	Variable	Symbol	MU Breach	Units
Working Pressure	P	10,000	Psig	Wall Thickness	t	1	inch
Yield Stress	S	70,100	Psi	Corrosion Allowance	C_a	0.01	inch
Outer Diameter	D_o	6	Inch	Tolerance	Tol	0.01	inch
Length	L	22.5	Inch	Weld Joint Efficiency	E	0.95	-

Analysis of the breach begins with the adjustment of shell thickness to account for corrosion and machining tolerances:

$$T_c = t - C_a - tol \tag{2.3}$$

where T_c is modified shell thickness, C_a corrosion tolerance, and a machining tolerance tol for the life of the shell. From shell thickness, corroded radius is found:

$$R_c = \frac{D_o}{2} - T_c \quad ` \tag{2.4}$$

where R_c is the resultant corroded shell inner radius, D_o is the nominal shell diameter, and T_c is the corrosion tolerance. Circumferential and longitudinal stresses or $T_{smincirc}$ and $T_{sminlong}$ are presented respectively:

$$T_{smincirc} = \frac{P*R_c}{((S*E)-(0.6*P))} \tag{2.5}$$

$$T_{sminlong} = \frac{P*R_c}{((2*S*E)+(0.4*P))} \tag{2.6}$$

which calculate minimum acceptable shell thicknesses based on the working pressure P, corroded shell inner radius R_c, Material Strength S, and weld joint efficiency E. From these stresses maximum internal pressures $P_{maxcirc}$ and $P_{maxlong}$ are found:

$$P_{maxcirc} = \frac{S*E*T_c}{(R_c+0.6*T_c)} \quad (2.7)$$

$$P_{maxlong} = \frac{2*S*E*T_c}{(R_c-0.4*T_c)} \quad (2.8)$$

In calculating, it was found that the circumferential shear stress (hoop direction) controlled the equation giving a maximum system pressure (before material deformation or yield) of 25 ksi. This was 2.5 times greater (for a safety factor of 2.5) than the maximum working pressure. Records of variables above and computed values are summarized in Table 2.3 below.

Table 2.3 Computed Properties of the Marquette Breach Relevant for its Shell

Variable	Symbol	Value	Units	Variable	Symbol	Value	Units
Corroded Shell Thickness	T_c	0.98	Inch	Yield Pressure (Circumferential)	$P_{smaxcirc}$	25	ksi
Corroded Internal Radius	R_c	2.02	Inch	Yield Pressure (Longitudinal)	$P_{smaxlong}$	80	ksi
Minimum Shell Thickness (Circumferential)	$T_{smincirc}$	0.333	Inch	Approximated Enclosed Volume	V	~ 4.72	liters
Minimum Shell Thickness (Longitudinal)	$T_{sminlong}$	0.147	Inch	Designed Enclosed Volume	V	4.5	liters

As an additional aside, the lifecycle graph (Figure 2.4) shows that at upwards of 1e8 cycles (Approximately 0.25 million years of firing, assuming a shot a day) the breach should still be able to withstand 14,279 psig, well over the peak operating pressure. It is with confidence that the breach will last longer than the lab given current designed usage.

Continuing, attention is turned to the breach's single unstayed head (as the other is capped by burst disks). "Unstayed" in this case refers to the idea that the head is attached to the cylindrical shell on its own and resists internal pressures without the aid of screws or braces attached on an external assembly. In this case, qualitative assessment, while viewing the internals of the unwelded tank head, matched closest with the b-2 unstayed head type shown for reference in Figure 2.6.

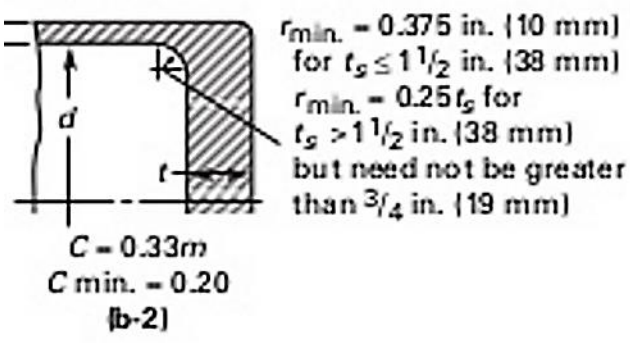

Figure 2.6 Breach's flat unstayed head configuration from ASME.

As before equations are taken from the ASME Pressure code. C below represents the typical unstayed head connection factor:

$$C = 0.33\frac{t_r}{t_s} \tag{2.9}$$

which is a constant modified by the ratio of the required shell thickness t_r, with the nominal shell thickness t_s. Using the connection factor C, the mininmum head thickness T_{hmin} is calculated:

$$T_{hmin} = d\sqrt{CP/SE} \tag{2.10}$$

Where d is the internal diameter, C is the head connection factor, P is working pressure, S is yield strength, and E is the welding factor. Using these values the maximum internal pressure can be found:

$$P_{hmax} = \frac{SE(t_a/d)^2}{2C} \tag{2.11}$$

where P_{hmax} is maximum pressure allowed by the nominal head thickness t_a, along with the other variable stated previously. Taking known values and relevant equations, the following information was computed and presented in Table 2.4 below.

Table 2.4 Computed Properties of the Marquette Breach Relevant for its Head

Variable	Symbol	MU Breach	Units	Variable	Symbol	MU Breach	Units
Nominal Shell Thickness	t_s	1	inch	Design Pressure	P	10,000	psig
Required Shell Thickness	t_r	0.353	inch	Actual Head Thickness	t_a	2	inch
Internal Diameter	D	4	inch	Welding Factor	E	.95	-
Head Connection Factor	C	Unwelded UG-34 Type b-2	-	Minimum Head Thickness	T_{hmin}	0.529	inch
Allowable Stress	S	70,100	Psi	Maximum Head Pressure	P_{hmax}	142,920	psig

Reviewing values, it is clear that the unstayed head is sufficient to the task of holding back pressures well in excess of working pressures. While the breach will only be pressurized to 10,000 psig, the breach head is capable of withstanding 142,920 psig, a safety factor over 10.

Finally, the breach can be both open and closed via a collar assembly, which is fastened via custom threading Figure 2.7. In the collar assembly there is a set of two threaded sections. The smaller threaded section of the barrel is attached to an inner collar piece, which is surrounded by a free sliding outer collar. The sliding outer collar is then attached to the breach by a second set of threads. As the location of the inner collar can be set independently to wide variety of distances along the barrel, knowing the minimum allowable engaged thread length of both the inner and outer collar was of high importance.

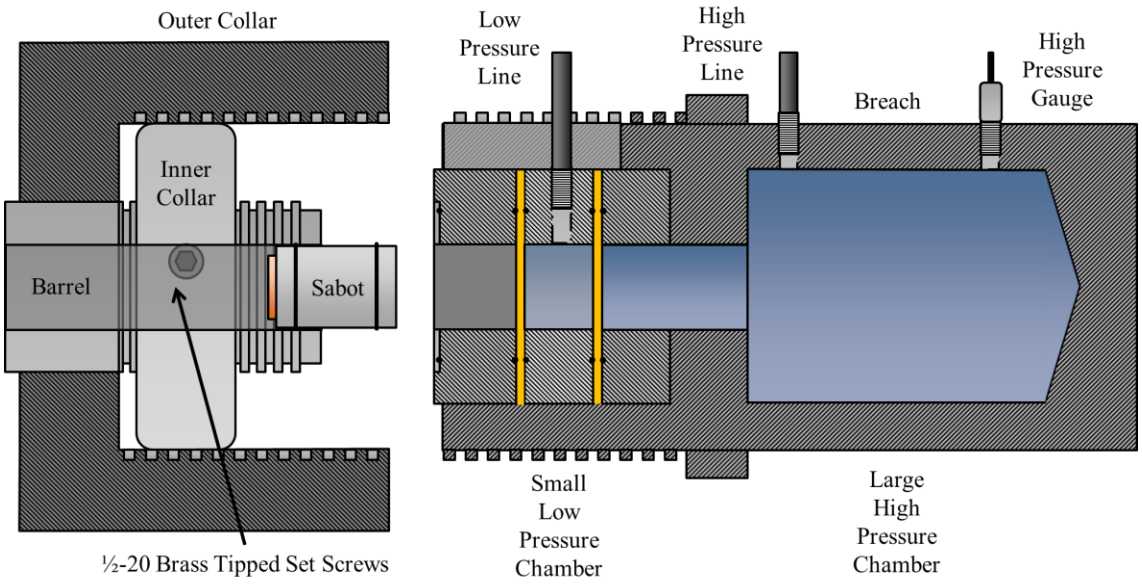

Figure 2.7 The breach assembly.

The equations utilized are based on the shear area covered by engaged threads on the minor threaded diameter. It is assumed here that both threaded sections are made of the same material, normal stresses are small compared to the shear stresses, shear area is half of the engaged length, and that the area experiencing stress covered by the major diameter threads is greater than the area covered by the minor diameter threads.

The expression below finds the force required, F_{req}, to keep the two sections together:

$$F_{req} = \frac{P}{\pi \frac{d_i^{\,2}}{2}} \tag{2.12}$$

where F_{req} is expressed by the maximum working pressure P, and the area characterized by the diameter over which the pressure is exerted d_i [144].

Next the minimum length L_{min} of engaged threads is found using:

$$L_{min} = \frac{P\left(\frac{d_i}{2}\right)^2}{0.577\frac{D_i}{2}S} \tag{2.13}$$

which requires the maximum working pressure P_{max}, d_i the diameter over which the internal pressure is distributed, S the yield strength of the material and D_i the minor diameter of the threads surmounting the smaller of the two mating sections. Finally the maximum pressure P_{max} is found:

$$P = \frac{0.577\, L\, \frac{D_i}{2} S}{\left(\frac{d_i}{2}\right)^2} \tag{2.14}$$

where the length of engaged thread is found using the same variables as before.

The first set of values calculated below in Table 2.5 is for the smaller of the two collars shown in Figure 2.7. While its position was adjustable, it was assumed that during any operation it remains fully affixed to the barrel with all thread area utilized. After

running calculations, it was found that the smaller collar with threaded engagement length of 2 inch had a built-in safety factor of 2.

Table 2.5 Computed Properties of the Marquette Breach Relevant for the Smaller of the Two Threaded Collars

Variable	Symbol	MU Breach	Units	Variable	Symbol	MU Breach	Units
Exposed Diameter	d_i	5.5	inch	Maximum Pressure	P	10,000	psig
Minor Diameter of Threaded Section	D_i	3.625	inch	Minimum Engaged Length	L_{min}	1.03	inch
Yield Strength	S	70100	Psi	Thread Shear Strength	τ	40447	psi

Next the outer thread, with position being variable with maximum engaged length limited by the configuration of the internal diaphragm chambers, was investigated in Table 2.6. From usage, the nominal length of thread utilized was in the range of 1.5 to 2 inches.

Table 2.6 Computed Properties of the Marquette Breach Relevant for the Larger of the Two Threaded Collars

Variable	Symbol	MU Breach	Units	Variable	Symbol	MU Breach	Units
Exposed Diameter	d_i	5.5	inch	Maximum Working Pressure	P	10,000	psig
Minor Diameter of Threaded Section	D_i	7.45	inch	Minimum Engaged Length	L_{min}	0.5	inch
Yield Strength	S	70100	inch	Force Applied	$\boldsymbol{F_{req}}$	237583	lb_f

Given this information it is suggested that the minimum engaged thread be at least 1.25 inches in length. Reviewing all information, the maximum safety factor for the breach section was 2 ft. based on adequate thread engagement of the small collar from Table 2.5. This gave acceptable confidence for safe operation being especially given to prevent the system from ever reaching pressures beyond the 10ksi working pressure.

To keep the breach sealed, the system was built with several internal sections to allow for the placement of burst disks. These internal sections mate together through the aid of O-rings, which are both slightly compliant and air-tight when compressed. To find the forces applied on each of these O-rings, one can convert the torque applied to the breach and collar by the torque wrenches into the compressive force felt by the internal sections and O-rings:

$$F_{breach} = \frac{F_{applied}\, L}{c_f\, D_o} \tag{2.15}$$

where compressive force between the internal sections and the barrel to the breach, F_{breach}, is found via the shortest toque wrench length L, by the force applied $F_{applied}$, the outer threaded diameter D_o and the coefficient of friction c_f [144]. Back solving for the force required $F_{applied}$ to keep the breach sealed without the use of O-rings, the above equation is manipulated to express F_{needed} in terms of F_{req}:

$$F_{needed} = \frac{c_f \, D_o \, F_{req}}{L} \tag{2.16}$$

Based on these equations, the force required and maximum force achievable was calculated and expressed in Table 2.7 below.

Table 2.7 Computed Properties for the Applied Torsion Given by the Breach Torque Wrenches

Variable	Symbol	MU Breach	Units	Variable	Symbol	MU Breach	Units
Length of Moment Arm	L	18	Inch	Maximum Application Force	$\boldsymbol{F_{applied}}$	100	lb_f
Coefficient of Friction	$\boldsymbol{c_f}$	0.2	-	Resultant Compressive Force	$\boldsymbol{F_{breach}}$	1152	lb_f
Threaded Diameter	$\boldsymbol{D_o}$	7.75	Inch	Engaging Force Required	$\boldsymbol{F_{req}}$	237583	lb_f
				Application Force Needed	$\boldsymbol{F_{need}}$	20624	lb_f

From these calculations it is clear that the forces applied by the torque wrenches available are insufficient to the complete sealing of the tank. Therefore, it is of high importance that compliant O-rings are utilized in order for the breach and chamber to "self-seal." For this reason, O-rings before every shot should be clean of particulates and re-lubricated with vacuum grease.

2.1.2 Barrel

The breach is directly attached to the barrel by means of a threaded collar assembly. An unslotted 14 ft. barrel, and slotted 12 ft. barrel are interchangeable within the assembly depending on experimental requirements. Before contacting Physics Applications Inc. for both the slotted and unspotted barrel, a number of manufacturers were contacted for the manufacture of both barrels. While a list of other gas gun manufacturing companies exist, the next closest full service gun company was Thoit Ingenierie in France [146]; therefore, many parts mentioned in later sections were purchased from non-specialized manufacturers. While the unslotted barrel was generally available in the 14 ft. barrel length, manufacturers, including Grand Valley Machining, which seemed best equipped to handle the construction of our barrel, were was unwilling to produce a single piece slotted barrel over 12 ft. in length due to boring bar machine lengths and tolerances. This constraint seemed to be consistent in both the final size made available through Physics Applications and in other slotted barrels at facilities such as Sandia's STAR lab.

While the barrel and rollers were purchased from Physics Applications, Inc., the I-beam, on which the barrel and breach rest, was purchased during the construction of the Engineering Hall.

Taking a sample from the barrel, it was found that both the breach and barrel were made from the same material. Utilizing the same pressure vessel equations from before and now including a much lower weld efficiency to account for the stress concentration made by the broached (slotted) barrel, one finds that the barrel, given its smaller bore and walls of equal thickness, is even better equipped to handle the high pressure experienced during a shot.

Equations (2.1) through (2.8), the equations for shell thickness, are again used to evaluate the pressures experienced by the barrel under operation. It is known here that the barrel is made of the same material as the breach. Table 2.8 below summarizes both the barrel's known characteristics and resultant operational specifications.

Table 2.8 Properties of the Marquette Unslotted Barrel

Variable	Symbol	Value	Units	Variable	Symbol	Value	Units
Working Pressure	P	10	Ksi	Minimum Wall Thickness	t	.875	inch
Yield Stress	S	70.1	Ksi	Corrosion Allowance	C_a	0.01	inch
Outer Diameter	D_o	3.75	Inch	Tolerance	Tol	0.01	inch
Length	L	168	Inch	Weld Joint Efficiency	E	1	-
Corroded Shell Thickness	T_c	.885	Inch	Corroded Internal Radius	R_c	1.145	inch
Minimum Shell Thickness (Circumferential)	$T_{smincirc}$	.159	Inch	Yield Pressure (Circumferential)	$P_{smaxcirc}$	39.1	ksi
Minimum Shell Thickness (Longitudinal)	$T_{sminlong}$	0.071	Inch	Yield Pressure (Longitudinal)	$P_{smaxlon}$	176.8	ksi

The slotted barrel has similar characteristics to the unslotted barrel with a shorter length of 12 ft. and the addition of a small triangular slot broached along the interior axis of the barrel.

A 15 ft. long barrel brush split into three sections ensures the longevity of the barrel and clears debris post shot. Brass fasteners and brushes are softer material than the steel composition of the barrel preventing scratching damage on the barrel's interior. For a secondary treatment a clean towel or rag given a light coating of machining oil or vacuum grease seals the exposed steel within the barrel.

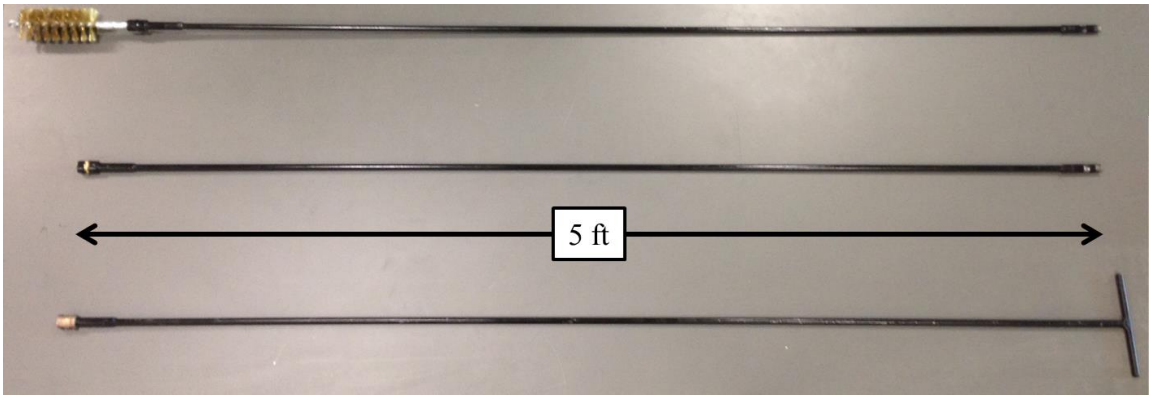

Figure 2.8 5 ft. sections of the brass barrel cleaning brush.

2.1.3 Sabot

Projectiles launched down the barrel consist of two parts, the sample and the sabot. In general, there are two types of sabots, one which separates from the projectile upon leaving the barrel and one which stays attached [147]. The sabot serves as a buffer between the projectile and gun barrel, preventing damage as well as keeping an airtight seal behind the projectile [44] [148]. In the case of a separating sabot once the sabot and projectile have left the barrel, the sabot can be stripped from the projectile by a stripping box, removed by gas, or fluids forcing the petals of a sabot apart. In cases where there is a lack of air pushing the sabot apart, imparting a spin on the projectile can often remove sabot sections with centrifugal force as shown in Figure 2.9.

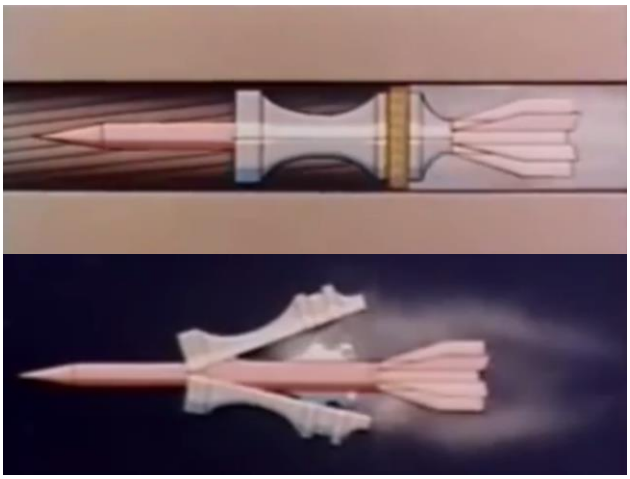

Figure 2.9 A sectioned sabot separating from a long rod penetrator [149].

Marquette's sabot is a lightweight full-bore plug fitting the interior of the barrel. Upon releasing gas, the back surface becomes a piston forcing both the sabot and the flyer it carries down the barrel and into the catch tank. A sabot is destroyed every shot so the design must be both effective and easy to manufacture. Sabots are made to be lightweight for optimum acceleration and strong, so as not to deform during travel down the barrel. The design utilized in experiments thus far is presented below in Figure 2.10 with right to left orientation indicative of sabot travel direction when facing the gun as in Figure 2.1.

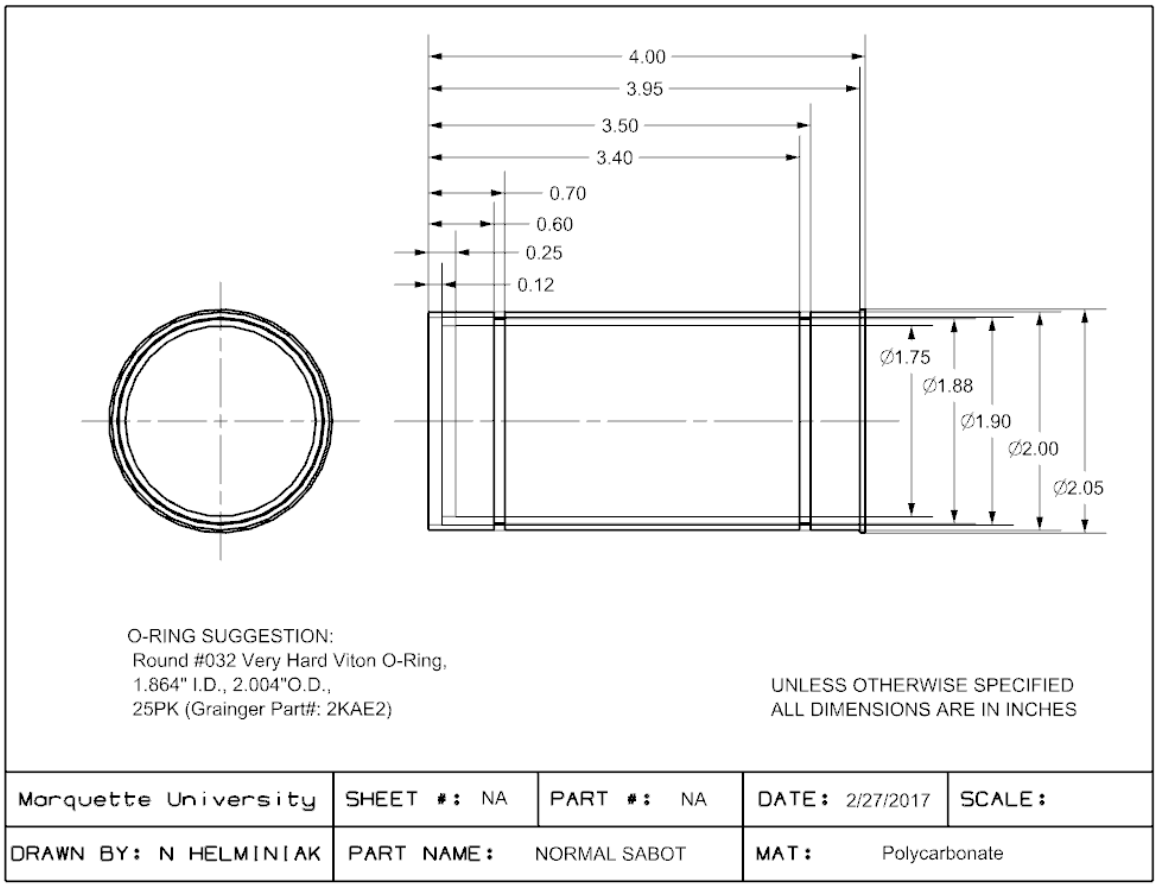

Figure 2.10 Sabot dimensions.

Sabots, manufactured thus far, have been of a typical lightweight polycarbonate plastic. 2-¼ inch rod stock plastic for manufacture has been purchased from McMaster Carr (8571K37), Grainger (2XPX9) and Midland Plastics (Call). O-rings utilized were Round #032 Very Hard Viton O-Ring, 1.864" I.D., 2.004"O.D., 25PK (Grainger 2KAE2).

Given these design considerations, a sabot is typically twice the barrel diameter in length and fits the barrel with an interference fit via two deformed O-rings. During the pull-down period of the catch tank, the sabot was prevented from moving down the barrel through a flared boat-tail. The flyer was held within the sabot via an interference fit with

a tiered hollowed pocket to allow for a free surface boundary condition on the upstream flyer surface in both simulation and experiment. As the design stands, the sabot during experiments experienced nearly an inch of free flight before impact. Finally, before every shot, to both enhance the sealing of the projectile against the barrel walls as well as reduce the coefficient of friction, the sabot was lathered in vacuum grease.

Below in Figure 2.11, a completed sabot is shown. The experimental sabot shown was given a slightly longer flared boat tail (extended backwards for a total 1/8 inch length) to prevent the back surface from chipping during machining, handling, and loading. In order to remove a sabot from the barrel after it has been loaded it is recommended that a hole be drilled on the sabot posterior and a bolt screwed in to allow for increased leverage in extrication.

Figure 2.11 Completed sabot design.

Later sabot designs may wish to incorporate an additional O-ring at the posterior end in order that two O-rings remain within the barrel during impact for pressure shear. In designs where velocity is of increasing importance, an internal cavity could also theoretically be made within the sabot to reduce mass.

2.1.4 Target Tank

The target tank is limited in the peak pressure it can withstand, as the catch tank that connects directly to the target tank is rated to withstand 125 psig.

The barrel ends within the target tank. A flange, shown in Figure 2.12, attached to the target tank contains a recessed internal O-ring, which allows the airtight mating of the barrel to the target tank (vacuum grease has been placed around this fitting to prevent residual leaking). Each barrel has a unique flange, which must be replaced when switching out barrels.

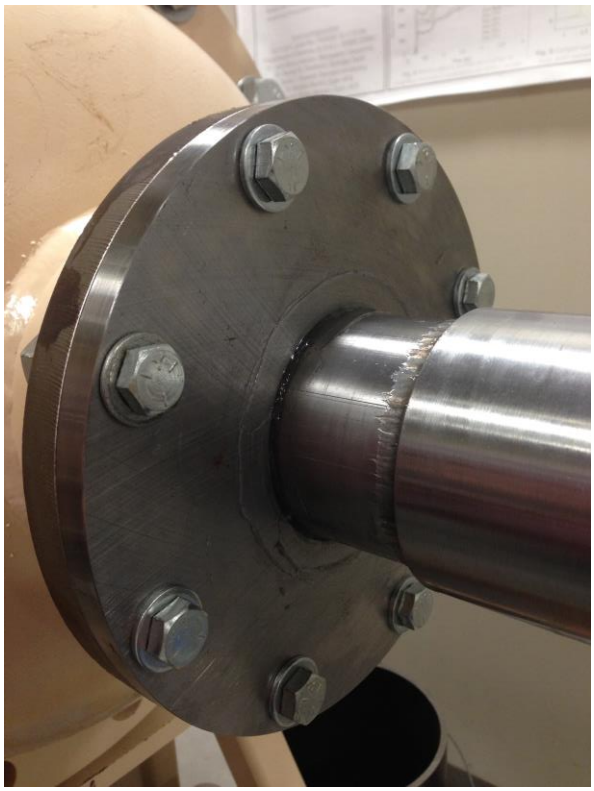

Figure 2.12 Flange mating the barrel with the target tank.

In order to find the theoretical torque needed with O-rings, one first needs to know the gun recoil velocity. From “Ballistics: theory and design of guns and ammunition” [150], one finds that the primary contributors to gun recoil force is the projectile and gas mass accelerating down and leaving the gun barrel. This force is calculated in section 4.7 and found for peak experimental parameters to be ~20 kips (89.13kN).

Using Mechanical Engineering Design [144], one can find the pre-torque load required by the mating flange. First the bolt stiffness is calculated:

$$k_b = \frac{A_d A_t E}{A_d l_t + A_t l_d} \tag{2.17}$$

where k_b, is the bolt stiffness, A_d is the nominal bolt diameter, A_t is the bolt tensile stress area, E is the modulus of elasticity, l_t is the bolt threaded length, and l_d is the unthreaded bolt length. Next the member stiffness is calculated using the method of Conical Frusta, which breaks up the loading of a bolted material by location and material. Each section stiffness is calculated using:

$$k_n = \frac{0.5774\,\pi\,E\,d}{\ln\left(\frac{(1.155t+D-d)(D+d)}{(1.155t+D+d)(D-d)}\right)} \tag{2.18}$$

where k_n is the member stiffness of a section, E is the modulus of elasticity, d is the bolt diameter, t is the section thickness, and D is the minor Frusta diameter. The method chosen often requires the addition of multiple spring rates which are added in this way:

$$\frac{1}{k_m} = \frac{1}{k_1} + \frac{1}{k_2} + \frac{1}{k_3} + \cdots \tag{2.19}$$

where the inverse of the total member stiffness is the sum of the inverse of each section member's stiffness. From these, one can characterize stiffness with a constant, C:

$$C = \frac{k_b}{k_b + k_m} \tag{2.20}$$

The preload is then calculated:

$$F_i = 0.75\, A_t\, S_p \tag{2.21}$$

where F_i is the bolt preload, A_t is the tensile area of the bolt, and S_p is the proofing strength of the bolt. This can be expressed as a torque:

$$T = K\, F_i\, d \tag{2.22}$$

where T is torque, and K is the bolt surface constant. In addition, the minimum number of bolts N can be found:

$$N = \frac{C\, n_L\, P_i}{S_p\, A_t - F_i} \tag{2.23}$$

With a resultant yielding factor of safety n_p:

$$n_p = \frac{S_p A_t}{C\left(P_i/N\right)+F_i} \tag{2.24}$$

The results of these calculations are included below in Table 2.9.

Table 2.9 Pre-load and Torque Calculations for the Barrel Mating Flange

Input			
d, Bolt Diameter (in)	0.5	E, Young's Modulus (Mpsi)	30
l_t, Threaded Length (in)	1.35	K, Torque Factor (-)	0.2
l_d, Unthreaded Length (in)	0.887	S_p, Proof Strength (kpsi)	85
A_r, Minor Area (in^2)	0.126	P_i, Separating Force (kip)	20
A_t, Tensile Area (in^2)	0.142	N, Bolts (-)	8

Frusta Layer Properties				
Layer (#)	***d (in)***	***D (in)***	***t (in)***	***E (Mpsi)***
1	0.5	0.75	0.7855	30
2	0.5	1.342	0.15	30
3	0.5	0.892	0.5125	27.5
4	0.5	0.75	0.123	30

Output			
k_m (Mlbf/in)	10.123	N Min (FOS 1)	2.313
k_b (Mlbf/in)	2.138	F_i Preload (kips)	9.046
C Stiffness Constant (-)	0.174	T_1 Pre-torque (lb*ft)	75.384
n_p Yielding FOS (-)	1.272	T_2 Pre-torque (lb*ft)	80.404

The target tank, shown in context within Figure 2.1, contains the apparatus from which to both set experiments and prepare diagnostics. It is where the actual experiments take place. Around the circumference of the target tank are six diagnostic ports, two 2-11½ NPT and four ½-14 NPT ports. Currently, two of the ports are utilized, one as a re-pressurization valve and the second as a diagnostic port (shown in Figure 2.13).

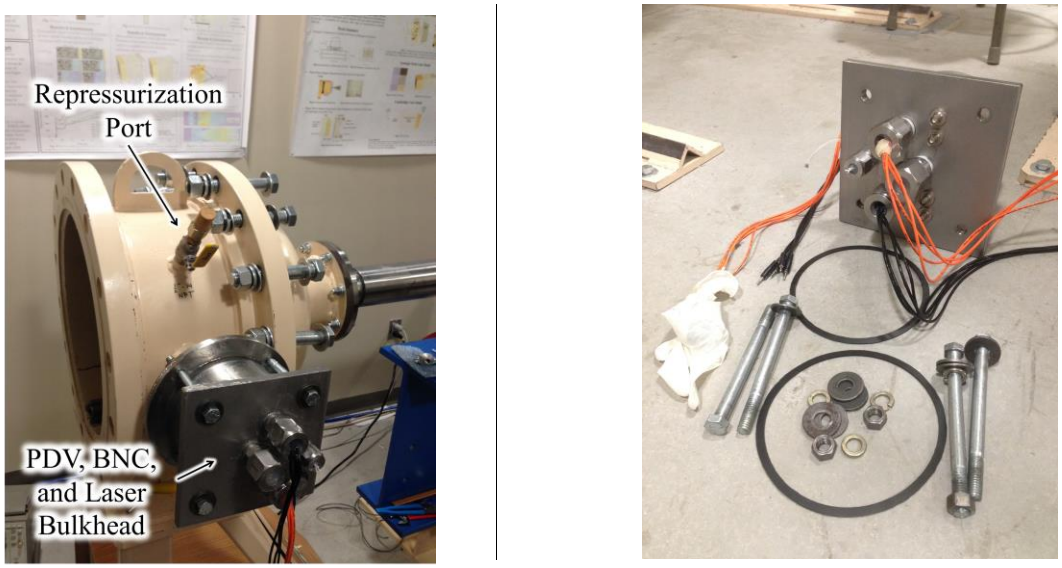

Figure 2.13 Target tank with external features and teardown of the bulkhead.

The re-pressurization port shown in Figure 2.14, allows for both the target tank and catch tank to be brought to atmospheric pressure without the need to fire or manually disassemble components. For optimal performance, the ball within the ball valve should be occasionally lubricated with a dab of vacuum grease to ensure a tight seal. The brass muffler decreases noise when the chamber re-pressurizes and provides a much larger

surface area for gas to flow though, preventing the injury of experimenters with exposed appendages near the low pressure orifice.

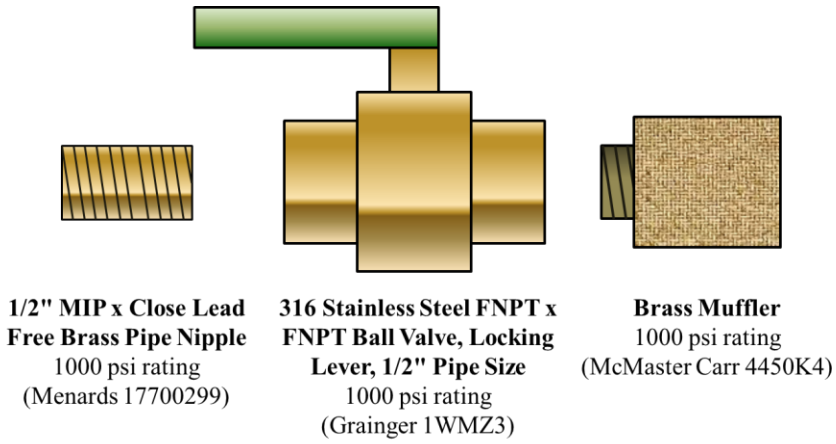

Figure 2.14 Vacuum re-pressurization valve.

The bulkhead (Figure 2.15) enlarges the working face through which the feedthrough cables are threaded in order to make full use of the entire 2 inch diameter afforded space. All other ports were closed with threaded plugs: 304 Stainless Steel Square Head Plug, MNPT, 1/4" Pipe Size (Fittings) (Grainger 1RRK3) and 304 Stainless Steel Square Head Plug, MNPT, 2" Pipe Size (Fittings) (Grainger 1RRL8).

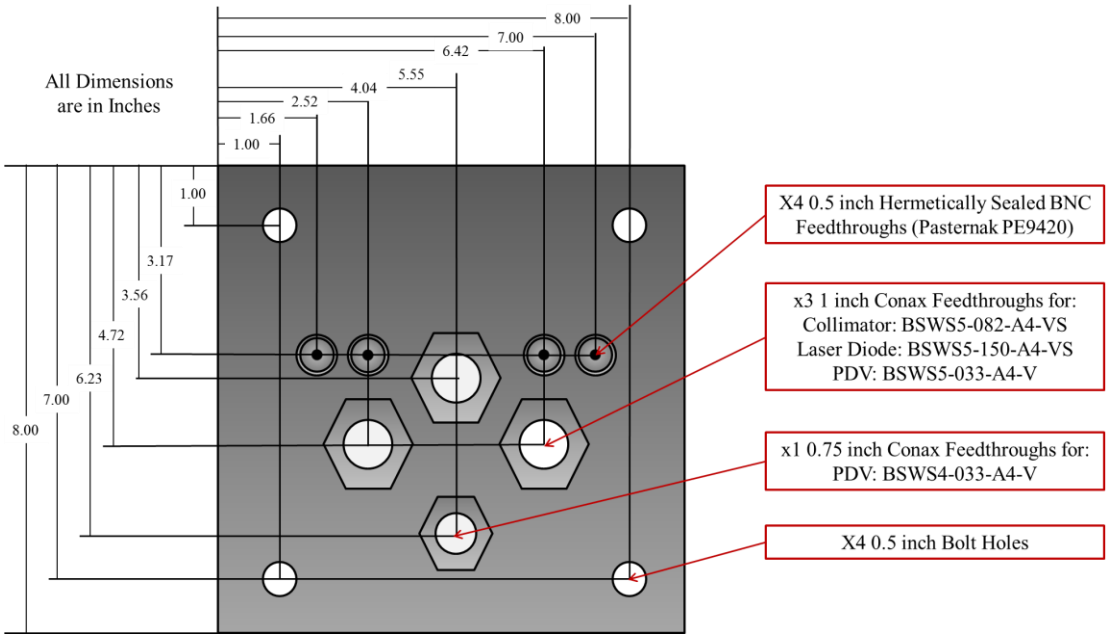

Figure 2.15 Bulkhead, dimensions, and components.

Within the target tank, there are four main assemblies utilized in every launch: the target plate, velocity block, target gage plug, and blast shield. After the velocity block is placed within the target tank, the target plate should be affixed and set in a configuration parallel to the muzzle. A dial indicator cantilevered off of a plug sitting within the barrel, as shown in Figure 2.16 accomplishes this task.

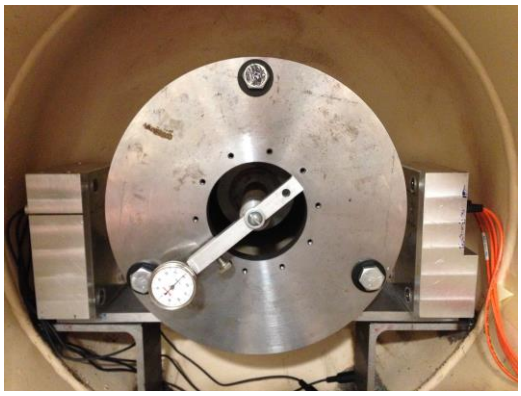

Figure 2.16 Dial indicator to align the target plate and a mounted sample.

To ensure that the target is seated properly the dial is spun around the diameter of the target plate for a minimum of twelve sample points (four between each bolt). These sample offsets are then input into the equation below:

$$R_{Align} = \tan^{-1} \frac{\frac{1}{N} \sum_{i=1}^{N} (x_i - \mu)^2}{L_{Radial\ Arm}} \tag{2.25}$$

where R_{Align} is the radial alignment, N is the number of samples, x_i is the individual sample, μ is the average value of the samples, and $L_{Radial\ Arm}$ is the length of the radial arm from the center of the plug to the center of the dial. A sample table of calculations is included below in Table 2.10.

Table 2.10 Sample Target Plate Alignment Calculation

Position	Measurement (inch)	Position	Measurement (inch)
1	0.049	7	0.050
2	0.050	8	0.051
3	0.050	9	0.050
4	0.050	10	0.050
5	0.050	11	0.051
6	0.050	12	0.051

Measurements are taken ± 0.0005 inches

$L_{Radial\ Arm}$ (inch)	Variance (inch^2)	$R_{alignment}$ (mill radians)
3.225	0.001154	0.3580

This yields the radial alignment of the target plate. A sample mounted to this plate (Figure 2.17) can then with careful affixation be made parallel with the gun barrel. It should be mentioned here that mounted targets should be affixed with screws with stress concentrations machined to allow the experiments to break away from the target mount plate without damage.

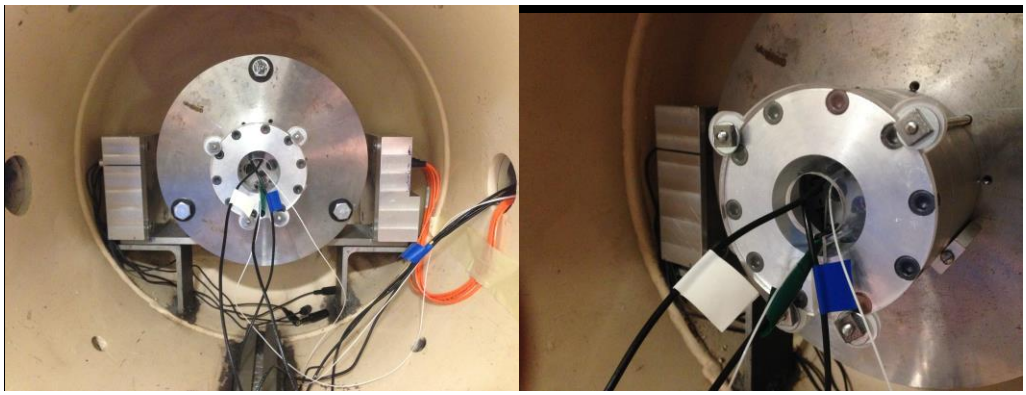

Figure 2.17 Sample mounted on the target plate.

Once the sample is secured onto the target plate, a blast shield (Figure 2.18) is placed to rest on the center track. This shield surmounts the target plate and extends down-range into the catch tank, protecting exposed wires along the walls of the target tank and directing debris to travel the length of the catch tank.

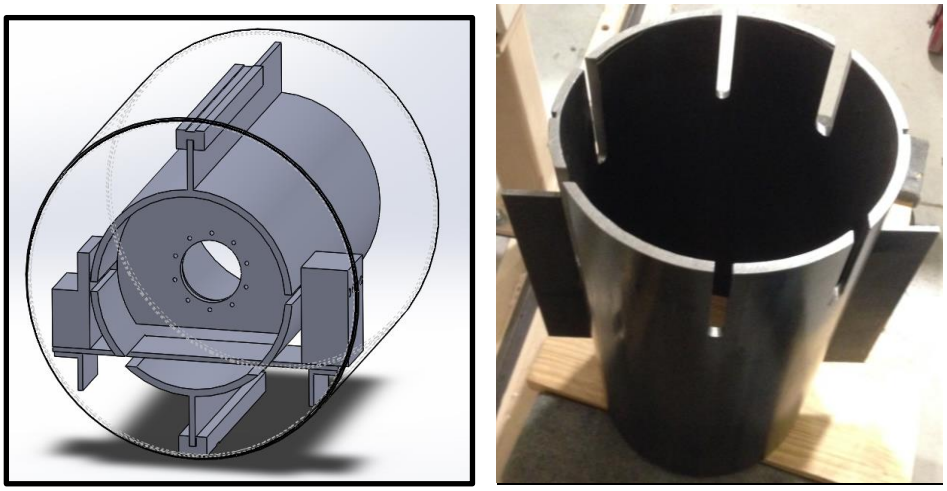

Figure 2.18 Blast shield CAD model and completed design.

2.1.5 Catch Tank

Affixed to the target tank, by means of eight steel bolts, is the catch tank manufactured by International Product Specialists Inc. (dimensions included in Appendix A). This tank is rated to a maximum pressure of 125 psig, well below the expected peak end pressures of both nitrogen and helium 10,000 psig shots. As before using section 4.7, one can calculate the pre-torque required on the bolts using equations (2.17) to (2.24). The results of these equations are tabulated below in Table 2.11.

Table 2.11 Pre-load and Torque Calculations for the Target/Catch Tank Interface

Input			
d, Bolt Diameter (in)	1	E, Young's Modulus (Mpsi)	30
l_t, Threaded Length (in)	4	K, Torque Factor (-)	0.2
l_d, Unthreaded Length (in)	2	S_p, Proof Strength (kpsi)	85
A_r, Minor Area (in^2)	0.551	P_i, Separating Force (kip)	20
A_t, Tensile Area (in^2)	0.606	N, Bolts (-)	8
Frusta Layer Properties			
d (i)	*D (in)*	*t (in)*	*E (Mpsi)*
1	1.5	2.7565	30
1	3.479	0.8575	30
1	3.693	0.185	0.0007
1	1.5	1.714	30
Output			
k_m (Mlbf/in)	0.040	N Min (FOS 1)	3.069
k_b (Mlbf/in)	3.280	F_i Preload (kips)	38.633
C Stiffness Constant (-)	0.988	T_1 Pre-torque (lb*ft)	643.875
n_p Yielding FOS (-)	1.253	T_2 Pre-torque (lb*ft)	624.450

The target tank has been modified both internally, to contain impacts, and externally, to hold the vacuum system (Figure 2.19). The target tank sits atop four rollers which allows access to the target tank or the catch tank man-way (80 foot-pounds pre-load torque required). The rollers also keep the catch tank aligned to the target tank, allowing the tanks to be quickly reconnected before a shot.

Figure 2.19 The catch tank: attaching the vacuum mount plate.

For future reference if needed, a drawing of the vacuum mount points is included in Figure 2.20 below, as this information is not available in any reference manuals or guides.

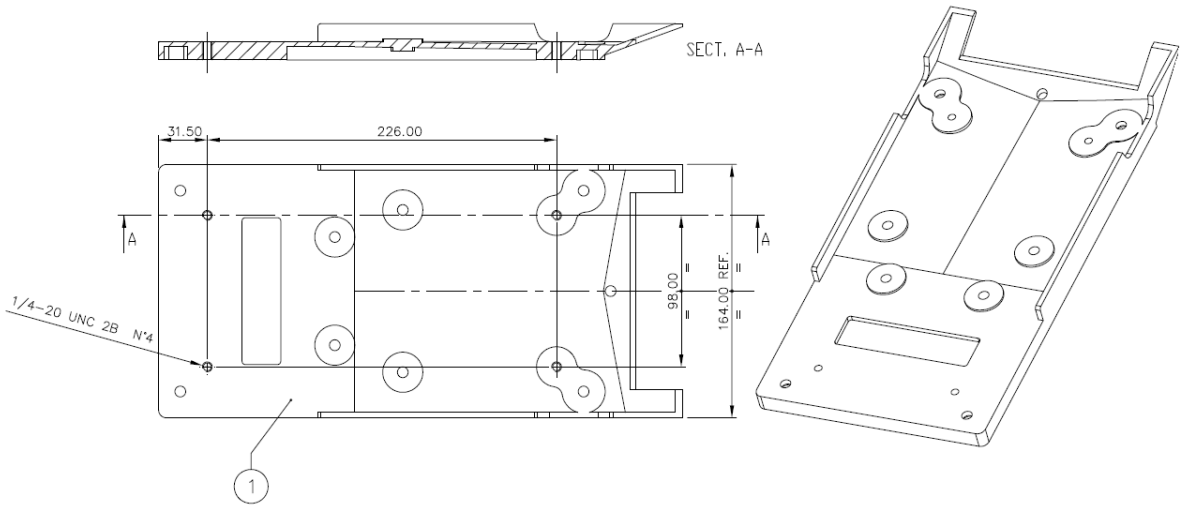

Figure 2.20 Agilent vacuum pump mounting points.

In order to slow the projectile and prevent penetration of the projectile out the rear of the catch tank, a swinging impact plate has been installed with relevant dimensions given in Figure 2.21 below.

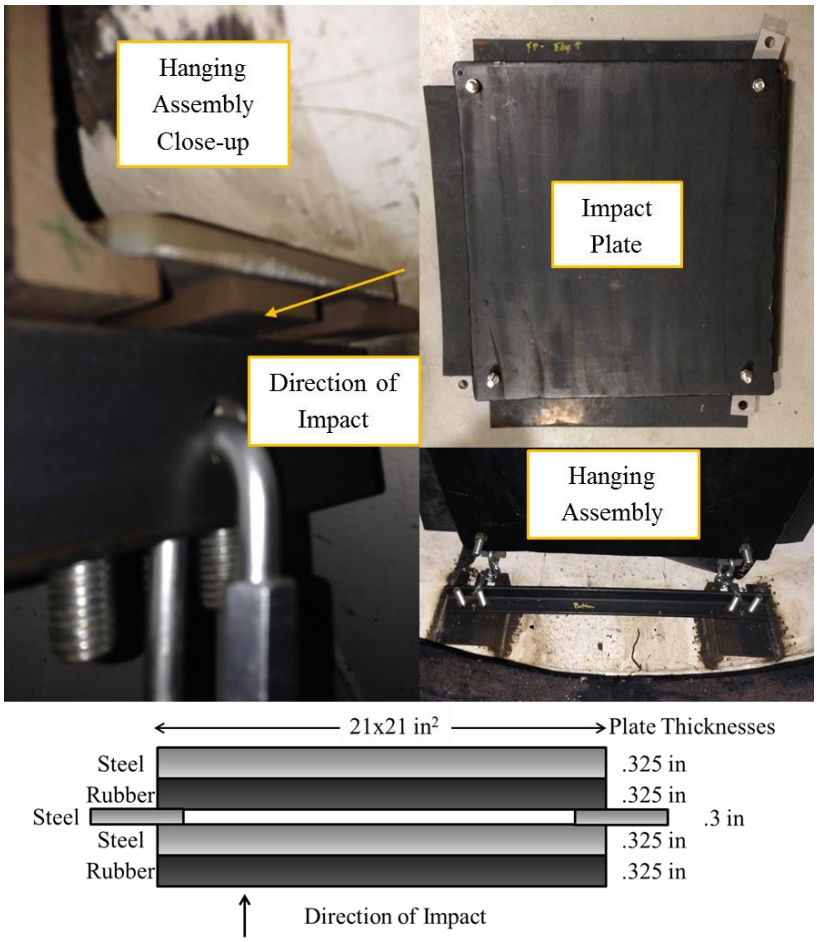

Figure 2.21 Impact plate.

This system relies on the safe transfer of impact load into the plate, then, through chains and into bolts mounted to the catch tank. An initial estimate of impact force is

difficult because while the initial momentum of the projectile is well characterized, the duration of impact and the final impact momentum is not. In any case, peak impact should occur if the projectile is launched using helium (as hydrogen is not advised) without hitting a target.

For an initial conservative analysis, one may first assume that the impact time was directly related to the sound speed and length of the polycarbonate sabot. Second, one assumes that the projectile within this time span loses all momentum. With this in mind, the following equation is generated:

$$t_{impact} \approx \frac{L_{sabot}}{a_o} \tag{2.26}$$

where t_{impact} is the time of impact, L_{sabot} is length of the sabot, and a_o is the sound speed of the projectile. Let us assume first assume a typical 4 inch (10.16 cm), 0.25 kg polycarbonate projectile (with a sound speed of 2270 m/s) traveling at the maximum expected velocity of 1.1km/s impacts the center of a steel plate. Using this information in conjunction with equation (2.26) one finds an impact time of 47.78 μs and initial momentum of 275 kg m/s. Observing Newton's Second Law [145], one can see that force is related to the change in momentum over a change in time:

$$\vec{F} = \frac{d(m\vec{V})}{dt} \tag{2.27}$$

where F is the force of impact, m is the mass of the impactor, V is the velocity of the impactor and t is the time of impact. Since the impact above can be assumed to act in a single direction, the vector form is reduced to a single scalar equation which yields an impact force of 61411 kN. Over the 81 cm^2 area of the impact, one finds a pressure of 760 MPa, which is over the typical yield of steel (~550 MPa). If this were the case, impacts might succeed in deforming or penetrating the steel and complete perforation of the plate would likely transfer negligible force onto the chains. In reality, the plate has both compliance in its' rubber layers and an ability to deform and swing with the impact. These two factors amongst others raise the duration of impact and decrease the force of impact felt by the catch plate.

To ensure that penetration is not a problem, one can use the Lambert and Zukas model [152] for ballistic penetration into rolled homogenous armor (hardened steel). One can ensure that the plates can handle impact using the ballistic limit equation below:

$$V_l = \left(\frac{l}{d}\right)^{0.15} (400{,}000)\sqrt{\frac{d^3}{m}\left[\frac{t}{d}(\sec(\theta))^{0.75} + \exp\left(-\frac{t}{d}(\sec(\theta))^{0.75}\right) - 1\right]} \qquad (2.28)$$

where V_l is the velocity at which a long rod projectile will penetrate, l is the projectile length, d is the projectile diameter, m is the mass of the projectile, t is the thickness of the plate, and θ is the angle of impact [150]. Using this equation and assuming the projectile is a typical sabot with length of 4 inches (10.16 cm) striking the full thickness of the

steel, the estimated ballistic limit is around 700 m/s. This is an overestimate as the projectile has a yield strength much lower than that of the steel. Even when carrying a sample of steel, the length of the sample is typically much lower than that of the sabot. In addition the impact plate in made in a layered configuration as seen in Figure 2.21. By layering the steel plates kinetic energy imparted by the projectile is greatly reduced. Should experiments within Marquette ever investigate penetration mechanics of long rod penetrators with length exceeding ¼ the length of the sabot, additional calculations should be performed to ensure safety. For typical experiments, including normal impact, pressure shear and shock consolidation, section 4.5 suggests that a projectile might reach a peak velocity of 720 m/s for nitrogen (at 10,000 psig or 68,947.6 kPa charge) and 1,120 m/s for helium. To ensure that the impact can withstand these peak velocities, an additional steel plate of thickness 0.5 inches (1.27 cm) should be affixed to the man-way as an additional layer of protection. It is also suggested that for velocities greater than half of the above ballistic limit additional calculations be performed using either ballistic penetration formulations and/or CTH calculations.

Assuming the projectile does not penetrate into the impact plate, one could assume that the momentum between the 0.25 kg projectile and 45 kg plate could transfer perfectly. In order to calculate this, it is assumed that the impact is perfectly elastic, functioning according to the below equation:

$$m_{proj}v_{proj} + m_{target}v_{target} = m_{total}v_{total} \quad (2.29)$$

The momentum of the system of the system is the same as before, but the velocity of the system is lowered from the 1.1 km/s velocity of the projectile to a total velocity of 6.1m/s. Time scale of impact also increases as the plate is allowed both to deform and swing. Assuming the chains linearly decelerate the impact plate over the ~ 5 cm travel distance of the plate, one finds a longer impact time of 8.33 m/s. Again solving for impact force, one finds a much lower force of 33 kN acting on the plate. The linear deceleration of the plate over estimates the time of impact, as chains will likely exert much greater deceleration forces the further the plate swings back, rather than a constant deceleration. However given the two time estimates it is likely that the lower limit will more accurately represent the loading behavior of the set of four chains and eight bolts given the compliance of the rubber on the plate and its ability to swing.

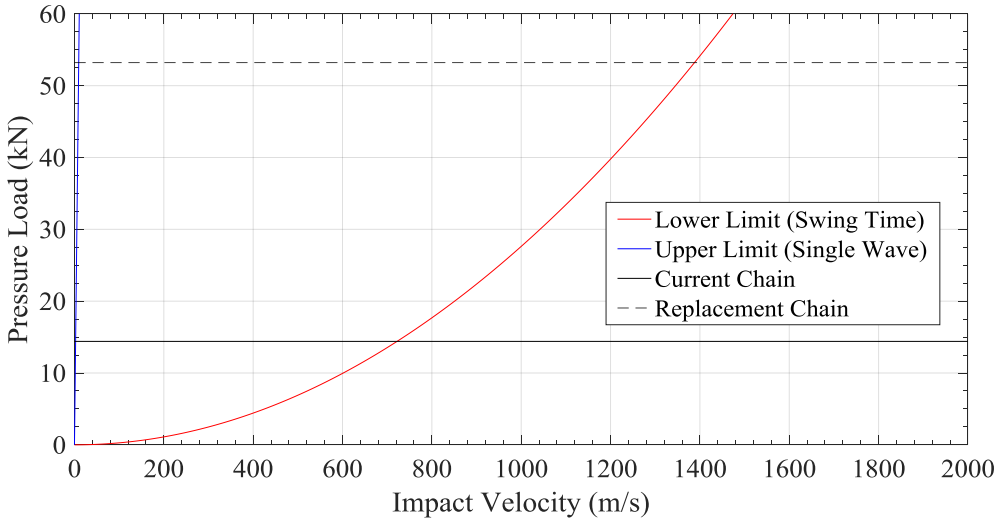

Figure 2.22 Range of pressure loads experienced by the chains securing the catch tank impact plate.

Hanging the plates require a set of eight 0.5 inch grade 4 bolts, each with a minimum tensile strength of 115 kpsi (792.9 MPa), that connect the plate to sets of chains supporting the impact plate within the target tank. Using the below formulas assuming the lower limit of imparted force [144]:

$$\text{Shear Stress} = \frac{F}{\pi r^2} \tag{2.30}$$

$$\tau_{\text{shear strength}} = 0.577\ \sigma_{\text{min tensile}} \tag{2.31}$$

one finds that use of four bolts yields a safety factor of 2.64. (8MPa vs. 457.5MPa)

Between the bolts and plate are four chains (Menards 3/16 inch proof coil chain) each able to support 3.6 kN (800 lbf) of static load. While these are appropriate for shots up to 1500 psig, for greater pressures, these should be switched out for chains each capable of supporting 13.3 kN (5,000 lbf) for operational safety. Additionally a second steel plate should be installed on the inside of the man-way door located on the rear of the target tank as a secondary stopping method.

Of the various analyses, penetration is difficult to characterize, especially for multicomponent or asymmetric construct. Calculations above are a rough indication of the target tank's ability to stop an unimpeded projectile, which should never occur (as the projectile should first impact a target, losing energy). With this in mind, care should be taken in experiments near the upper limits of the Marquette 2-inch gas gun especially if researchers ever choose to use helium to ensure the safety of equipment and personnel.

2.2 Active Gun Components

2.2.1 Control System

A remote firing system keeps researchers a safe operating distance from gun systems under high pressure. In order to accomplish this, Marquette's two inch gas gun utilizes a National Instruments Data Acquisition System (cDAQ-9187 or DAQ for short) connected between Labs 040 and 041 via a single boosted USB 2.0 extension cable.

Figure 2.23 Early testing utilizing remote labview control station.

The DAQ is housed within an electrical control box (Figure 2.24) mounted directly to the I-Beam supporting the 2 inch gun. The internals of this system consist of the DAQ itself, a power distribution board, relays controlling AC Voltage, a DC Power supply, and a number of USB AC to DC converters for monitoring valve status.

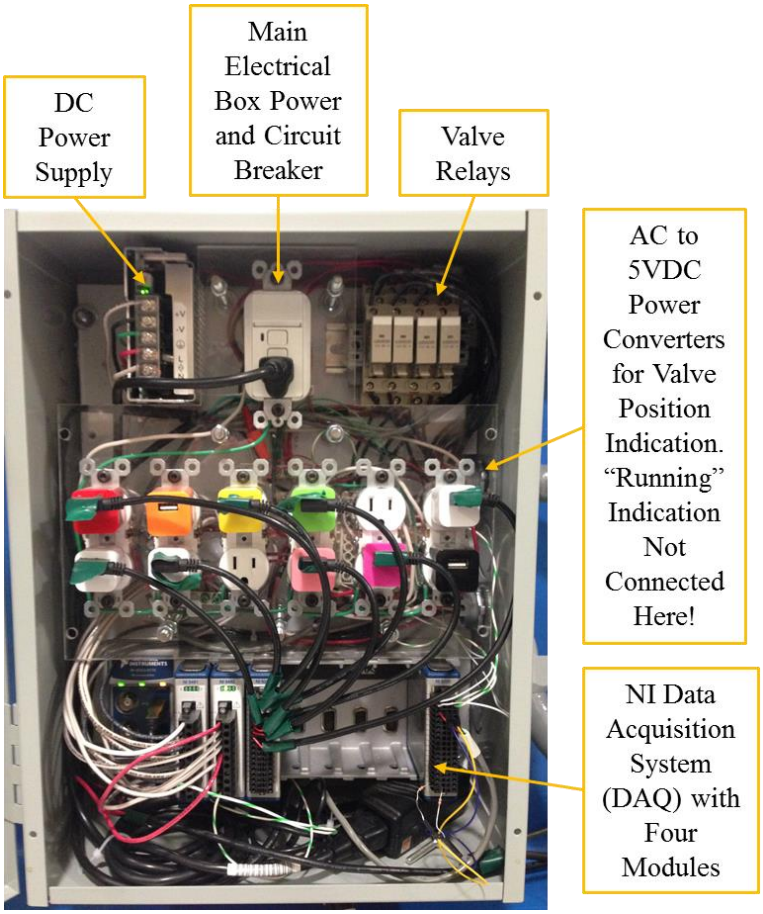

Figure 2.24 Main electrical control box.

The DAQ can both send and receive data through up to eight custom function cards. Currently the DAQ is equipped with four cards listed with name functionality and purpose in Table 2.12.

Table 2.12 National Instuments Modules

Name	Functionality	Purpose
NI 9481	4 Channel Single Pole Single Throw (SPST) Relay With support for: 30 VDC (2 A), 60 VDC (1 A), or 250 VAC (2 A)	The first relay module is used in switching the primary Swagelok electric valves utilized for change system pressure distribution.
NI 9482	4 Channel Electromagnetic Relay (An updated NI 9481) With support for: 60 VDC (1 A), or 250 VAC (1.5 A)	A second relay module controls valves for: running the Haskel, sealing the catch tank from the vacuum system, and controlling the vacuum pump
NI 9205	32 Channel (16 Diff) ±10 VDC Voltage Module With support for: 250 ksamples/sec and 16 bit resolution.	The first voltage module monitors valve (Open, Closed, Running) status 0 or 5V from the Swagelok valve.
NI 9205	32 Channel (16 Diff) ±10 VDC Voltage Module With support for: 250 ksamples/sec and 16 bit resolution.	The second voltage module takes measurements from 0-5 volts down to the millivolt range.

These switches and voltage monitors are displayed on the receiving computer through LabVIEW software. From here, each of the minor electrical circuits will be discussed with an electrical circuit diagram.

The first of the circuits is the electrical valve distribution system. The distribution circuit (shown in Figure 2.25) is one of four circuits which takes AC voltage from the

wall outlet and uses it to power both a 12 VDC power supply and the electrical valves themselves. This circuit is contained mainly within the electrical control box but does extend into the electrical high pressure valves by PVC conduit. In order to control the valves, signals from each terminal will relay power from the 12 VDC power supply. When excited, the relay will either drive the electrical valve open or closed. While powered, the valves will send out a 120V electrical signal from one of three lines, “Open”, “Closed” or “Running” to indicate the status of the valve. In order to read this signal, a number of USB power converters were utilized to transform the 120 VAC to 5V DC. The resultant signal from the USB power converters do not send out a straight 0-5 VDC signal, but instead convert the input AC current to a DC square wave with a peak 5 VDC amplitude.

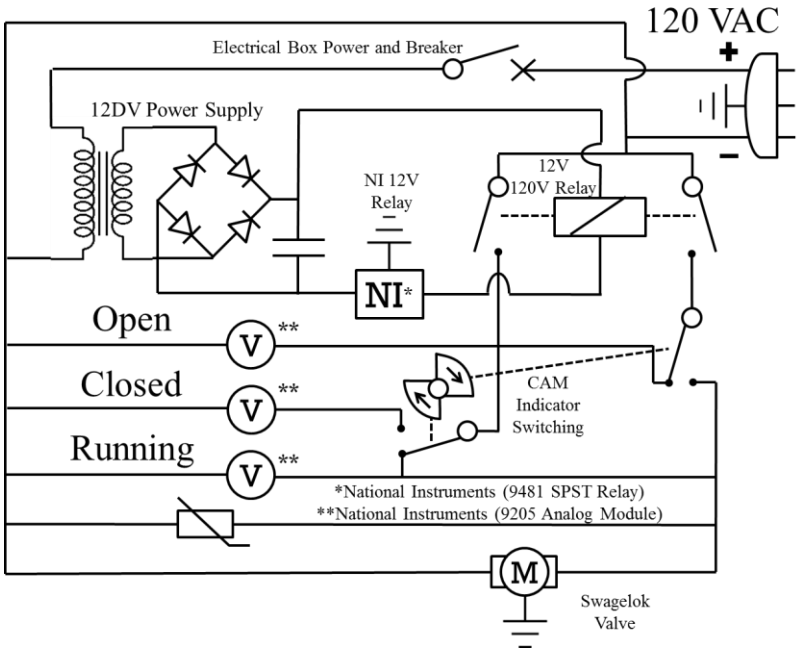

Figure 2.25 Single 10ksi distribution electrical system utilizing NI 9481 and 9205 modules.

In order to control the vacuum remotely (see Figure 2.26 circuit), a 12 VDC signal (open or closed by the National Instruments DAQ) is sent from the electrical control box to a breakout box containing a high amp electromagnetic relay. This relay makes or breaks a high amperage 120 VAC current circuit (designated by a labeled power outlet within the lab) controlling whether the Agilent Vacuum pump is on or off.

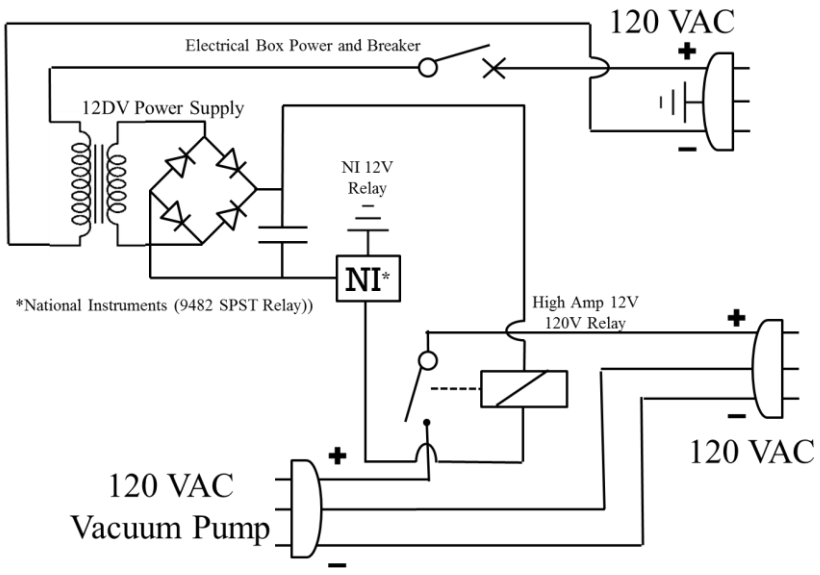

Figure 2.26 Vacuum pump switch.

Much like the vacuum pump, the Haskel is controlled via a breakout box, shown in Figure 2.27 below, which sends a 12 VDC signal to a relay which switches 120 VAC power on and off to the solenoid controlling the air pressure driving the Haskel pressure booster.

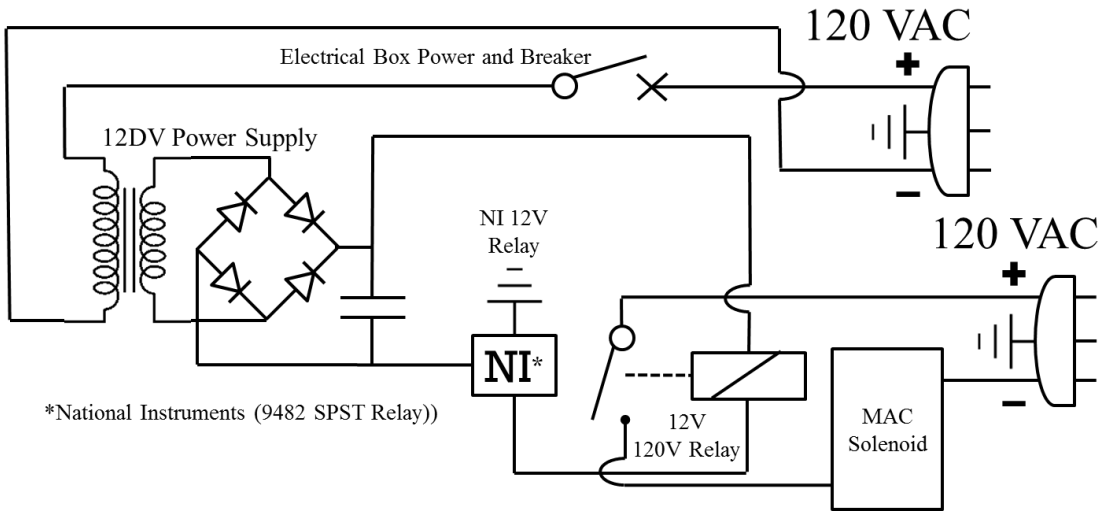

Figure 2.27 Haskel power circuit operating the MAC solenoid.

Signals coming from the two high pressure transducers and KJL vacuum transducer are sent directly into a second NI 9205 Module. Since the KJL vacuum transducer is powered by an external power supply, a pair of resistors connecting the signal to the ground of the NI module were added in accordance with recommendations given in Figure 2.28 below.

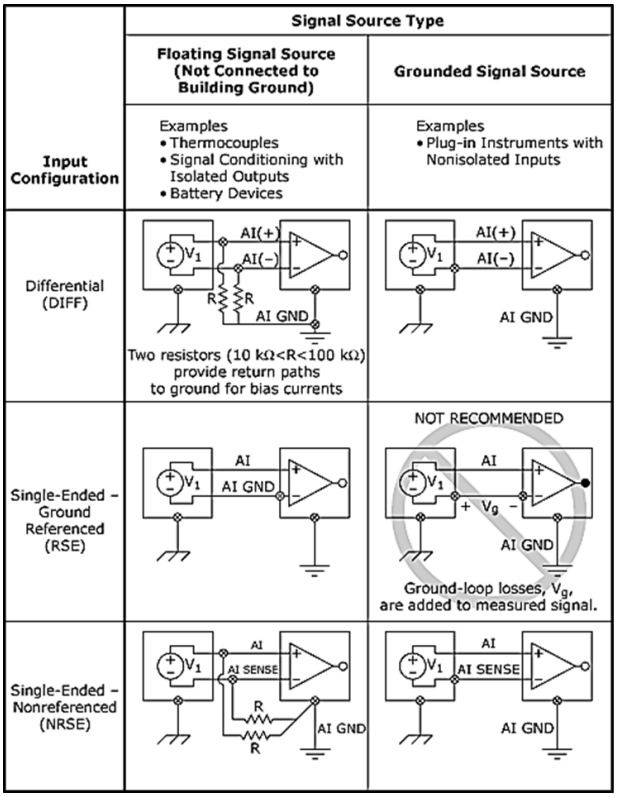

Transducer	Impedance Characteristic
Thermocouples	Low (<20 ohm)
Thermistors	High (>1 kohm)
Resistance Temperature Detector	Low (<1 kohm)
Solid-State Pressure Transducer	High (>1 kohm)
Strain Gauges	Low (<1 kohm)
Glass pH Electrode	Very High (1 Gohm)
Potentiometer (Linear Displacement)	High (500 ohm to 100 kohm)

Figure 2.28 National Instruments signal connection guide [153].

From the LabView terminal, control of the gun is managed through two main graphical interfaces. The first is a diagnostics screen (Figure 2.29), which provides oscilloscope readings, errors from various modules and some legacy controls from the older flow control system to the Haskel.

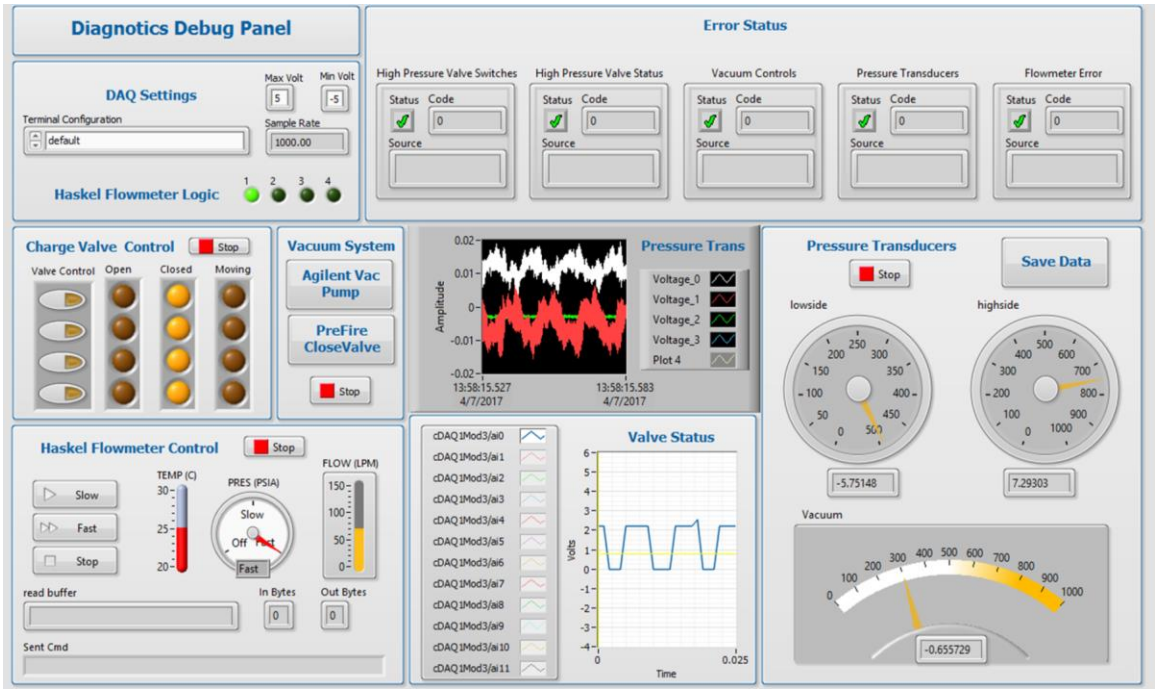

Figure 2.29 Operator debug screen.

The second gun control is a panel with a graphical representation of the system (Figure 2.30). It is intended that this screen be easier to understand than the previous diagnostics screen with interactive valves and indicator lights, which map the flow of gas into and out of the chambers, as well as graphical chambers which fill as a percentage of set pressures. It is important that users use only the Debug **or** Pictographic display while operating the gas gun (this includes pretests and experiments)!

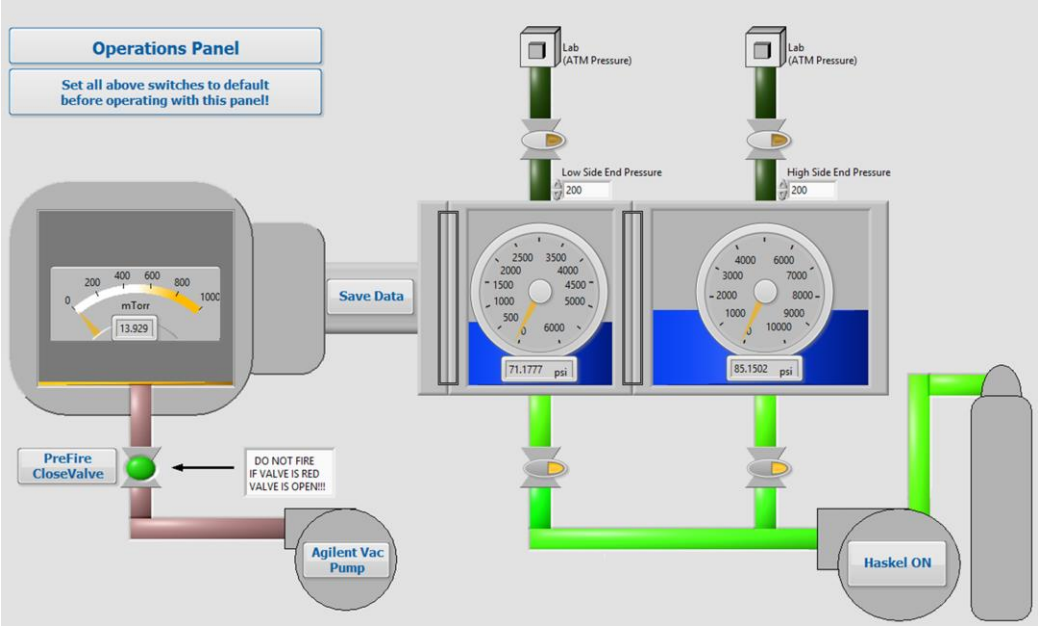

Figure 2.30 Pictographic gun control display.

Behind the running graphical user interfaces (GUIs) are a number of logical systems for each of the DAQ Modules. These systems use LabVIEW software to both send and receive data from the NIDAQ housed in the electrical control box.

The pressure distribution controls shown in Figure 2.31 utilize two DAQ Channels to both send and receive data from the four electrical high pressure valves. DAQ Module 3 controls the signals sent out to the valves. Within this logical path, the state of a valve controls a 5 VDC solenoid sending 120 VAC power to either close or open a valve. When a valve enters a state of "Open" (Channels 0-4), "Running" (Channels 8-12), or "Closed" (Channels 4-8), an electrical 120 VDC signal is sent back to the DAQ through a 120 VAC to 5 VDC USB transformer. These signals are used as limit thresholds to return the valve state to the user in the form of running lights.

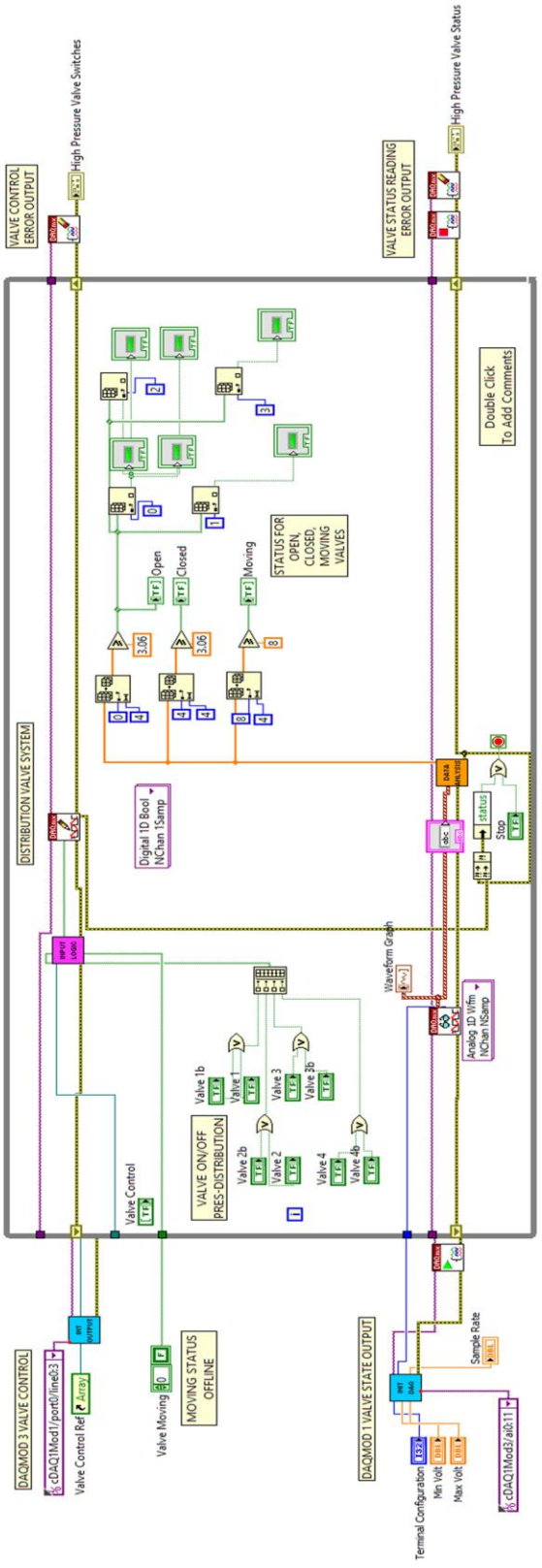

Figure 2.31 Pressure distribution control system.

The control loop in Figure 2.32 controls the remainder of the switch state components on the Marquette gas gun. As can be observed, the three channels in use include the Aglient vacuum pump (Channel 1), the vacuum safety valve separating the vacuum pressure transducer and Aglient pump from high pressures during shots (Channel 2), and finally the control switch for the Haskel pressure booster (Channel 3). As with the pressure distribution controls, the status of these values are also returned to the user display with running lights.

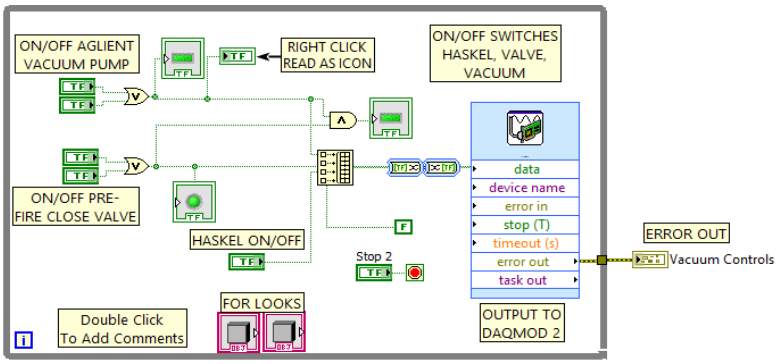

Figure 2.32 Haskel, safety vacuum valve, and Agilent pump switch control.

Signal data from each of the pressure transducers arrives to the DAQ in the form of voltages ranging from 0-5 VDC. These signals are converted to pressure units through the use of linear transformation equations (Figure 2.33). High side breach pressure (Channel 0), low side breach pressure (Channel 1), and vacuum pressure (Channel 2) are each fed into a data collection table, which collects data each second from the time the

control system is initialized until the system is stopped. Before stopping the Labview run, it is important to save data for later analysis. Data is output in the form of three space delimited files including time of collection and computed pressure.

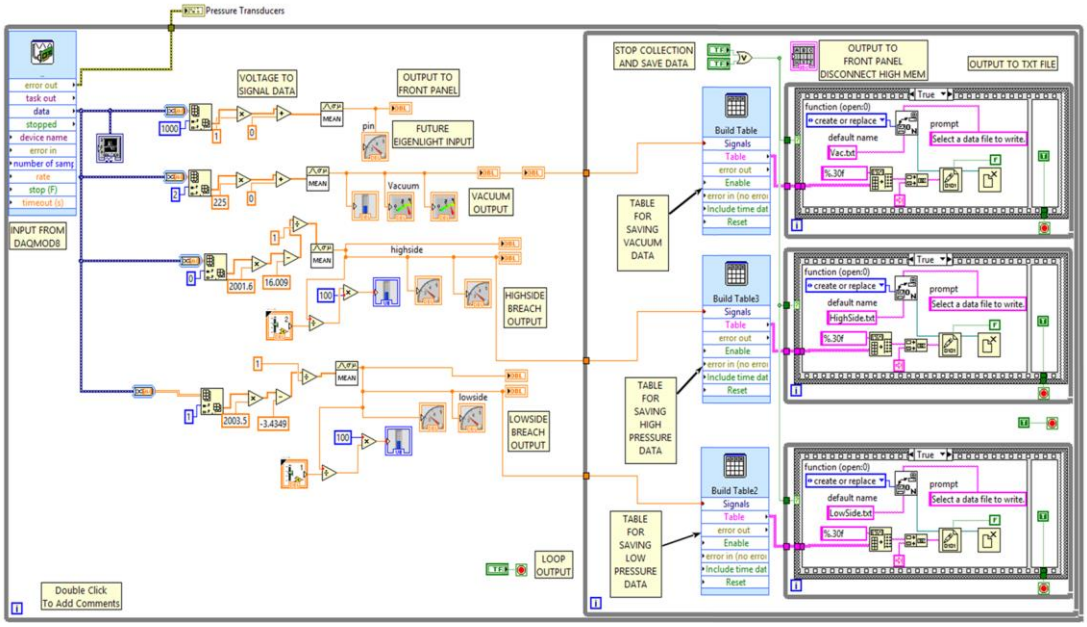

Figure 2.33 Signal data collection from the high and low pressure chambers as well as vacuum pressure.

Finally a legacy Haskel flow controller is included (Figure 2.34). While this system is not presently utilized, it proves that our system has the ability to send and receive additional serial signals through the USB extension from a RMA-LP2600A Omega flow controller. This was not a straightforward procedure and required decreasing the loop cycle time, a VISA Serial connection and multiple command selector loop. It is intended that by inclusion of this legacy system if additional serial signals are required in the future, researchers will have a guide upon which to look back.

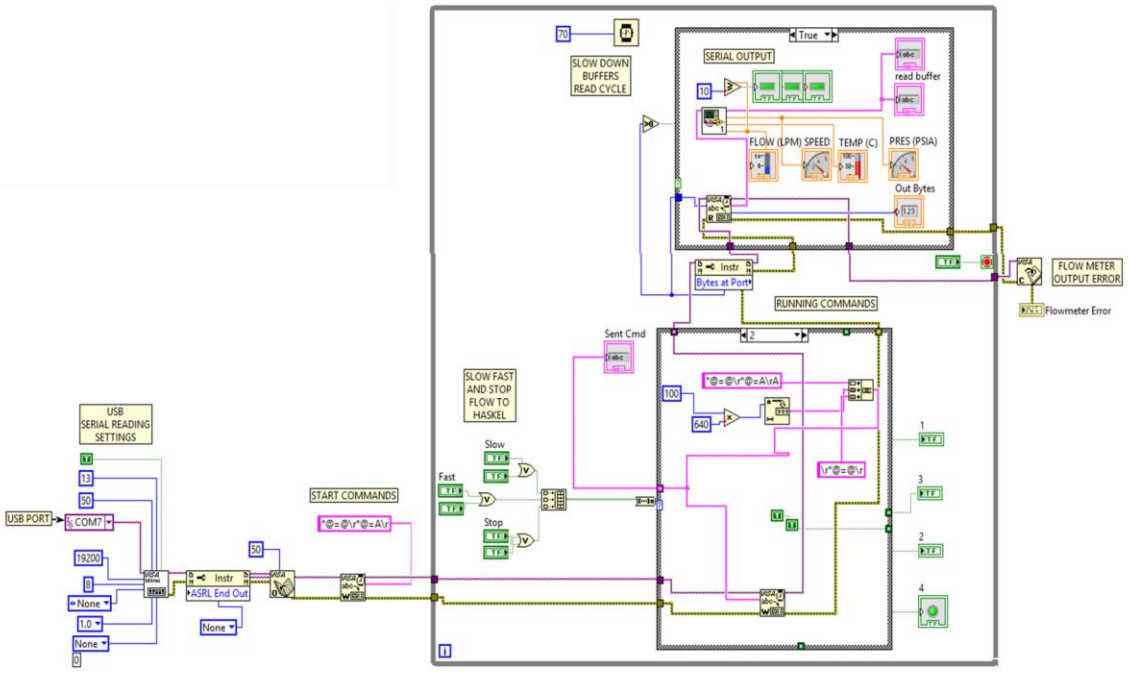

Figure 2.34 Legacy Haskel flow control diagram.

The “Prolific” serial to USB connector no longer was supported by Windows 10, but a reversion of device driver to version 3.3.2.102 within the device manager made the device operable.

2.2.2 Pressurization System

The pressurization system takes gas provided through either the building’s pressurized air supply or a nitrogen gas tank and increases the pressure through a “Haskel” gas booster system. The system, as suggested, only requires air pressure to

operate, using differences in piston area (a 62/152 area ratio) and a network of check valves to pressurize during both the forward and return stroke of the “dual stage” Haskel. This pressurization system was convenient, as it was driven solely through gas pressure without a need for electronics; a conceptualization of the internal views is shown below in Figure 2.35.

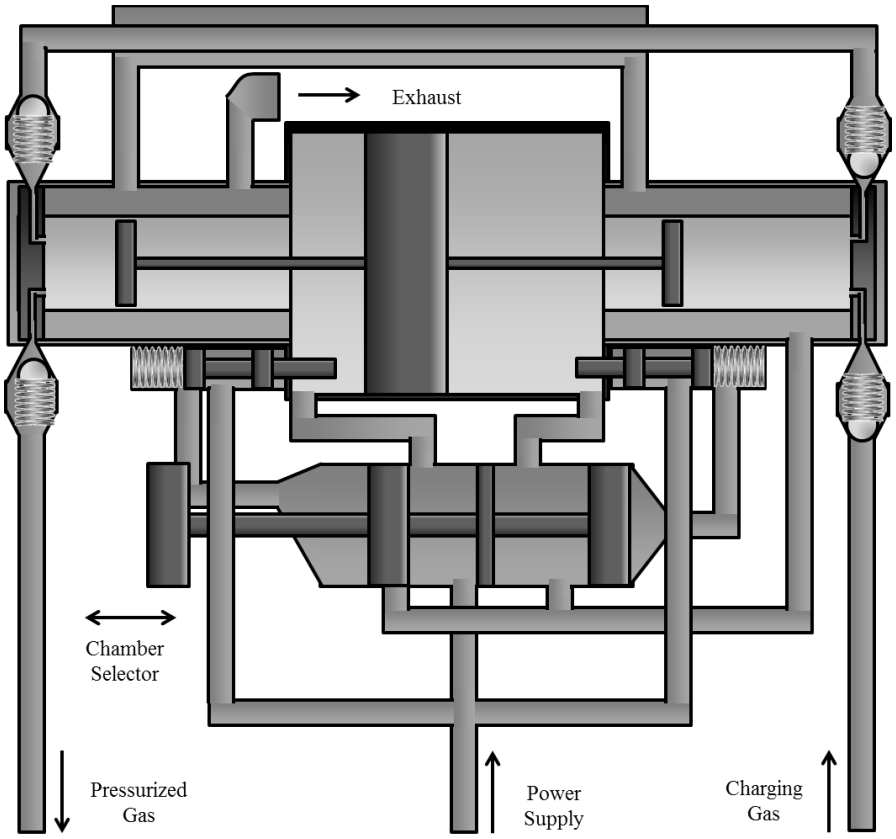

Figure 2.35 Conceptualized artistic rendition of the pressure booster’s interior mechanism.

In order to control the pressurization system, three main requirements needed to be addressed. First, the Haskel required a driving gas. As Marquette had a built-in air system, a line was installed directly to the Haskel's air inlet. Marquette's air supply has been known in the past to contain water condensed out of the compressed air, especially after muggy summer months. Marquette's Shock Physics lab, situated in the basement of Engineering Hall, is one of a few locations in which the water will collect. To mitigate rust damage to the Haskel, both a release valve and water separator were added. Secondly, to turn the Haskel on and off, a MAC solenoid valve was placed within the Haskel's air power supply line. The solenoid only allows air flow when electrically charged and fails in a "fail close" configuration. This means that in the event of an outage, or the requirement for an experiment to immediately end, interrupted power prevents the experiment from proceeding out of the researcher's control. Finally, gas can be supplied to the Haskel by an alternative method to charging from shop air taken from the same supply as the gas powering the Haskel. This secondary means uses pressurized nitrogen or helium from a high-pressure tank, which allows for faster charging as well as improved shot performance. The aforementioned design is shown below in Figure 2.36.

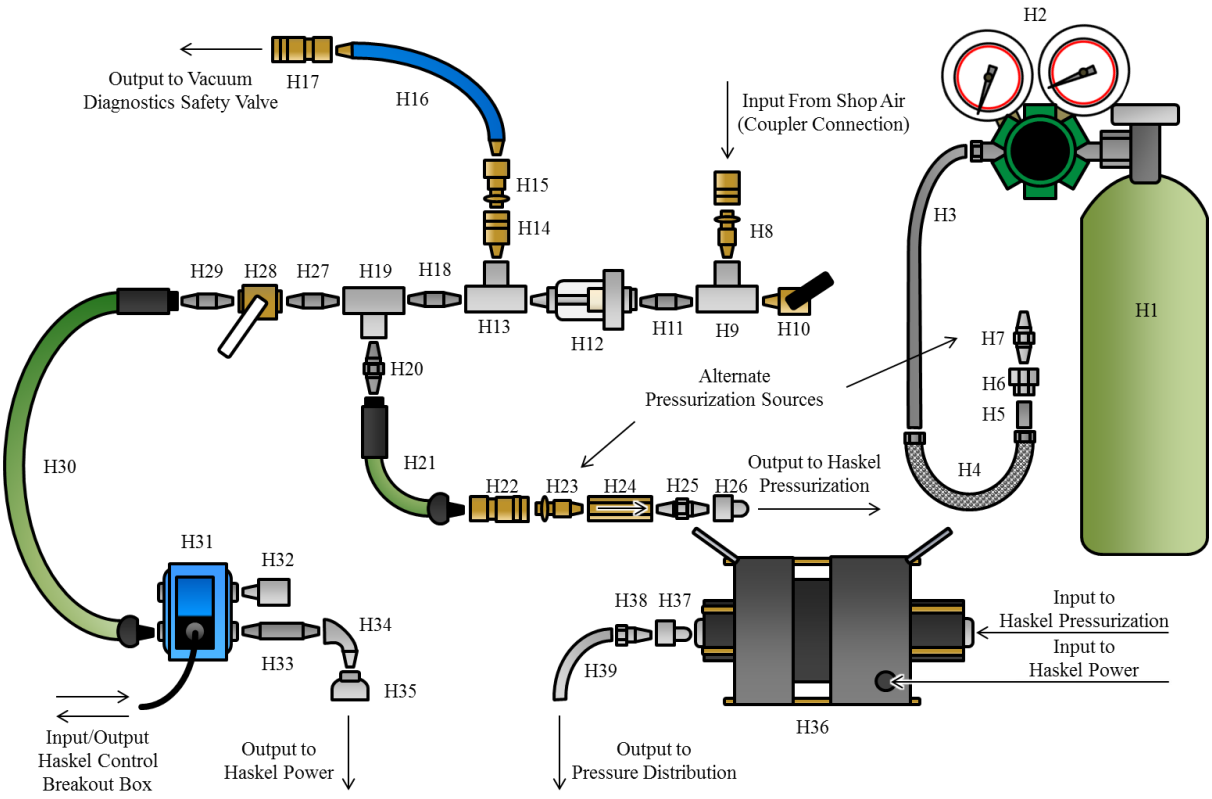

Figure 2.36 Pressurization system reference sheet.

In addition to the power and supply air to the Haskel, the system also includes a line which extends back to the vacuum system. This extra gas line feeds the vacuum safety valve (discussed later in section 2.2.7). Low-pressure connections consisting of NPT wound in 2-3 turns of white PTFE pipe tape for a better air seal. While the NPT galvanized fittings were inexpensive and relatively easy to assemble, their pressure rating was too low to use for high-pressure applications. So in cases where necessary Swagelok components were utilized. After components were assembled, connections were checked for leaks using “Mega Bubble Leak Detector,” a blue solution which bubbled around

leaking joints. A complete list of components, which a can be cross referenced with Figure 2.36, can be found in Table 2.13 below.

Table 2.13 Pressurization System Callout Table

Callout	Part Name	Supplier	Part Number	Notes	Inlet	Outlet
H1	Nitrogen Tank	Airgas	NI 300	3,000 psig max	---	CGA-580
H2	Nitrogen Regulator	McMaster-Carr	6677A13	Regulates to 200-3,000psi	CGA-580	1/4" F Swag
H3	SS Tubing	Badger Fluids	SS-T4-S-065-20	Rated 20,000 psig	1/4" M Swag	1/4" M Swag
H4	PTFE Hose	Badger Fluids	SS-XT4SL4SL4-48	Rated 3,500 psig	1/4" F Swag	1/4" F Swag
H5	SS Tubing	Badger Fluids	SS-T4-S-065-20	Rated 20,000 psig	1/4" M Swag	1/4" M Swag
H6	Adaptor	Badger Fluids	SS-400-7-4		1/4" F Swag	1/4" F NPT
H7	Fitting	Badger Fluids	SS-4-HN	Rated 8,000psig High Pressure Alternate Enters Haskel Pressurization Port at H23	1/4" M NPT	1/4" M NPT
H8	Male Plug	Menards	IP-14M-BM	Rated 250 psig	1/4" Series Plug	1/4" M NPT
H9	Pipe Tee	Menards	311_T-14	Rated 150 psig	1/4" F NPT	1/4" F NPT
H10	Mini Ball Valve	Unknown		---		
H11	Close Pipe Nipple	Menards	309_14XCL	Rated 150 psig	1/4" M NPT	1/4" M NPT
H12	Water Separator	Amazon	30252A	Rated 90 psig	1/4" M NPT	1/4" F NPT
H13	Pipe Tee	Menards	311_T-14	Rated 150 psig	1/4" F NPT	1/4" F NPT
H14	Male Coupler	Menards	IC-14M-BM	Rated 250 psig	1/4" M NPT	1/4" Series Coupler
H15	Female Plug	Menards	IP-14F-BM	Rated 250 psig	1/4" Series Plug	1/4" F NPT
H16	25' Air Hose	Home Depot	PA117701AV	Rated 300 psig	1/4" M NPT	1/4" M NPT
H17	Female Coupler	Menards	IC-14F-BM	Rated 250 psig	1/4" F NPT	1/4" Series Coupler
H18	Close Pipe Nipple	Menards	309_14XCL	Rated 150 psig	1/4" M NPT	1/4" M NPT
H19	Pipe Tee	Menards	311_T-14	Rated 150 psig	1/4" F NPT	1/4" F NPT
H20	Hex Nipple	Grainger	46M442	Rated 1,200 psi	1/4" M NPT	1/4" M NPT
H21	Whip Hose	Menards	HFZ3802YW2B	Rated 300 psig	1/4" F NPT	1/4" M NPT
H22	Female Plug	Menards	IP-14F-BM	Rated 250 psig	1/4" Series Plug	1/4" F NPT
H23	Male Coupler	Menards	IC-14M-BM	Shop Air Alternate Enters Haskel Pressurization Port at H23	1/4" M NPT	1/4" Series Coupler
H24	Check Valve	Matheson	SEQ400V	Rated 3,000 psi	1/4" F NPT	1/4" F NPT
H25	Fitting	Badger Fluids	SS-4-HN	Rated 8,000 psi	1/4" M NPT	1/4" M NPT
H26	Adaptor	Airline	26250-2	Rated 10,000psig Into Haskel Pressurization Port	1/4" F NPT	1/4" M HPX
H27	Close Pipe Nipple	Menards	309_14XCL	Rated 150 psig	1/4" M NPT	1/4" M NPT
H27	Ball Valve	Menards	NL950X4	Rated 600 psig	1/4" F NPT	1/4" M NPT
H28	Close Pipe Nipple	Menards	309_14XCL	Rated 150 psig	1/4" M NPT	1/4" M NPT
H29	Whip Hose	Menards	HFZ3802YW2B	Rated 300 psig	1/4" F NPT	1/4" M NPT
H31	Solenoid	Neff Automation	912B-PM-111CA	Rated 150 psig	1/4" F NPT	1/4" F NPT
H32	Adj Check Valve	Hy-Lok	CVA-M4N-S316	Cracking at 100 psig Rated 3,000psig	1/4" M NPT	1/4" M NPT
H33	2 inch Pipe Nipple	Menards	301_114X2	Rated 150 psig	1/4" M NPT	1/4" M NPT
H34	Street Elbow	Menards	311_SE90-14	Rated 150 psig	1/4" F NPT	1/4" M NPT
H35	Reducing Coupling	Menards	311_RC-1214	Rated 150 psig	1/4" F NPT	1/2" F NPT
H36	Haskel Gas Booster	Haskel	AGT-62/152H	Pressurize up to 25,000psig	1/4" F HPX	1/4" F HPX
H37	Adaptor	Airline	26250-2	Rated 10,000psig Out of Haskel Pressurized Port	1/4" F NPT	1/4" M HPX
H38	Fitting	Badger Fluids	SS-400-1-4			
H39	SS Tubing	Badger Fluids	SS-T4-S-065-20	Rated 20,000 psig	1/4" M Swag	1/4" M Swag

The final system, sans nitrogen/helium pressure tank, can be seen in the below Figure 2.37.

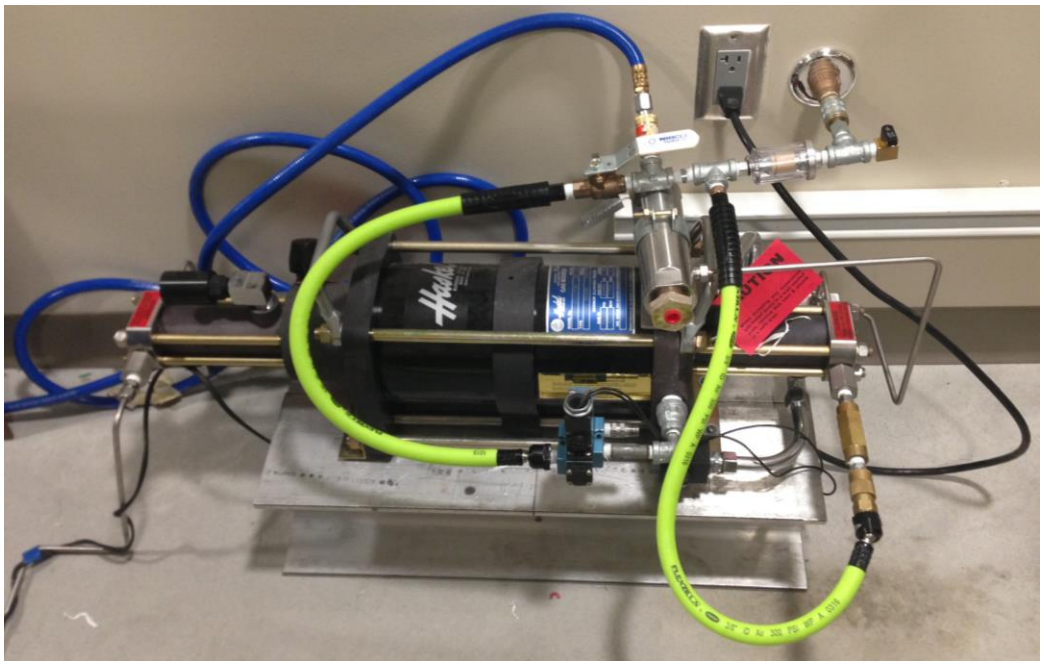

Figure 2.37 Completed pressurization system.

2.2.3 Distribution System

The distribution system received gases from pressurization, through a series of valves and regulators, and allows gases both into and out of the breach's dual diaphragm system. Immediately upon entering this system, gases are split into three lines: the high side breach, the low side breach and the pressure relief valve. This pressure relief valve is

placed so that system air can never exceed the design working pressure of components and breach (~10,000 psig). Both high side and low side systems are very similar, each containing a regulator surrounded both in front and behind by a pair of pressure gauges. Both of these gauges have been set to allow the gun to be set manually if necessary to limit the pressure supplied to high and low side. The high side contains a regulator, which can be set up to 10,000 psig, while the low side is limited to a maximum regulated pressure of 6,000 psig. Past the sets of gauges, motorized valves with manual override allow for air to enter into both the high and low side breach cavities. A needle valve serves to limit the flow, if necessary. Both sides then have pressure transducers, which monitor the pressures within the chambers, as well as flexible hoses allowing for the limited motion of both chamber components during disuse, loading, and firing. Each of these flexible hoses is in fact a pin-pricked hydraulic line hose with the tiny holes placed along its length to prevent pressure bubbles from forming and rupturing the outer hose lining. A second set of valves allows for the bleeding of both chamber needle valves; again, this allows for the reduction of air flow out of the chambers and can be tuned to the experimenter's needs. Electronic wiring is contained within PVC tubing and routed directly to the main gun control box.

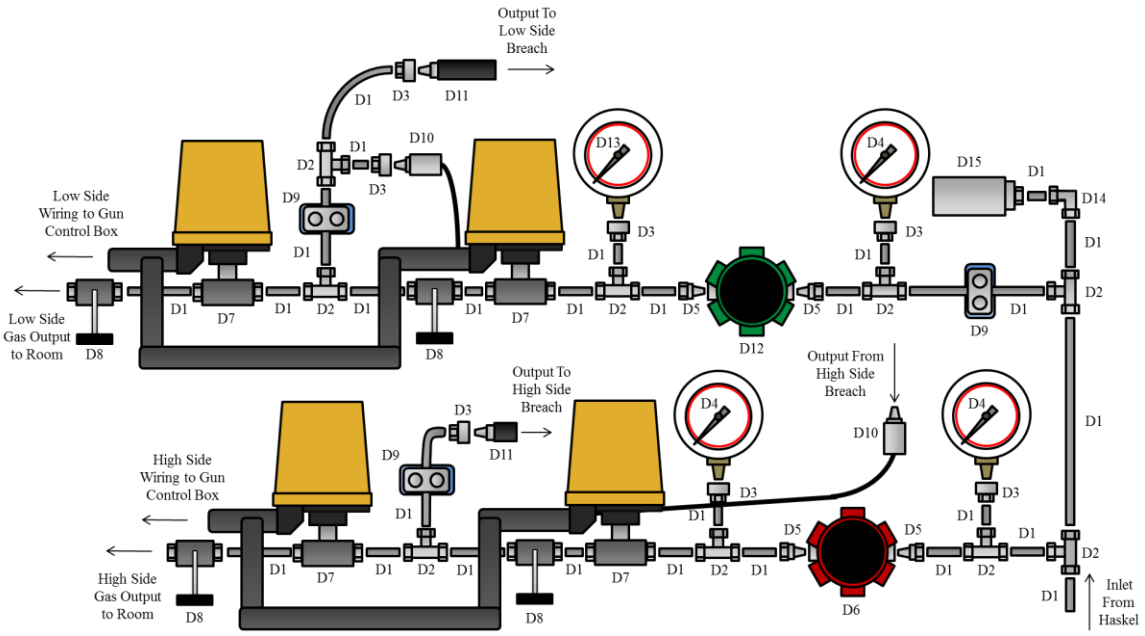

Figure 2.38 Distribution system reference sheet.

The distribution system, unlike the pressurization system, functioned exclusively at high pressure. This meant that nearly all components sourced were from Swagelok, a company specializing in high pressure tubing and fittings. Exceptions to this rule were the high pressure hosing and omega pressure transducers both rated for the system's working pressure. Their fittings utilize a set of two interlocking ferrules with pressure fit to the piping. These nuts and ferrules made it easy to create custom length piping sections from component to component. After tightening each of the nuts, a go-no-go gauge, included on the Swagelok wrench, verified that the nut had been tightened to the correct torque.

To check the system for leaks, a blue solution of "Mega Bubble Leak Detector" was utilized. The system was first pressurized to ~100 psig and the solution dabbed onto

the connecting sections. In the few areas where pressure leaked out of the system, bubbles quickly formed and the connections were either tightened (Swagelok) or removed and retaped (NPT). The complete listing of components within the distribution system are shown in Figure 2.38 are listed on Table 2.14.

Table 2.14 Distribution System Callout Table

Callout	Part Name	Supplier	Part Number	Notes	Inlet	Outlet
D1	SS Tubing	Badger Fluids	SS-T4-S-065-20	Rated 20,000 psig	1/4" M Swag	1/4" M Swag
D2	FS Tee	Badger Fluids	SS-400-3		1/4" F Swag	1/4" F Swag
D3	FS to FNPT Fitting	Badger Fluids	SS-400-7-4		1/4" F Swag	1/4" F NPT
D4	10k Gauge	Badger Fluids	PG1-100B-PG10k-LAOX		1/4" M NPT	
D5	FS to MNPT Fitting	Badger Fluids	SS-400-1-4		1/4" F Swag	1/4" M NPT
D6	10k Regulator	Badger Fluids	RS(H)2-02-6-WP	Rated 10,000 psig Regulates from 0-10150psig	1/4" FNPT	1/4" FNPT
D7	Automated Ball Valve	Badger Fluids	SS-H83PS4-42AC	Rated 10,000 psig	1/4" F Swag	1/4" F Swag
D8	Needle Valve	Badger Fluids	SS-3HNRS4	Rated 10,000 psig	1/4" F Swag	1/4" F Swag
D9	Mounting Bracket	Badger Fluids	304-S1-PP-4T		---	---
D10	High Pressure Transducer	Omega	PX309-10KG5V	Rated 10,000 psig	1/4" M NPT	
D11	High Pressure Hose	Badger Fluids	2380N-04V91	Rated 10,000 psig	1/4" M NPT	1/4" M NPT
D12	6k Regulator	Badger Fluids	KHP1WXB4C2S200J0	Rated 6,000 psig Regulates from 50-6000psig	1/4" FNPT	1/4" FNPT
D13	6000 Gauge	Badger Fluids	PG1-100B-PG6000-LAOX		1/4" M NPT	
D14	FS Angle	Badger Fluids	SS-400-9		1/4" F Swag	1/4" F Swag
D15	10k Pressure Relief	Badger Fluids	RV4NF4NF10	Rated 10,000 psig	1/4" F Swag	

The finished distribution system, show in Figure 2.39, is shown bolted to the side of Marquette's 2 inch gun.

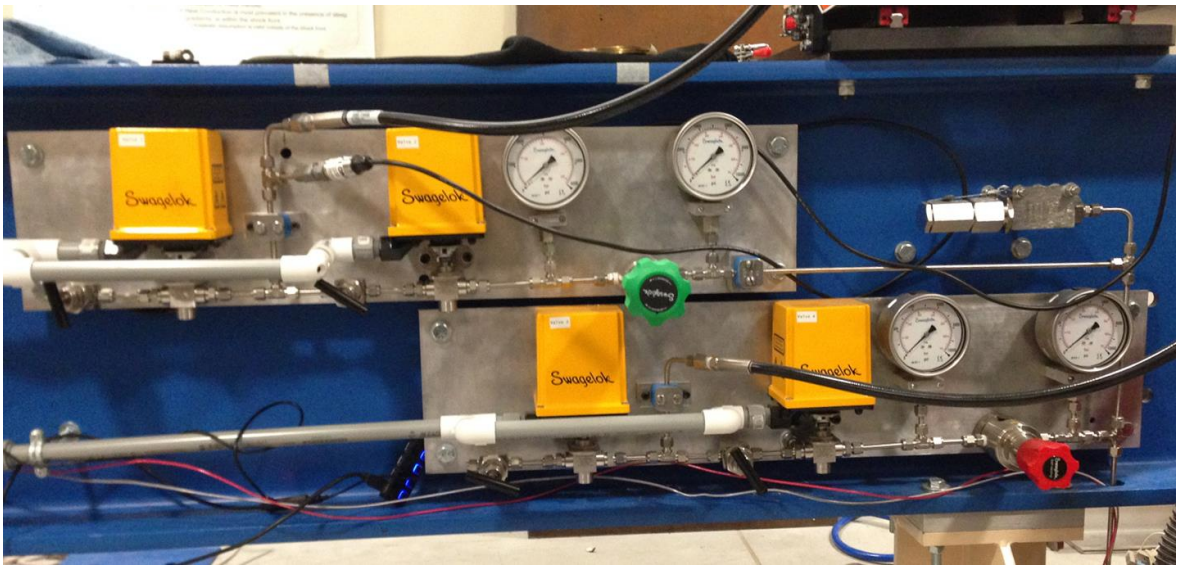

Figure 2.39 10ksi pressure distribution system for high and low side breach chambers.

2.2.4 Dual Diaphragm Launch System

In order to conduct experimental research, a gas gun must be able to store a gas propellant charge up to the desired pressure and, when required, quickly release all available gas into the barrel. In common practice, an initial thought might be to use a valve. However, if the valve is opened too slowly, peak pressures kept within the breach will not affect the sabot as the sabot will begin accelerate away from the breach even if that pressure is much lower than the breach pressure.

In order to provide the control of a valve with the fast acting requirement of a gas gun, four major designs, three of which are presented below in , are found in use by other institutions: fast acting valves; wrap-around breaches; single diaphragm; and double diaphragm. Fast acting valves [97] as named are quick acting valves, which can be

actuated with electricity, gas or explosives. Traditional “fast actuating” valves are low cost and straightforward to operate; they are also generally the slowest of the four designs.

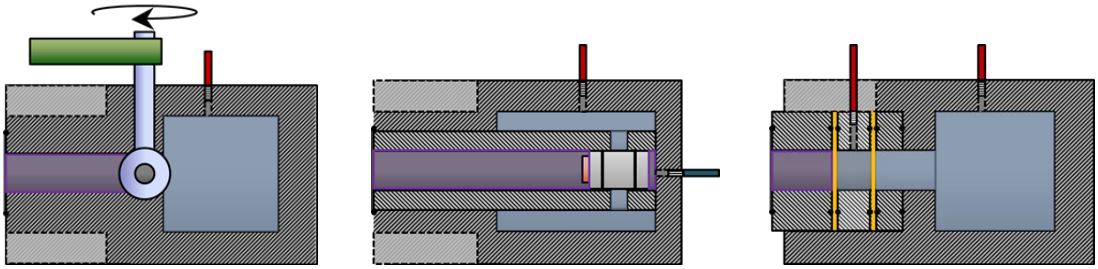

Fast Acting Valve Wrap-Around Breach Dual Diaphragm

Figure 2.40 Three common types of firing mechanism. High pressure gas within the breach can be seen in blue while evacuated volume is colored purple.

Wrap-around breaches use the sabot as the method for blocking gas pressure. A sabot is typically held in place by a vacuum on the rear surface while a high pressure gas pressurizes filling an area on the surface of the sabot. This high pressure gas is not allowed to pass to the front or rear of the sabot by means of two O-rings. To fire the vacuum on the rear of the sabot is removed and a low pressure gas moves the sabot forward until the high pressure gas inlet passes the rear O-ring and the gun fires. This limits design choices, as the material properties and geometry of the sabot must withstand and seal the full firing pressure from fore and aft section of the sabot, while still being able to carry the projectile down the barrel. The wrap-around breach is generally more expensive than a fast acting valve and requires more control to operate correctly.

Diaphragms or burst disks are (often) made of round sheets of material such as plastic or metal. These disks fail when the pressure differentials, existing across the two

surfaces, exceed the strength of the material [98] [151]. Often these disks are manufactured with stress concentrations on their surfaces allowing them to petal upon failure, preventing disk material from traveling down the barrel. While single disk systems are effective, they fail at set pressures once a nominal pressure has been reached, which leaves less control in the hands of researchers. In order to regain this control loss, a dual diaphragm system, similar to the one used in this system, affords control at relatively low cost and high reliability.

Several variations on the burst disk design exist with researchers seeking increased control over burst disk failure. Burst disk strength can be reduced by heat, which can be applied through the barrel or directly onto the disks themselves, until failure without affecting the barrel or breach. Alternately, disks can be punctured with a firing pin with a variety of punch shapes to initiate failure [94].

In short the dual diaphragm launch system combines the fast acting nature of a single burst disk with the control of a fast acting valve and is less complex in geometry than a wrap-around breach. In order to manage the flow of pressurized air in and out of the dual chambers, a series of four valves and two regulators are utilized. Shots are conducted through use of a dual diaphragm system with burst disks that fail for a given pressure differential. Once the system fires, it propels a sabot down the barrel holding a flyer whose impact is often the beginning of the shock experiment. The sequence of events used to both prepare and fire a dual diaphragm system is included below in Figure 2.41.

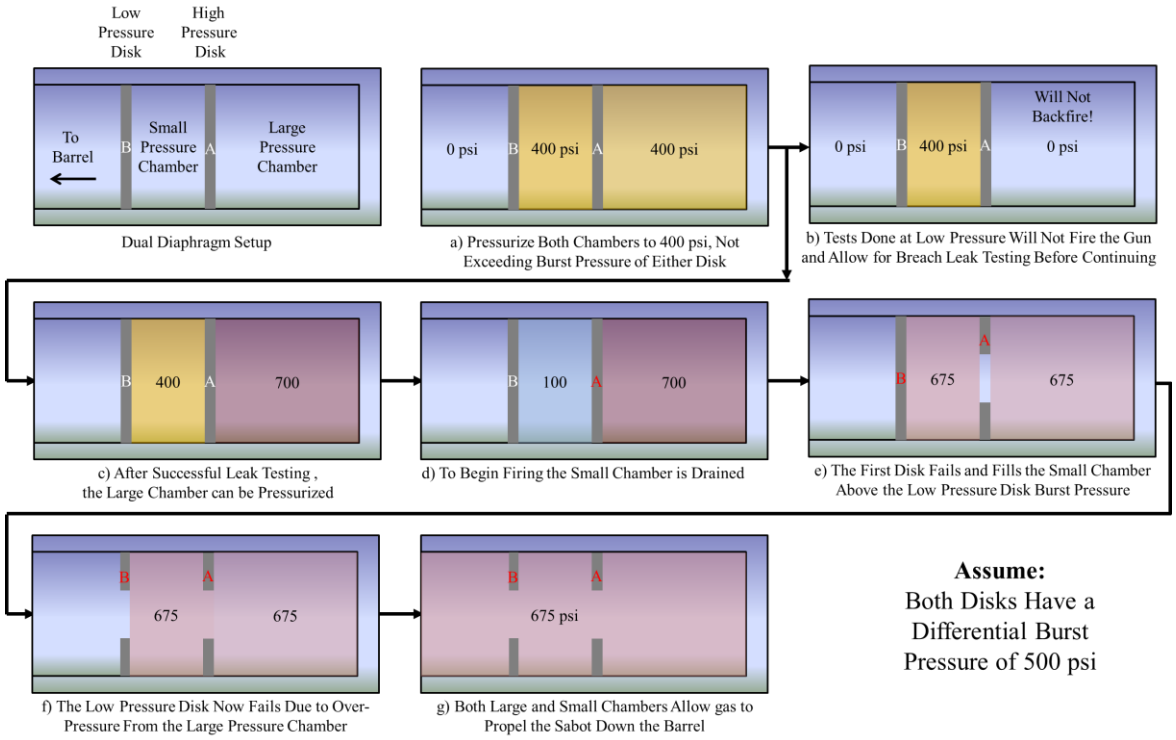

Figure 2.41 Dual diaphragm system firing sequence.

2.2.5 Light Gate Assembly

The Light Gate Assembly shown in Figure 2.42, housed within the target tank, measures flyer velocity upon exiting the barrel. A series of four laser diodes and collimators, each spaced a nominal distance of 0.75 inches apart, throw by the laser diodes and are received into light collimators before the signal is boosted giving a set voltage. Once connected to an oscilloscope, a trigger can be set to record the fall and subsequent rise in voltage as the flyer and sabot pass through the laser beams. The velocity blocks are operated by means of a switch placed on the front of the target tank. A second outlet remains always on to provide power for the oscilloscope.

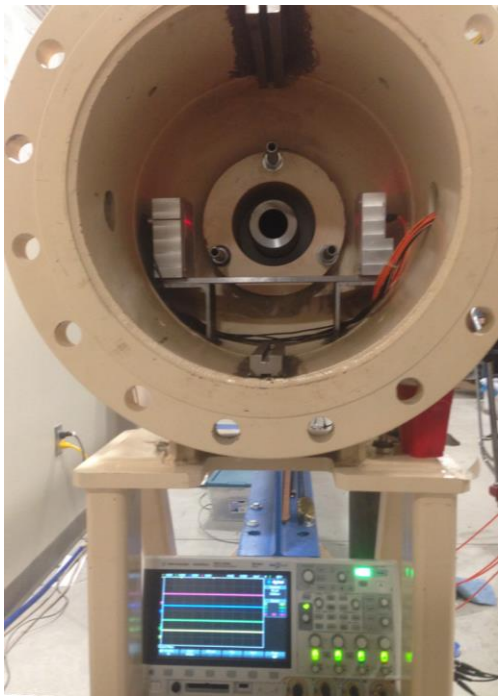

Figure 2.42 Laser gate experimental setup.

The velocity gates are made of machined aluminum blocks with dimensions shown in Figure 2.43 below. This setup fits laser diodes (ThorLabs F220SMA-B w=633 nm f=10.99mm NA=0.25 SMA Fiber Collimation) which shine visible red light (600 Nm) into laser collimators, which focus light onto detectors (ThorLabs PDA36A Si Amplified Detector 350-1100mm) on the opposing light gate. Each of the velocity gates is also fitted with acrylic windows, which helps to protect the collimators and detectors during a shot.

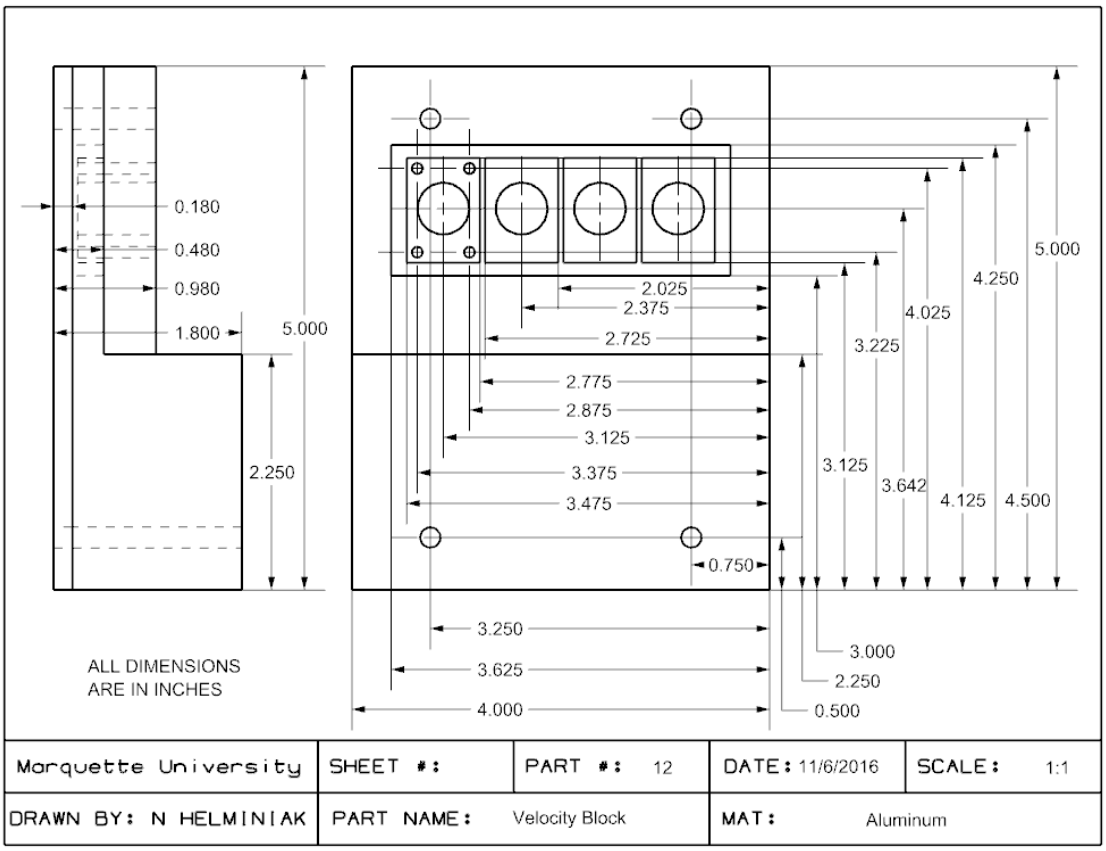

Figure 2.43 Light gate dimensions.

In order to find the projectile velocity, the point is chosen at which the light first falls below 90% of steady state, to detect the tip of the flyer.

The first four falls should then correspond to the temporal location of the flyer tip. Knowing the length of the sabot and the distances between laser beams, combined with the temporal data afforded by the oscilloscope, one can determine the average velocity (assuming minimal acceleration) experienced by the flyer just prior to collision with the target.

$$V_{projectile} = \frac{1}{3}\left(\frac{\Delta x_{GapA}}{\Delta t_A} + \frac{\Delta x_{GapB}}{\Delta t_B} + \frac{\Delta x_{GapC}}{\Delta t_C}\right) \quad (2.32)$$

Figure 2.44 presents data taken from a shot that had a polycarbonate sabot and conical shaped flyer (390 psig, 0.1187 m, 0.4322 kg). Using the method describe above, the average projectile velocity was calculated to be 194.4 m/s. Only the first four drops are used to measure arrival time, as the sabot impacts the material prior passing out of the first laser's line of sight. This matches well with an expected velocity of 190.19 m/s and measured down barrel, Photon Doppler Velocimetry measurement of 197.25 m/s.

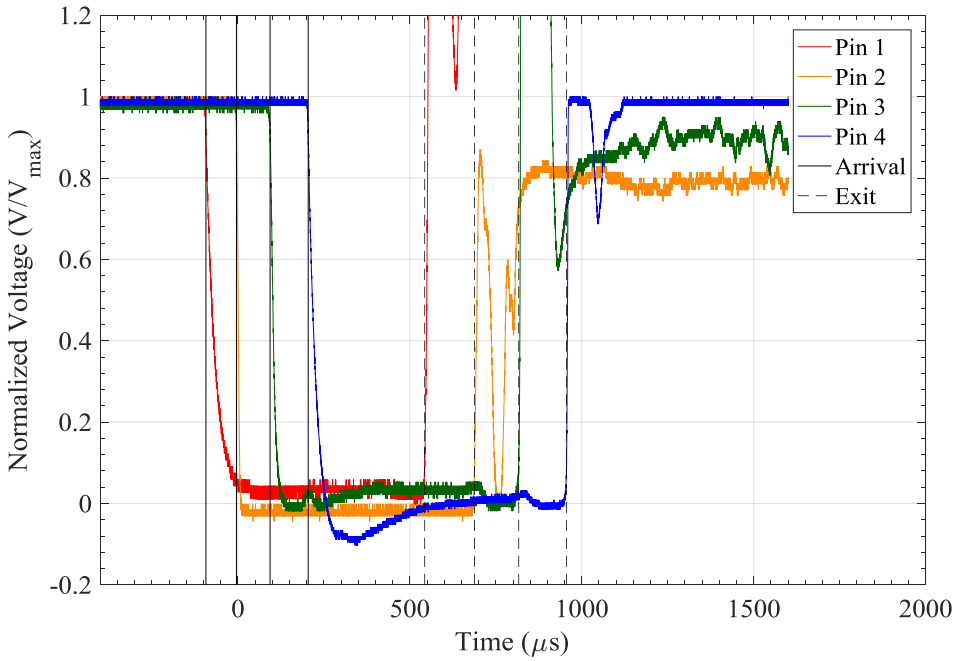

Figure 2.44 Light gate reading from a 390 psig, 0.4322 kg shot.

Using the time between the projectile's arrival and exit, one can use the average velocity to calculate the length of the projectile. Calculations here find a sabot length between 0.123 m and 0.145 m; these lengths are longer than the length expected by measurements of projectile length prior to launch. This is likely due to the fact that compressed gases behind the sabot bend and distort light behind the sabot, making light gate measurements once the sabot exits the barrel unreliable. With this in mind, light gate measurements for projectile velocity should only use the arrival signals to determine projectile velocity.

2.2.6 Photon Doppler Velocimetry and Dynasen Pin System

The Photon Doppler Velocimetry (PDV) and Dynasen pin system shown in Figure 2.45 are the primary means of collecting experimental data during shock experiments. These systems can measure velocities and location of projectiles and target at single instants in time, which are states utilized in conjunction with hydrocode simulations to determine pressure, stress and temperature states of materials within the experiment [154].

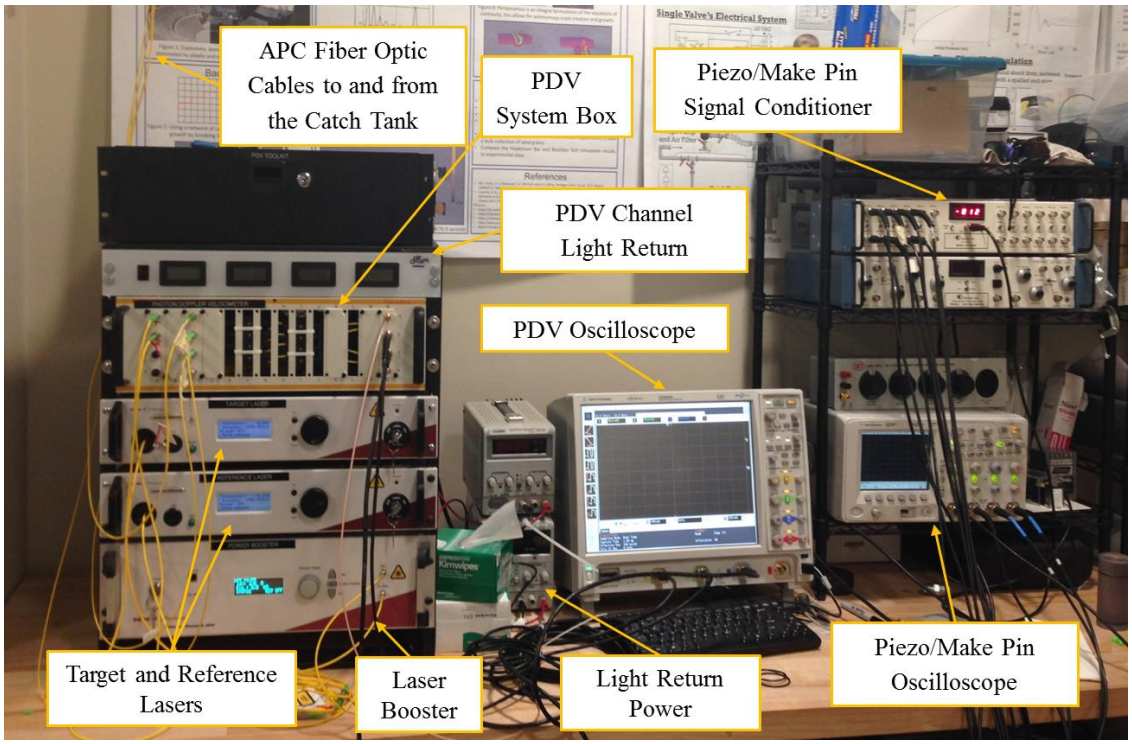

Figure 2.45 Photon Doppler Velocimetry and Dynasen pin system.

The Photon Doppler Velocimetry System (PDV) utilizes lasers emitted at a set wavelength to track velocities of exposed material surfaces [155] [156]. Light travels at a constant velocity; this creates interesting phenomena when observers from reference frames observe a light source traveling both toward and away from the observer. Since as previously mentioned light remains constant in speed, a wavelength of light, emanating from a moving source and that same source at rest within the observers reference frame, will have a different wavelength. In physics, this phenomena is known as the Doppler Effect, named after Christian Doppler, after he noted the red and blue shift seen in astrophysical observations of stars [157]. Stars known to emit a certain wavelength of light will be observed to have wavelength of light shifted depending on whether the star

is moving towards or away from the earth (see Figure 2.46). A common way of experiencing the Doppler Effect is a traveling ambulance siren. Sound waves emanating through the siren change based on how fast and in what direction the ambulance is moving.

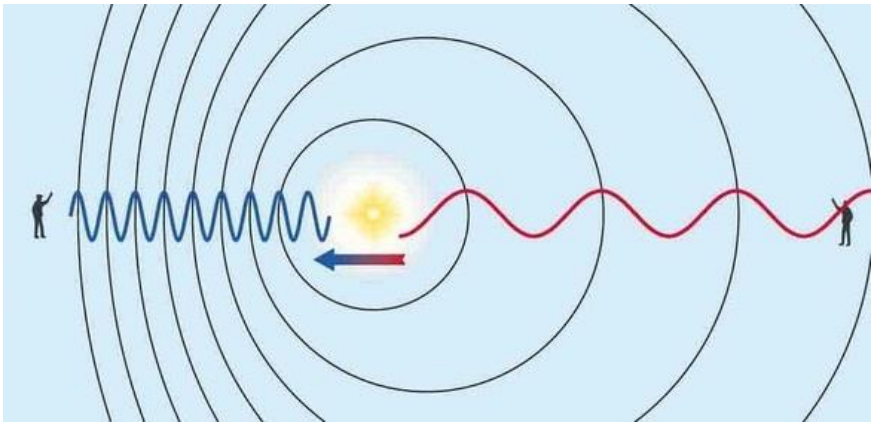

Figure 2.46 Red and blue shift in stars [158].

This relation between light wavelength and velocity is given by the following equation:

$$z = \frac{\lambda_{obsv} - \lambda_{emit}}{\lambda_{emit}} \tag{2.33}$$

where z is the dimensionless shift (z<0 approaching or blue shift, and z>0 moving away or red shift), λ_{emit} is the normal wavelength of the object without velocity and λ_{obsv} is the observed wavelength of the object.

In the experiments, light is emitted by a collimator onto a target at a set wavelength. That light travels through the air and hits a sample point. When that point is in motion, the light reflected back will be shifted based on the velocity of the sample. The difference between the two wavelengths allows researchers to determine sample velocity.

Light returning from each of the samples depends on two main factors, the angle at which the light returns from the sample and the surface reflectively. While some samples such as those made of gold have excellent reflectivity. Polycarbonate and poly(methyl methacrylate) have near zero reflectivity allowing the majority of light to pass straight through the sample. This can be solved with a sputter coating machine (shown below in Figure 2.47).

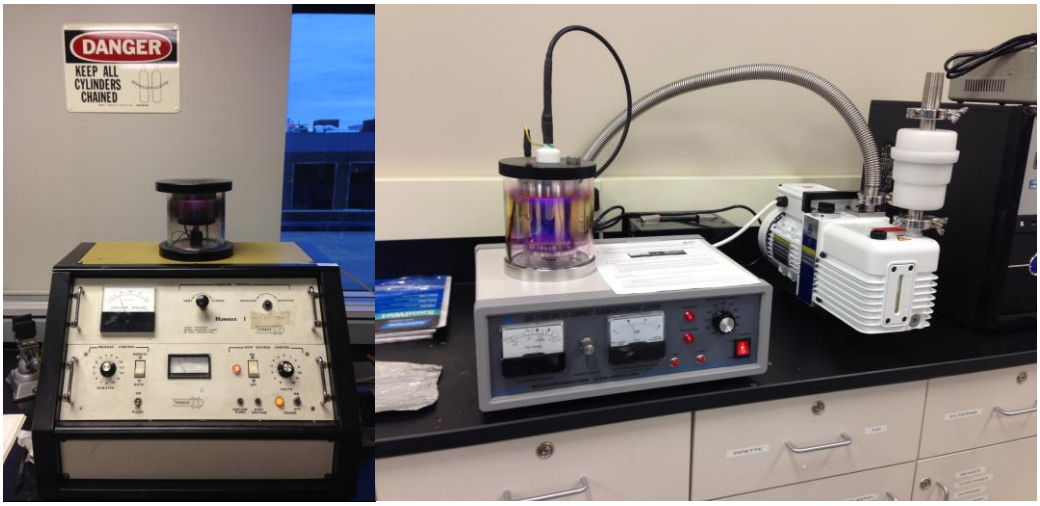

Figure 2.47 Sputter coating machines in Marquette's Mechanical Engineering Department (Technics Hummer 1) and Dental School (MTI GSL-1100x-SPC-12) respectively.

These sputter coaters can deposit a layer of metal such as gold or platinum, though gold works best for the wavelengths of our lasers. Figure 2.48 displays a typical curve of sputtering rates for various metals; samples generally were coated for 5-15 minutes for adequate coverage, though breaks were taken every 2 minutes to ensure samples, especially those made of plastic would not boil.

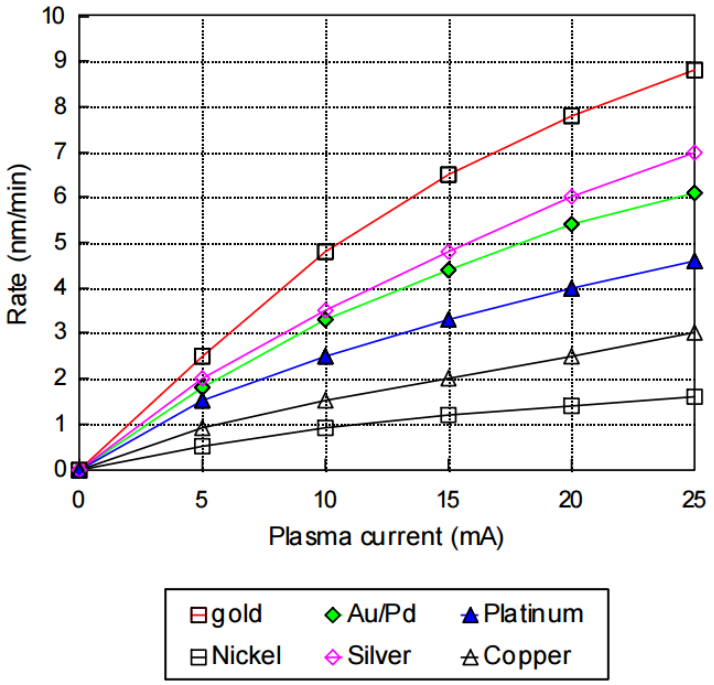

Figure 2.48 Sputtering rates for the Marquette Dental School sputter machine [159].

A smooth coated sample, like the acrylic shown in Figure 2.49, is not enough to guarantee a signal as light must also be returned from the surface to the Fiber optic collimators.

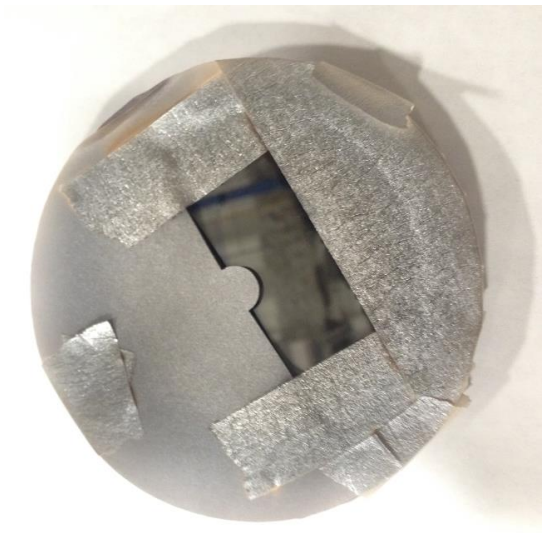

Figure 2.49 Sputter coated acrylic sample.

To ensure a light signal return, a retro reflective surface made by micro machining or laser etching is recommended. There are two different types of machine-able retro-reflectors, square and triangular. Other materials such as the retro-reflective beads on roads were also tested with excellent experimental results. The method of affixing the beads to the sample surface, however, interfered with readings of actual material behavior.

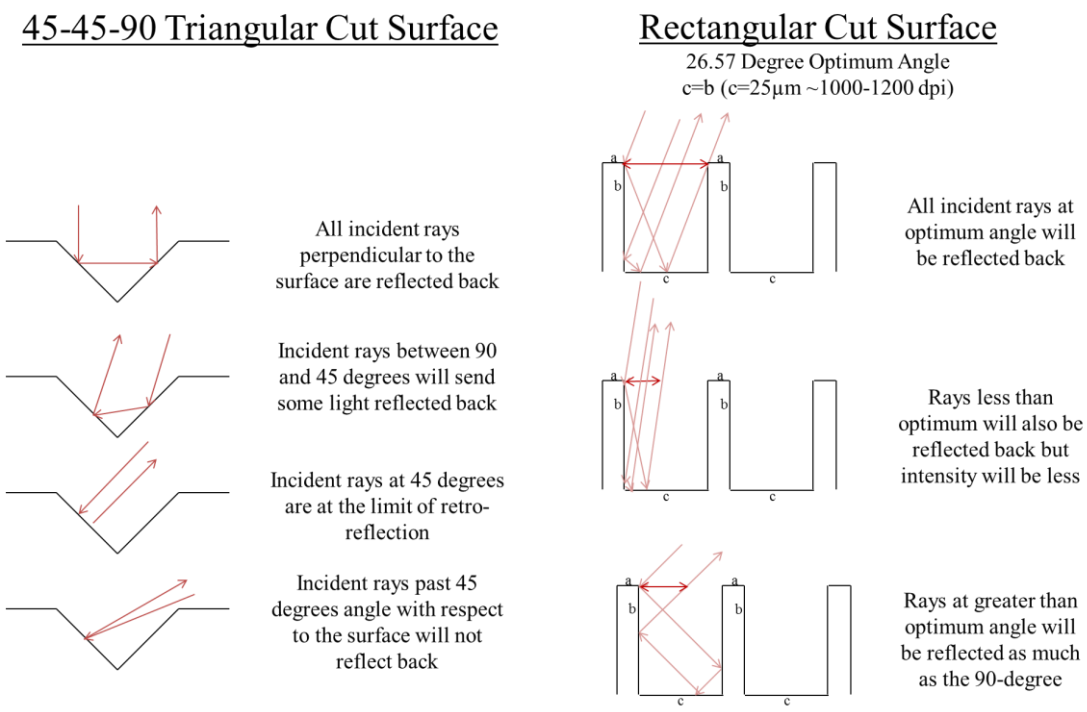

Figure 2.50 Recommened surface profiles.

Retro-reflective surfaces like those shown in Figure 2.50 allow for return signals even if the alignment of the emitting collimator is less than perfect.

While PDV in shock physics is used primarily for the measuring of material surface velocities, a sample investigation is analyzed here for a down barrel velocity reading taken during a 390 psig, 0.4322 kg shot. As shown below in Figure 2.51 collimators are typically placed on an adjustable bridge, which can orient the collimator to a target (a traditional target is not included in the setup below). Once oriented, a fast acting super glue should be used to keep the collimator in place followed by a manufacturer recommended epoxy to retain orientation during tank pull-down and during the impact, as superglue shatters at high pressures.

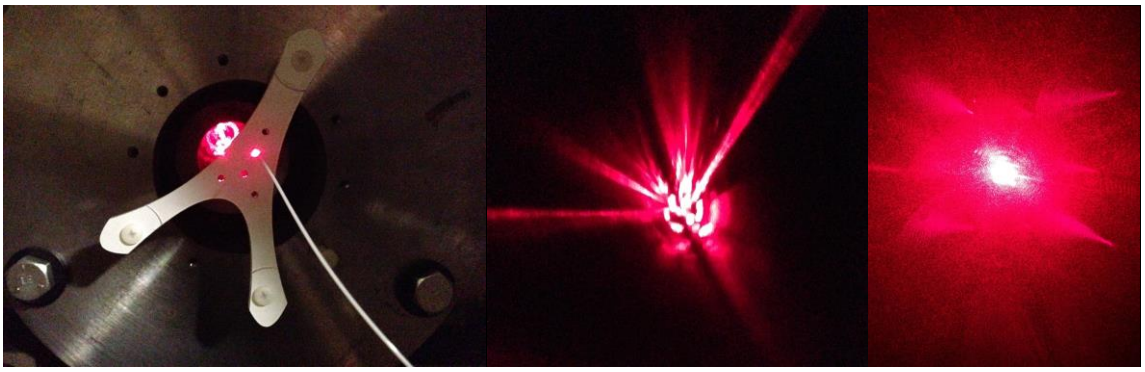

Figure 2.51 Down barrel PDV.

Assuming that light can be both emitted and received, this can be accomplished with a single probe. Data captured by the PDV system is converted to a voltage waveform and that signal is captured on the PDV oscilloscope shown in Figure 2.52.

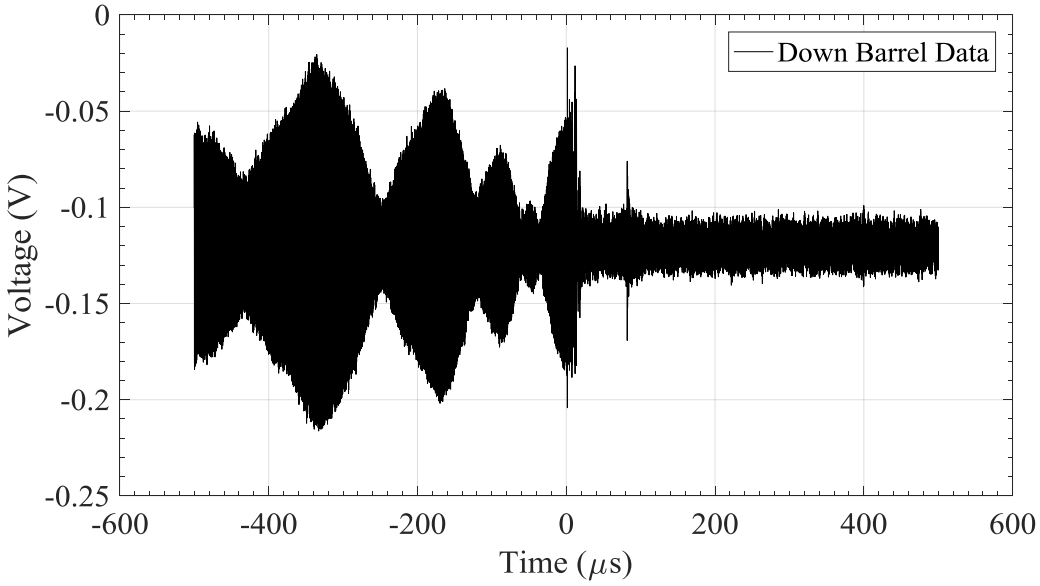

Figure 2.52 Raw PDV output for the down barrel probe.

Data taken from the PDV may at first seem difficult to interpret; this is due to the fact that the relevant reading lies within the frequency of the waveforms rather than the voltage of the signal. To convert the data into more understandable graphs, a Fourier Fast transform is utilized. This algorithm samples spans of time in data and sorts the frequencies within that waveform. The output is shown below in Figure 2.53 for the first 1 microsecond of data (in most cases, one should sample in small time spans).

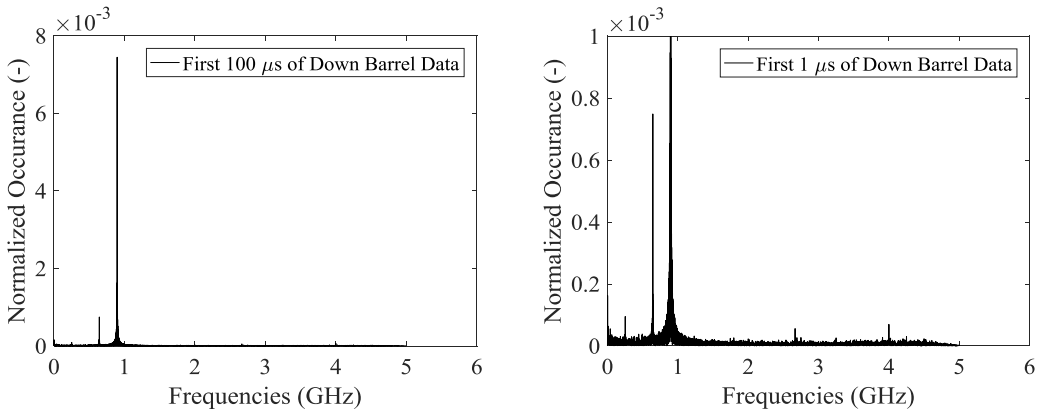

Figure 2.53 Plots of identical datasets displaying FFT output.

From each of these sampled data sets, there will be frequencies which are found more often than others. Typically the peak data is the correct signal, but in some cases it might be the second or even third highest peak. Since one must calculate the FFT to find peak data and this calculation is time consuming, FFTs completed by this researcher save a sorted ranking of each FFT per time step. Once the FFT has run its course, the following equation is utilized, shown here for the highest per time sample:

$$Measured\ Velocity = \frac{Freq_{Highest} - Freq_{Beat}}{2}\ Wavelength_{Emitted} \quad (2.34)$$

where the measured velocity during a sampled length of time is a function of half the difference between the highest sample frequency $Freq_{Highest}$ and the beat frequency $Freq_{Beat}$ experienced within that sampled time, multiplied by the emitted wavelength $Wavelength_{Emitted}$. The beat frequency, which has not yet been mentioned, is the baseline frequency measured by the probe for zero velocity. In the case of the down barrel probe, velocities captured were always measured above zero velocity. Probe data collected measuring the rear of a target sample had a large span of zero velocity data, which was used as the beat frequency. Finally the emitted wavelength is established from the reference laser (part of the PDV System) and has a typical value ranging from 1550-1550.005 nm using Marquette's current setup. Using this equation a plot of the captured down barrel velocity is shown in Figure 2.54:

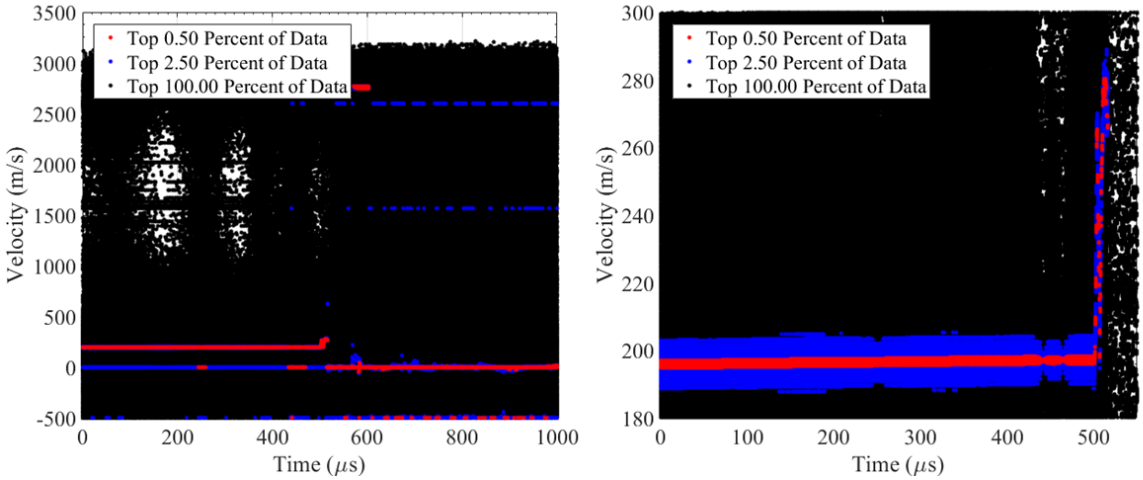

Figure 2.54 Final data collected from the down barrel PDV.

Data between 0 and 500 microseconds captures the velocity of the projectile traveling down the barrel peaking at a velocity of 197.25 m/s, which compares well with anticipated light gate measurements mentioned in section 2.2.5. Data after 500 microseconds is no longer valid as the probe has been disrupted. By 550 microseconds, the probe has been severed from the laser fiber optic line. As anticipated, only the top 0.5% of data seems to show the correct velocity. As more data is included to 2.5%, the trend of the velocity is still captured, but the spread of velocities increases. By the time 100% of data is included the velocity trend can no longer be seen.

In addition to PDV probes, Dynasen pins can be used to find time of arrival at direct set points on a target's surface. This is useful for triggering data collection from the PDV probes. Alternately, three pins when spaced out over target within the flyer impact area can return the alignment of flyer and target at impact. Mounting the pins can be difficult, but after drilling a hole an epoxy specific to the bonded materials plus a weight

or clamp keeps the pins from shifting during set time. Pins come in two main types: piezoelectric pins that when crushed create a voltage spike and make-pins that when impacted with a conductive material create a circuit.

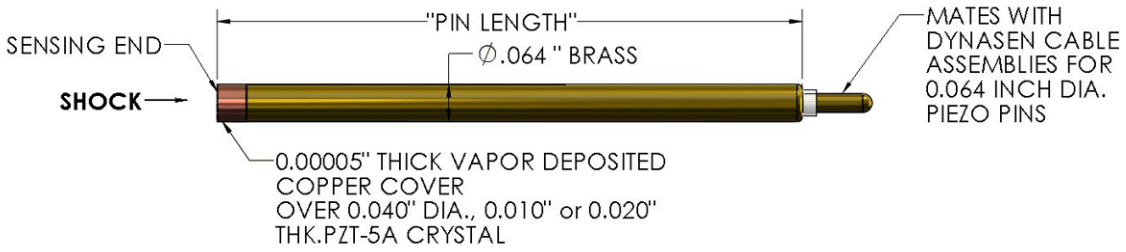

Figure 2.55 Piezoelectric pin [160].

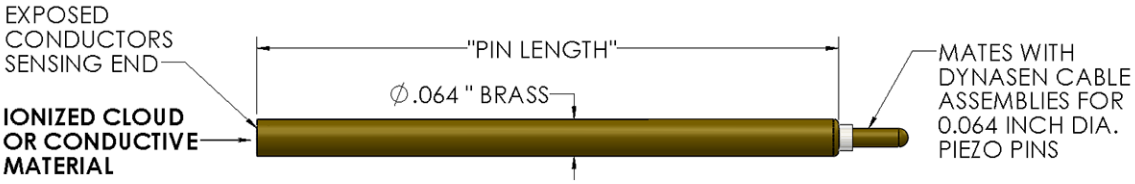

Figure 2.56 Conductive make-pin [160].

These pins as mentioned in the above figure can be connected to sensing equipment via purpose built BNC cables also sold by Dynasen. Alternatively, though not recommended by the manufacturer, once the cables have been used they can and have successfully been reused by soldering the two wires onto the exposed probe pin end.

2.2.7 Vacuum System

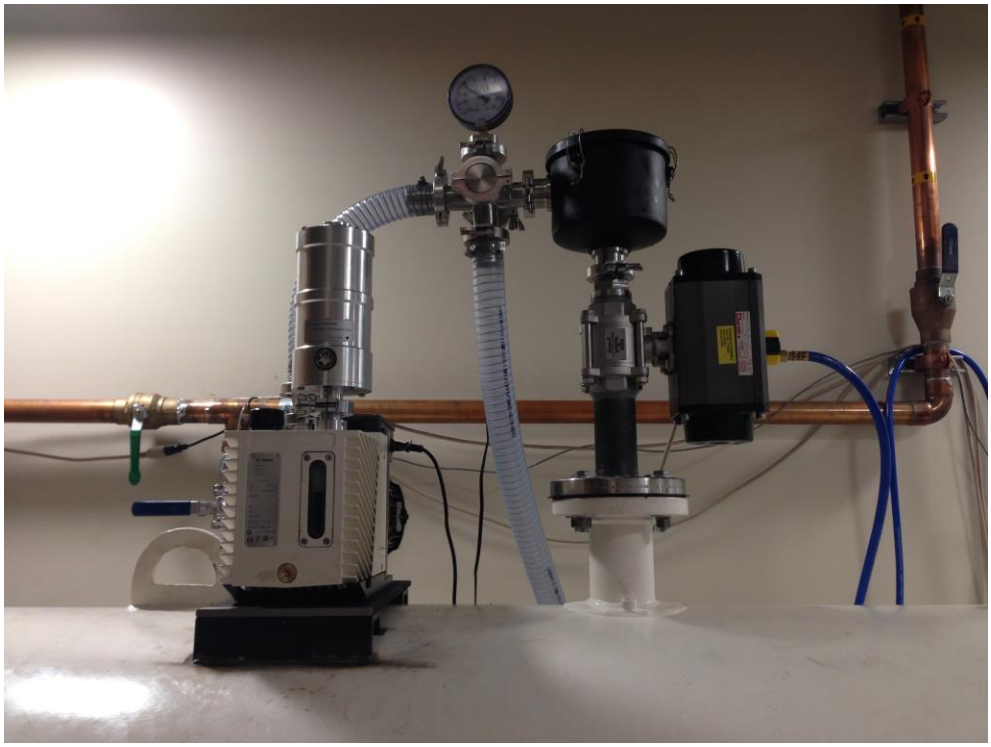

Figure 2.57 The Marquette 2 inch gun vacuum system.

Downrange of the barrel, a target and catch tank can be rolled apart to access specific experimental setups, or vacuum seal prior to firing. While the target tank is used as the experimental hub for the collision, the vacuum system allows the entire gun assembly to come to equilibrium pressure with a post firing pressure, below the range of a single atmosphere. To enable this, both the target and catch tank are vacuumed down to ~60 millitorr pressure at the onset. This keeps the projectile free of any forward pressure during the shot and allows the shot to be contained within the system. A series of two

vacuum gauges shown below in Figure 2.58, allows for monitoring of vacuum pressure between 0 to -30 in Hg (Dial Gauge) and 2000 to 1 millitorr (KJL Thermocouple [161]). The dial gauge functions using a bourdon tube, which contracts and expands based on the pressure within the system actuating the dial. These gauges are the same types that are often used in high-pressure applications. The thermocouple gauge measures the voltage across a wire exposed to the pressure within a chamber, based on the pressure molecules that are able to take more or less heat away from the wire affecting voltage readings. In general, higher pressures take more heat away and correspond to lower voltages. In practice, these gauges are often used as controllers, switching rough pumps (used for viscous or Knudsen flow) like Marquette's Agilent rotary vane vacuum to finer pumps like a turbo molecular pump (used for molecular flows) [162].

Two gauges were chosen, as the useful ranges through which they measure pressure are different. Even though a gauge might be advertised to read down to 0 absolute pressure readings with an error of ±0.5 in Hg (12.7 Torr), the guage would not be able to resolve the range between 50-100 millitorr used in gas gun experiments. Thus, a physical gauge allowed for experimenters to physically observe the rough status of vacuum and pressurization in the tank without the use electrical equipment, in case of fault. For fine measurements the electrical KJL gauge measured pressures with manufacturer set points around 100 and 500 millitor, around the region of experimental interest. An additional benefit of the KJL gauge was the ability to send an electrical signal to the control system for remote observation of vacuum pressure in the Labview terminal.

Before firing the vacuum safety valve should be closed to isolate the KJL gauge from sudden pressure shocks occurring during experimentation. After firing is complete, remaining particulates are scrubbed from the system by forcing air down the barrel and opening the manual valve to Marquette's rough vaccum pump, after passing through a filter.

Figure 2.58 Vacuum gauges: high pressure and low pressure.

A complete assembly of the vacuum system is shown below in Figure 2.59.

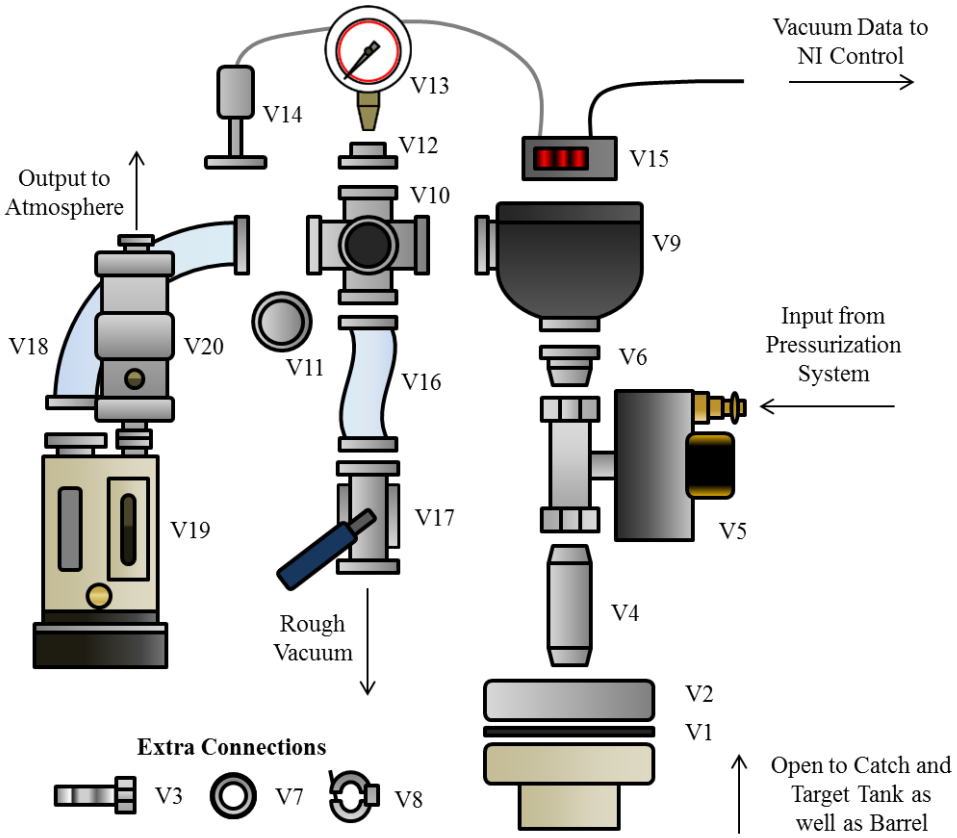

Figure 2.59 Distribution system reference diagram.

Bringing the system pressure down to a complete vacuum is often difficult with leaks being hard to both locate and seal. Leaks are to be expected wherever there is a joint between two separate components, so care in the preparation of components before mating saves time. Grease should be freshly applied to all separated O-ring seals exposed to vacuum. Grease has also been applied to NPT threading after pipe tape as well as a very light coating on KF40 couplings. For positive pressure, applied bubble solution allows for visual identification of depressurization; however, bubble solution placed on sections under vacuum also bubbles, but on the inside of the opaque apparatus, which is not helpful.

There are two main methods for detecting vacuum leaks. In situations where the pressure dwells between both the high and low pressure gauges for longer than expectation (~1 hour), one should scan the suspect sections by simply listening for leaks. At the time of this report, only DOW Corning vacuum grease was available for use within the shock lab. Given a slight size mismatch on the pressure diagnostic, bulkhead grease applied around the joining collar would slowly be pulled into the system.

When vacuum pressure falls below 2000 millitorr and reaches a steady state such that the leak rate into the system counteracts the vacuum applied, helium can be utilized to detect the leak. A wand expelling helium placed near the suspected leak will cause the pressure to quickly rise because the smaller molecular diameter of helium flows more quickly through exposed orifices raising the steady state pressure [163]. For a more controlled application, a plastic bag can easily allow only desired regions of exposure and conserve helium. In fact, hydrogen could be used with greater effect; however, as mentioned throughout this and other sections, hydrogen flammability raises concern.

While vacuum grease can be used in all sealing cases, Apiezon Q is a less sticky and cost effective method of sealing leaks. Apiezon Q has the consistency of a putty, with an even greater viscosity as compared with grease. When observed on other systems, it neither dried nor stuck to the hand of the researcher and also remained reusable. Apiezon Q however is not recommended for sealing O-rings. Dow Corning Vacuum Grease and Apiezon Q can be sourced from both vacuum suppliers as well as McMaster-Carr. The complete list of parts that make up the Vacuum System are catalogued within Table 2.15 below.

Table 2.15 Vacuum System Callout Table

Callout	Part Name	Supplier	Part Number	Notes	Inlet	Outlet
V1	Gasket	McMaster Carr	8516T238		ANSI 2”	
V2	Pipe Flange	McMaster Carr	44685K16		ANSI 2” pipe	2” FNPT
V3						
V4	Schedule 80 Pipe	McMaster Carr	46755K65	5” Length	2” MNPT	2” MNPT
V5	Vacuum Safety Valve	DuraValve	2” DM340	Rated 1000psig	2” FNPT	2” FNPT
V6	2” Adaptor	Ideal Vacuum	P106111		2” MNPT	KF-40
V7	KF 40 Centering Ring	Ideal Vacuum	P101962		KF40	
V8	KF 40 Clamp	Ideal Vacuum	P106717		KF40	
V9	Dust Filter	Kurt J Lesker	PFI843KF40B		KF40	
V10	6-Way	Ideal Vacuum	P102644		KF40	KF40
V11	Blank	Ideal Vacuum	P101204		KF40	
V12	¼” Adaptor	Ideal Vacuum	P101312		KF40	¼” FNPT
V13	Vacuum Gauge	Wika	4253397		¼” MNPT	
V14	1/8” Adaptor	Ideal Vacuum	P101311		KF 40	1/8” FNPT
V15	Thermocouple Gauge	Kurt J Lesker	KJL615TC-K		1/8” MNPT	
V16	6’ Flex Hose	Ideal Vacuum	P103808		KF 40	KF 40
V17	Ball Valve	Ideal Vacuum	P103570		KF 40	KF 40
V18	1’ Flex Hose	Ideal Vacuum	P103803		KF 40	KF 40
V19	Vacuum Reducer	Ideal Vacuum	P101230		KF 40	KF 25
V20	KF 25 Centering Ring	Ideal Vacuum	P101962		KF 25	
V21	KF 25 Clamp	Ideal Vacuum	P106717		KF 25	
V22	Vacuum Pump	Agilent	DS 602		KF 25	
V23	Oil Exhaust Filter	Agilent	949-9392		KF 25	KF 25

2.2.8 Some Notes on Machining

In the experimental realm of shock physics, preparation work and machining will take the lion share of work time. It is assumed here that the reader already has both the knowledge and skills to design and draft, that is to say make-up the dimensions for sculpting a part from a blank piece of material.

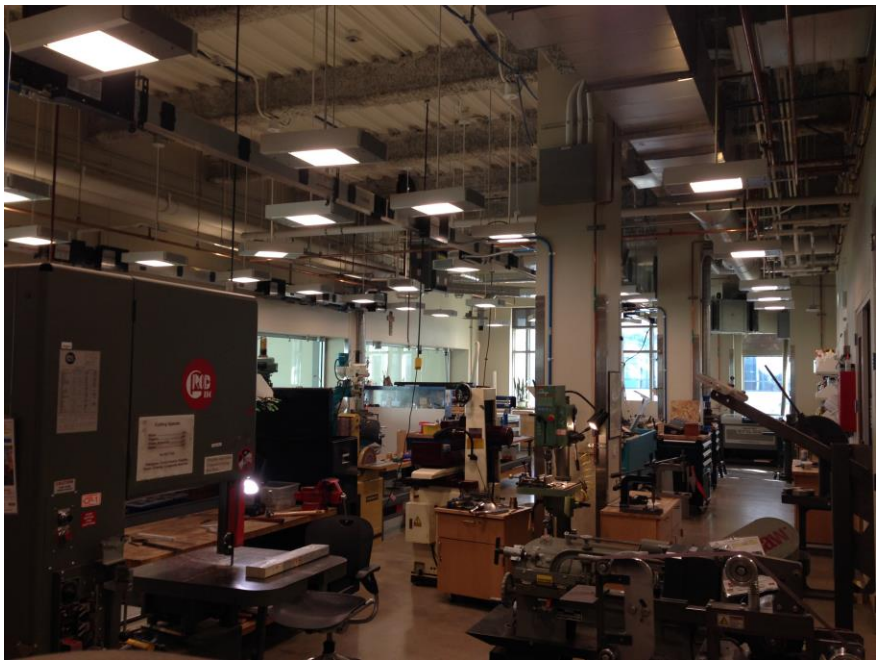

Figure 2.60 Marquette machine shop.

During this study all of the machines within Marquette's machine shop, shown above, were utilized. While not perfect for every task, each of the tools within the shop were, when taken collectively, enough to perform experiments within an acceptable tolerance (in most cases down to a few thousandths accuracy). There are always more ways to complete a given machining task and the number of options increases with the number or tools available.

A significant portion of time in the design and manufacture of experiments will be spent in the design and machining of the targets and mounts to the highest degree of accuracy possible, while also making sure to accomplish tasks in a timely fashion and with care not to damage the machining equipment. In general, this can be accomplished

by following five rules. First, set the machine's axis to a convenient location on the part before removing material. One also must know how much material there is to being with in order to make an accurate prediction of the finalized dimensions. Second, once a material has been cut, removing burrs will keep a part square when clamping or affixing to another part and also prevent cuts on unwary users. Third, on a similar note, clamp when possible the squarest sections to make optimal use of the work piece. Fourth, check the size and quality of the tool in use; tools can wear down in size and chips in a tool can at best slow down cutting time and at worst ruin a good part.

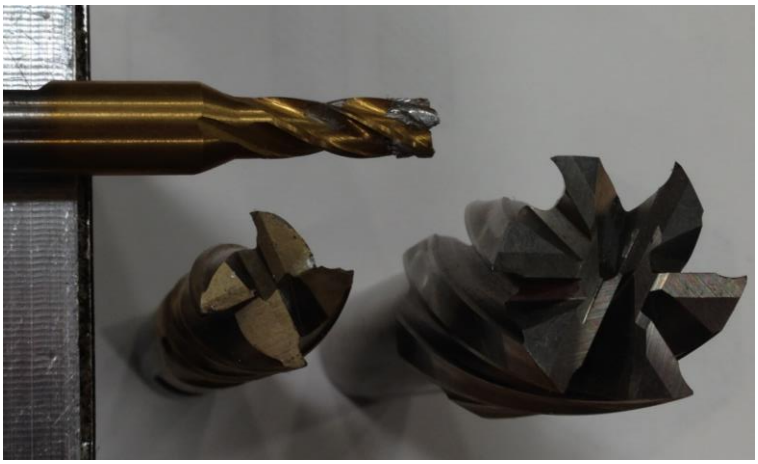

Figure 2.61 Examples of available milling tools from left to right, chipped teeth, clogged flutes, ideal tool.

Fifth and finally, use the proper feeds and speeds, this will not only increase the tools work-life and optimize speed but it will also make for even cuts. Take it slow, the machines are dangerous; measure twice cut once, being conservative when nearing

completion. Think before doing and follow the machinist's advice! With practice on the various machines, improvement will be made.

Figure 2.62 A myriad of tools are available to achieve higher precision machining. gauge blocks (mill), dials (mill and lathe) and the wiggler (mill) are all excellent tools to keep the dimensions of one's part on point.

Of these five rules, the most tedious of the tasks was in the choosing of feeds and speeds, especially as every single part required special treatment. When machining with high speed steel, it is possible to tell the proper machine feeds and speeds by the look of the removed material, often referred to as chips. Should the tool be translating too fast, cutting too deep, or the rpm be set too high, the chips will change color from silver to gold to blue. For high speed steel, gold and blue chips mean that one is machining too aggressively!

Figure 2.63 Steel chips from left to right: blue, silver, and gold.

Unfortunately for other commonly machined materials, such as polycarbonate, brass, wood and aluminum, and when using carbide tooling, the method for noticing the proper machine settings are not as easily noticed. Choosing improper settings with other tooling and material will often be heard or felt and, if not immediately stopped, will often damage the cutting tool.

Therefore, before beginning any job in the shop one should have a rough idea of the cutting speeds and feeds to use. To make it simple, the equation below is suggested to be used for lathing, milling, and only in the hobbyist setting. This is meant to be a simplified version for a quick calculation before turning on the machine. For large material runs, where tool wear and time per part are more valuable, consult the Machinists handbook [164] or textbook on machining! For the mill and drill press, one should use the below equation where N is the Spindle rpm, V is the feed in ft/min, F_f and F_d are the feed and depth factor (.8), and D tool diameter (or part diameter for the lathe) in inches:

$$N = \frac{12\,V\,F_f\,F_d}{\pi\,D} \approx \frac{4\,V}{D} \tag{2.35}$$

The equation above, when combined with the values in Table 2.16 below, and typical lower feed rate utilized when hand machining, are generally good as ballpark estimates for the speeds to run mill, drill press and lathe using high speed steel bits. For carbide bits one can general increase rpm by 2-3 times. For hole diameters less than an 1/8 inch, it is recommended to add lubrication to the drill bit and pay extra close attention to prevent chips from clogging up the flutes, which are the only path of exit during drilling. On the mill finishing pass, one should take off a lesser amount of material, decrease the feed rate and increase the rpm for the best possible finish (if looks or flatness is important).

Table 2.16 A crude Feed Rate Table for Common Items (for more precise numbers, please consult the Machinist's Handbook [164])

Material	Approximate Material Feed Rate HHS (choose average or adjust to lower for harder material variant)	Recommendations
Titanium	70-110 ft/min	Carbide Tooling
Ferritic and Austenitic Stainless Steel	25-75 ft/min	Carbide Tooling
Low Carbon Steel	65-110 ft/min	Carbide Tooling
Medium Carbon Steel	25-100 ft/min	Carbide Tooling
Copper Alloys	100-350 ft/min	High Speed Steel and Dull the Cutter
Aluminum	350-600 ft/min	Two Flute High Speed Steel
Polycarbonate	350-1000 ft/min	High Speed Steel
Some resultant RPM will max out the mill lathe and drill press, use highest comfortable setting.		

Identifying the difference between high speed steel and carbide is a simple matter. In general, carbide bits are both heavier than their counterparts for a given size. For mill bits, a gold coating is added while high speed steel bits remain silver. Lathing tools made from carbide are often pre-shaped and mounted within steel, while high speed steel tools are the same material throughout.

Other materials such as plastic, wood, and rubber within this study were cut utilizing the epilog engraver, scroll saw, chop saw, and band saw. While all but the epilog engraver were not great for precision cutting, these machines were all clearly labeled for operation.

3. EXPERIMENTAL SETUP

Each experiment will be different, though it will use the same common elements within each shot: the gun, diagnostic equipment and samples. Each of these elements has the ability to cause harm to operators and to others: high pressure gases, high velocity projectiles, laser light capable of harming optical tissue and pulmonological hazards such as fine particulates, like silica. Each of these common items is addressed in the protocol outlined below to provide a safe, repeatable standard operation procedure relevant to most gas gun experiments and basic record of past experiments.

3.1 Firing Procedure and Safety Protocol

Standard Operating Procedure (SOP) – June 10, 2017 Edition
Marquette University
Setup Procedure for Two-Inch Gas Gun

The following is to be used in conjunction with the PDV Standard Operating Procedure.

Date: _____/ /_____

Preliminary Information

1.__ Schedule shot with the MARVL visualization lab.
2.__ Record pre-shot data:

Sponsor/Grant: _____
Experiment Designer(s): _____
Please attach a CAD drawing or relevant simulation if applicable!

Type:
- o Flyer Plate
- o Reverse Ballistic
- o Pressure Shear
- o Conical
- o Other: _____

Basic Schematic:

Brief Description:

_____

_____

_____

_____

Target Material(s) Description

Material	Description	Thickness (mm)	Diameter (mm)	Mass (g)	Density (g/cc)	Location Start (x,y,z)	Location End (x,y,z)

Projectile Specifications: _____ grams, _____ cm (length) – for theoretical shot vel.

Desired Shot Velocity: _____ m/s

Anticipated light gate event time (First fall to last rise): _____ µs

High Pressure Disk Material: _____, Quantity:___, Pressure Rating: _____ psi

Low Pressure Disk Material: _____, Quantity:___, Pressure Rating: _____ psi

Set Pressures: Low Side: _____psig, High Side: _____psig

Impact Plate Resistance: GO / NO GO

For High Pressure Shots

3.__ If applicable, set the small and large chamber pressures using the high and low pressure regulators attached to the distribution system.

Gun Maintenance

4.__ Check the breach, barrel, target tank, and catch tank for foreign objects left by previous shot or for objects left by employees after the previous shot. Apply vacuum grease as needed!
5.__ Clean the barrel using the push-rod to clear any debris from previous shots.
6.__ Check the security of the steel back plates, mates, and chains on the downrange end of the catch tank.

Target Setup: Velocity Laser Block

7.__ Orient the velocity blocks, lasers and collimators on the velocity plate, aligning the collimators to pick up a ~5 Volt signal. Make sure that all screws are properly attached. Place the velocity block setup into the target tank and recheck the four channels recording peak velocity, the ability of the beams to be broken, and the relation between the channels and their location within the velocity block path. (Velocity Pin 1 is closest to the muzzle; pins increasing in number increase in distance away from the first pins by a nominal distance of 0.75 inches for each subsequent pin,)

Final Velocity Recordings (Pre-Vacuum)

Velocity Pin 1	Voltage	DC Offset _____
Velocity Pin 2	Voltage	DC Offset _____
Velocity Pin 3	Voltage	DC Offset _____
Velocity Pin 4	Voltage	DC Offset _____

Trigger Level: _____, Trigger Time: _____, Trigger Channel _____,
Time Divisions:_____ microsec/div

Channel	1	2	3	4
mV/div				
impedance				

Target Setup: Target Plate Orientation

8.__ Attach the target plate to the three mounting bolts and use the radial surface dial to check radial symmetry. The alignment should in general be less than a milli-radian in offset. If target plate is already attached, recheck alignment.
Alignment: _____ milli-radians

Target Setup: PDV Settings

9.__ Ensure Laser/High Pressure warnings signs are on the door.
10.__ Ensure PDV probes and PZT/shorting pins are epoxied into the target ensure PDV are within the acceptable range of light return (better than -30dBm).
11.__ Take a picture of the target prior to assembly onto the holder.
12.__ Place the target into the target holder. Wear protective mask and eyewear if necessary.

13.__ In the case of pressure-shear/conical shots, align blank projectile, placed in the muzzle of the barrel, to the target fixture ensuring angles mate. Afterwards, remove blank projectile.
14.__ Take an additional picture of final assembled target and attach.
15.__ Measure the distance between the target and the end of the barrel. Record this value. Try to minimize or eliminate free flight.
16.__ Check responsivity/light return of PDV probes again.
17.__ Feed PDV probes out of the hermetic bulkhead and connect to the patch cables leading into the system. LABEL patch cables corresponding to probe placement.

a) Probe #1 – Placement_____ - Channel #_____
b) Probe #2 – Placement_____ -Channel #_____
c) Probe #3 – Placement_____ - Channel #_____
d) Probe #4 – Placement_____ - Channel #_____

18.__ Recheck the light return on the PDV and the functionality of the velocity block:

Target Laser Wavelength: _____ (nm)

Reference Laser Wavelength: _____ (nm)

Expected Base Beat Frequency: _____ (GHz, theory)

Measured Sample Frequency: _____ (GHz, experimental)

Booster Laser Power: _____ mA

1 - Target Power: _____ (dBm), Combined Power: _____ (dBm)
2 - Target Power: _____ (dBm), Combined Power: _____ (dBm)
3 - Target Power: _____ (dBm), Combined Power: _____ (dBm)
4 - Target Power: _____ (dBm), Combined Power: _____ (dBm)

Trigger Source: _____ (1, 2, 3, 4, or external)

Trigger Level: _____, Trigger Time: _____

Time Divisions:_____microsec/div

Channel	**1**	**2**	**3**	**4**
mV/div				
impedance				

19. Terminate emission of PDV until later checks.

Target Setup: PZT/Shorting Pins Settings

20. ___ Connect PZT/shorting pins. LABEL placement.

a) Pin #1 – Placement_____ - Channel #_____ - Type:_____
b) Pin #2 – Placement_____ - Channel #_____ - Type:_____
c) Pin #3 – Placement_____ - Channel #_____ - Type:_____
d) Pin #4 – Placement_____ - Channel #_____ - Type:_____

Trigger Source: _____ (Summation/Direct from Channel #)
Trigger Level: _____, Trigger Time: _____
(Recommended less than 500 mV trigger threshold for PZT pins)
Time Divisions:_____microsec/div
Recommendations:
a) Set scope to 5 V/div, 500 ns/div.
b) Use the "EXT OUT" from the Dynessen to the external trigger "EXT TRIG IN" on the PDV scope.
c) Impedance SHOULD BE 1 Mohm
d) DC Offset SHOULD BE THE SAME FOR ALL CHANNELS:

Channel	**1**	**2**	**3**	**4**
mV/div				
impedance				

External Trigger Sent to: _____

2. ___ Test Trigger setup between summation circuit, pin scope, and PDV scope.

a) Set the trigger.
b) Perform battery test of each BNC cable with a trigger at less than 150mV.
c) Set posttest triggers to <500 mV for actual PZT pins.
d) Place each signal at zero offset.
e) Trigger the delay 2 μs to the left of center.

3.__ Once satisfied with target alignment and in-target diagnostics, slide the blast shield into place.
4.__ Recheck light return for PDV, and triggering once blast shield is in place.
Vacuum Process
5.__ Place the large O-ring between the catch tank and target tank, lubricate if needed.
6.__ Re-check that all non-essential items are taken out of the target tank and catch tank.

7.__ Close the vacuum tank and attach all eight bolts coupling the target tank and catch tank.
8. ___Close the catch tank man-way and use all eight bolts to secure the hatch.
9.___Close the breach with burst disks making sure that all 6 O-rings are in place and undamaged.
10.___Note the ideal reservoir tank burst disk pressure and trigger tank burst disk pressure on the data sheet (should have been previously recorded).
11.__ Make sure that all ports and the barrel are locked down, especially PDV bulk-head and Breach Tank.
12.__ Check that air hose is connected to the Haskel pump on the high pressure side of the system.
13.__ Turn on Labview and the NI Daq Chassis before checking functionality and beginning pull-down.

- __ Open the vacuum safety valve.
- __ Open the building vacuum valve.
- __ Once the system has reached a pressure of -20inHg close the building vacuum valve.
- __ Turn on the Agilent pump.
- __ Open valves 1-4 on the pressure side.
- __ Run the Haskel.
- __ Stop Haskel.
- __ Close valves 1-4.

14.__Test the seals within the breach using low pressure air, before releasing this air pressure.
15.__ Ensure that air within the large and small chambers is released and is not under pressure during put down. In addition, make sure that all high pressure valves are closed.
16.__ Send out a warning to adjacent labs that a pressurization will commence within the next two hours, corresponding with previously schedule time.
17.__ Run the Agilent to the desired millitorr range.

Prior to Pressurization

18.__ Perform a final recheck on all diagnostic systems, and record any changes:

a)__ PDV Light Return
b)__ PZT/Shorting Pin Triggering Circuit
c)__ Laser Velocity Setup

19.__ Record the final vacuum pressure on the data sheet.
20.__ Setup computers with Skype or FaceTime to record the pressure gauges and oscilloscopes.
21.__ Evacuate non-essential personnel and alert nearby labs of impending test.

22.__ Ensure scope settings have been recorded.
23.__ Arm oscilloscopes to be triggered.
24.__ Engage lasers so that PDV probes are emitting light.
25.__ Capture preliminary data on PDV scope to establish pre-shot beat frequency, if any measurements greater than 1 millisecond are being made.
26.__ Perform final checks – begin firing procedure only after PDV check and setup check are complete.
27.__ Ensure that at least one pair of laser safety goggles has been placed outside of EH 040 for use after the shot.
28.__ Perform a personnel sweep of the room to ensure no persons are in the room.
29.__ Check Room EH 028 and EH 028a to insure no personnel are in the room.
30.__ Post personnel at either end of the hall to ensure that there will be no persons in the hallway during the shot.

PROCEED TO NEXT PAGE FOR FIRING INSTRUCTIONS

Firing Procedure for Two Inch Gas Gun

To shoot the two-inch gun. The safety procedure includes the following checks:

1.__ Acquire final approval

Signatures for Shot Approval:
Lab Supervisor
Print:
_____
Sign:
_____

Experiment Lead
Print:
_____
Sign:
_____

Gun Personnel Information (Important):
Projectile Specifications: _____grams, _____cm (length) – for theoretical shot vel.
Anticipated Shot Velocity: _____m/s
High Pressure Disk Material: _____, Quantity:___, Pressure Rating: _____psi
Low Pressure Disk Material: _____, Quantity:___, Pressure Rating: _____psi
Set Pressures: Low Side: _____psig, High Side: _____psig

2.__ Gun personnel execute the following steps remotely. Understand that during this stage the gun may fire!!!

a.__ Open Haskel pump valve to pressurize both sections of the breach.
b.__ Once the low pressure is reached, close the low pressure chamber.
Final Low Pressure Pre Creep: _____psig,
c.__ Once the pressure within the breach exceeds low side set pressure, close the vacuum safety valve!
Final Lowest Vacuum Pressure: _____psig,
d.__ Once high pressure chamber within the breech reaches target pressure, close the high pressure breach.
Final Low Pressure: _____psig, High Pressure: _____psig
e.__ Signal experimenters that the gun is ready to fire. Give count and release the small chamber.
f.__ Do Not! begin to ventilate and re-pressurize the vacuum system.

Post Shot

3.__ Designated personnel enter the room with laser safety glasses on; turn off the PDV system.

4.__ Open the vacuum safety valve and record the final system vacuum pressure:

Post Shot Vacuum Pressure: _____inHg.

5.__ Open the manual vacuum release ball valve and electric ball valves between the room air and breach chambers.

6.__ Once the system reaches 20 in Hg, open the building vacuum valve to cycle air through the system for at least 5 min. to remove particulate.

7.__ Collect data from the oscilloscopes (do not turn off oscilloscopes until data has been reviewed).

8.__ Take a picture of all oscilloscope screens to ensure settings are saved.

9.__ Record all data within the big gun notebook and in the experiment history report; ensure all relevant paperwork is attached to the shot log.

10.__ If necessary, wear protective masks and eyewear.

10.__ Open the catch tank to examine the shot results.

11.__ Collect critical components into a large plastic bag and record it with date and other information as a post-shot collection.

12.__ Take photographs as necessary.

13.__ Clean up any particulate left in the catch tank.

14.__ Clean the barrel.

Final Notes:

_____

_____

_____

4. THEORETICAL VS. EXPERIMENTAL GUN BEHAVIOR

4.1 Breach Charging Time

In order to reach pressures above either shop air or the nitrogen supply tank, a Haskel pressure booster is utilized. In practice, one could derive the pump curve with the performance curve Figure 4.1, in additional to the inlet condition and losses from the various components. This is beyond the scope of this paper, as all components leading from the Haskel to the breach were chosen to meet safety requirements; finding components that were both compatible and operated at high-pressure greatly limited availability of choices.

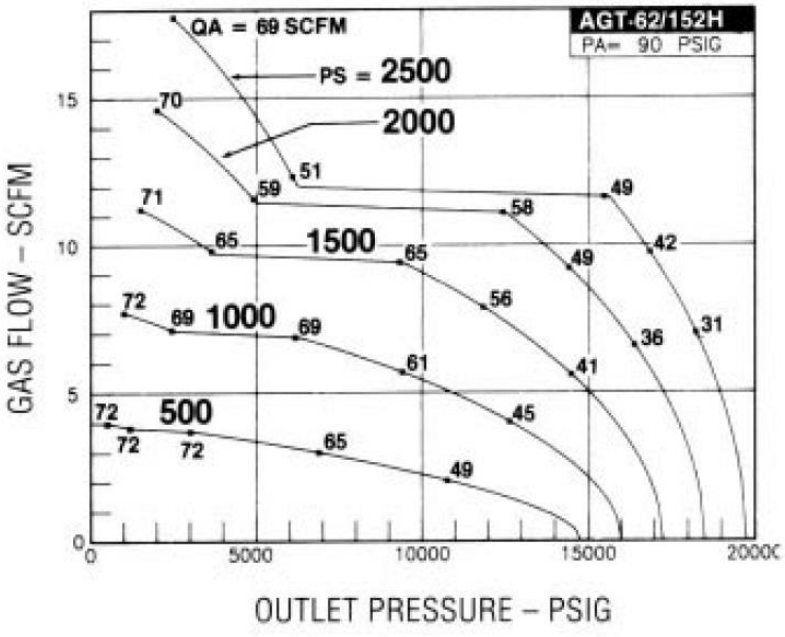

Figure 4.1 Performance curve for the AGT-62/152H Haskel Pressure Booster [165]. P_S is the gas supply pressure (psig), P_a is the driving pressure (psig), P_o is the outlet pressure (psig), and QA is the gas flow of the outlet gas (SCFM).

Optimization of the pressurization system mainly focused on reducing numbers of bends and choosing the largest possible flow area. Looking at the pump curve, one finds the range of pressure supply, PS, to the system ranges from 500-2,500 psig, within these ranges a final breach pressure of 10,000 psig is attainable. While testing it was noted that the Haskel was able to operate with the shop air supplied by the building. By assuming a linear relation between pressure supply and final outlet pressure, it also appears that the Haskel would be capable of pressurizing the breach to ~14,000 psig simply with the shop air supply pressure of 100 psig. Given the flattening of the curves in Figure 4.1 it was anticipated that pressurized air to the breach using shop air supply while slow would have a relatively constant flow rate and result in a linear increase in breach pressure over time.

Recalling the control section of this report (2.2.1), one might recall mention of a needle valve regulating flow from the shop into the Haskel (Figure 2.34). While this served as an interim control device, it was eventually swapped out in favor of solenoid valve, which is less restrictive and effectively increases flow from the shop to the Haskel. In Figure 4.2, the pressurization of the breach for various driving conditions, under shop air supply and driving gas are shown.

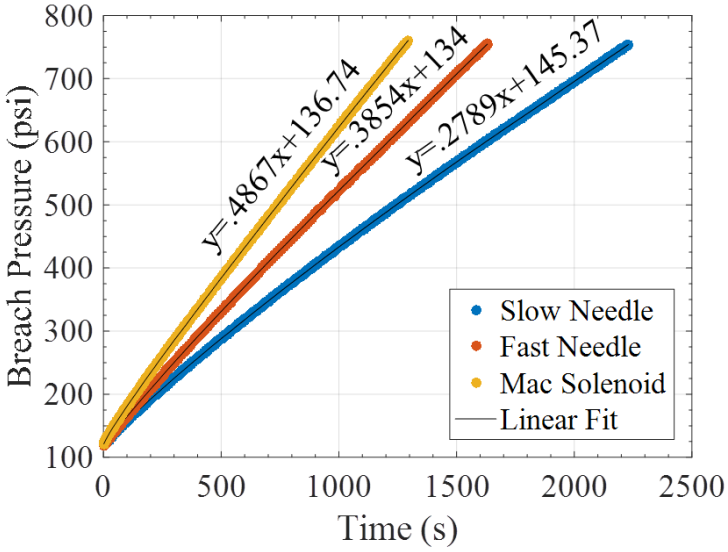

Figure 4.2 Pressurization curve of the combined small and large chamber volume within the breach for different flow control valves to the Haskel drive air supply.

As can clearly be seen, the flow of air to the Haskel is least impeded by the solenoid valve. With this configuration, an extremely linear rise in pressure within the breach is observed with respect to time. Reviewing Figure 4.1, one will note that a supply pressure of 100 psig is not presented; the lowest supply pressure of 500 psig has a near linear pump flow rate out to 3,000 psig. Comparing Figure 4.2 with the trend in Figure 4.1, one can anticipate that the effect of reduced flow rate would be less noticeable as compared with higher supply pressures, though this may reduce pump performance at higher outlet pressures (making the linear fit over estimate performance) and increase pumping times.

A rough estimate of pressurization time using the shop air supply was conducted to evaluate the need of a nitrogen tank for high-pressure shots. It is assumed that the volume filled comprises the entire breach (both high and low side chambers), as the small

chamber comprises a volume significantly smaller volume than that of the high side chamber. Assuming the pressure continues to increase linearly, one can conclude that the time to reach a set pressure given supply pressure of 100 psig to is given by the equation:

$$t = \frac{P_f}{0.5} \tag{4.1}$$

where t is the total pressurization time in (seconds), P_f is the final set pressure, within the entire breach (in psig), and 0.4867 (psi/s) is the rate of pressurization found observed in Figure 4.2 above. This assuming the pressurization does not slow, the total time to pressurize to a 10,000 psig shot, using shop air, is ~5.56 hours. This is why for shots above 1000 psig, which take just over a half-hour, researchers should seriously consider use of the nitrogen tank!

4.2 Burst Disk Failure

In order to release the gases, within the breach, the dual diaphragm system relies on the mechanical failure properties of materials such as: mylar, aluminum, bronze copper and steel. These round plates of material, known as burst disks, fit between pressure chambers within the breach assembly. When these disks are stressed beyond yield strength, they fail, petaling open and releasing driving gases into the gun barrel.

While most burst disks are supplied by Physics Applications Inc. with burst pressure ranges pre-labeled (determined by experimental pressure testing) they are expensive, $50-$100 a shot, and had high failure pressure (1297 psi minimum). Lower pressures were needed to fire at velocities for pressure shear and burst disks produced at Marquette promised lower cost per shot. In this author's experience developing new firing methods for Marquette's smaller ¼ gas gun, the fast acting valve was supplemented with mylar disks cut from sheets, often used as the transparency sheets for light projectors. Using this same material, larger unscored disks were created and pressurized until failure, the results of which are shown later in Figure 4.9. Selections of burst disks are shown below in Figure 4.3.

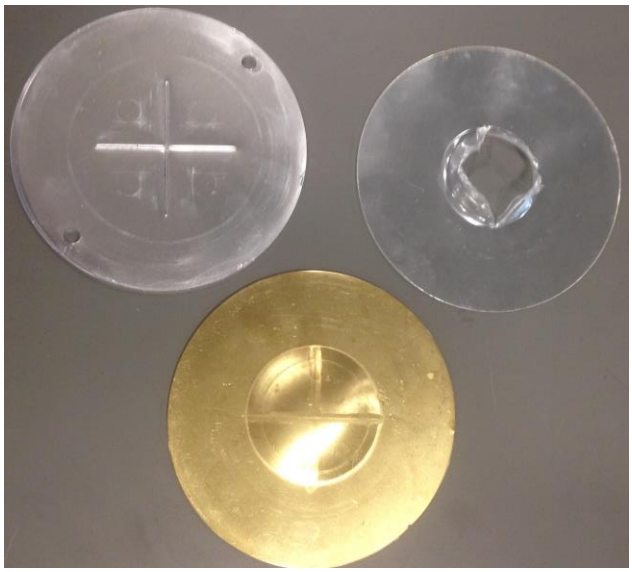

Figure 4.3 Burst disks in varying states of failure; note the bulging effect of the bronze disk, which changes the internal volumes of both chambers.

Metal burst disks, shown above, are available to purchase from Physics Applications Inc. (disks arrive flat with score marks), while mylar disks are produced from 20 gauge, 0.004 inch thick, “Universal Brand Laser Printer Transparency’s #65125,” by laser cut to size. Initial attempts were made at producing in-house burst disks, either by using low powered laser marks on mylar or punches on copper. Concerns regarding consistency especially in early tests made externally manufactured disks preferable.

In addition to the mylar burst disks, a single copper disk was tested. However, instead of merely petaling the center, the copper disk separated from the remainder of the disk and was expelled down the barrel. This was not acceptable, as damage to the internal of the barrel would decrease performance, Figure 4.4.

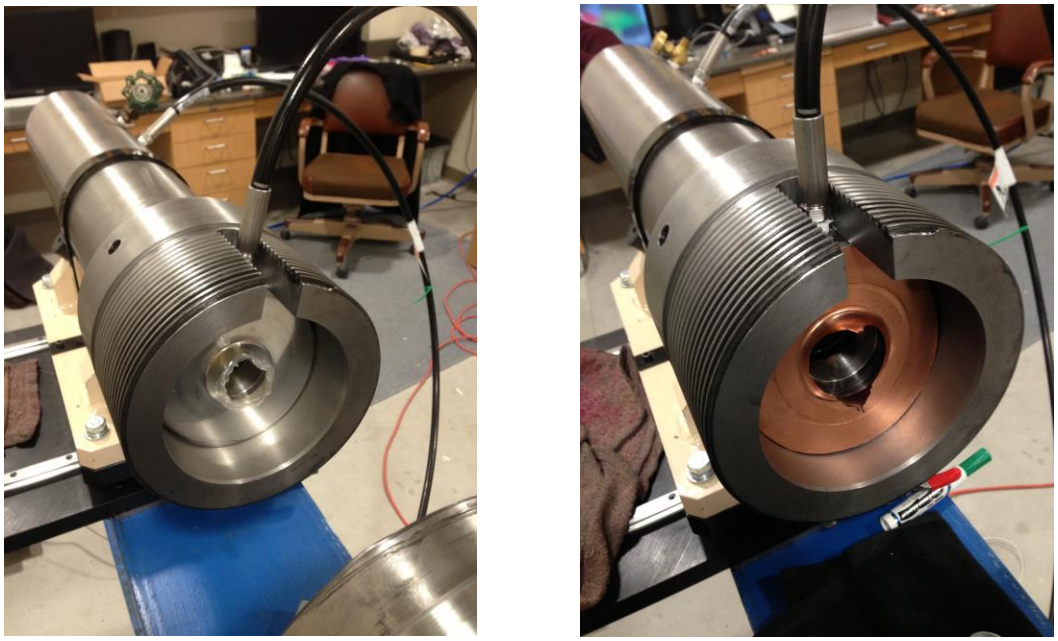

Figure 4.4 Examples of proper (left) and improper disk failure (right).

Before each shot, it is of utmost importance to choose burst that will fail in a controllable manner. In order to aid discussion, the disk between the small chamber and gun barrel shall be referred to as the “low pressure disk” and the disk between the small chamber and the large chamber as the “high pressure disk” (see Figure 2.7).

To create a method for choosing burst disks, one must make and follow rules. As mentioned above burst disk come with a pre-labled range of burst pressure; therefore, this section will assume that the nominal value or range of burst pressure values are known a-priori. With this in mind, the most important rule is that the gun, if it fires, should always fire in the correct direction and not backfire into the breach. To ensure this, the low pressure disk must always be either of the same failure pressure, or lower than the high pressure disk, else the gun would only be able to function properly as a typical single disk system, or at worst backfire.

From here, one can begin with the investigation of a burst disk system utilizing a pair of 0.125 inch thick (nominal) scored aluminum burst disks, with nominal burst pressure of 1538 psi (this is an average of the minimum and maximum burst pressures provided by Physics Applications Inc.). This system, with chosen burst disk, has two degrees of freedom: the small and large chamber set pressure. In order to fire the gun, pressures within the large chamber must exceed the failure pressure of the high-pressure disk, while at the same time, the low-pressure disk must never exceed the burst pressure of the high pressure disk. Remember that burst disks fail by an excess in differential pressure. By pressuring the small chamber to a set value (up to the low-pressure burst

disk burst pressure), one can also raise the pressure within the large chamber to the same value plus the burst pressure of the high-pressure disk (Note that Pabs ≈ 0 downstream of the breach). In order to assist with the understanding of this, a diagram displaying the range of stable operational pressure set points is included in Figure 4.5 below.

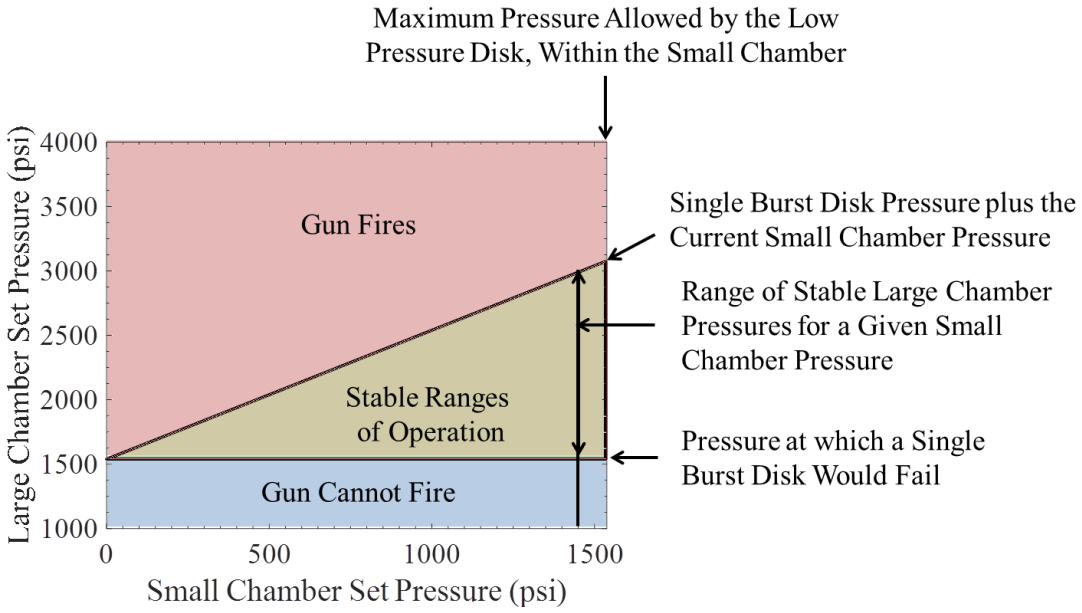

Figure 4.5 Range of theoretical set pressures for a 0.125 Alum-Alum burst disk configuration using nominal burst pressure.

Unfortunately, burst disks do not fire at a set pressure, but rather a range of pressures. Disks provided by Physics Applications Inc. are provided with both a high and low pressure burst value. Additionally, effects such as creep, mentioned in section 2.2.4, mean that factors of safety around all three bounds are needed, further limiting the stable ranges of operation.

To prevent the first disk from firing, the pressure difference across the gun barrel and small chamber must be less than the minimum burst pressure of the disk. To ensure this, the chamber should be set at a pressure 85% of the minimum burst disk pressure, the first of three boundary conditions. This safety factor underestimates the burst disk strength at low pressures and allows for pressure creep as the high pressure burst disk, under higher pressures, deforms into the small chamber cavity. This factor may need to be lowered especially for low-pressure burst disks, as creep has a much larger effect relative to the burst pressure of the disk. To calculate the small chamber set pressure, the following equation is proposed:

$$\mathrm{SmChamber}_{Presmax} = 0.85\ (Disk_{LPmin}) \tag{4.2}$$

where $\mathrm{SmChamber}_{Presmax}$ is the set pressure of the small chamber and $Disk_{LPmin}$ is the minimum know burst pressure of the low pressure disk.

To this point, it is has been expected that the minimum and maximum burst pressures are well characterized; this cannot be assumed. Therefore, ranges restricting maximum and minimum large chamber pressure are chosen to ensure the gun fires when desired and does not fire under other circumstances. The large chamber is therefore restricted to pressures between 80% and 20%, bounding the experimental use between the extreme combinations of burst disk failure and non-failure. It should be noted that the 85%, 80%, and 20% values are arbitrarily chosen to afford extra allowance to the manufacturer or laboratory quoted burst pressure range. These factors may need to be

adjusted as preloading loading disks to test the seal of the breach, temperature of the breach or conditions in which the disks are kept will affect burst pressure. Based on these considerations equations with initial safety factors are presented below:

$$\text{LgChamber}_{minPres} = HPDisk_{maxburst} + (0.2\ (2\ HPDisk_{minburst} - HPDisk_{maxburst})) \quad (4.3)$$

$$\text{LgChamber}_{maxPres} = \text{SmChamber}_{Presmax} - HPDisk_{maxburst} + \text{LgChamber}_{minPres} + (0.8\ (2\ HPDisk_{minburst} - \text{LgChamber}_{minPres})) \quad (4.4)$$

where $\text{LgChamber}_{minPres}$ and $\text{LgChamber}_{maxPres}$ are the acceptable range of large chamber pressure, $HPDisk_{minburst}$ and $HPDisk_{maxburst}$ are the quoted range of pressures at which the high pressure disk will burst and $\text{SmChamber}_{Presmax}$ is the maximum pressure within the small chamber.

The three equations, (4.2) (4.3) (4.4), bound our available pressure settings given a set of burst disks. To better showcase the utility of these equations, a brief example is given. For this example, a set of 0.125 inch thick scored aluminum disks with a burst range of 1297-1779 psi, is considered. From this information, one computes the sample space shown below in Figure 4.6.

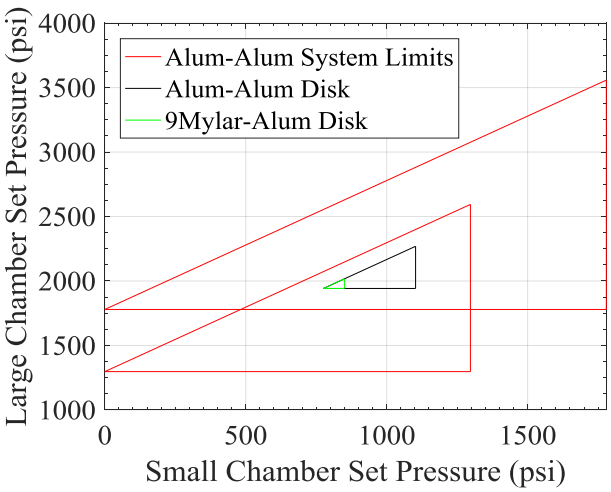

Figure 4.6 Plot for the effective working range of 0.125 inch Alum – 0.125 inch Alum burst disk configuration including a 9 Ply Mylar – 0.125 inch Alum burst disk configuration.

In the figure, the outer triangle space shows the stated limits of the burst disk as a function of small chamber pressure. Adding in safety afforded by the 20% and 80% offsets, one arrives at the final range of high and low chamber pressure settings for the aluminum disks. If running at a lower breach pressure, one could also use a system consisting of a low pressure disk made of 9 bonded mylar disks and a high pressure disk of 0.125 inch Aluminum to save in shot costs. Consideration of cost is unnecessary as the sample space for the dual aluminum setup includes the same sample space. A list of available burst disks with usable sample spaces is shown below in Table 4.1. Burst pressure data for mylar was taken from in-house testing, while metal disk burst pressures were taken from Physics Applications Inc. values quoted on disks. The author recommends that for least likelihood of failure the minimum large chamber pressure is used. Caution should be taken with mylar burst disks, especially at lower pressures as burst values have been recovered from single tests with an unknown range of burst pressure!

Table 4.1 Compiled List of Available Paired Disk Set Pressures

Setup	Minimum Low Burst Pressure (psi)	Minimum High Burst Pressure (psi)	Maximum High Burst Pressure (psi)	Small Chamber Maximum Set Pressure (psig)	Minimum Percent Above Burst	Maximum Percent Above Burst	Large Chamber Minimum Pressure (psig)	Large Chamber Maximum Pressure (psig)	Minimum Over Pressure	Maximum Over Pressure
1 Mylar	100	100	100	85	20%	80%	120	169	120.0%	169.0%
2 Mylar	300	300	300	255	20%	80%	360	507	120.0%	169.0%
3 Mylar	450	450	450	382.5	20%	80%	540	760.5	120.0%	169.0%
4 Mylar	525	525	525	446.25	20%	80%	630	887.25	120.0%	169.0%
5 Mylar	600	600	600	510	20%	80%	720	1014	120.0%	169.0%
7 Mylar	800	800	800	680	20%	80%	960	1352	120.0%	169.0%
9 Mylar	1000	1000	1000	850	20%	80%	1200	1690	120.0%	169.0%
9 Mylar and 0.125 inch Thick Alum	1000	1297	1779	850	20%	80%	1942	2016.6	109.2%	155.5%
0.125 inch Thick Alum	1297	1297	1779	1102.45	20%	80%	1942	2269.05	109.2%	174.9%
0.05 inch Brass Low	2195	2195	3010	1865.75	20%	80%	3286	3839.95	109.2%	174.9%
0.05 inch Brass High	3055	3055	4189	2596.75	20%	80%	4573.2	5344.39	109.2%	174.9%
0.063 inch Brass Low	3671	3671	5032	3120.35	20%	80%	5494	6421.75	109.2%	174.9%
0.063 inch Brass High	5441	5441	7460	4624.85	20%	80%	8144.4	9518.33	109.2%	174.9%
.09 inch Brass	7565	7565	10371	6430.25	20%	80%	11322.8	13233.81	109.2%	174.9%

It was mentioned above that the burst disks within the lab were either purchased with a pre-labeled range of burst pressures or created and tested in lab. Investigating further, it was found that most burst disks were created then tested or modeled within a

Finite Elements package such as ANSYS before manufacture. Analytically, the design space for burst disks, both with and without grooves, was limited to one notable mention within Henri Bernier's work [167]:

$$p = \frac{A}{1+3.75(\varepsilon/e)^3} e^{3/2} (\varepsilon/e)^{-\frac{1}{2}} \tag{4.5}$$

where ε is groove thickness, e is the burst disk thickness, and p is pressure. However, the formula within this work is incomplete, as the variable *A* is left as an open variable describing "diaphragm dimensions, the depth of the groove and material properties." Further investigation into the origins of this formula lead to a paper by JJ Rast [169].

In his paper, Rast includes a formulas for hemispherical disks:

$$P_{burst} = 2\frac{\sigma_{ult}\, d}{a} \tag{4.6}$$

Where the burst pressure P_{burst}, is a function of $\sigma_{ult}$the ultimate strength of the diaphragm, d is the material left at the bottom of the groove, and a is the radius of the unsupported disk area. Though equations expressing burst pressures in flat round disks could not be found, though data for scored and unscored flat disks is included in Figure 4.7 below.

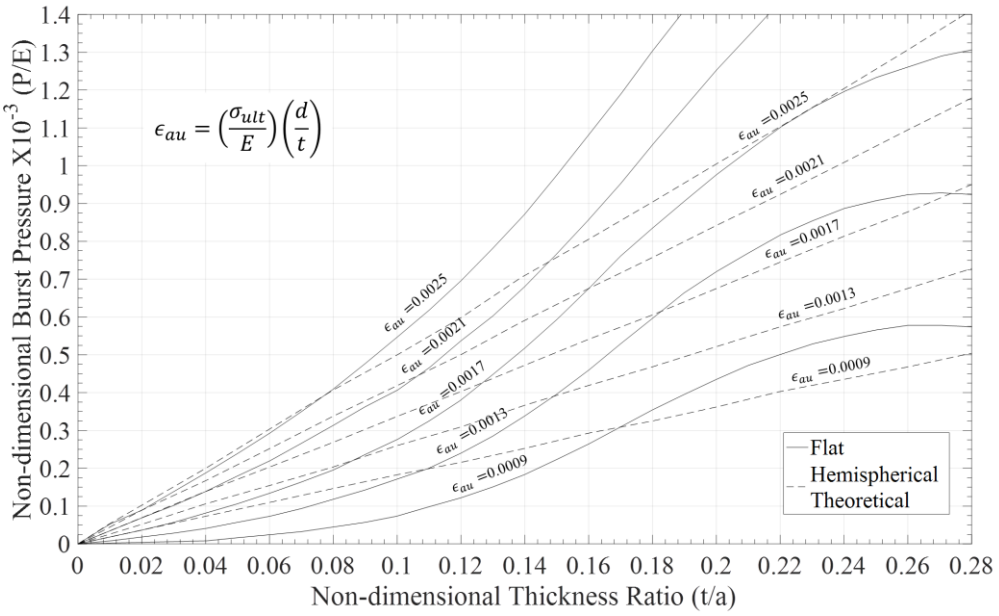

a) Burst Pressure vs. Thickness Ratio for Flat and Hemispherical disks without scores

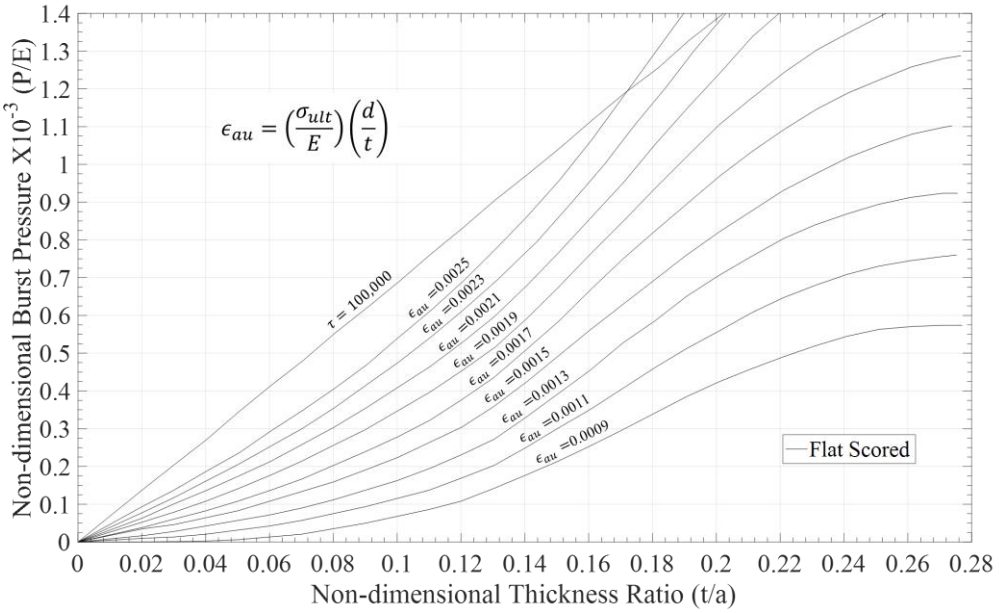

b) Burst pressure vs. thickness ratio for flat scored disks

Figure 4.7 Plot of burst pressure vs thickness ratio for various stainless steel 304 and 305 round burst disks. This where P is the burst pressure, E is the modulus of elasticity, t is the disk thickness, r is the diaphragm bend radius, a is the radius of the unsupported disk area, d is the material left at the bottom of the groove, $\boldsymbol{\sigma_{ult}}$ is the ultimate strength of the diaphragm, $\boldsymbol{\sigma_{au}}$ is the apparent strength of the diaphragm, $\boldsymbol{\epsilon_{ult}}$ is the ultimate strain, and $\boldsymbol{\epsilon_{au}}$ is the apparent ultimate strain.

While the above curves does account for some disk relevant dimensions and Elastic Modulus, it does not apply to disks made of materials available to the lab. Aside from these sources, references for burst disk pressure, both with and without cut grooves, were not found. As mentioned before, forums recommend simulation packages, such as ANSYS, or characterizing burst pressure through experiment. Therefore, a quick formula for mylar has been proposed and derived below, assuming thin sheet disks with fixed boundaries around their circumference.

First, the failure of the mylar disk will be assumed to be similar to a spherical tank, with internal pressure shown in Figure 4.8. This was a valid assumption as experimental results for mylar show that material deformation before failure was approximately hemispherical in shape. This was not the case for metal disks which were found to have much lesser deformation before burst.

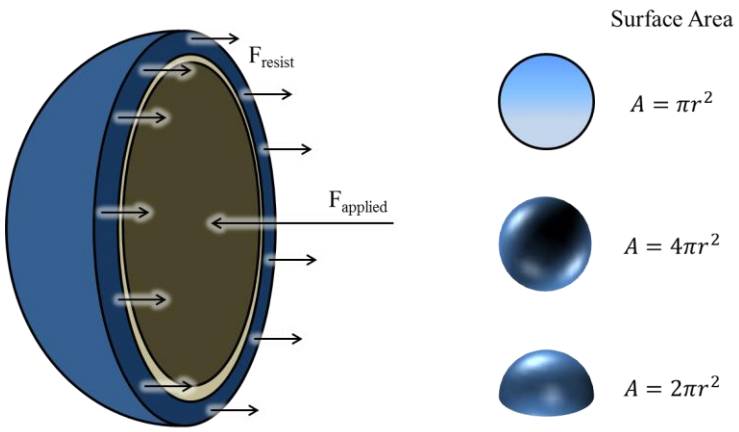

Figure 4.8 Burst disk failure approximation.

Beginning with a force balance, it is assumed that the pressure applied over the projected area of the internal sphere wall will balance with the materials strength exerted along the diameter of the sphere.

$$P_{burst}(\pi {r_i}^2) = \sigma_{ult}(\pi {r_0}^2 - \pi {r_i}^2) \tag{4.7}$$

It is understood that the outer radius is related to the inner radius by the thickness of the material.

$$r_o = r_i + t \tag{4.8}$$

Substituting in this relation and simplifying,

$$P_{burst}(\pi {r_i}^2) = \sigma_{ult}(\pi (r_i + t)^2 - \pi {r_i}^2) \tag{4.9}$$

$$P_{burst}(\pi {r_i}^2) = \sigma_{ult}(\pi {r_i}^2 + 2\pi r_i t + \pi t^2 - \pi {r_i}^2) \tag{4.10}$$

$$P_{burst} = \frac{\sigma_{ult}(2\pi r_i t + \pi t^2)}{\pi {r_i}^2} \tag{4.11}$$

one arrives at the base equation:

$$P_{burst} = \frac{\sigma_{ult}(2r_i t + t^2)}{{r_i}^2} \tag{4.12}$$

However, since the burst disk is originally flat, the hypothetical spherical thickness is half that of the original thickness assuming homogenous deformation of the original material (please see Figure 4.8). This means our final equation for the failure of thin disks is:

$$P_{burst} = \frac{\sigma_{ult}\left(2r_i\left(\frac{t_o}{2}\right) + \left(\frac{t_o}{2}\right)^2\right)}{{r_i}^2} \tag{4.13}$$

Where P_{burst} is the burst pressure, σ_{ult} is the material ultimate strength, t_o is the original disk thickness, and r_i is the outer radius minus the thickness. The resultant equation for the range of Mylar's strength is plotted below (shown as an upper and lower blue line in Figure 4.9) against experimental data, with each data point representing a single test for a thickness of disk(s) loaded at a rate of 0.4867 (psi/s). Measurement error, included in plot below, stem from the pressure gauges used to measure the pressure within the tank at burst, which measured in 200 psi increments.

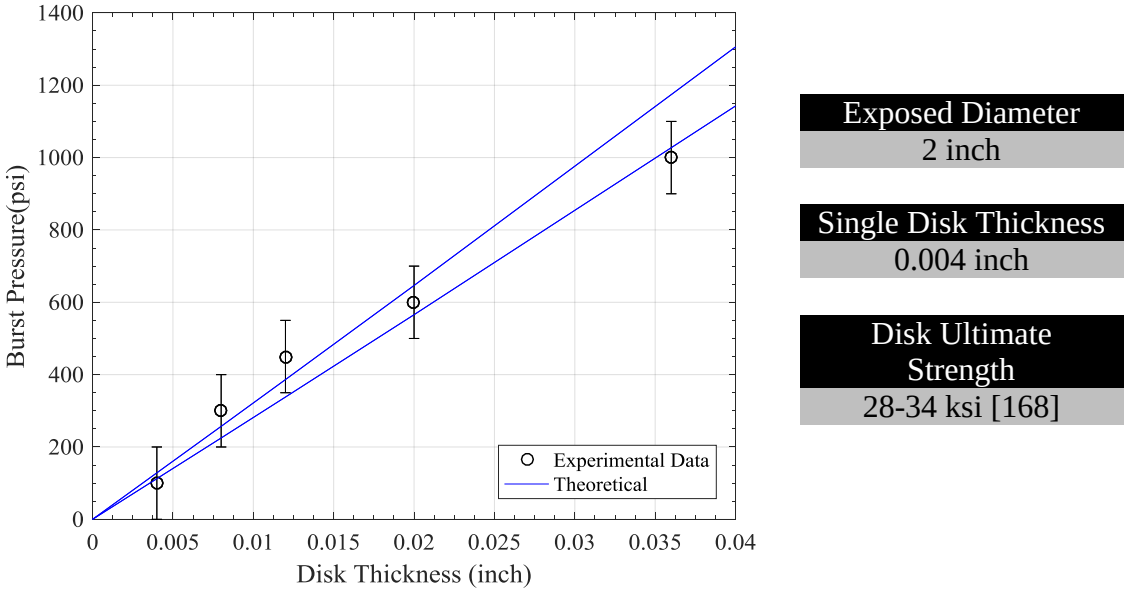

Figure 4.9 Pressure vs. thickness for mylar with material characteristics.

While this curve appears to fit the data very well and shows promise, it is important to note again that this assumes the disks have a universal internal stress state and deform to a half sphere; thus, it is valid only for disks with high ratios of exposed diameter to disk thickness. Comparing Figure 4.9 with Figure 4.7 one will note that only the theoretical calculation given by Rast [170] for unscored hemispherical disks shares a similar linear nature. This makes sense given the formulation of (4.13) which assumed disks would deform to a hemispherical shape before failure. Equations (4.13) and (4.6) largely differ by a factor of 2 with the author's derivation dividing material strength time thickness by the exposed disk radius whereas the formulation within Rast's paper uses the exposed disk diameter. It should be noted that both formulations fit the general trend, if not the true trend of the data they wish to model respectively, this suggests that there may be additional research to be done in the field of burst disk mechanics.

Upon closer review of literature, a formula, of similar nature to the author's has been derived by Peter Barlow [170] relating a cylindrical pipes (rather than a disk's) materials ultimate strength σ_t, thickness t, and outer diameter d_o to burst pressure $P_{burst(cyl)}$:

$$P_{burst(cyl)} = \frac{2\,\sigma_{ult}\,t}{d_o} \tag{4.14}$$

In fact, as long as the radius of the disk is much greater (x50) than the thickness the t^2 term in Equation (4.13) is negligible and reduces to Equation (4.14).

4.3 Taylor Testing

An unintended but beneficial consequence of testing utilizing a polycarbonate sabot during a normal impact between a steel flyer and large plate was a sabot with a shorted length and an enlarged cross-section. This redistribution of sabot mass was a result of both plastic and inelastic deformation occurring upon impact. The resultant sabot shape was reminiscent of similar tests carried out by G.I. Taylor [171], which related dynamic yield stress of materials to the velocity of impact for cylinders where the ratio of end length to initial lengths are greater than 0.5. Reviewing his paper we find the impact velocity V is expressed in the following formula:

$$V = \left(\left(\frac{L_i - X}{2(L_i - L_f)} \frac{1}{\ln(L_i/X)} \right) \frac{\rho_p}{\sigma_y} \right)^{-\frac{1}{2}} \quad (4.15)$$

where σ_y is yield stress, ρ_p is density, V is the impact velocity, L_i is the initial length, L_F is the final length, and X is the length of the undeformed section.

This formula was then applied to the sabot shown in Figure 4.10 below.

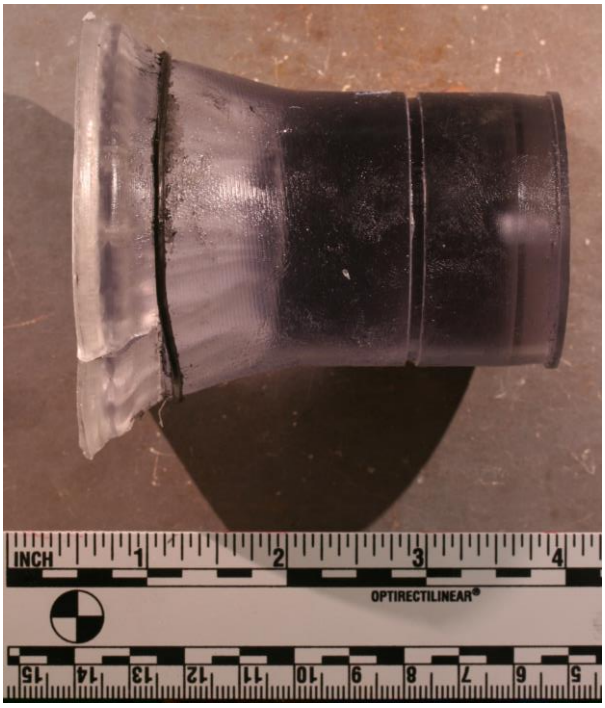

Figure 4.10 Post shot sabot profile, for a projectile shot at 600 psig.

In the derivation of Taylor's formula, cylinders are of uniform diameter over the length. The Marquette cylindrical sabot, however, has a tiered hollow pocket (see Figure 2.10), which modify the initial assumptions of Taylor's equation.

In order to address this, the dimensions of the sabot have been taken removing the lengths added by the lips. The initial length is easily found by referencing the dimensions of the drafted sabot in Figure 2.10 and the final length can also be measured by discounting the length added by the lighter shades of polycarbonate captured in Figure 4.10.

Utilizing this above formula (4.15), one finds the sabot's impact velocity within Table 4.2.

Table 4.2 Reverse Taylor Test for Impact Velocity

Variable	Magnitude	Variable	Magnitude
σ_y	9000 psi	L_i	3.875 inch
ρ_p	0.044 lb./inch^3	L_f	3.379 inch
V	268 ft./s	X	2 inch

The calculated velocity of 268 ft./s underestimates data taken from the piezoelectric pins (280 ft./s) by approximately 5%, with error stemming from a non-uniform sabot cross-section and interference from features such as the aforementioned sabot lips and original mounted flyer (not shown). While the Taylor equation gave a good estimate for velocity in this test, at higher pressures, it is thought that the Taylor test will lose accuracy. This due to the clear plastic deformation, and fracture noticed, in other sabots, like the one shown in Figure 4.11 below:

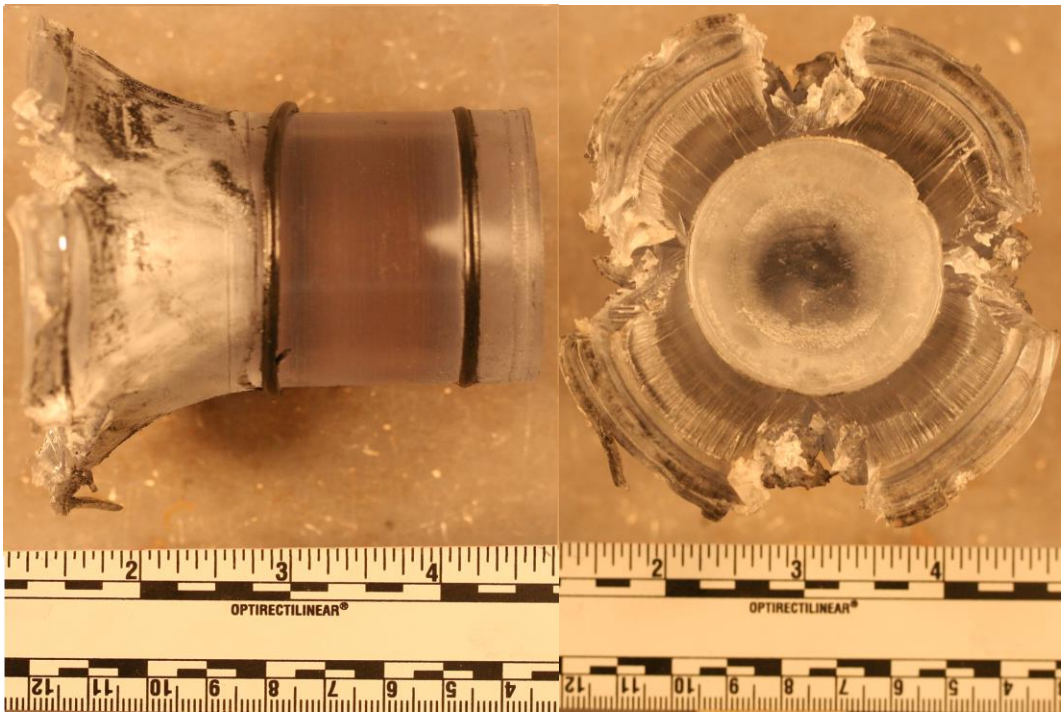

Figure 4.11 Post shot sabot profile; sabot shot at 960 psig.

4.4 Catch Tank Pull Down

In the muzzle velocity calculations, it was assumed that there was no forward pressure on the sabot. To achieve this, the entire section forward of the sabot, comprising a ~2.5m^3 volume, was pulled down to pressures below ~200 mTorr for flyer plate studies. For future pressure shear studies, a recommended pressure of ~50 mTorr was suggested by Bill Reinhardt of the Aeroballistics Range Association. This was later noted to be the pull down pressure utilized by the Georgia Tech Shock Physics team, upon visit to their facility.

These low pressures are maintained not only to prevent forward pressure on the sabot during flight, but also to prevent pillows of air from accumulating in front of the

flyer on its trajectory down the barrel, which can interfere with both experiment orientation as well as data collection.

To reach these pressures, an Agilent DS602 pump was utilized in conjunction with Marquette University's shop vacuum system. While the building vacuum system was able to both pull a vacuum quickly and later provide a path for post shot particulate removal, the shop vacuum bottomed out at ~21 in Hg (533400 mTorr), well above both target pressures. The Agilent pump, known in the industries as a "scroll" roughing pump, works well between atmospheric pressure in the region of viscous flow.

In order to determine the region in which the pump operated, the Knudsen number, a non-dimensional number charactering the mean free path of a particle and a relevant length, D, often the diameter through which a flow is piped [173], was used.

$$\mathrm{Kn} = \frac{\lambda}{D} \tag{4.16}$$

For spherical particles, the mean free path λ can be expressed:

$$\lambda = \frac{k\,T}{\sqrt{2}\,\pi\,d^3\,P} \tag{4.17}$$

where P is pressure, T is temperature, d is the molecular diameter, and k is the Boltzmann's constant. Typical temperature within the lab is 295 K, the piping diameter is 3.5 cm and the gas filling both the vacuum and target tanks is air (primarily nitrogen).

Looking at the CRC handbook [174] one finds the Boltzmann's constant, 1.38064852×10^{-23} $m^2kgs^{-2}K^{-1}$ and the mean molecular diameter of a diatomic nitrogen molecule, 364 picometers.

Before using these equations, a brief explanation of the three flow regimes, shown in Figure 4.12, may be helpful. As a vacuum pump begins to evacuate a chamber, flow initially is of a viscous nature, molecules have a relatively short mean free path, and collisions between molecules are frequent. This means that initially particles will often "flow" in the same direction as voids created by the moving of particles, Group A, in a single direction will allow other particles behind the original moving front, Group B, to fill the void space. A third group of particles, Group C, will also push Group B forward as they collide between Group C and the group behind them, Group D, et cetera. In short, there is a high potential pressure between high and low pressure areas. As flow begins to transition to Knudsen flow, more and more space is free of particles and groups of particles become increasing sparse. Particle groups quickly intermingle, increasingly less likely to travel in the desired direction, as areas and the difference between the high and low pressure sources becomes much lower, decreasing flow rate. Finally, as flow transitions to the molecular range, particles have higher likelihood to collide with the walls of the container holding them rather than colliding with another particle. This means that decreasing pressure becomes more a question of a particle bouncing out of the system and unable to return than a flow that can be influenced.

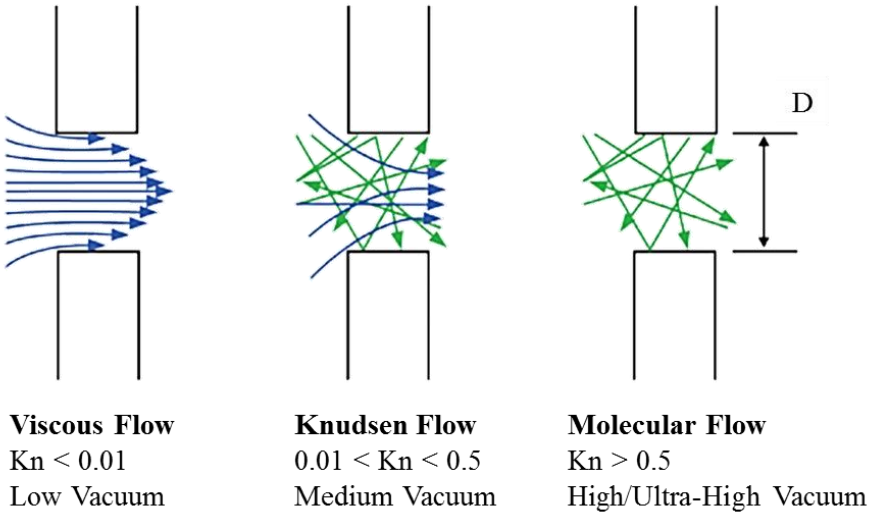

Figure 4.12 Three vacuum flow regimes [175].

One can utilize the regions of known flow behavior in Figure 4.12, along with equations (4.16) and (4.17), to find the pressures at which our system will transition between flows (show below in Table 4.3).

Table 4.3 Flow Regimes [176]

Flow Region	Viscous Flow	Knudsen Flow	Molecular Flow
Defined Domain	$\lambda < \frac{L}{100}$	$\frac{L}{100} < \lambda < \frac{L}{2}$	$\lambda > \frac{L}{2}$
Condition Specific Regions	0.6921 < PL	0.6921 > PL > 0.0138	PL < 0.0138
Experimental Specific Pressures (Pa)	19.7743 < P	19.7743 > P > 0.3943	P < 0.3943
Experimental Specific Pressures (mTorr)	148.3 < P	148.3 > P > 2.9575	P < 2.9575

While the vacuum did not cross into the region of defined molecular flow, it did pass through the transition region. The system's proximity to the molecular flow and the systems depressurization curve was compared to the characteristics of both viscous and

molecular flow. According to Y. Senda [177], one can calculate the pump-down time by examination of flow at both conditions. As mentioned within his paper, the flow rate of a gas evacuated from a system is normally calculated by a flow rate equation shown below:

$$Q = C\ (P_1 - P_0) \tag{4.18}$$

where Q is the flow rate, C is conductance, P_0 is the low pressure side and P_1 is the high pressure side. The conductance for the system varies based on the flow condition and formulas are included below in Table 4.4.

Table 4.4 Conductance Values for Long Pipes [178]

	Viscous Flow	Molecular Flow
Conductance	$\frac{1349\ D^4\ P}{L}$	$\frac{121\ D^3}{L}$

D in the above table is smallest hose diameter in the vacuum pumping line, P is the current pressure and L is the length of the hose line

To solve the problem of a transition region Y. Senda employs the use of a transferring pressure which marks a transition between the regions of viscous and molecular flow [177].

$$\pi = \frac{S_o}{C_c} \tag{4.19}$$

where π is the transference pressure, S_o is the pumping speed and C_c is the conductance coefficient for viscous flow (found in Table 4.4). From this, one can switch between two equations:

one for viscous flow:

$$P \approx P_o \, exp(-\frac{t \, S_o}{V}) \tag{4.20}$$

and one for molecular flow:

$$P \approx \frac{2 \, \pi \, V}{t \, S_o} \tag{4.21}$$

where P is the final pressure, P_o is the initial system pressure, t is the elapsed time, S_o is the pump speed, and V is the system volume.

In order to test our system, which did not have a constant pumping speed, the pumping curve from the Agilent DS602 vacuum pump was fit with a piecewise 3rd order polynomial curve as shown in Figure 4.13 below.

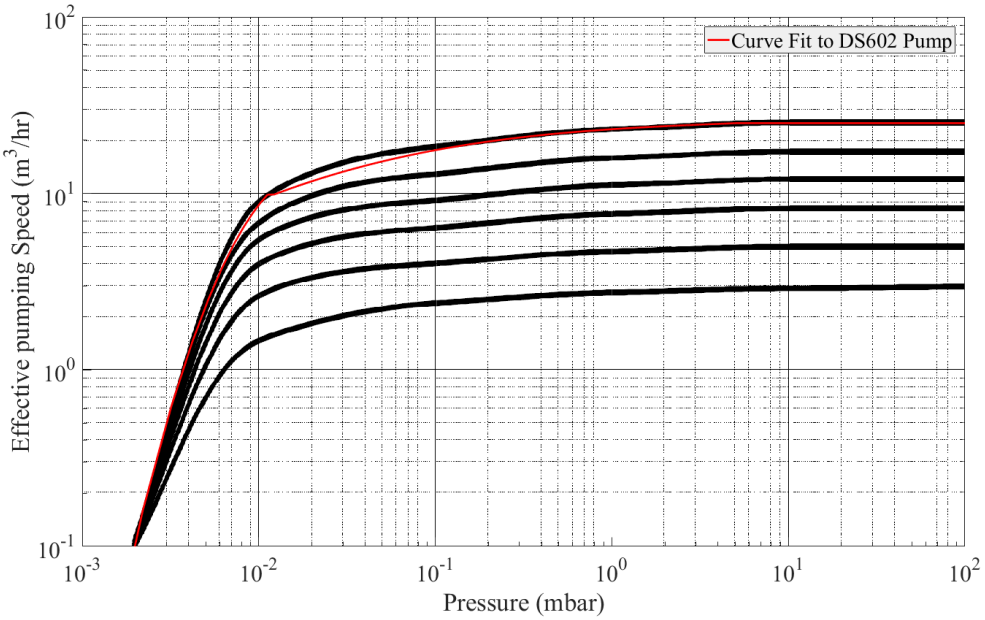

Figure 4.13 Manufacturer pump curve with fitting [179].

Based on literature from the manufacturer the black curved lines were generated by placing a vacuum gauge on the top of the vacuum pump inlet and turning the pump on. The lab's Agilent DS602 pump curve is the upper most black line with other models curves below.

This curve was employed, along with initial conditions, to solve for the estimated time required to evacuate the chamber show in Figure 4.14 below. As can be seen, the high pressure data taken from the vacuum gauge falls along the viscous flow curve. Between the high pressure and low pressure data, there is a region where measurements cannot be taken as the gauges do not overlap in measuring range. Around the start of the low pressure data, taken with the digital KJL vacuum gauge, flow begins to transition between molecular and viscous flow (Knudsen Flow). Before gas flow is reached characteristics of a fully molecular flow, leaks and outgassing within the system begin to take effect and reduce the speed at which the vacuum is pulled. This is until the system

reaches a state of equilibrium between the gases entering and the gases pulled from the system.

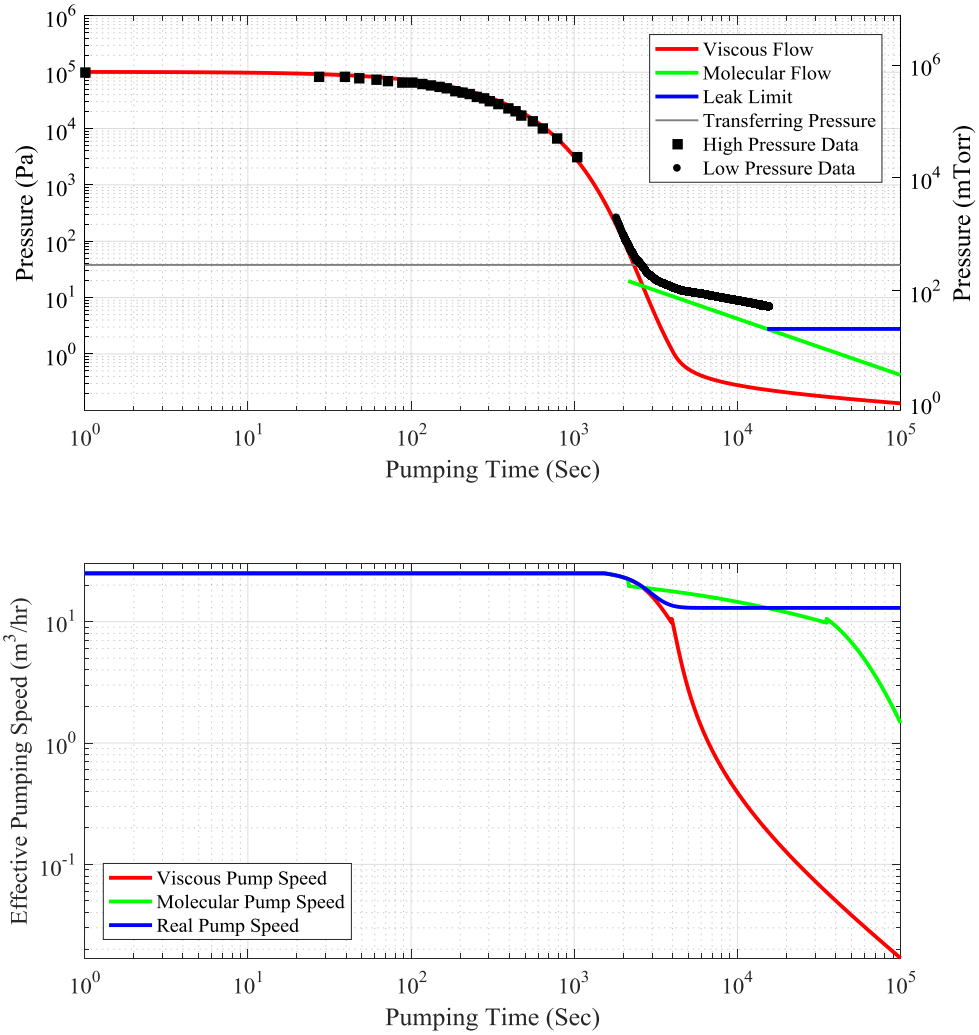

Figure 4.14 Pressure and pumping speed within the system as a function of time.

As can be seen from Figure 4.14, the numerical fit matches well with experimental data. Missing data between high and low pressure regions results from vacuum gauges with operational regions that do not overlap (see section 2.2.7). System leaks noted here were determined by first reaching a low pressure and monitoring the increase of pressure

over a period of 10 minutes. The lowest leak rate identified was around 1 millitorr per 30 seconds, though a more typical rate is around 0.5 millitorr per second, which is the rate utilized in the figure above. This leak rate stems from both traditional leaks, as well as the outgassing of various materials such as the rubber on the impact plate within the catch tank. This outgassing phenomenon was especially noticeable when, in an effort to find a method of slowing the sabot, a plethora of old lab cotton coats were added to the breach. While the coats did a good job of slowing the projectile and lessening the impact against the impact plate within the catch tank it also dramatically increased the amount of time to pull down the system to well over 3 hours.

4.5 Muzzle Velocity

This section presents the derivation of the most common methods of estimating maximum muzzle velocity and the travel time of the sabot down the barrel.

ISOBARIC

While the experimental behavior of the gun remains in progress, a need to anticipate projectile velocity accurately was required. In order to anticipate behavior, various models were tested and compared to ensure the best possible fit. Before researching additional methods of determining projectile velocity, a series of ideal gas relations were used, which assume that gas properties remain uniform both behind the sabot and throughout the breach chamber.

Isobaric, the simplest of models, assumed that the pressure behind the projectile was constant meaning that since the area aft of the projectile was also constant an acceleration and velocity could be easily determined.

The force F, moving the projectile, is simply the pressure P acting on the sabot's aft area A:

$$F_{surface} = P_{projectile\ surface}\ A \tag{4.22}$$

The force balance is simply the mass m, and acceleration a of the particle influenced by the frictional force f, and pressure force.

$$F_{surface} - f = ma \tag{4.23}$$

As the pressure behind the projectile P is constant, a constant force is applied meaning that the acceleration is also constant.

$$P_{projectile\ surface} = \text{Constant} = P_i \tag{4.24}$$

$$\frac{P_i\ A - f}{m} = a$$

(4.25)

One can integrate backwards, to solve for both velocity v, and position x, with respect to time t:

$$v(t) = at + v_o \qquad \text{where } v_o = 0 \text{ and } v(0) = 0 \tag{4.26}$$

$$x(t) = \frac{a}{2}t^2 + v_0 t + x_o \text{ where } x_o = 0 \text{ and } x(0) = 0 \tag{4.27}$$

Since the known position at the final time is the barrel length L, one can find the final time t_f through the use of equations (4.25) and (4.27):

$$x(t_f) = L = \frac{P_i\, A - f}{2\, m} t_f{}^2 + 0 + 0 \tag{4.28}$$

$$\sqrt{\frac{2\, m\, L}{P_i\, A - f}} = t_f \tag{4.29}$$

As the equation for final velocity is also known one can substitute the final time from equation (4.29) to find the isobaric velocity in equation (4.26):

$$v = \frac{P_i\, A - f}{m}\, t_f \tag{4.30}$$

$$v = \frac{P_i\, A - f}{m} \sqrt{\frac{2\, m\, L}{P_i\, A - f}} = \sqrt{\frac{2\, m\, L\, (P_i\, A - f)^2}{(P_i\, A - f)\, m^2}} \tag{4.31}$$

$$v = \sqrt{\frac{2\, L\, (P_i\, A - f)}{m}} \tag{4.32}$$

This equation, however, was anticipated to be inaccurate, as the initial amount of gas stored within the starting volume would have to expand to fill the increasing volume behind the projectile, as it traveled along the barrel. An isothermal equation allowed for the pressure behind the projectile to vary, as the chamber increased in volume.

ISOTHERMAL

Beginning with the work-energy method, the kinetic energy of the sabot composed of the sabot's the mass m, and velocity v, is balanced with the frictional force f, exerted over the barrels length L, and pressure P, acting on the sabot for from the initial V_i to final V_f volume:

$$KE = \int_{V_i}^{V_f} P\, dV - f\, L = {}^{1}/_{2}\ m\, v^2 \qquad (4.33)$$

The frictional force f, used here can either be assumed to be a constant characterized by the coefficient of friction between the lubricated rubber orings and steel barrel and the normal force of contact between the orings and the barrel or a function of velocity. Typical hand mounting of the sabot into the breach is easy and requires little force. The friction opposing motion is negligible with respect to the high pressures driving the sabot during an experiment so while equations are formulated with friction this is omitted in calculations.

The current pressure can be found by the ideal gas law through the use of volume V, number of moles n, universal gas constant R, and temperature T:

$$P = \frac{n\,R\,T}{V} \tag{4.34}$$

A substitution of equation (4.33) into equation (4.34) and factoring out the constants allows for the integration of work done on the projectile by the compressed gas:

$$KE = \int_{V_i}^{V_f} \frac{n\,R\,T}{V}\,dV - fL \tag{4.35}$$

$$KE = nRT \int_{V_i}^{V_f} \frac{dV}{V} - fL \tag{4.36}$$

$$KE = nRT \ln\left(\frac{V_f}{V_i}\right) - fL \tag{4.37}$$

Since the initial pressure P_i and initial velocity V_i are equal to the constants removed:

$$P_i V_i = nRT \tag{4.38}$$

the substitution of equation (4.38) into equation (4.37) yields,

$$^1/_2\, mv^2 = P_i V_i \ln\left(\frac{V_f}{V_i}\right) - fL \tag{4.39}$$

The final volume is equivalent to the initial volume, plus the surface area of the bore A, multiplied by the length of the barrel L:

$$V_f = V_i + AL \tag{4.40}$$

So, substituting equation (4.40) into (4.39) and solving for v, one finds the isothermal sabot velocity equation:

$$v = \sqrt{\frac{2P_i V_i \ln\left(\frac{V_i + AL}{V_i}\right)}{m} - \frac{2fL}{m}} \tag{4.41}$$

ADIABATIC

The isothermal formulation did not account for the molecules of gas to change temperature. According to the Joule-Thompson effect as the gas chamber emptied, much in the same way a spray can or air can empties, the gas would decrease in temperature, removing some energy in the form of pressure. Therefore, a reversible adiabatic condition, implying isentropic gas expansion was assumed. As the volume expansion of

the gases are quite fast, the system will certainly generate entropy (leading to overestimates in sabot velocity), however the adiabatic assumption is certainly better than the isobaric or isothermal assumptions. Again, a work-energy method was used with the sabot's mass m and velocity v, balanced against the frictional force f exerted over the barrels length L and pressure P acting on the sabot from the initial V_i to final V_f volume:

$$\int_{v_i}^{v_f} PdV - fL = {}^{1}/_{2}\, mv^2 \tag{4.42}$$

This time, the polytrophic relationship (with an exponent of γ, for an adiabatic process) [180] relating pressure to volume V and the ratio of specific heats γ was used to separate pressure into its variable and constant components:

$$\ln(PV^{\gamma}) = \text{Constant} = PV^{\gamma} \tag{4.43}$$

$$P = \frac{C}{V^{\gamma}} \tag{4.44}$$

Substituting equation (4.42) into equation (4.44), one can remove the constant and integrate with respect to volume:

$$\int_{V_i}^{V_f} \frac{C}{V^\gamma} dV = C \int_{V_i}^{V_f} \frac{dV}{V^\gamma} = \frac{C(V_f^{1-\gamma} - V_i^{1-\gamma})}{1-\gamma} \quad (4.45)$$

A second substitution of (4.45) in to (4.42), allowed the equation to be simplified for velocity:

$$^1/_2 \, mv^2 = \frac{C(V_f^{1-\gamma} - V_i^{1-\gamma})}{1-\gamma} - fL \quad (4.46)$$

$$v = \sqrt{\frac{2C(V_f^{1-\gamma} - V_i^{1-\gamma})}{m(1-\gamma)} - \frac{2fL}{m}} \quad (4.47)$$

Replacing the constant C, in equation (4.47) with its definition in (4.44), the velocity assuming isothermal conditions is found:

$$v = \sqrt{\frac{2P_i V_i^\gamma (V_f^{1-\gamma} - V_i^{1-\gamma})}{m(1-\gamma)} - \frac{2fL}{m}} \quad (4.48)$$

STRANGE AND SWIFT

It was assumed, that amongst these equations, an adiabatic solution would have the best chance of modeling projectile behavior amongst the author's known gas modeling equations. Early research showed promise as a similar study by Strange and

Swift [181] also utilized an adiabatic equation to model gas behavior with an able equation of state. In the equation below, variables include initial pressure P_o, initial volume V_o, the specific heat ratio K, the area on the rear of the sabot A, mass m, moles of ideal gas n, gas co-volume per mole b, and the sabot velocity v:

$$v = \sqrt{\frac{2P_o(V_o - nb)\left(1 - \left(\frac{V_o - nb}{V_o - nb + Ax}\right)^{K-1}\right)}{m(K-1)}} \tag{4.49}$$

It should be noted that both the nitrogen and helium behave as ideal gases and so alternate equations of state such as Able and Van der Waals have only small effects on the velocity profiles of the gas gun. Both helium and nitrogen are modeled as ideal gases up to the pressures utilized in this experimental setup with compressibility factors close to 1, as shown in Figure 4.15. It should be kept in mind that high pressures are only seen at the very onset of breach depressurization and quickly fall back to ideal behavior. To properly include more complex equations of state would increase computational time as state would have to be found for each time step.

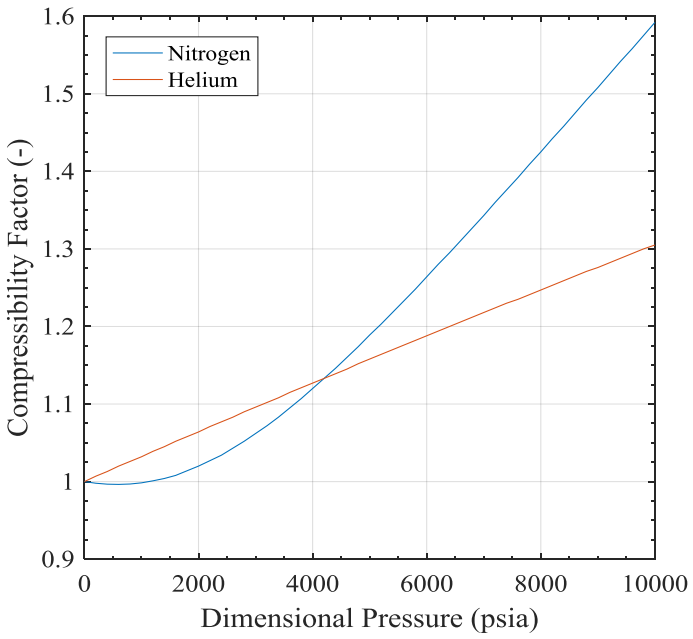

Figure 4.15: Compressibility factors of nitrogen and helium [182].

LAGRANGE

Until this point, it has been assumed that the gas within the system behaves in a uniform fashion. However, state properties are non-uniform as the gas gun fires. In doing so, the true energy of the gas has been neglected and, this requires correction with an extended deviation, which mirrors that of one done by Ballistics Theory and Design [150]. This equation approximates the gradient of information within the barrel and breach as Lagrangian, utilizing Lagrange's own method [183]. The equations within the text assume that the breach pressure is created utilizing an explosive charge (i.e. supersonic shock/pressure wave). In practice, this gives generally higher initial acceleration, as the expanding gas creates a favorable pressure gradient at the onset and through the initial flight of the projectile before decaying. This is opposed to a

compressed gas shot, which starts with a uniform pressure state and decays immediately to an unfavorable gradient with pressure waves interacting and creating an expanding series of problems.

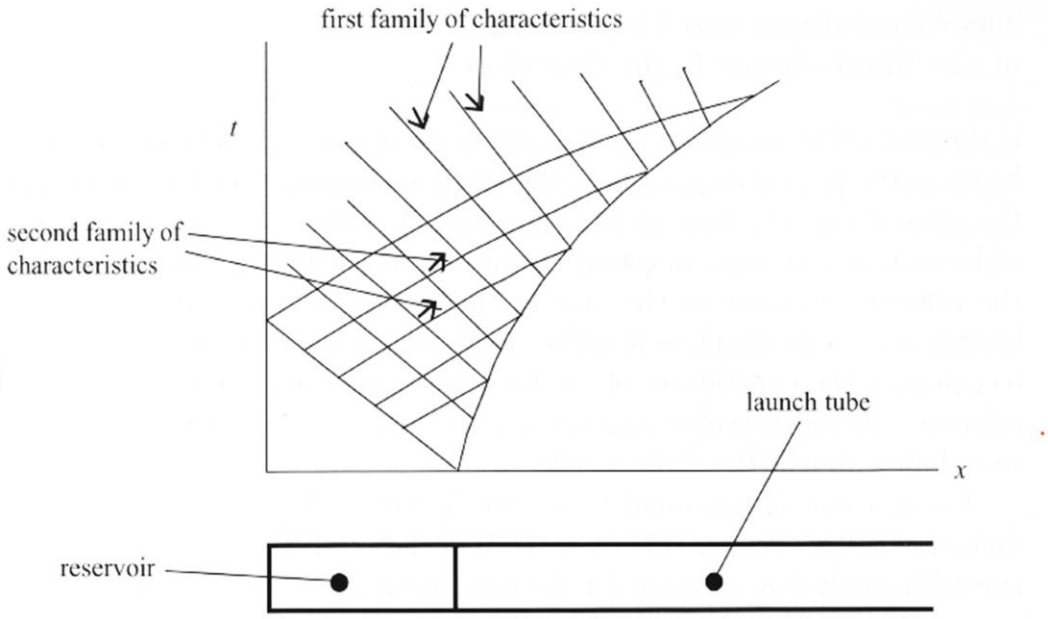

Figure 4.16 An x-t diagram of pressure waves emanating from the voids left by the sabot [150].

The derivation below has been completed following the aforementioned derivation assuming no explosives charge. Assuming a 1D behavior is an acceptable assumption, though the diameter differences between the breach and barrel make it an imperfect one. Later calculations will assume that the breach is of the same diameter as the barrel while the amount of gas as compared with the experimental setup remains constant. As in profiles derived before, it is assumed that the gas density profile is a function of time and is uniform in space. While this assumption might be valid for slow

moving and well insulated systems, projectile velocities (as presented later in this section) are expected to reach up to 1.1 km/s, while gas sound speeds such as that of nitrogen 354.4 m/s and helium 972 m/s can fall below this value. Methods derived here manage energy without referencing equation of state. However, in order to find the initial mass of the gas, an Ideal Gas Equation of state has been utilized with compressibility factor.

One begins with the continuity equation with variables ρ for density, t for time and V_{xg} for gas volume behind the sabot:

$$\frac{\partial p}{\partial t} + \frac{\partial}{\partial x_g}\left(\rho V_{xg}\right) = 0 \tag{4.50}$$

The above equation can be expanded using the product rule:

$$\frac{\partial p}{\partial t} + V_{xg}\frac{\partial p}{\partial x_g} + \rho\frac{\partial V_{xg}}{\partial x_g} = 0 \tag{4.51}$$

Since there is no density gradient that term is removed:

$$\frac{\partial p}{\partial t} + \rho\frac{\partial V_{xg}}{\partial x_g} = 0 \tag{4.52}$$

$$\frac{1}{\rho}\frac{\partial p}{\partial t} = -\frac{\partial V_{xg}}{\partial x_g} \tag{4.53}$$

The density is simply the mass of the gas G, over the volume of the container V:

$$\rho(t) = \frac{G}{V(t)} \tag{4.54}$$

The volume being a function of area A and barrel length L, can be inserted:

$$V(t) = AL(t) \tag{4.55}$$

$$AL(t)\rho(t) = G \tag{4.56}$$

Differentiating with respect to time:

$$\frac{1}{L}\frac{dL}{dt} = \frac{\partial V_{xg}}{\partial x_g} \tag{4.57}$$

Integrating with respect to x_g, while utilizing the knowledge that $x_g = 0$ when $V_{xg} = 0$, one finds a relation with velocity v:

$$\frac{v}{L} = \frac{V_{xg}}{x_g} \tag{4.58}$$

While this does not give a complete property gradient within the gas gun, it does give a linear gas velocity gradient and allows for the derivation of the kinetic energy of the gas:

$$KE_g = \int_0^L \frac{1}{2} m_g V_{xg}^2 \, dx_g = \frac{1}{6} \rho A L v^2 = \frac{1}{6} G v^2 \tag{4.59}$$

The book, Ballistics Theory and Design, continues with an adiabatic condition utilizing the ratio of specific heats γ, initial pressure P_i, final pressure P_f, initial volume V_i, final volume V_f, and breach length L_{Br}, assuming that the breach and bore are of the same area A, underestimating the idealized profile:

$$\frac{P_f}{P_i} = \left(\frac{V_f}{V_i}\right)^{-\gamma} = \left(\frac{(L_{Breach}+L)A}{(L_{Breach})A}\right)^{-\gamma} \tag{4.60}$$

With the adiabatic condition, the pressure work W, acting on the rear surface of the projectile is expressed:

$$W = AP_i \int_0^L \left(\frac{L_{Breach}+x}{L_{Breach}}\right)^{-\gamma} dx \tag{4.61}$$

The resultant equation (4.61) was inserted into an energy balance, accounting for the kinetic energy of the gas (4.59), and the resistance from friction and kinetic energy of the sabot (4.42), where m is the sabot mass, and f is the force of friction:

$$\frac{1}{6}cv^2 + {}^1\!/_2\, mv^2 + fL = AP_i \frac{(L+L_{Br})^{1-\gamma} - (L_{Br})^{1-\gamma}}{(1-\gamma)(L_{Br})^{-\gamma}} \tag{4.62}$$

The initial pressure:

$$P_i = \frac{\lambda G}{AL_{Br}} \tag{4.63}$$

$$\lambda = RT \tag{4.64}$$

$$\left(\frac{G}{3} + m\right) v^2 = 2A \frac{\lambda G}{AL_{Br}} \frac{(L+L_{Br})^{1-\gamma} - (L_{Br})^{1-\gamma}}{(1-\gamma)(L_{Br})^{-\gamma}} - 2fL \tag{4.65}$$

$$v = \sqrt{\frac{2A\lambda G(L_{Br})^{1-\gamma}}{AL(1-\gamma)(L_{Br})^{-\gamma}\left(m+\frac{G}{3}\right)}\left[\frac{(L_{Br}+L)^{1-\gamma}}{(L_{Br})^{1-\gamma}} - 1\right] - \frac{2fL}{\left(m+\frac{G}{3}\right)}} \tag{4.66}$$

Simplifying, one arrives at the Lagrangian definition for projectile velocity:

$$v = \sqrt{\frac{2\lambda G}{(1-\gamma)\left(m+\frac{G}{3}\right)}\left[\frac{(L_{Br}+L)^{1-\gamma}}{(L_{Br})^{1-\gamma}} - 1\right] - \frac{2fL}{\left(m+\frac{G}{3}\right)}} \tag{4.67}$$

A new kinetic energy balance consists of this above gas energy along with the projectile kinetic energy, drag, and adiabatic energy derived above. This equation does not account for gun cambridge (the difference between the barrel diameter and breach diameter) between the barrel and breach.

$$\frac{1}{6}Gv^2 + {}^1\!/_2\, mv^2 + fL = \frac{G(V_f^{1-\gamma} - V_i^{1-\gamma})}{1-\gamma} \tag{4.68}$$

$$\frac{1}{6}Gv^2 + {}^1\!/_2\, mv^2 = \frac{G(V_f^{1-\gamma} - V_i^{1-\gamma})}{1-\gamma} - fL \tag{4.69}$$

$$Gv^2 + 3mv^2 = \frac{6G(V_f^{1-\gamma} - V_i^{1-\gamma})}{1-\gamma} - 6fL \tag{4.70}$$

$$v^2(G + 3m) = \frac{6G(V_f^{1-\gamma} - V_i^{1-\gamma})}{1-\gamma} - 6fL \tag{4.71}$$

$$v = \sqrt{\frac{2P_iV_i^{\gamma}(V_f^{1-\gamma} - V_i^{1-\gamma})}{(1-\gamma)(G+3m)} - \frac{6fL}{(G+3m)}} \tag{4.72}$$

PIDDUCK AND KENT

Lagrange's problem was later extended, as the forward moving projectile created vacuum spaces behind itself as it traveled forward. Information of state takes time to travel from the rear of the projectile to the back of the breach. From the Newton-Laplace equation it can be seen that the sound speed of a gas is a function of density and pressure:

$$a_o = \sqrt{\frac{\gamma P}{\rho}} \tag{4.73}$$

where a_o is the sound speed of the gas, γ the ratio of specific heats, P is the gas pressure, and ρ is the gas density. However, if one assumes that these gases can be well characterized by the kinetic theory of gases, one finds that:

$$P = \frac{1}{3}\rho {c_{rms}}^2 \tag{4.74}$$

where c_{rms} is the root mean square of molecular sound speed. Substituting, it can be seen that the sound speed of the gas can be characterized by the root mean squared of the gas and the specific heat of the gas.

$$a_o = \sqrt{\frac{\gamma}{3}\,{c_{rms}}^2} \tag{4.75}$$

One can find the root mean squared speed of a molecule from the temperature and molar mass of the gas:

$$c_{rms} = \sqrt{\frac{3RT}{M}} \tag{4.76}$$

Where R is the ideal gas constant, T is temperature, and M is molar mass. Substituting one final time, the common formulation for the sound speed of a gas is found:

$$a_o = \sqrt{\frac{\gamma RT}{M}} \tag{4.77}$$

As can be seen, the sound speed of the gas varies from gas to gas with smaller molecular compounds having a generally higher sound speed. In addition, raising gas temperature also raises gas sound speed. Reviewing the literature, experimenters have had great success in increasing gas gun performance through the use of smaller molecular compounds. However Hallock Swift notes that while he and his team at NRL we able to "demonstrate initial gas temperatures up to 3000 K... [with] sound speed increases up to a

factor of 2.5 above room temperature… expected. In every case, the light-gas gun could be made to achieve launch velocities as great as those achieved when the gun was fired at room temperature, but no performance increase could be achieved" [166].

Three gases are commonly utilized in gas gun as the driving gas. At standard pressure and atmosphere, these include nitrogen, with a sound speed of 354.4 m/s, helium at 972 m/s, and hydrogen at 1270 m/s. Nitrogen has the lowest of the three sound speeds, but is readily available. Hydrogen is the fastest of the three, but gases has a tendency to react with oxygen and is hazardous. Helium is the second fastest, but it is the most expensive.

To understand the effects of sound speed on velocity, one can look to an equation by Hernri Bernier [167], which utilizes the perfect gas equation, coupled with constant specific heat:

$$P = P_o \left[1 - \frac{\gamma - 1}{2 * a_o} v\right]^{\frac{2\gamma}{\gamma - 1}} \tag{4.78}$$

Where P is the final pressure, P_o is the initial pressure, γ is gas specific heat, a_o is gas sounds speed, and v is velocity. Bernier mentions that for a complete release of gas, that is to say the gas has the ability to expand behind the projectile infinitely, (p=0), one can generate a theoretical peak projectile velocity given by the equation:

$$v_{lim} = \frac{2a_o}{\gamma - 1} \tag{4.79}$$

Using this equation, Bernier proceeds to tabulate the relative effectiveness of each gas (Table 4.5).

Table 4.5 Maximum Projectile Velocity of Various Gases

Gas	Γ	a_o (m/s)	v_{max}
Nitrogen	1.4	343	1715
Helium	1.663	970	2926
Hydrogen	1.406	1258	6197

As one can see gases of a lower molecular size tend to have a higher sound speed and though the specific heat can negatively affect peak velocity, the sound speed is generally hundreds of magnitudes higher in effect. The peak velocities shown in Table 4.5 do not take the projectile mass, breach to bore diameter, nor a reasonable length of gun barrel into account.

It is for this major reason that by changing the gases, one can radically change the gun's peak velocity, a variable that the above equations fail to take into account. Notable steps to the derivation of the Pidduck and Kent solution included work by Huguenot [184], Love [43], Pidduck and Kent [42]. These all share a role in applying the pressure wave theory caused by the expansion disturbances of the forward motion of the projectile. The resultant equation is as follows, assuming that the breach and barrel are of the same diameter. This solution accounts for non-uniform density and pressure:

$$v = a_o\sqrt{\frac{\widetilde{a_o}}{\gamma-1}}\sqrt{\frac{1-\left(1+\frac{\gamma\left(\frac{p_o A_1 L}{m a_o^2}\right)}{G/m}\right)^{(1-\gamma)}}{\gamma-1}} \tag{4.80}$$

Where $\widetilde{a_o}$ is related to G/m by:

$$\frac{G}{m} = \frac{2\gamma}{\gamma-1}\widetilde{a_o}(1-\widetilde{a_o})^{-\frac{\gamma}{\gamma-1}}\int_0^1(1-\widetilde{a_0}\mu^2)d\mu \tag{4.81}$$

which can be expanded by a mixed power binomial series or solved numerically. This equation can also be corrected to account for differences in barrel and breach diameter by adjusting the sound speed and driving pressure:

$$p_c = p_o\left(1+\left[\left(\frac{\gamma+1}{2}\right)^{1/2}-1\right]\left(1-\frac{A_1}{A_o}\right)\right)^{\frac{2\gamma}{(\gamma-1)}} \tag{4.82}$$

$$a_c = a_o\left[1+\left[\left(\frac{\gamma+1}{2}\right)^{1/2}-1\right]\left(1-\frac{A_1}{A_o}\right)\right] \tag{4.83}$$

Additional information on the derivation and formulation of the Pidduck and Kent model, which the author found useful, were found in the following sources: [186][187][188] and further numerical formulations can be found in [189][190][191][192].

From Siegel, one could divide the operational parameter space of a gas gun into three non-dimensional constants, which can and have been used to explore gas gun performance space [44], shown in the three equations below and which can be seen within the above equations:

$$\bar{m} = \bar{p} = \frac{G}{m} \tag{4.84}$$

$$\bar{x} = \frac{PA_cL}{ma_s^2} \tag{4.85}$$

$$\bar{u} = \frac{u}{a_s} \tag{4.86}$$

where $\bar{m}$, $\bar{x}$, and $\bar{u}$ are dimensionless mass (or pressure), length, and velocity respectively. G is the mass of the gas within the breach, m is the mass of the projectile, P is the breach pressure, A_c, is the barrel cross-sectional area, L is the position of the projectile along the barrel, a_s is the sound speed of the driving gas, and u is the velocity of the projectile.

Table 4.6 Summary of Pressure Velocity Relations

Model	Equation(s)	
Isobaric	$v = \sqrt{\frac{2L\,(P_i A - f)}{m}}$	(4.32)
Isothermal	$v = \sqrt{\frac{2P_i V_i \ln\left(\frac{V_i + AL}{V_i}\right)}{m} - \frac{2fL}{m}}$	(4.41)
Adiabatic	$v = \sqrt{\frac{2P_i V_i^{\gamma}(V_f^{1-\gamma} - V_i^{1-\gamma})}{m(1-\gamma)} - \frac{2fL}{m}}$	(4.48)
Lagrange	$v = \sqrt{\frac{2\lambda G}{(1-\gamma)\left(m+\frac{c}{3}\right)}\left[\frac{(L_{Br}+L)^{1-\gamma}}{(L_{Br})^{1-\gamma}} - 1\right] - \frac{2fL}{\left(m+\frac{G}{3}\right)}}$	(4.72)
Pidduck and Kent	$v = a_o \sqrt{\frac{\widetilde{a_o}}{\gamma-1}} \sqrt{\frac{1-\left(1+\frac{\gamma\left(\frac{p_o A_1 L}{m a_o^2}\right)}{G/m}\right)^{(1-\gamma)}}{\gamma-1}}$	(4.80)

Utilizing the above models, the velocity profiles for pure nitrogen and a 0.25kg sabot, traveling without friction effects are plotted in Figure 4.19 below. Initial testing utilized building air, which is mostly comprised of nitrogen, and friction effects are also considered negligible, but are not zero, so it is assumed that velocities shown here are slightly above expected experimental observations. Other gases such as hydrogen or helium (included in Figure 4.17 below), having higher sound speeds, increase peak velocity attained by the projectile as expected from equation (4.79). Experimental data, taken from: velocity blocks, dynasen pins, PDV, and reverse Taylor testing, within the Figure 4.17, seem to have good agreement with initial analytical estimate of peak projectile velocity.

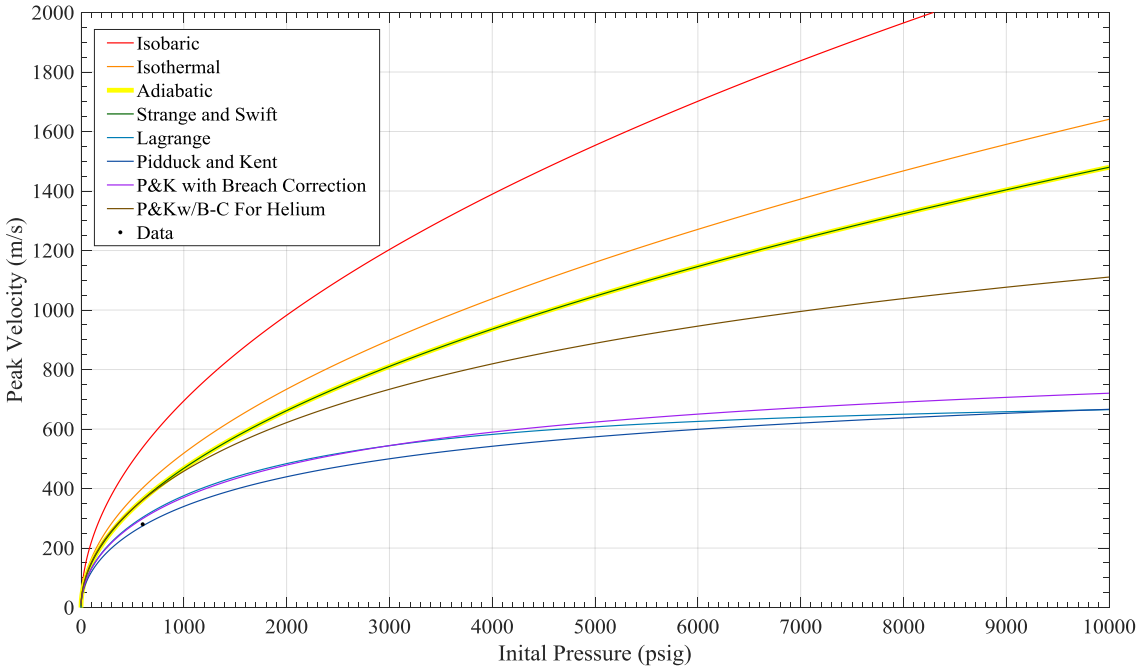

Figure 4.17 Approximate gas gun pressure velocity profile for a variety of models for a 0.25 kg projectile.

From this, it can be seen that for a typical experiment one might expect peak velocities around 720 m/s with nitrogen and 1120 m/s with helium. Only a single experiment for a 0.25 kg sabot has been conducted thus far and the slight underperformance is likely due to frictional forces between the sabot and the barrel. To reduce this effect, vacuum grease should be used to coat the sabot prior to loading into the barrel. Silicone greases such as the Dow Corning high vacuum grease are shear thinning meaning that its viscosity decreases under shear stain. This also helps reduce frictional effects. Experiments conducted up to 600 psig, (the peak pressurization tested), and at other pressure and mass configurations have since shown good agreement with the non-dimensionalized breach corrected Pidduck and Kent equation shown in Figure 4.18.

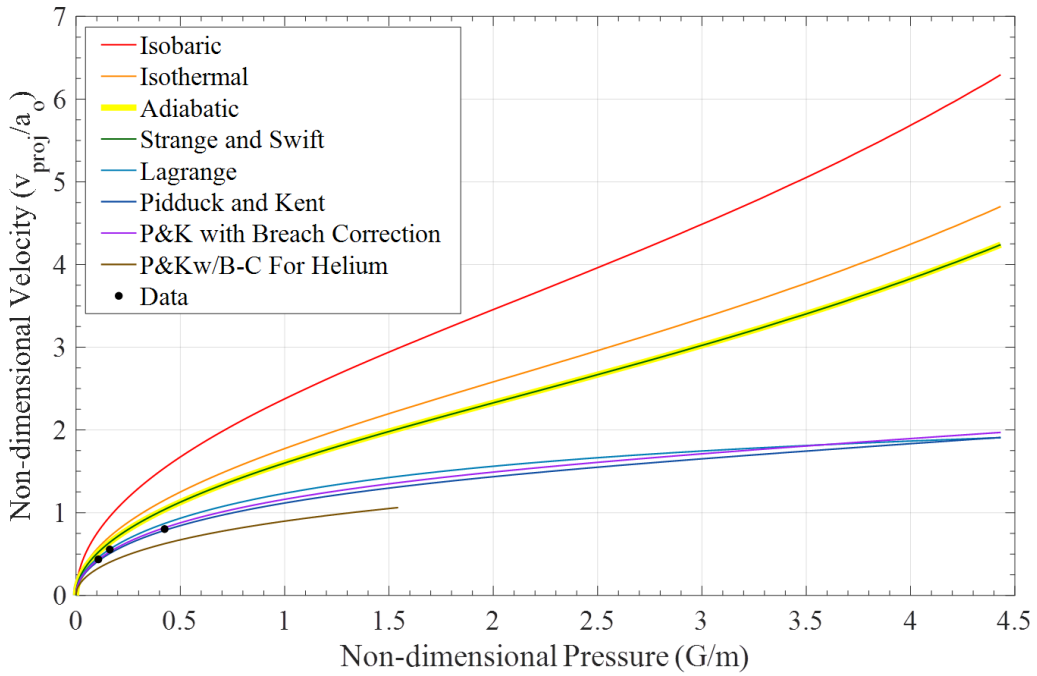

Figure 4.18 Non-dimensionalized pressure velocity curves with three observed tests.

The above graph is useful as it allows for the evaluation of pressure velocity relations for multiple projectile masses rather than a single mass as presented in Figure 4.17. Unfortunately, while non-dimensionalization works well over a range of pressures and projectile masses, it does not account for differences in the properties of the driving gas. Helium, while known to achieve higher velocities than nitrogen, has a much higher sound speed and lower molecular weight than Nitrogen and thus appears below the Nitrogen curve in Figure 4.18.

From the Pidduck and Kent solution, instantaneous velocity is calculated as a function of length along the barrel. From this estimation in velocity, one can also back

out the total time required for the sabot to travel the length of the barrel using the following equation:

$$t = \int_0^L \frac{1}{v_p(x)} dx \tag{4.87}$$

where the time t for the projectile to fly the length of the barrel L is the length of the barrel, and $v_p(x)$ is the velocity of the projectile at point x along the barrel. Using calculated data, one can estimate time using the trapezoidal method as shown in Figure 4.17 below. Please note here that the number of trapezoids shown here are low so as to demonstrate the principle, for better estimates of time one should decrease the distance between each trapezoidal sample. The trapezoidal rule used in this calculation is included alongside Simpson's rule in Appendix B for increasing accuracy with larger distances between samples and shorter calculation times.

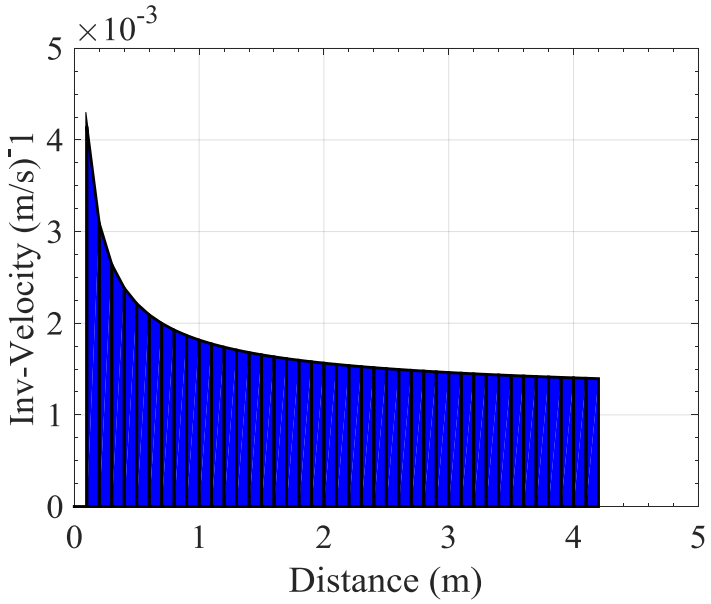

Figure 4.19 Estimation of sabot travel time (converged to 7.87 millisec) for a 0.25 kg projectile with a breach pressure of 10,000 psig.

4.6 Post Shot Pressure

By pulling a vacuum on the system a sub-atmospheric post shot pressure was expected for most shots. This section quantifies the range of post shot pressures expected for various breach pressures. To calculate the pressures, either the expected post shot pressure free or Joule expansion [185] was assumed. One can assume free expansion, as conduction of through the walls of the system, was known to operate at a much longer time scale than the shot itself. As with the above equations, one could assume that the gas within the chamber can be modeled as an ideal gas under adiabatic conditions, assuming that the internal energy of the system does not change, that is to say that the effects of

heat transfer and work done on the system are negligible. The resultant equation , for isentropic expansion, relates the pressure and volume of initial and final gas states:

$$P_f = P_i \left(\frac{V_i}{V_f}\right)^{\gamma} \tag{4.88}$$

where P_f is the final pressure, P_i is the initial pressure, V_i is the initial volume, V_f is the final volume, and γ is the gas specific heat. This equation, unlike the previous section, simply jumps between states rather than iterating between time steps and assumes no change in internal energy.

Utilizing the Engineering Equation Solver Package (EES), free expansion was solved using state tables making use of known gas properties, initial pressure, initial volume of the breach and the finial volume of the system to solve for free expansion. Initial breach pressures are given in psig and final system pressures are given in in Hg to ease comparison with existing dial gauge instrumentation within the shock physics lab (Figure 4.20).

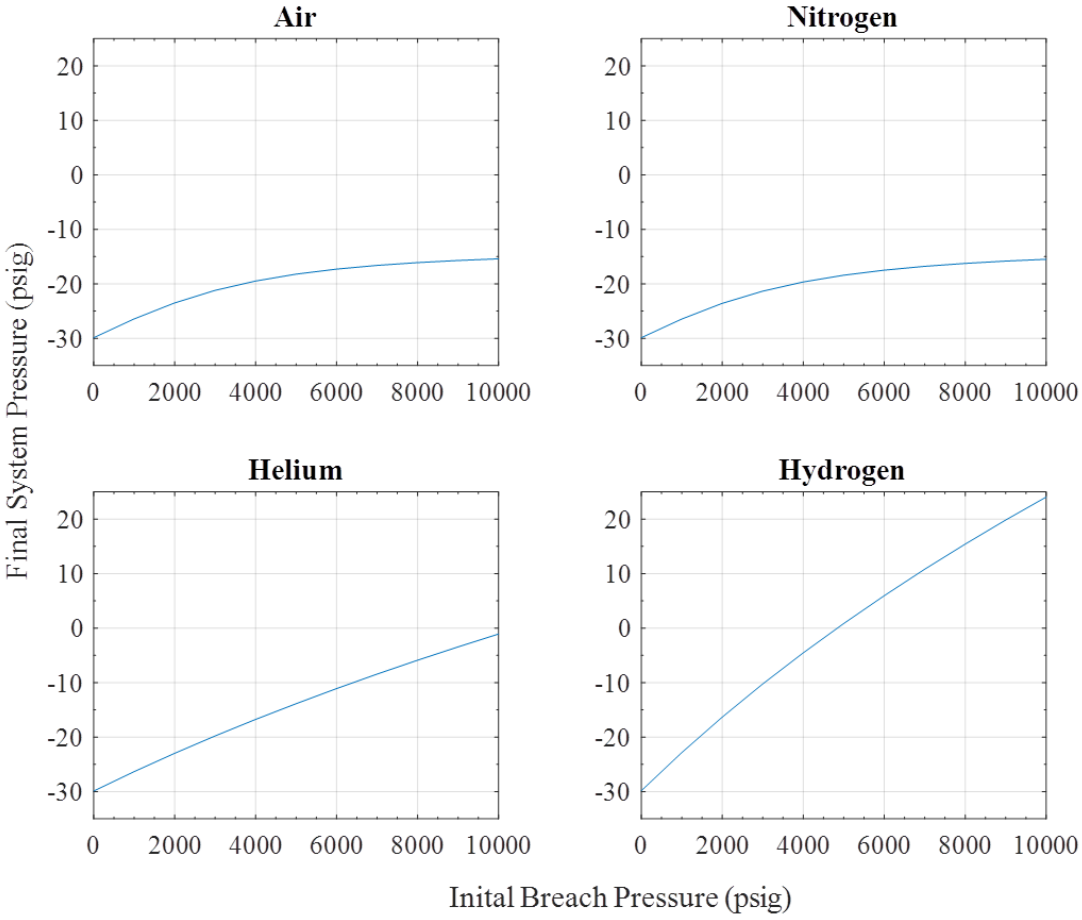

Figure 4.20 Final system pressures based on initial breach pressures.

While air, nitrogen, and helium all end with system pressures below the standard atmospheric conditions, hydrogen ends at a pressure above an atmosphere. This, in addition to hydrogen's more flammable characteristics, makes it a candidate to avoid when choosing a driving gas for Marquette's current 2 inch system.

4.7 Gun Recoil

When designing the static gun components back in section 2.1, the peak recoil force of the gun was required in order to find the preloading required by the various threaded components.

From the definition of force [145], or using a momentum balance one finds that:

$$F = \frac{\Delta M}{\Delta t} \tag{4.89}$$

Force F can be expressed as the relation between the change in momentum M over the change in time t. From D.E. Carlucci and S. S. Johnson [150], one finds that the total momentum of a gas gun can be expressed as:

$$\Delta M = \left(m + \frac{G}{2}\right) v_{Muzzle} \tag{4.90}$$

where M is the total momentum, m is the mass of the projectile, G is the mass of the propellant and v_{Muzzle} is the muzzle velocity. From the previous section 4.5, all of these variables are known, so the calculation of gun recoil force can be calculated for peak operational pressure for both nitrogen and helium in Table 4.7.

Table 4.7 Gun Recoil Force

Variable	Nitrogen	Helium	Units
Breach Pressure	68.95 (10,000)	68.95 (10,000)	bar (psig)
Projectile Mass	0.25	0.25	Kg
Gas Mass	1.094	0.38	Kg
Travel Time	0.00787	0.00546	Sec
Projectile Velocity	718.33	1106	m/s
Total Momentum	572.51	486.64	kg m/s
Recoil Force	72.75	89.13	kN

5. CONCLUSIONS

5.1 Future Work

5.1.1 Gas Gun Improvements

While the work presented within this report has effectively designed a working gas gun, which has been tested and utilized successfully in experimental testing, there will always be ways to improve the system. Having reviewed the overall design through the writing of this report, there are a few design modifications which should take precedence.

5.1.2 Reinforcement of the Impact Plate and Target Tank

The first modification would be the bolstering of the impact plate. As mentioned in section 2.1.5, the current steel chain used to restrain the impact plate is under spec for breech pressures exceeding 1500 psig. While the chain should never be imparted with the full force of gun recoil, a simple increase in chain diameter to one capable of

withstanding a dead load of 5,000 lbf. is inexpensive and easy to implement. Additionally, it is proposed that a second steel plate be surmounted within the man-way cover on the rear of the catch tank. Addition of this plate would not decrease performance and would provide a second layer of defense within the catch tank. Finally, it was noted that projectiles tended to fall to the floor of the catch tank after impact with the impact plate. While this has not yet damaged the floor of the catch tank a rubber mat might provide an additional cushion to pad the tank interior, reducing the chance of damage to the tank interior.

5.1.3 Target Alignment

Through the build cycle much time was spent ensuring maximum work space within the target tank, as space was at a premium. While experiments have successfully taken place alignment of the flyer samples with the targets have been accomplished by feel and line of sight. To this end a number of alignment techniques were discussed but are yet to be fully implemented:

The Touch Method

The simplest of the three proposed alignment techniques the “Touch Method”, aligns the projectile to the sample. In restoration of the Parthenon this method was used to mate a blank piece of marble against an older sample of original material for a precise fit matching all contours (Figure 5.1). When sample and target do not match, the target is adjusted. While this method is simple and easy to understand, it has several flaws. The most difficult part of alignment in this method is the need to move the sabot down and

back the entire length of the barrel, as the sabot will not fit between the target and barrel. Shortening the sabot means the sabot will experience free flight where the sabot's motion is unconstrained. Removing the target plate after aligning the sabot is also a poor option, as this voids the alignment. After the final placement of the projectile and target, the true alignment of the projectile with the target plate cannot be quantified until readings from break pins are collected post experiment.

Figure 5.1 Mating of two marble blocks [193].

The Harvard Method

For alignment of normal planar impact (as explained by Markos Hankin, Lab Manager), Harvard utilizes a laser, optical flat and beam splitter to align the barrel sabot and target to the same point (Figure 5.2). The laser is first aligned to the barrel by use of an optical flat inserted facing the laser, first in the aft section of the barrel then in the muzzle. Laser alignment is determined when the laser reflects back to the point of origin

from both locations. After the laser has been aligned to the barrel, the beam splitter is affixed to the muzzle and the target is affixed with an optical flat. Since the beam splitter is aligned with the length of the barrel, the first beam sent to the splitter should be reflected back to the laser source. This is useful, as it provides one method of verifying barrel alignment. The second portion of the laser beam is allowed through the splitter and is reflected back from the optical flat affixed to the target. This system makes an excellent alignment tool, as the laser light traveling the length of the barrel provides a method of alignment that can be tuned by eye and by hand to within milli to micro radian accuracy or higher (depending on the length the laser light travels).

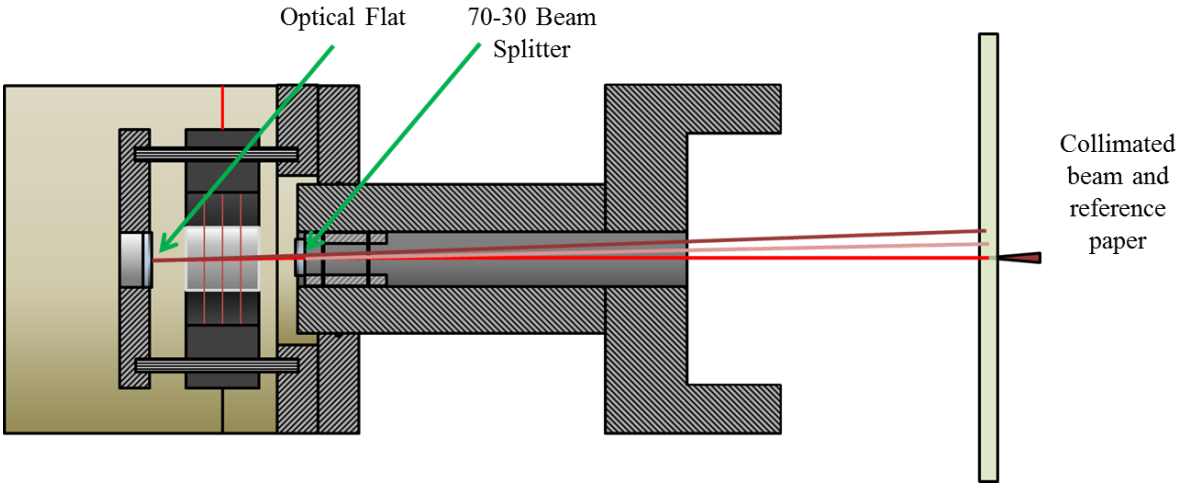

Figure 5.2 Diagram of the Harvard optical alignment method.

This system was considered for use in alignment of Marquette's samples but was eventually discarded due to a need to machine specialty optical flats for the various angles needed in pressure shear.

The Brown Method

Another method of target alignment published by Brown University [194] (shown in Figure 5.3), utilizes an auto-collimating telescope along with a 90^{o} prism with mirrored surfaces on specific surfaces. Like the Harvard method, it uses laser light emitted and bounced off mirrored surfaces on the muzzle and target surface. Unlike the Harvard method, the brown method captures light between the target and flyer. Given the shorter distance that the light travels, measurements need to be more precise. Older autocollimators allow for this fine measurement of reflected light by eye for alignment error of $2*10^{-5}$ radian, though many modern systems have dropped this functionality for digital readouts (which often display a single peak received signal), which may hinder the alignment of multiple signals on one collimator.

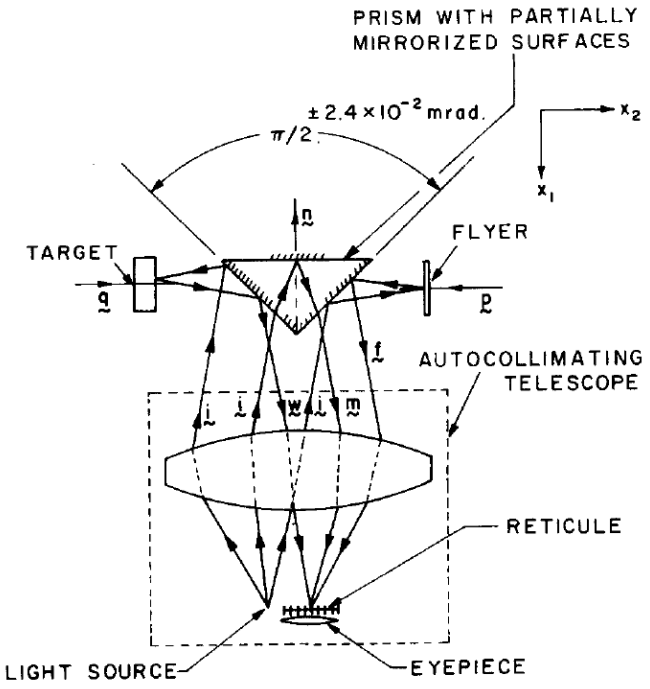

Figure 5.3 Optical alignment by use of the auto-collimating telescope [194].

A brief design, bouncing the light from an external auto collimator to the 90 degree prism using up to two penta-prisms, was initially considered as shown in Figure 5.4. While the Brown method promised the ability to align oblique pressure shear, flyer plate alignment and the lack of space between the target and muzzle made placing and aligning of equipment such as prisms, optical flats and the autocollimator itself both tricky and time consuming.

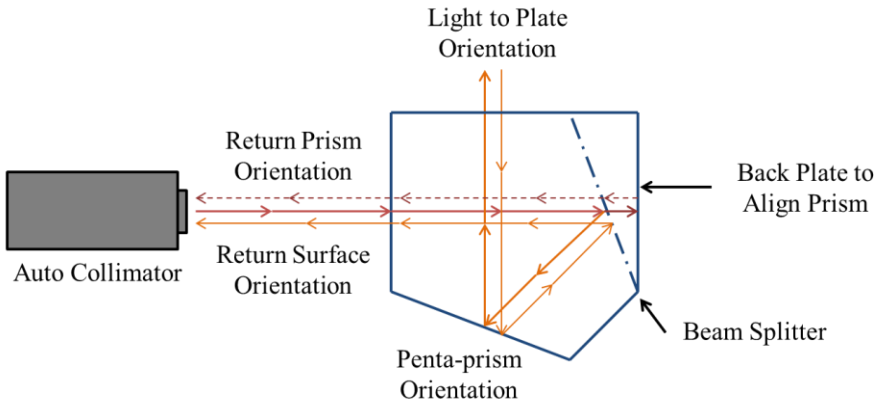

Figure 5.4 Proposed method to employ the Brown method into the Marquette gas gun design.

The Split Mirror Method

A final method proposed by the author is the use of an optical table placed between the target and muzzle. Using a small rotatable table, mounting a laser beam splitter and 2D optical receiver plate, it is thought that a significant range of oblique angles could be aligned with relatively minimal difficulty during alignments.

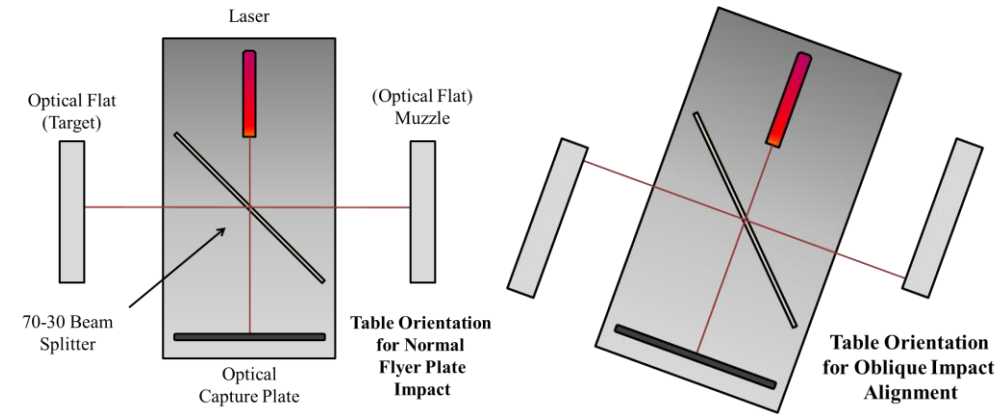

Figure 5.5 A novel proposed method for the alignment of oblique impacts used in pressure shear.

5.1.4 Examination of Surface Finishes for use with PDV

Within section 2.2.6, a brief examination of retroreflective surfaces for PDV was discussed. These patterns, while manufactured at Marquette via laser cutting and machining are recognizable (Figure 5.6) as the rectangular and triangular cuts desired, the end results, while nominally accurate in shape are, at micrometer size, quite rough.

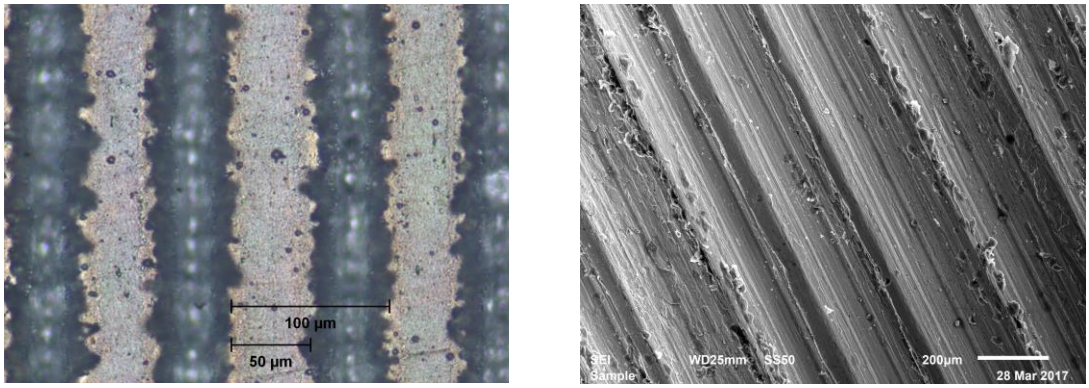

Figure 5.6 Samples cut by a metal cutting laser and triangular machining bit.

Since data arrives from the surface of samples shallower surface cuts and smaller, accurate, features lower than the 50 – 200 µm (shown above) should provide better data. To this end research into finer manufacturing techniques are underway with promising work being performed at UW Madison (Figure 5.7) by Dr. Min and his Nano-Machining Lab, which may be able to provide better surface definition for samples [195].

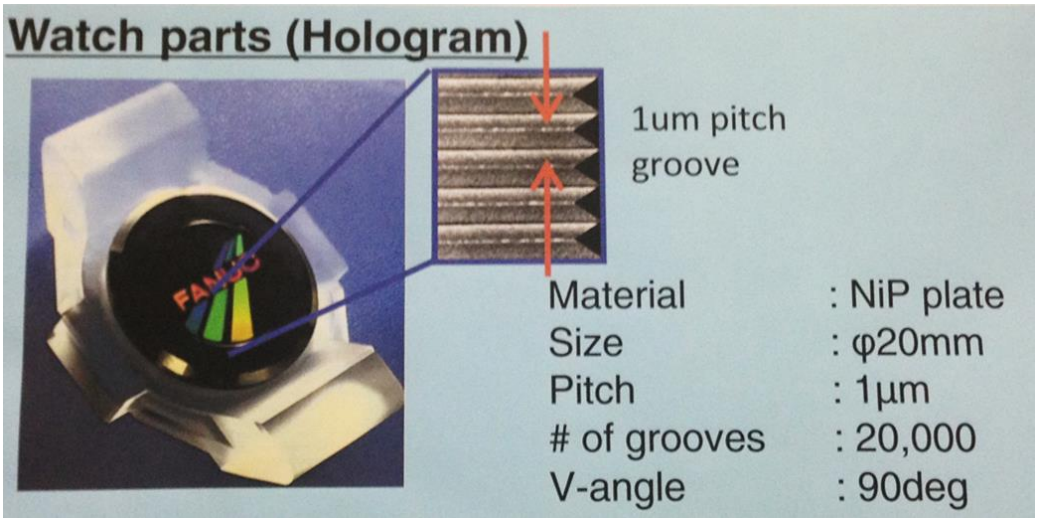

Figure 5.7 Demonstration of the ROBONANO α-0iB, creating a retroreflective surface.

5.1.5 Use of CTH and Shock Wave Theory for Experimental Design

Due to priorities and time constraints, this research was unable to conduct extensive work within CTH ($(ChartD^2)^{3/2}$, **C**hartD squared to the **T**hree **H**alves) with simulations, such as like those shown below in Figure 5.8 or provide a complete section within this work regarding wave propagation. After having read other works of past graduate students within the Marquette University Shock Physics Lab Group, the author is convinced that the enterprising reader will discover much information covering CTH,

KO, and Wave theory in a significant portion of past Marquette graduates work, mentioned in section 1.2.3.

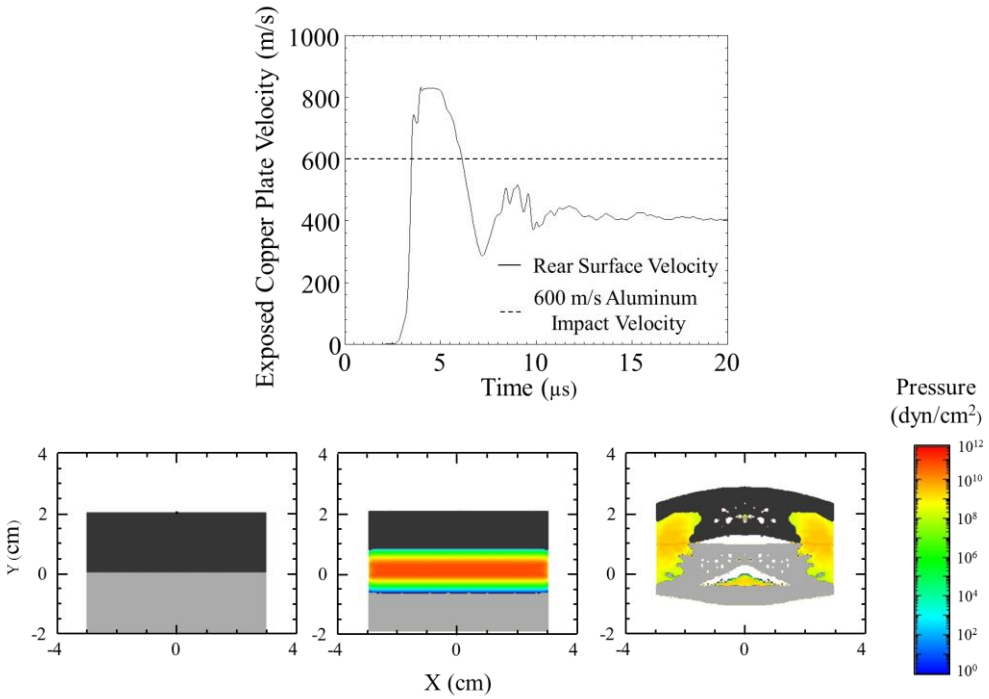

Figure 5.8 Flyer plate impact of aluminum impacting copper at 600m/s.

5.1.6 Experimental Testing

While some experimental testing is underway, initial testing has resolved a number of minor details regarding optimal setup of PDV, laser gates and firing procedure. It has only been within the most recent 2-3 shots that usable data has been recorded and can be utilized for extensive research. Some of the future types of experimental work are outlined in Figure 5.9 below.

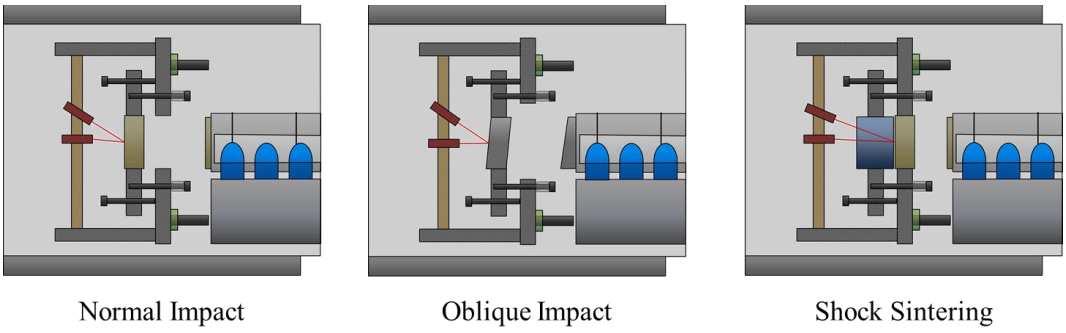

Figure 5.9 Three common types of shock physics experiments.

Normal [196] and oblique impacts can be used to characterize wave speeds through materials for use characterizing high stress material response, and shock sintering allows for the development of new composite materials. Oblique impacts [197] allow for the investigation of normal (longitudinal) as well as shear (transverse) waves (similar to the two modes of vibration one might induce in a spring (Figure 5.10).

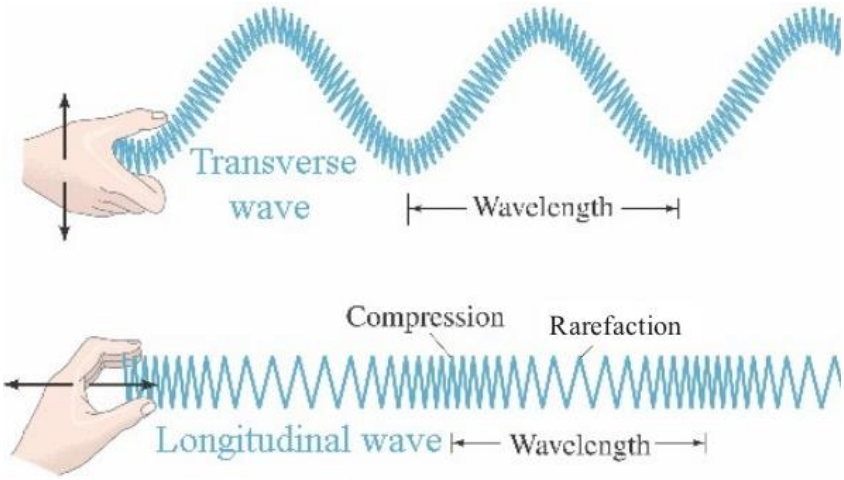

Figure 5.10 Transverse and longitudinal waves.

Shock sintering utilizes high pressure to shock bond granular materials together. While traditional manufacturing techniques for composite materials often involve heating materials for long time periods. This melts grain together, but comes at the cost of annealing and loss of original grain structure. By shock sintering, the outer surfaces of individual grains melt, welding grain to grain, then cool quickly maintaining grain structure. A test shot for the shock sintering of a Sodium Dodecyl Sulfate with Sodium Carbonate is shown below (Figure 5.11). Though materials in this shot did not likely undergo sintering, the methods used in this shot provided researchers with a proof of concept and confidence in the gas guns ability to perform such future experimental work.

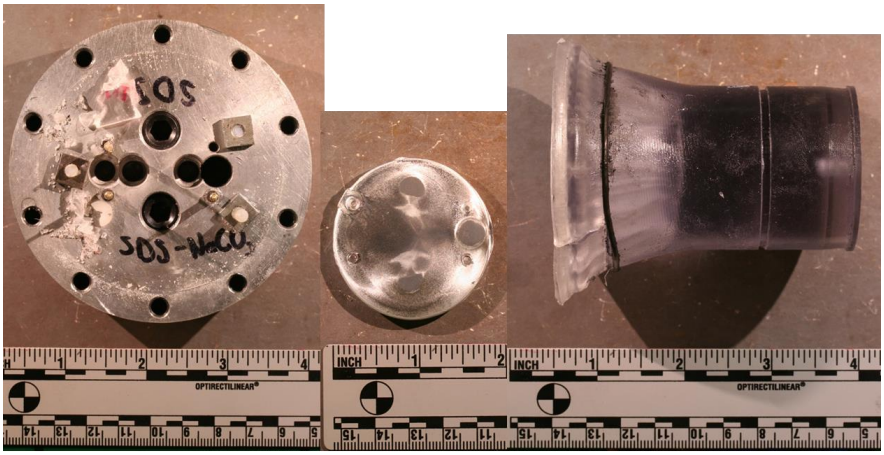

Target Flyer Sabot

Figure 5.11 1-9-2017 test shot for the shock consolidation of powders.

5.2 Closing

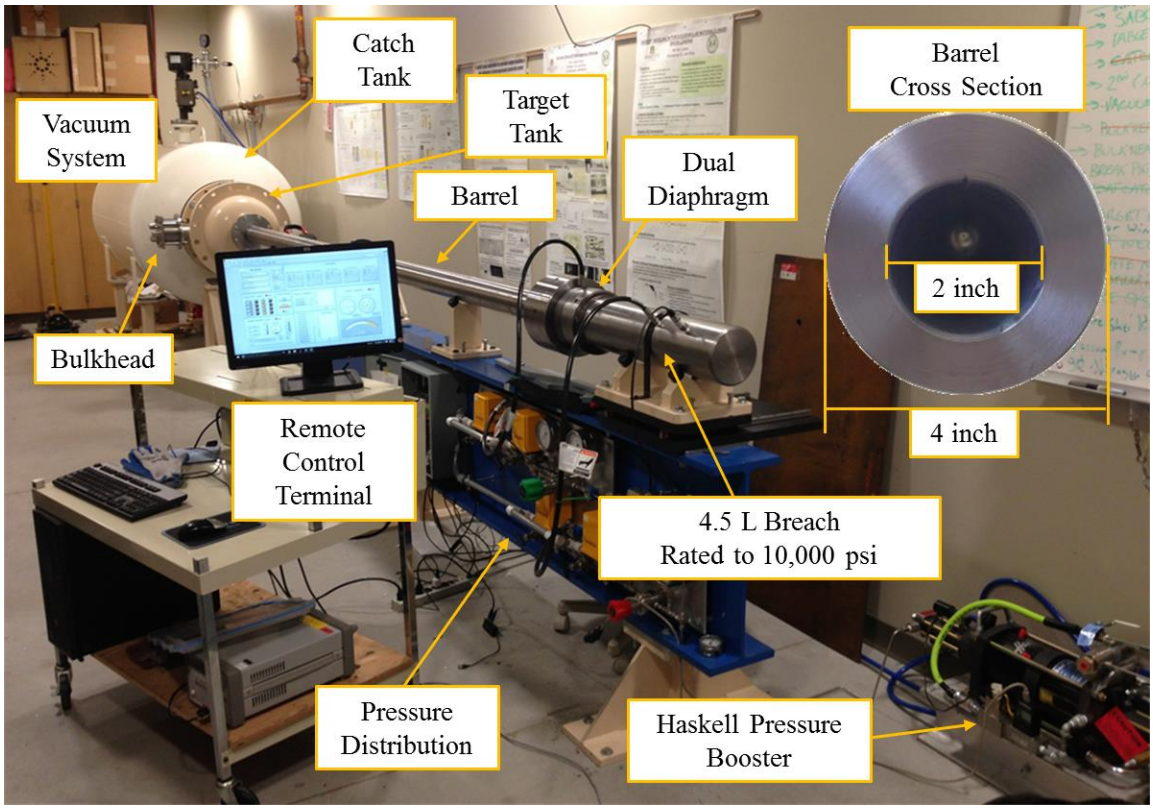

Figure 5.12 Completed 2 inch single stage dual diaphragm gas gun.

This concludes the master's thesis, it is not by any means comprehensive, but it is unlikely that it could ever be. After the construction of this system, it was intended to provide a broad overview of the single stage gas gun setup and a brief introduction to the major components on which the Marquette 2 inch single stage dual diaphragm gas gun operates, this has been completed herein. It is my hope that some reader in the future might use this as a foundation to produce an even more substantial work. To this reader "take what you can and burn the rest"! If you need help or clarification, please contact me, as it would be a pleasure to return the contact. Unfortunately, time spent within this universe is finite, so there may eventually be complications with communications.

Questions then should be asked to a colleague or held until meeting with The Higher Authority. The author's family has a saying, amongst others, which the author has found useful in research "man plans, God laughs."

God Bless,

Nathaniel ϟteven Helminiak

6. WORKS CITED

[1] Ferrill, A., 1997. The origins of war: From the stone age to Alexander the Great. Westview Press.

[2] Thieme, H., 2005. Die ältesten Speere der Welt-: Fundplätze der frühen Altsteinzeit im Tagebau Schöningen. Archäologisches Nachrichtenblatt, 10(4), pp.409-417.

[3] Lahr, M.M., Rivera, F., Power, R.K., Mounier, A., Copsey, B., Crivellaro, F., Edung, J.E., Fernandez, J.M., Kiarie, C., Lawrence, J. and Leakey, A., 2016. Inter-group violence among early Holocene hunter-gatherers of West Turkana, Kenya. Nature, 529(7586), pp.394-398.

[4] KUBÍKOVÁ, B., 2013. Re-assessment of Objects Referred to as Sling Missiles in the Prehistoric Archaeology of the Near East (Doctoral dissertation, Masarykova univerzita, Filozofická fakulta).

[5] Lukas, Dominik. 2016. "The Site." Çatalhöyük Research Project.

[6] Clark, Chip, and Hartmut Thieme. "What Does It Mean to Be Human?" Oldest Wooden Spear | The Smithsonian Institution's Human Origins Program. Smithsonian's National Museum of Natural HistoryClark, 01 Mar. 2010. Web. 21 May 2017.

[7] Sarzec Édouard de. Découvertes en Chaldée. Paris, Leroux, 1884-1912, pp. 36, 68, 94-103, 174-195.; Frayne, Douglas R. RIME 1.09.03.01, ex. 01.

[8] Patrick, Pouyssegur. "Work Stele of Vultures." *Stele of Vultures | Louvre Museum | Paris*. Louvre Museum, Paris, France, n.d.

[9] Frayne, Douglas R. "CDLI P222400: Stele of Vultures." CDLI - Cuneiform Digital Library Initiative. Louvre Museum, Paris, France, RIME 1.09.03.05, Ex. 01, 2007. Web

[10] The Editors of Encyclopædia Britannica. 2016. "Bronze Age." *Encyclopædia Britannica*. Encyclopædia Britannica, Inc.

[11] The Editors of Encyclopædia Britannica. 2017. "Iron Age." *Encyclopædia Britannica*. Encyclopædia Britannica, Inc.

[12] Ramsey, S., 2016. Tools of War: History of Weapons in Medieval Times. Vij Books India Pvt Ltd.

[13] Siculus, Diodorus, and Russel M. Geer. *The Library of History*. Cambridge: Harvard UP, 2006. Print.

[14] Ross, W.D., 1936. Aristotle's Physics a Revised Text.

[15] Toomer, Gerald J. "Archimedes." Encyclopædia Britannica. Encyclopædia Britannica, Inc., 01 Feb. 2017. Web. 27 May 2017.

[16] da Vinci, Leonardo. 1956. Leonardo Da Vinci by Instituto Geografico De Agostini. New York: Reynal in association with William Morrow, 1956. Print.

[17] 2.009. 2007."Archimedes's Steam Cannon." *2.009 Archimedes's Steam Cannon*. <http://web.mit.edu/2.009/www/experiments/steamCannon/ArchimedesSteamCannon.html>.

[18] Encyclopedia.com. 2001 "The Chinese Invention of Gunpowder, Explosives, and Artillery and Their Impact on European Warfare." Science and Its Times: Understanding the Social Significance of Scientific Discovery. <http://www.encyclopedia.com>.

[19] Chase, Kenneth Warren (2003). Firearms: A Global History to 1700. New York: Cambridge University Press. ISBN 978-0-521-82274-9.

[20] Phillips, Charles. 2017. "Battle of 'Ayn Jalut." *Encyclopædia Britannica*. Encyclopædia Britannica, Inc., <https://www.britannica.com/event/Battle-of-Ayn-Jalut>.

[21] Machiavelli, N., 2009. The Art of War. University of Chicago Press.

[22] De Milemete, Walter. 1326. “Early Cannon” De Nobilitatibus Sapientii Et Prudentiis Regum Manuscript. Musee de l'Armee, Paris.

[23] Hooper, E. H., Chisholm, H. and Phillips, W. A. 1910-1911. “Rifle.” Encyclopaedia Britannica. NY. Volume V23, Page 329

[24] Damerow, P., Freudenthal, G., McLaughlin, P. and Renn, J., 1992. Exploring the Limits of Preclassical Mechanics: A Study of Conceptual Development in Early Modern Science: Free Fall and Compound Motion in the Work of Descartes, Galileo, and Beeckman. Berlin et at: Springer. pg 153.

[25] A. Favaro, Amici e corrispondenti di Galileo, 3 vols. ed. Paolo Galluzzi, (Firenze, 1983), 3, 1247-1315.

[26] Galilei, G., 1914. Dialogues concerning two new sciences. Dover.

[27] Newton, I. (1687). Philosophiae naturalis principia mathematica. Londini, Jussu Societatis Regiæ ac Typis Josephi Streater. Prostat apud plures Bibliopolas.

[28] Bernoulli, J., 1695 Explicationes, annotationes, additiones ad ea, quae in actis sup. anni de curva elastica, isochrona paracentrica, velaria, hinc inde memorata, paratim controversa legundur; ubi de linea mediarum directionum, alliisque novis. Acta Eruditorum, 1, pp.65-80.

[29] PHGCOM. 2006. “Blunderbuss, Espingole 1760 France”. Photographed at Musee de l'Armee

[30] Da Veiga, J.P., Baker, E. 1804. *Twenty-three Years Practice and Observations with Rifle Guns*. Nabu Press; Primary Source ed. Edition

[31] Robins, B. and Curtis, W.S., 1972. New principles of gunnery. Richmond Publishing Company Limited.

[32] Euler, L. (2005). Foundations of differential calculus. 1st ed. New York: Springer.

[33] Locke, John: electro-chronograph picture and date of $10,000 award from Sky and Ocean Joined: The U. S. Naval Observatory 1830-2000, Steven J. Dick, Cambridge Univ. Press (2002), p. 91.

[34] Bashforth, Francis. 1866. Description of a Chronograph adapted for measuring the varying velocity of a body in motion through the air and for other purposes, London: Bell and Daldy

[35] Bashforth, F., 1873. Tables of Remaining Velocity, Time of Flight, and Energy of Various Projectiles, Calculated from the Results of Experiments Made with the Bashforth Chronograph, 1865-1870. London: Asher and Co.

[36] Bashforth, Francis; *Reports on experiments made with the Bashforth chronograph...*, 1878-1879; pg 4, H.M Majesty's Stationery Office, Harrison & Sons, London

[37] Bashforth, Francis, *A revised account of the experiments made with the Bashforth chronograph...*, 1890; pg 135-136, Cambridge at the University Press

[38] Mayevski, N., 1872. Traité de balistique extérieure. Gauthier-Villars.

[39] Coast Artillery School. 1917. *Reference Notes for Use in the Course in Gunnery and Ammunition*, Coast Artillery School Press, pg 12.

[40] Siacci, F., 1882. Balistica elementare: Per Francesco Siacci. Con tavola. Voghera Carlo.

[41] Ingalls, J.M., 1886. Exterior ballistics in the plane of fire. D. Van Nostrand.

[42] Kent, R.H., 1936. Some Special Solutions for the Motion of the Powder Gas. Physics, 7(9), pp.319-324.

[43] Love, A.E.H., and Pidduck, R.P. 1921, Philosophical Transactions of the Royal Society, A222, pg 167.

[44] Seigel A.E. , 1965 Theory of High Speed Guns. ADARDograph 91, National Technical Information Service, Advisory Group for Aerospace Research and Development Neuilly-sur-seine (France).AD475 660

[45] Raudzens, George (October 1990), "War-Winning Weapons: The Measurement of Technological Determinism in Military History", The Journal of Military History, Society for Military History, 54 (4): 403–434, doi:10.2307/1986064, JSTOR 1986064

[46] Rlbberlin., DIREKTOR. 2008 “French soldiers by a cannon 23 July 1870 in the Franco-Prussian War which lasted from 1870-1871.” Brown University Providence, RI

[47] Thomas,W. 2012. “M1903 Springfield rifle, USA. Caliber .30-06.” From the collections of Armémuseum (Swedish Army Museum), Stockholm.

[48] Royde-Smith, R. G. 2017. "World War II." *Encyclopædia Britannica*. Encyclopædia Britannica, Inc., <https://www.britannica.com/event/World-War-II>.

[49] Hogg, I.V., 2013. German Artillery of World War Two. Frontline Books.

[50] Haskell, J.R., 1881 “Accelerating-Gun” US Patent 241,978 (A) — 1881-05-24

[51] Birnie, R., 1907. “The Multicharge Gun” Gun Making in the United States. US Government Printing Office.

[52] "Оружие Второй Мировой: "Дора" и "Густав"." *DMIRIX.RU // о том, чего я не знал...* N.p., 27 June 2014. Web. 04 June 2017. <http://dmirix.ru/ultra/oruzhie-vtoroj-mirovoj-dora-i-gustav/>.

[53] BArchBot. 1942. “Hochdruckpumpe V-3, vermutlich auf dem Versuchsgelände auf der Insel Wolin nahe Misdroy” German Federal Archives. Sammlung von Repro-Negativen (Bild 146).

[54] Regan, G.O., 2008. A brief history of computing. Springer Science & Business Media.

[55] ARL Technical Library "Courtesy of Michael John Muuss “U. S. Army Photo: ENIAC and Computers” http://ftp.arl.army.mil/~mike/comphist/

[56] "NASA's Juno Probe Recognised by Guinness World Records as Fastest Ever Spacecraft." *Guinness World Records*. N.p., 07 July 2016. <http://www.guinnessworldrecords.com/news/2016/7/nasa%E2%80%99s-juno-probe-recognised-by-guinness-world-records-as-fastest-ever-spacecraft>.

[57] Leonard, B. ed., 2010. History of Strategic and Ballistic Missile Defense: Volume I: 1944-1955. DIANE Publishing.

[58] Lutzen, J. (1983), Euler 's Vision of a General Partial Diferential Calculus for a Generalized Kind of Function, Mathematics Magazine, 56, No. 5,299-306.

[59] Johnson, J. N. and Cheret (1998), Classic Papers in Shock Compression Science: Me'moire sur la the'orie du son by Poisson, Springer, New York.

[60] Salas, M.D., 2007. The curious events leading to the theory of shock waves. Shock Waves, 16(6), pp.477-487.

[61] Stokes, G. G. (1 848), On a Difficulty in the Theory of Sound, 33, [111], 349-356.

[62] Rankine, W. J. M. (1 870), On the thermodynamic theory of waves of finite longitudinal disturbances, Phil. Trans. Roy. SOC. London, 160,277-286.

[63] Johnson, J. N. and Cheret (1998), Classic Papers in Shock Compression Science: Me'moire sur la propagation du movement dans les corps et plus spe'cialement dans les gaz parfaits by P.H. Hugoniot, Springer, New York.

[64] Meyers, M.A., 1994. Dynamic behavior of materials. John wiley & sons.

[65] Alder, B., 1967. Methods in computational physics (Vol. 7). Academic Press.

[66] Wilkins, M.L., 2013. Computer simulation of dynamic phenomena. Springer Science & Business Media.

[67] Hertel Jr, E.S., SAND97-1015c Submitted to the 1997 International Workshop on New Models and Numerical Codes for Shock Wave Processes in Condensed Media September 15-19, 1997, Oxford, England.

[68] Bystrom. "Sled Track." Sandia National Laboratories, Web.

[69] Workman, E.J., Development of New Gun Using Helium Gas for Projectile Acceleration (Vol. 70). Final Report NMSM/RDD.

[70] Charters, Alex C. "Development of the high-velocity gas-dynamics gun." International Journal of Impact Engineering 5.1-4 (1987): 181-203.

[71] Downs, T.J., 2006. The development of a single stage light gas gun and velocity measurement system. Marquette University Master’s Thesis

[72] Crozier, W.D. and Hume, W., 1957. High-Velocity, Light-Gas Gun. Journal of Applied Physics, 28(8), pp.892-894.

[73] Swift, H.F., 2005. Light-gas gun technology: a historical perspective. In High-Pressure Shock Compression of Solids VIII (pp. 1-35). Springer Berlin Heidelberg.

[74] Norris, R.S. and Kristensen, H.M., 2006. Global nuclear stockpiles, 1945-2006. Bulletin of the Atomic Scientists, 62(4), pp.64-66.

[75] Fraunhofer EMI, "ARA Member-Site." ARA Member-Site, <https://www.aeroballistics.org/>.

[76] Hypervelocity Impact Society (HVIS). "The Hypervelocity Impact Society." <http://www.hvis.org/>.

[77] American Physical Society. "Topical Group on Shock Compression of Condensed Matter." <https://www.aps.org/units/gsccm/>.

[78] Bundy, M., Kennan, G.F., McNamara, R.S. and Smith, G., 1984. The President's Choice: Star Wars or Arms Control. Foreign Affairs, 63(2), pp.264-278.

[79] Charters, Alex C. "Development of the high-velocity gas-dynamics gun." International Journal of Impact Engineering 5.1-4 (1987): 181-203.

[80] "Free Royalty Free World Map Projections Printable, Blank Maps." Printable, Blank World Outline Maps • Royalty Free • Globe, Earth. <http://www.freeusandworldmaps.com/html/World_Projections/WorldPrint.html>.

[81] Crozier, W.D. and Hume, W., 1957. High-Velocity, Light-Gas Gun. Journal of Applied Physics, 28(8), pp.892-894.

[82] Fowles, G.R., Duvall, G.E., Asay, J., Bellamy, P., Feistmann, F., Grady, D., Michaels, T. and Mitchell, R., 1970. Gas gun for impact studies. Review of Scientific Instruments, Vol 41(7), pp.984-996.

[83] Bogdanoff, D.W., 1997. Optimization study of the Ames 0.5 ″two-stage light gas gun. International journal of impact engineering, 20(1-5), pp.131-142.

[84] Mitchell, A.C., Nellis, W.J. and Trainor, R.J., 1982, April. The Lawrence Livermore National Laboratory two-stage light-gas gun. In W.J. Nellis, L. Seaman and R.A. Graham eds. AIP Conference Proceedings (Vol. 78, No. 1, pp. 613-615). AIP.

[85] Ahrens, T.J., 1987. 6. Shock Wave Techniques for Geophysics and Planetary Physics. Methods in Experimental Physics, 24, pp.185-235.

[86] Martinez, A.R., Sheffied, S.A., Whitehead, M.C., Olivas, H.D. and Dick, J.J., 1994, July. New LANL gas driven two-stage gun. In S.C. Schmidt, J.W. Shaner, G.A. Samara and M. Ross eds.,, AIP Conference Proceedings (Vol. 309, No. 1, pp. 1643-1646). AIP.

[87] Asay, J.R., 1981. Sandia National Laboratories shock thermodynamics applied research (STAR) facility (No. SAND-81-1901). Sandia National Labs., Albuquerque, NM (USA).

[88] Hardage, B.A., 1965, February. Design and Construction of a Helium Gas Gun for Hypervelocity Impact. In Proceedings of the Oklahoma Academy of Science Vol. 45, pp. 129-138.

[89] Ozden, S., Autreto, P.A., Tiwary, C.S., Khatiwada, S., Machado, L., Galvao, D.S., Vajtai, R., Barrera, E.V. and M. Ajayan, P., 2014. Unzipping carbon nanotubes at high impact. Nano letters, 14(7), pp.4131-4137.

[90] Jensen, B.J., Cherne, F.J., Prime, M.B., Fezzaa, K., Iverson, A.J., Carlson, C.A., Yeager, J.D., Ramos, K.J., Hooks, D.E., Cooley, J.C. and Dimonte, G., 2015. Jet formation in cerium metal to examine material strength. Journal of Applied Physics, 118(19), p.195903.

[91] Young, Jr, R. and Rushing, R., 1996, September. Expanded impact test capabilities of the Arnold Engineering Development Center. In Space Programs and Technologies Conference (p. 4241).

[92] Piekutowski, A.J. and Poormon, K.L., 2006. Development of a three-stage, light-gas gun at the University of Dayton Research Institute. International journal of impact engineering, 33(1), pp.615-624.

[93] Martis, C.J., Putatunda, S.K., Boileau, J. and Spray, J.G., 2014. The static and dynamic mechanical properties of a new low-carbon, low-alloy austempered steel. Materials Science and Engineering: A, 589, pp.280-287.

[94] Dannenberg, R.E. and Stewart, D.A., 1965. Techniques for improving the opening of the main diaphragm in a large combustion driver.

[95] Stewart, S.T., 2004, March. The shock compression laboratory at Harvard: a new facility for planetary impact processes. In Lunar and Planetary Science Conference (Vol. 35).

[96] Swisdak, M. and Peckham, P., 1985. Validation Tests in Building 327-50-Pound Bombproof (No. NSWC/TR-85-384). NAVAL SURFACE WEAPONS CENTER SILVER SPRING MD.

[97] Hutchings, I.M. and Winter, R.E., 1975. A simple small-bore laboratory gas-gun. Journal of Physics E: Scientific Instruments, Vol 8(2), p.84.

[98] Rast, J.J., 1961. The design of Flat-Scored High-Pressure Diaphragms For use in Shock Tunnels and Gas Guns (No. BALLISTICS RESEARCH-29). NAVAL ORDNANCE LAB WHITE OAK MD.

[99] Mock, W., Holt, W.H., 1976. Report NSW/DL TR-3473, Naval Surface Weapons Center, Dalgren, VA.

[100] Russell, R.T., Starks, K.S., Grote, D.L., Vandersall, K.S., Zhou, M. and Thadhani, N.N., 1999, June. Design of New Muzzle for 80mm Diamter Single-Stage Gas Gun. In APS Shock Compression of Condensed Matter Meeting Abstracts.

[101] Scully, C.N. and Cowan, D.L., 1960, April. Hypervelocity Gun for Micrometeorite Impact Simulation Employing Capacitor Discharge in a Condensed Phase. In Proceedings of Fourth Hypervelocity Impact Symposium. Wol. III, Eglin Air Force Base, Florida

[102] Hutchings, I.M. and Winter, R.E., 1975. A simple small-bore laboratory gas-gun. Journal of Physics E: Scientific Instruments, 8(2), p.84.

[103] Bourne, N.K., Rosenberg, Z., Johnson, D.J., Field, J.E., Timbs, A.E. and Flaxman, R.P., 1995. Design and construction of the UK plate impact facility. Measurement Science and Technology, 6(10), p.1462-1470.

[104] Jones, D.R., Eakins, D.E., Hazell, P., Chapman, D.J. and Appleby-Thomas, G.J., 2012, March. Development of the gas gun driven expanding cylinder technique. In M.L. Elert, W.T. Buttler, J.P. Borg, J.L. Jordan and T.J. Vogler eds.,, AIP Conference Proceedings (Vol. 1426, No. 1, pp. 1141-1144). AIP.

[105] Burchell, M.J., Cole, M.J., McDonnell, J.A.M. and Zarnecki, J.C., 1999. Hypervelocity impact studies using the 2 MV Van de Graaff accelerator and two-stage light gas gun of the University of Kent at Canterbury. Measurement Science and Technology, 10(1), p.41.

[106] Igra, O. ed., 2016. Hypervelocity Launchers (Vol. 10). Springer.

[107] Lexow, B., Wickert, M., Thoma, K., Schäfer, F., Poelchau, M.H. and Kenkmann, T., 2013. The extra-large light-gas gun of the Fraunhofer EMI: Applications for impact cratering research. Meteoritics & Planetary Science, 48(1), pp.3-7.

[108] Pavlenko, A.V., Balabin, S.I., Kozelkov, O.E. and Kazakov, D.N., 2013. A one-stage light-gas gun for studying dynamic properties of structural materials in a range up to 40 GPa. Instruments and Experimental Techniques, 56(4), pp.482-484.

[109] Porat, Y. and Gvishi, M., 1980. The performance of a short-barrelled gas gun. Journal of Physics E: Scientific Instruments, 13(5), p.504.

[110] Gupta, S.C. and Sikka, S.K., 1996. Some investigations on shock wave induced phase transitions. Shock Waves, 6(6), pp.345-359.

[111] Ming-Qiang, H., Zi-Zheng, G., Kun-Bo, X., Jian-Dong, Z., Yan, C. and Jin-Chao, N., 2014. Experimental study on hypervelocity impact characteristics of density-grade thin-plate.

[112] Kawai, N., Tsurui, K., Hasegawa, S. and Sato, E., 2010. Single microparticle launching method using two-stage light-gas gun for simulating hypervelocity impacts of micrometeoroids and space debris. Review of Scientific Instruments, 81(11), p.115105.

[113] Akahoshi, Y, Furukawa, K, Matsuda, E & Hata, H 2004, New test range for Two-Stage Light Gas Gun in Kyushu Institute of Technology. in PM Bainum, L Furong & T Nakajima (eds), Advances in the Astronautical Sciences. vol. 117, pp. 919-926, 10th International Conference of Pacific Basin Societies, ISCOPS, Tokyo, Japan, 10-12 December.

[114] Zhao-xia, M., Jie, H., An-hua, S., Hua-yu, H., Yi, L. and Sen, L., 2015. The Analysis Technique for Ejecta Cloud Temperature Based on Atomic Spectrum. Procedia Engineering, 103, pp.357-364.

[115] Zheng, Zhijia, Enzhi Wang, Xiaoli Liu, et al. 2017. The Dynamic Response of Brittle Materials under Impact Loading. International Journal of Nonlinear Sciences and Numerical Simulation. 18(2): 115-127

[116] Grieshaber, M.J., 2015. Design of a Single Stage Gas Gun. The UNSW Canberra at ADFA Journal of Undergraduate Engineering Research, 7(1).

[117] Brown, J.R., Chappell, P.J.C., Egglestone, G.T. and Gellert, E.P., 1989. A gas-gun facility for material impact studies using low-velocity, low-mass projectiles. Journal of Physics E: Scientific Instruments, Vol 22(9), p.771-774.

[118] Doolan, C., 2001. A two-stage light gas gun for the study of high speed impact in propellants (No. DSTO-TR-1092). AERONAUTICAL AND MARITIME RESEARCH LAB SALISBURY (AUSTRALIA) WEAPONS SYSTEMS DIV.

[119] Strange, Dave. 1982, "Research Launchers." *General Info*. Physics Applications Inc., http://physicsapp.com/general_info.htm

[120] Gouge, M.J., Baylor, L.R., Combs, S.K., Fisher, P.W., Foster, C.A., Foust, C.R., Milora, S.L. and Qualls, A.L., 1993. Ballistics considerations for small-caliber, low-density projectiles (No. CONF-9309263--2). Oak Ridge National Lab., TN (United States).

[121] H. Kuhn. Mechanical Testing and Evaluation, volume 8, pages 943{983. ASM Handbook, September 2000. URL http://www.asminternational.org.

[122] Pettersson, T.S., Lefevre, P. and LHC Study Group, 1995. The large hadron collider: conceptual design. CERN, Geneva, Tech. Rep. CERN-AC-95-05 LHC.

[123] Mocker, A., Bugiel, S., Li, Y., Hiller, J., Hornung, K., Simolka, J., Strack, H., and Srama R. 2017. Hypervelocity impact experiments with a small 100kV electrostatical accelerator. Proceedings of the 14th Hypervelocity Impact Symposium. University of Kent, Canterbury, UK

[124] Charters, A.C., 1987. Development of the high-velocity gas-dynamics gun. International Journal of Impact Engineering, 5(1-4), pp.181-203.

[125] Ference, S.L., Borg, J.P. and Cogar, J.R., 1999. Source term investigation of TBM bulk chemical target intercepts: phase I test report. NSWC-DD TR99-82.

[126] Downs, T.J., 2006. The development of a single stage light gas gun and velocity measurement system. Marquette University. Master's Thesis.

[127] Lloyd, A.N., 2006. The static and dynamic compaction characteristics of porous silica powder : an experimental and numerical approach. Marquette University. Master's Thesis.

[128] Fraser, A., 2009. Mesoscale behavior of an aluminum-manganese dioxide-epoxy mixture under shock loading: from milli to nano-sized aluminum particles. Marquette University. Master's Thesis.

[129] Morrissey, M.P., 2009. The Aerodynamics of the knuckleball pitch: An experimental investigation into the effects that the seam and slow rotation have on a baseball. Marquette University. Master's Thesis.

[130] Ward, A., 2011. Investigation of Aluminum Equation of State Generation. Marquette University. Master's Thesis.

[131] Braun, C. and Borg, J., 2011, June. One-Dimensional Strain Initiated by Rapid Compaction of a Heterogenous Mixture. In APS Shock Compression of Condensed Matter Meeting Abstracts. Marquette University. Master's Thesis.

[132] Jordan, K.B., 2011. Direct numeric simulation of shock wave structures without the use of artificial viscosity. Marquette University. Doctoral Dissertation.

[133] Van Vooren, A.J., 2013. A multi-scale approach to a greater understanding of the behavior of heterogeneous materials under dynamic loading. Marquette University. Master's Thesis.

[134] Huang, L., 2013. Numerical Simulation Model on Irreversibility of Shock-Wave Process.

[135] LaJeunesse, J.W., 2015. Implications of heterogeneity in the shock wave propagation of dynamically shocked materials. Marquette University. Master's Thesis.

[136] Schumaker, M.G., 2015. A study of mesoscale simulations for planar shock experiments on heterogeneous granular materials Marquette University. Master's Thesis.

[137] Sable, P.A., 2016. Ramifications of projectile velocity on the ballistic dart penetration of sand. Marquette University. Master's Thesis.

[138] Beaver L. Marquette University. Master's Thesis.

[139] Teitz, E.M., 2017 Characterization of the Shock Wave Structure in Water. Marquette University. Master's Thesis.

[140] Central Steel and Wire Company. "Product Guide Form 1254." (n.d.): n. pag. Resources/ProductGuide. Central Steel and Wire Company, 13 Mar. 2015. Web.

[141] Morrison, J.L.M., 1948. The Criterion of 'Yield'of Gun Steels. Proceedings of the Institution of Mechanical Engineers, 159(1), pp.81-94.

[142] Edupack, C.E.S., 2005. Granta design limited. Cambridge, England, UK.

[143] Boiler, A.S.M.E., 1998. ASME Boiler and Pressure Vessel Code: An International Code. American Society of Mechanical Engineers.

[144] Shigley, J.E., Mischke, C.R. and Budynas, R.G., 2004. Mechanical engineering design Ninth Edition. McGraw-Hill, pg 410-451

[145] Yunus, A.C. and Cimbala, J.M., 2006. Fluid mechanics fundamentals and applications Third Edition. International Edition, McGraw Hill Publication, 185201. Pg 244.

[146] Plassard, F., Mespoulet, J. and Hereil, P., 2011. Analysis of a single stage compressed gas launcher behaviour: from breech opening to sabot separation. In 8th European LS-DYNA Users Conference (pp. 1-11).

[147] Stilp, Alois J. 2005. "Sabot Designs for Launching Penetrators and Projectiles." High-Pressure Shock Compression of Solids VIII. Springer Berlin Heidelberg, 201-225.

[148] Swift, H.F., Hohler, V., Sabot and Launch Techniques for Hypervelocity Impact Studies. Proceedings of the 45th ARA Meeeting.

[149] MAG Klan, 2016, APFSDS long rod penetrator animation and slow motion impacts https://www.youtube.com/watch?v=v48578CkNEo

[150] Carlucci, D.E. and Jacobson, S.S., 2013. Ballistics: theory and design of guns and ammunition. CRC Press.

[151] Andrews, D.R., 1983. The bursting diaphragm as a fast-acting valve. Journal of Physics E: Scientific Instruments, 16(3), p.192.

[152] Zukas, J.A., Nicholas, T., Swift, H.F., Greszczuk, L.B., Curran, R.D. and Malvern, L.E., 1983. Impact dynamics. Journal of Applied Mechanics, 50, p.702.

[153] National Instruments. 2016. "Field Wiring and Noise Considerations for Analog Signals." Field Wiring and Noise Considerations for Analog Signals - National Instruments. National Instruments, <http://www.ni.com/white-paper/3344/en/>.

[154] klopp, K.W. & Clifton R. J. & ShawkitT. G. 1985. Pressure-Shear Impact and the Dynamic Viscoelastic Response of Metals Mechanics of Materials 4. 387-393.

[155] Bowden, M.D. and M.P. Maisey. The development of a heterodyne velocimeter for use in sub-microsecond time regimes. Optical Technologies for Arming, Safing, Fuzing and Firing III. 2007: SPIE.

[156] Strand, O.T., Velocimetry Using Heterodyne Techniques. 26th International Congress on High-Speed Photography and Photonics. 2005: SPIE.

[157] Doppler, C., 1842. Ueber das farbige Licht der Doppelsterne und einiger anderer Gestirne des Himmels: Versuch einer das Bradley'sche Aberrations-Theorem als integrirenden Theil in sich schliessenden allgemeineren Theorie. In Commission bei Borrosch & André.

[158] 2002, “Doppler Effect” Brooks Cole Publishing, Thomson Learning.

[159] Technilogies, Q.U.O.R.O.M., 2002. Sputter Coating Technical Brief. Document No. TB-SPUTTER, (2).

[160] Charest, Jacques A. "The Ultimate Source for Shock Sensors." Dynasen. N.p., 2014. Web. 12 Apr. 2017.

[161] Lesker, K.J. "Controller 615 Series Kurt J Lesker Company." KJLC® 615 Series Thermocouple Gauge Controller. Kurt J Lesker, n.d. Web. 11 May 2017.

[162] Lesker, K.J. 2001. “Pressure Measurement Technical Notes.” Kurt J. Lesker company. Web. <http://www.lesker.com/newweb/gauges/gauges_technicalnotes_1.cfm>

[163] O'Hanlon, J.F., 2005. A user's guide to vacuum technology. John Wiley & Sons. Pg 86-87

[164] Oberg, E., Jones, F.D., Horton, H.L., Ryffel, H.H. and Geronimo, J.H., 2004. Machinery's handbook (Vol. 200). New York: Industrial Press.

[165] "Haskel International: Gas Booster Catalog." High Pressure Pumps, Gas Boosters and Valves. Haskel International, n.d. Web

[166] Swift, H., 2005. Light-gas gun technology: a historical perspective. High-Pressure Shock Compression of Solids VIII, pp.1-35.

[167] Bernier, H., 2005. Scaling and Designing Large-Bore Two-Stage High Velocity Guns. In High-Pressure Shock Compression of Solids VIII (pp. 37-83). Springer Berlin Heidelberg.

[168] "Mylar® Film and Sheet Properties." Grafix® Plastics, 2007. Web.

[169] Rast, J.J., 1961. The design of Flat-Scored High-Pressure Diaphragms For use in Shock Tunnels and Gas Guns (No. BALLISTICS RESEARCH-29). NAVAL ORDNANCE LAB WHITE OAK MD.

[170] Stewart, M., 2015. Surface Production Operations: Volume III: Facility Piping and Pipeline Systems. Gulf Professional Publishing.

[171] Taylor, G., 1948, September. The use of flat-ended projectiles for determining dynamic yield stress. I. Theoretical considerations. In Proceedings of the Royal Society of London A: Mathematical, Physical and Engineering Sciences (Vol. 194, No. 1038, pp. 289-299). The Royal Society.

[172] "Haskel International: Gas Booster Catalog." High Pressure Pumps, Gas Boosters and Valves. Haskel International, n.d. Web

[173] Bird, R.B., Stewart, W.E. and Lightfoot, E.N., 2007. Transport phenomena. John Wiley & Sons.

[174] Haynes, W.M., 2014. CRC handbook of chemistry and physics. Haynes, WM, ed. 2014, CRC Handbook of Chemistry and Physics, 95th edn.(Boca Raton, FL: CRC Press), ISBN 9781482208689.

[175] Pfeiffer Vacuum. "1.2.6 Types of Flow." Types of Flow. <https://www.pfeiffer-vacuum.com/en/know-how/introduction-to-vacuum-technology/fundamentals/types-of-flow/>.

[176] Adam, H., Bolz, A., Boy, H., Dohmen, H. and Umrath, D.W., 1998. Fundamentals of Vacuum Technology. Cologne, 198p.

[177] Senda, Y., Theoretical Analysis of Vacuum Evacuation in Viscous Flow and Its Applications. Atmosphere, 100(100), pp.0-1.

[178] 'Vacuum handbook (rev. ed.),' 1982 pp39-41, Nippon-Shinku-Gijutsu Co., Ltd. (1982)

[179] "Varian DS602 Rotary Vane Vacuum Pump User`s Installation Manual." Agilent Vacuum Technologies. Ideal Vacuum Products, July 2009. Web. 11 May 2017.

[180] Cengel, Y. A. and Boles, M. A., 2015. Thermodynamics: An Engineering Approach. New York: McGraw-Hill,. Print.

[181] Strange, D.E. and Swift, H.F., Approximate methods for evaluating light gas gun performance, 43rd Meeting of the Aeroballistic Range Associating, Oct., 1992.

[182] Klein S.A. 2016. EES: Engineering Equation Solver. F-Chart Software.

[183] Lagrange, J.L., 1853. Mécanique analytique (Vol. 1). Mallet-Bachelier.

[184] Hugoniot, H., 1889. Propagation du mouvement dans les corps. Chapitre V. Sur les discontinuités qui se manifestent dans la propagation du mouvement. Journal de l'École Polytechnique, 58, pp.68-125.

[185] Prescott Joule, J., 2011. Joint Scientific Papers of James Prescott Joule. Joint Scientific Papers of James Prescott Joule, by James Prescott Joule, Cambridge, UK: Cambridge University Press, 2011.

[186] Vinti, J.P. and Kravitz, S., Tables for the Pidduck-Kent Special Solution for the Motion of the Powder Gas in a Gun. Aberdeen Proving Ground: BRL R-693,. Jan 1949. 7· Love, AEH, and Pidduck, FB The Lagrange Ballistic Problem. Phil. Trans. Roy. Soc, 222, p.167.

[187] Corner, J., 1950. Theory of the interior ballistics of guns.

[188] Morrison, W.F., Wren, G.P., Oberle, W.F. and Richardson, S.L., 1993. The Application of Lagrange and Pidduck-Kent Gradient Models to Guns Using Low Molecular Weight Gases (No. ARL-TR-48). ARMY RESEARCH LAB ABERDEEN PROVING GROUND MD.

[189] Baer, P.G. and Frankle, J.M., 1962. The simulation of interior ballistic performance of guns by digital computer program (No. BRL-1183). ARMY BALLISTIC RESEARCH LAB ABERDEEN PROVING GROUND MD.

[190] Bogdanoff, D.W. and Miller, R.J., 1995. New higher-order Godunov code for modelling performance of two-stage light gas guns. NASA Technical Memorandum 110363.

[191] Baer, P.G., 1970. Prediction of High Velocity Solid Propellant Gun Performance by Gas Dynamic Computer Program. ARMY BALLISTIC RESEARCH LAB ABERDEEN PROVING GROUND MD.

[192] Holst, T.L., 1983. Numerical computation of transonic flow governed by the full-potential equation. NASA Technical Memorandum 84310.

[193] PBS 2008. "Secrets of the Parthenon.". Public Broadcasting Service, n.d. <http://www.pbs.org/wgbh/nova/ancient/secrets-parthenon.html>.

[194] Kumar, P. and Clifton, R.J., 1977. Optical alignment of impact faces for plate impact experiments. Journal of Applied Physics, 48(3), pp.1366-1367.

[195] Inada, A., Min, S., Ohmori, H., "Micro Cutting of Ferrous Materials Using Diamond Tool under Ionized Coolant with Carbon Particles," Annals of the CIRP, Vol. 60, No. 1, pp. 97-100, 2011.

[196] Williams, B., Higdon, D., Gattiker, J., Moore, L., McKay, M. and Keller-McNulty, S., 2006. Combining experimental data and computer simulations, with an application to flyer plate experiments. Bayesian Analysis, 1(4), pp.765-792.

[197] Prakash, V. and Clifton, R.J., 1993. Time resolved dynamic friction measurememts in pressure-shear. ASME Applied Mechanics Division-publications-AMD, 165, pp.33-33.

Appendix A: Catch Tank Dimensions

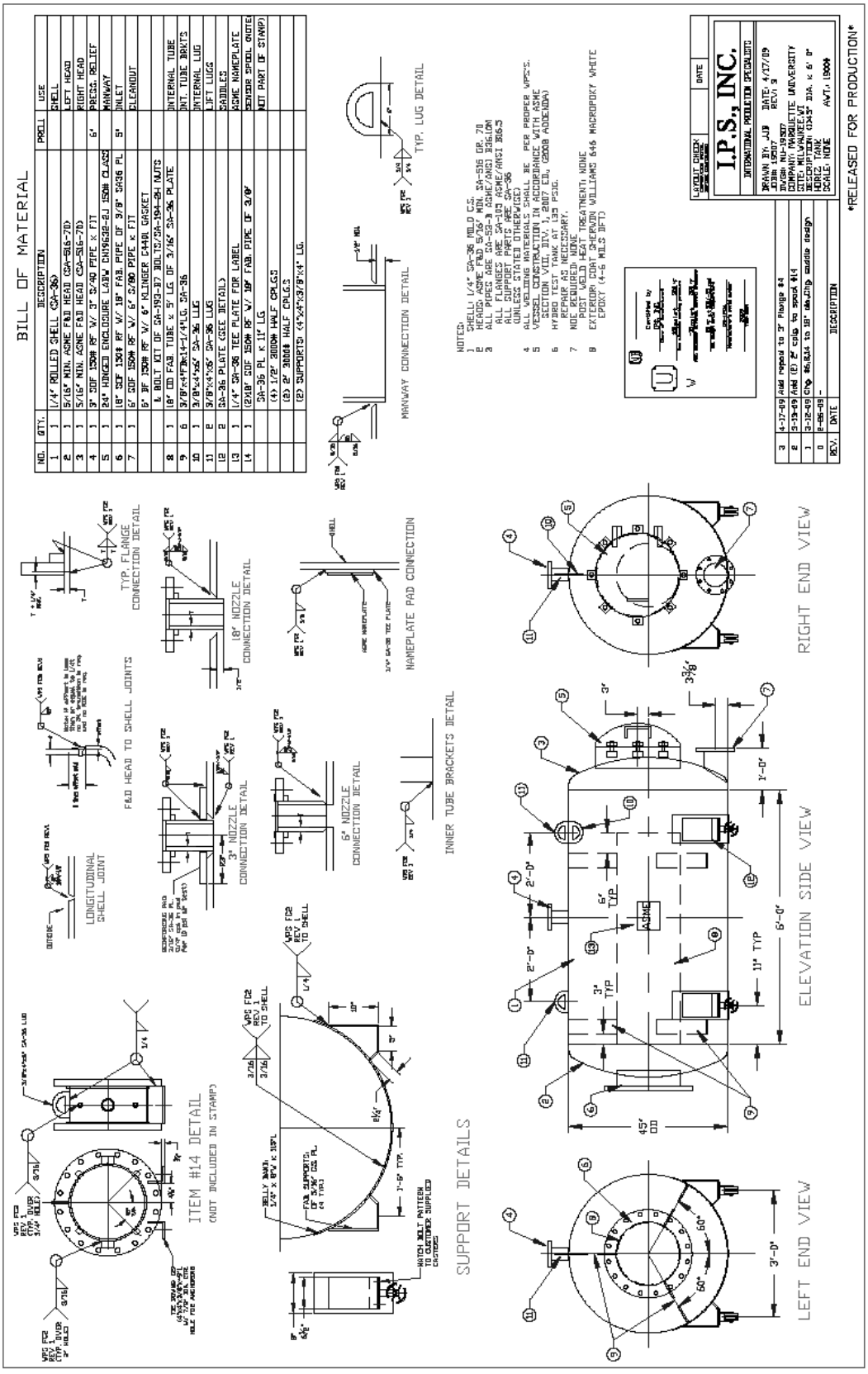

Appendix B: MATLAB Program for Anticipated Experimental Characteristics

The following code estimates projectile velocity, sabot travel time and light gate settings based on initial breach pressure, sabot mass, and initial pressure. It should be noted that this script is only accurate up to 10,000 psig as the ideal gas formulation with Z tables for nitrogen and helium included up to this pressure used to reference gas properties.

```
%% Calculating Travel Time and Peak Velocity
%  Uses Trap Stepping Integration Method
%  Powered by Corrected Pidduck and Kent
%  Created by Nathaniel Helminiak (2015-2017)
%  Forward Complaints to ---> nathanielhelminiak@yahoo.com
%  Should works for simple gases
%  Uses Ideal Gas Assumption ^  Typically Overestimates
%  Single Stage Gas Gun Variables can be changed.... (Be careful...)

%% The Setup
clc, clear all, close all

%% Inputs / Variables
%  psi is the Inital Breach Pressure in PSI
psi=400;%400;%507;
%  m is the projectile mass (kg)
m=0.6538;
%  l is the sabot length (m)
l=0.1524;
%  P_o is Initial Pressure within the Breach (Pa)
P_o=psi*6.89476e+3;
%  A is the Interior Barrel Area (m)
A = 0.002025802;
%  x_p is Distance Along the Barrel Length (m)
%  IMPORTANT THIS MATRIX GIVES THE RESOLUTION FOR THE TIME APPROX!!!!
%  SEE FIGURE THAT PLOTS FOR A VISUAL AID (REC 0.00001)
x_p=0:0.00001:4.2672;
%  Volume 0.0045 m^3
V_o=0.0045;
%Find the Compressibility Factor
%Z=1; To Disregard Compressibility Factor
ZP=linspace(0,10015,51);
ZHelium=[1,1.007,1.013,1.02,1.026,1.032,1.039,1.045,1.052,1.058,1.064,1
.071,1.077,1.083,1.09,1.096,1.102,1.108,1.115,1.121,1.127,1.133,1.139,1
.145,1.152,1.158,1.164,1.17,1.176,1.182,1.188,1.194,1.2,1.206,1.212,1.2
18,1.224,1.23,1.235,1.241,1.247,1.253,1.259,1.265,1.271,1.276,1.282,1.2
88,1.294,1.3,1.305];
ZNitrogen=[1,0.9979,0.9967,0.9964,0.9969,0.9984,1.001,1.004,1.008,1.014
,1.02,1.027,1.034,1.043,1.052,1.062,1.072,1.083,1.095,1.107,1.12,1.133,
1.146,1.16,1.174,1.189,1.203,1.218,1.233,1.248,1.264,1.28,1.295,1.311,1
```

```
.327,1.343,1.36,1.376,1.392,1.409,1.425,1.442,1.458,1.475,1.492,1.508,1
.525,1.542,1.558,1.575,1.592];
Z = interp1(ZP,ZNitrogen,psi);
%  n= PV/RT <-- An Ideal Gas EOS with compressiblity factor
n=(P_o.*V_o)./(Z*8.3144598.*300);
%  G is mass gas (kg) --> I use Nitrogen 14 gram / mole
%G=(4.*n)/1000; %Helium
G=(14.*n)/1000; %Nitrogen
%  SS is the Sound Speed of the Gas (m/s)
%SS=972;  %Helium
SS=349; %Nitrogen
%  y is Specific Heat Ratio (-)
%y = 1.66; %Helium
y = 1.4;  %Nitrogen

%% PnK Velocity With Breach Correction
%  PnK Specific Calculations (Essentially a Lookup Table...)
asquiwga=0:0.001:0.99;
for i=1:length(asquiwga)
fun = @(mu) (1-asquiwga(i).*mu.^2).^(1/(y-1));
GM(i)= (2.*y./(y-1)).*asquiwga(i).*((1-asquiwga(i)).^(-y./(y-
1))).*integral(fun,0,1);
end
%plot(GM,(asquiwga./(y-1)).^.5)
asquiwg = interp1(GM,asquiwga,G/m);
a_oc=SS*(1+((((y+1)/2).^.5)-1)*(1-(1/2)));
P_oc=P_o.*(1+(sqrt((y+1)./2)-1).*(1-(1/2))).^((2.*y)./(y-1));

% PnK Solution With Breach Correction
for i=1:length(x_p)
v(i)  = 2*a_oc*((asquiwg./(y-1)).^.5)*((1-
((1+((y*(((P_oc.*A.*x_p(i))/(m.*a_oc.^2)))).*(G./m)))^(1-y))).*(y-
1)).^.5;
end
vel=v;
v=v.^-1;

%% Plots the Time Approximation from the PnK Solution with Breach
Correction!
z1=plot(x_p,v,'color',[0.625, 0.125, 0.9375]);
xverts = [x_p(1:end-1);x_p(1:end-1);x_p(2:end);x_p(2:end)];
yverts = [zeros(1,length(v)-1);v(1:end-1);v(2:end);zeros(1,length(v)-
1)];
hold on
p = patch(xverts,yverts,'b','LineWidth',1.5);

% The Trapezoidal Rule
Inital_Pressure=psi;
Peak_Velocity=max(vel);
Travel_Time = trapz(x_p(2:end),v(2:end));

% Simpson's Rule
if mod(length(v),2) == 0
    n_length=length(v)-1;
else
    n_length=length(v);
```

```
end

yfirst=v(2);
yevens=0;
for i=1:(n_length/2)-1
yevens=v((i*2)+1)+yevens;
end
yevens=yevens*4;
yodds=0;
for i=1:(n_length/2)
yodds=v((i*2))+yodds;
end
yodds=yodds*2;
ylast=v(n_length);
Travel_Time_2= ((((x_p(end)-
x_p(1))/n_length))/3)*(yfirst+yevens+yodds+ylast);

%  For Velocity Blocks
% 0.75 in
ShortDistBtwPins=0.0195; % m
TwoPinOscopeTime=(1/Peak_Velocity)*ShortDistBtwPins;
% 0.75 in x4
LongDistBtwPins=0.0762;  % m
FourPinOscopeTime=(1/Peak_Velocity)*LongDistBtwPins;
% Sabot Length
SabotLength=l;  % m
SabotOscopeTime=(1/Peak_Velocity)*SabotLength;


%  Add Some Labels and Personal Preferances
xlabel('Distance (m)')
ylabel('Inv-Velocity (m/s)^-1')
box on
grid on
set(gca,'FontSize',18,'FontName','Times');
set(gca,'XMinorTick','on','YMinorTick','on')

%% Output Results To User

fprintf('\nThe Breach Nitrogen Pressure was %4.2f psi\n',psi);
fprintf('The Sabot Mass was %4.4f kg\n',m);
fprintf('The Gas Mass was %4.4f kg\n',G);
fprintf('The Sabot Length was %4.4f m\n',l);
fprintf('From this one can find:\n');
fprintf('     Trapezoidal Rule Sabot Travel Time: %4.2f millisec \n',
Travel_Time*10^3);
fprintf('     Simpsons Rule Sabot Travel Time: %4.2f
millisec\n',Travel_Time_2*10^3);
fprintf('     Estimated Peak Velocity: %4.2f m/s\n',Peak_Velocity);
fprintf('     Light Gate Drop or Rise Event Time: %4.2f
microsec\n',FourPinOscopeTime*10^6)
fprintf('     Sabot Passage Event Time: %4.2f
microsec\n',SabotOscopeTime*10^6)
fprintf('     Total Light Gate Oscope Event Time: %4.2f
microsec\n',(SabotOscopeTime*10^6)+(2*FourPinOscopeTime*10^6))
```

Appendix C: MATLAB Program for Non-dimensional Pressure Velocity Profiles

In this appendix the code for the direct creation of non-dimensional pressure velocity curves (Figure 4.18) and can be easily modified to create dimensional curves (Figure 4.17). As noted before in Appendix B the Z table included for nitrogen and helium are included up to 10,015 psig. This script could be easily updated to include even greater pressures.

```
%% Gas Gun Velocity Calculator
%  Created by Nathaniel Helminiak (2015-2017)
%  Forward Complaints to ---> nathanielhelminiak@yahoo.com
%  Should works for simple gases
%  Uses Ideal Gas Assumption ^
%  Single Stage Gas Gun Variables can be changed.... (Be careful...)


%% The Setup
clc, clear all, close all
hold on

%% Inputs / Variables
%  P_o is Initial Pressure within the Breach (Pa)
P_o=0:10000:6.8948e+7;
%  A is the Interior Barrel Area (m)
A = 0.002025802;
%  x is the Barrel Length (m)
x= 4.2672;
%  m is the projectile mass (kg)
m=.247;
%  Volume 0.0045 m^3
V_o=0.0045;
%Find the Compressibility Factor
%Z=1; To Disregard Compressibility Factor
ZP=linspace(0,10015,51);
ZNitrogen=[1,0.9979,0.9967,0.9964,0.9969,0.9984,1.001,1.004,1.008,1.014,1.02,1.027,1.034,1.043,1.052,
1.062,1.072,1.083,1.095,1.107,1.12,1.133,1.146,1.16,1.174,1.189,1.203,1.218,1.233,1.248,1.264,1.28,1.29
5,1.311,1.327,1.343,1.36,1.376,1.392,1.409,1.425,1.442,1.458,1.475,1.492,1.508,1.525,1.542,1.558,1.575,
1.592];
Z = interp1(ZP,ZNitrogen,P_o/(6.89476e+3));
%  n= PV/RT <-- An Ideal Gas EOS
n=(P_o.*V_o)./(Z*8.3144598.*300);
%  G is mass gas (kg) --> I use Nitrogen 14 gram / mole
G=(14.*n)/1000;
%  SS is the Sound Speed of the Gas (m/s)
SS=349;
%  y is Specific Heat Ratio (-)
y = 1.4;
%  R is the Specific Gas Constant
R=287.058;
```

```
%  T_0 is the Inital Gas Temp (K)
T_0=300;
%  l is the Breach length (m)
l=0.5715;
% Govm is Non-Dim Pressure
Govm=G./m;

%% The Isobaric Simulation
%  Pressure behind the projectile is constant (Overestimate)
v=(2.*P_o.*A.*x./m).^.5;

%  Plots the Isobaric Solution
z1=plot(Govm,v./SS,'color',[1 0 0])
z1(1).LineWidth = 1;


%% Add Some Labels and Personal Preferances
box on
grid on
set(gca,'FontSize',18,'FontName','Times');
set(gca,'XMinorTick','on','YMinorTick','on')
xlabel('Non-dimensional Pressure (G/m)')
ylabel('Non-dimensional Velocity (v_p_r_o_j/a_o)')
%axis([0 10000 0 2000])


%% Isothermal
%  Tempurature of the gas behind the projectile remains constant (Overestimate)
v=((2.*P_o.*V_o.*log((V_o+A.*x)./V_o))/m).^.5;

%  Plots the Isothermal Solution
z1=plot(Govm,v./SS,'color',[0.996078 0.537255 0]);
z1(1).LineWidth = 1;


%% Adiabatic Simulation
%  No change in entropy (Overestimate)
v=((((((P_o.*V_o.^y)./(1-y)).*((V_o+A.*x).^(1-y)))-((P_o*V_o)/(1-y)))*2/m).^.5);

%  Plots the Adiabatic Solution
z1=plot(Govm,v./SS,'y');%'Color',[0.73333 .5333333 0])
z1(1).LineWidth = 4;


%% Strange and Swift Simulation
%  b is the gas co-volume per mole
b=(4.*3.64e-10)*6.022140857*10^-23;
%  Adiabatic solution with Able Gas Equation of State
v=((2.*P_o.*(V_o-n.*b).*(1-(((V_o-n.*b)./(V_o-n.*b+A.*x)).^(y-1))))/((y-1).*m)).^.5;

%  Plots the Strange and Swift Solution
z1=plot(Govm,v./SS,'color',[0 0.392157 0.003922])
z1(1).LineWidth = 1;


%% Lagrange From Analytical and Computational Balistics
```

```
% Lagrange Specific Calculations
lamda=R.*T_0;                          % Lamda
phi=(2./(1-y)).*((((x+l)./(l)).^(1-y))-1);     % units (-)

%  Lagrange Solution
v=(((lamda.*G)./(m+(G./3))).*phi).^.5;        %units of m/s

%  Plots the Larange Solution
z1=plot(Govm,v./SS,'Color',[0 0.490196 0.709804])
z1(1).LineWidth = 1;

%% Pidduck and Kent
% PnK Specific Calculations (Essentially a Lookup Table...)
asquiwga=0:0.001:0.4;
for i=1:length(asquiwga)
fun = @(mu) (1-asquiwga(i).*mu.^2).^(1/(y-1));
GM(i)= (2.*y./(y-1)).*asquiwga(i).*((1-asquiwga(i)).^(-y./(y-1))).*integral(fun,0,1);
end
for i=1:length(G)
asquiwg(i) = interp1(GM,asquiwga,G(i)./m);
end

% PnK Solution Without Breach Correction
for i=1:length(P_o)
P_oc(i)=P_o(i);
a_oc=SS;
v(i)  = 2*a_oc*((asquiwg(i)./(y-1)).^.5)*((1-((1+((y*(((P_oc(i).*A.*x)/(m.*a_oc.^2)))./(G(i)./m)))^(1-
y))).(y-1)).^.5;
end

%  Plots the PnK Solution
z1=plot(Govm,v./a_oc,'color',[0.054902 0.298039 0.631373])
z1(1).LineWidth = 1;


%% Pidduck and Kent with Breach Corrected (The Best)
% PnK Specific Calculations (Essentially a Lookup Table...)
asquiwga=0:0.001:0.99;
for i=1:length(asquiwga)
fun = @(mu) (1-asquiwga(i).*mu.^2).^(1/(y-1));
GM(i)= (2.*y./(y-1)).*asquiwga(i).*((1-asquiwga(i)).^(-y./(y-1))).*integral(fun,0,1);
end
for i=1:length(G)
asquiwg(i) = interp1(GM,asquiwga,G(i)./m);
end

% PnK Solution With Breach Correction
for i=1:length(P_o)
P_oc(i)=P_o(i).*(1+(sqrt((y+1)/2)-1)*(1-(1/2)))^((2*y)/(y-1));
a_oc=SS*(1+((((y+1)/2)^.5)-1)*(1-(1/2)));
v(i)  = 2*a_oc*((asquiwg(i)./(y-1)).^.5)*((1-((1+((y*(((P_oc(i).*A.*x)/(m.*a_oc.^2)))./(G(i)./m)))^(1-
y))).(y-1)).^.5;
end

%  Plots the PnK Solution with Breach Correction!
z1=plot(Govm,v./a_oc,'color',[0.625, 0.125, 0.9375])
```

```
z1(1).LineWidth = 1;


%% Pidduck and Kent Corrected Helium (The Best Again but Different)
% must clear old variables
clc, clear all,
hold on
%  P_o is Initial Pressure within the Breach (Pa)
P_o=0:1000:6.8948e+7;
%  A is the Interior Barrel Area (m)
A = 0.002025802;
%  x is the Barrel Length (m)
x= 4.2672;
%  m is the projectile mass (kg)
m=.247;
%  Volume 0.0045 m^3
V_o=0.0045;
%Find the Compressibility Factor
%Z=1; To Disregard Compressibility Factor
ZP=linspace(0,10015,51);
ZHelium=[1,1.007,1.013,1.02,1.026,1.032,1.039,1.045,1.052,1.058,1.064,1.071,1.077,1.083,1.09,1.096,1.1
02,1.108,1.115,1.121,1.127,1.133,1.139,1.145,1.152,1.158,1.164,1.17,1.176,1.182,1.188,1.194,1.2,1.206,1.
212,1.218,1.224,1.23,1.235,1.241,1.247,1.253,1.259,1.265,1.271,1.276,1.282,1.288,1.294,1.3,1.305];
Z = interp1(ZP,ZHelium,P_o/(6.89476e+3));
%  n= PV/RT <-- An Ideal Gas EOS
n=(P_o.*V_o)./(Z*8.3144598.*300);
%  G is mass gas (kg) --> I use Helium 4 gram / mole
G=(4.*n)/1000;
%  SS is the sound speed of the gas <-pretty important
SS=972;
%  y is specific heat ratio
y = 1.66;
% Govm is Non-Dim Pressure
Govm=G./m;

%  PnK Specific Calculations (Essentially a Lookup Table...)
asquiwga=0:0.001:0.99;
for i=1:length(asquiwga)
fun = @(mu) (1-asquiwga(i).*mu.^2).^(1/(y-1));
GM(i)= (2.*y./(y-1)).*asquiwga(i).*((1-asquiwga(i)).^(-y./(y-1))).*integral(fun,0,1);
end
%plot(GM,(asquiwga./(y-1)).^.5)
for i=1:length(G)
asquiwg(i) = interp1(GM,asquiwga,G(i)./m);
end

% PnK Solution With Breach Correction
for i=1:length(P_o)
P_oc(i)=P_o(i).*(1+(sqrt((y+1)/2)-1)*(1-(1/2)))^((2*y)/(y-1));
a_oc=SS*(1+((((y+1)/2)^.5)-1)*(1-(1/2)));
v(i)  = 2*a_oc*((asquiwg(i)./(y-1)).^.5)*((1-((1+((y*(((P_oc(i).*A.*x)/(m.*a_oc.^2)))))./(G(i)./m)))^(1-
y))./(y-1)).^.5;
end

%  Plots the PnK Solution with Breach Correction!
z1=plot(Govm,(v./a_oc),'color',[0.466667 0.30961 0])
```

```
%approx 1.3
z1(1).LineWidth = 1;


%% Experimental Data

%Data Point 1 Early Polycarb Shot?
clear Govm P_o n G
%  P_o is Initial Pressure within the Breach (Pa)
P_o=[600].*6.89476e+3;
%  A is the Interior Barrel Area (m)
A = 0.002025802;
%  x is the Barrel Length (m)
x= 4.2672;
%  m is the projectile mass (kg)
m=.247;
%  Volume 0.0045 m^3
V_o=0.0045;
%Find the Compressibility Factor
%Z=1; To Disregard Compressibility Factor
ZP=linspace(0,10015,51);
ZNitrogen=[1,0.9979,0.9967,0.9964,0.9969,0.9984,1.001,1.004,1.008,1.014,1.02,1.027,1.034,1.043,1.052,
1.062,1.072,1.083,1.095,1.107,1.12,1.133,1.146,1.16,1.174,1.189,1.203,1.218,1.233,1.248,1.264,1.28,1.29
5,1.311,1.327,1.343,1.36,1.376,1.392,1.409,1.425,1.442,1.458,1.475,1.492,1.508,1.525,1.542,1.558,1.575,
1.592];
Z = interp1(ZP,ZNitrogen,P_o/(6.89476e+3));
%  n= PV/RT <-- An Ideal Gas EOS
n=(P_o.*V_o)./(Z*8.3144598.*300);
%  G is mass gas (kg) --> I use Nitrogen 14 gram / mole
G=(14.*n)/1000;
%  SS is the Sound Speed of the Gas (m/s)
SS=349;
%  y is Specific Heat Ratio (-)
y = 1.4;
%  R is the Specific Gas Constant
R=287.058;
%  T_0 is the Inital Gas Temp (K)
T_0=300;
%  l is the Breach length (m)
l=0.5715;
% Govm is Non-Dim Pressure
Govm(1)=G./m;

%Data Point 2 5_3_2017
clear P_o n G
%  P_o is Initial Pressure within the Breach (Pa)
P_o=[400].*6.89476e+3;
%  A is the Interior Barrel Area (m)
A = 0.002025802;
%  x is the Barrel Length (m)
x= 4.2672;
%  m is the projectile mass (kg)
m=.4322;
%  Volume 0.0045 m^3
V_o=0.0045;
%Find the Compressibility Factor
```

```
%Z=1; To Disregard Compressibility Factor
ZP=linspace(0,10015,51);
ZNitrogen=[1,0.9979,0.9967,0.9964,0.9969,0.9984,1.001,1.004,1.008,1.014,1.02,1.027,1.034,1.043,1.052,
1.062,1.072,1.083,1.095,1.107,1.12,1.133,1.146,1.16,1.174,1.189,1.203,1.218,1.233,1.248,1.264,1.28,1.29
5,1.311,1.327,1.343,1.36,1.376,1.392,1.409,1.425,1.442,1.458,1.475,1.492,1.508,1.525,1.542,1.558,1.575,
1.592];
Z = interp1(ZP,ZNitrogen,P_o/(6.89476e+3));
%  n= PV/RT <-- An Ideal Gas EOS
n=(P_o.*V_o)./(Z*8.3144598.*300);
%  G is mass gas (kg) --> I use Nitrogen 14 gram / mole
G=(14.*n)/1000;
%  SS is the Sound Speed of the Gas (m/s)
SS=349;
%  y is Specific Heat Ratio (-)
y = 1.4;
%  R is the Specific Gas Constant
R=287.058;
%  T_0 is the Inital Gas Temp (K)
T_0=300;
%  l is the Breach length (m)
l=0.5715;
% Govm is Non-Dim Pressure
Govm(2)=G./m;



%Data Point 3 5_10_2017
clear P_o n G
%  P_o is Initial Pressure within the Breach (Pa)
P_o=[400].*6.89476e+3;
%  A is the Interior Barrel Area (m)
A = 0.002025802;
%  x is the Barrel Length (m)
x= 4.2672;
%  m is the projectile mass (kg)
m=.6538;
%  Volume 0.0045 m^3
V_o=0.0045;
%Find the Compressibility Factor
%Z=1; To Disregard Compressibility Factor
ZP=linspace(0,10015,51);
ZNitrogen=[1,0.9979,0.9967,0.9964,0.9969,0.9984,1.001,1.004,1.008,1.014,1.02,1.027,1.034,1.043,1.052,
1.062,1.072,1.083,1.095,1.107,1.12,1.133,1.146,1.16,1.174,1.189,1.203,1.218,1.233,1.248,1.264,1.28,1.29
5,1.311,1.327,1.343,1.36,1.376,1.392,1.409,1.425,1.442,1.458,1.475,1.492,1.508,1.525,1.542,1.558,1.575,
1.592];
Z = interp1(ZP,ZNitrogen,P_o/(6.89476e+3));
%  n= PV/RT <-- An Ideal Gas EOS
n=(P_o.*V_o)./(Z*8.3144598.*300);
%  G is mass gas (kg) --> I use Nitrogen 14 gram / mole
G=(14.*n)/1000;
%  SS is the Sound Speed of the Gas (m/s)
SS=349;
%  y is Specific Heat Ratio (-)
y = 1.4;
%  R is the Specific Gas Constant
R=287.058;
```

```
%  T_0 is the Inital Gas Temp (K)
T_0=300;
%  l is the Breach length (m)
l=0.5715;
% Govm is Non-Dim Pressure
Govm(3)=G./m;


%hold on
ExperiemtnalBreachPressure=[Govm(1),Govm(2),Govm(3)];
ExperimentalPeakVelocity=[280./SS, 193.78./SS ,152./SS];
plot(ExperiemtnalBreachPressure,ExperimentalPeakVelocity,'k.','MarkerSize',15);


%% Legend
legend('Isobaric','Isothermal','Adiabatic','Strange and Swift','Lagrange','Pidduck and Kent','P&K with
Breach Correction','P&Kw/B-C For Helium','Data')
```

Appendix D: MATLAB Program for Agilent 602s Vacuum Curves

Matlab code within this section recreates vacuum pull down curves seen in Figure 4.14. This is useful for anticipating total pull down time to a desired final pressure, determining the behavior of vacuum pumps and a tool with which to diagnose the severity of leaks. Users should be able to modify the input section to match systems other than Marquette's vacuum system for pressures below atmospheric pressure though the Aglient 602s pump curve would need to be replaced with the desired vacuum pump.

```
%% Combined Vaccum Model Calculator
%  Created by Nathaniel Helminiak (2015-2017)
%  Forward Complaints to ---> nathanielhelminiak@yahoo.com
%  Based of the vacuum operation theory of Yasuhiko Senda
%  Assumes vacuum to operate in the viscous flow regime
%  until a transfering pressure is reached
%  after which the flow moves toward molecular operation.
%  Uses a pump curve fit from an Agilent DS602 Vacuum pump

%% The Setup
clc, clear all, close all

%% Inputs / Variables

% Inital Pressure
PresPai=101300; %Pa

%Leak Rate
LeakRate=0.005; %Pa/Sec Note Time Step!!!

% Simulation Run Time
TotalTime=100000; % Sec

% Length from the pump to the end of the pressure vessel
L=7; %m

% Smallest Hose Diameter to Vacuum Pump
D=0.028; %0.0381;          % m

% Volume of the System
V=2500;                    % L

%% Constants (Not Variable Yet)

% Time Step
TimeStep=1; % Sec

%PFinalA=10
```

```
%P_trans=1


%% Calculates Viscous Flow No Leaks (SavePres)
PresPa=PresPai; %Pa
for i=1:TimeStep:TotalTime
   SavePres1(i)=PresPa;
   Pres=PresPa.*0.01; %mbar
   if Pres>=100
   pumpspeed=27;
   elseif Pres>=0.012
   pumpspeed=1761.*exp(-0.015.*((-
0.0000003).*(86.73.*log(Pres)+733.24).^3+0.0008.*(86.73.*log(Pres)+733.24).^2-
0.7406.*(86.73.*log(Pres)+733.24)+520.09));
   elseif Pres<0
   pumpspeed=0;
   else
   pumpspeed=1761.*exp(-0.015.*(0.0079.*(86.73.*log(Pres)+733.24).^2-
6.264.*(86.73.*log(Pres)+733.24)+1565.5));
   end
   if pumpspeed>25
      pumpspeed=25;
   end
   savepumpspeed1(i)=pumpspeed; %pumpspeed m^3/hr

Po=PresPa;                % Pa
So=(1000./60).*pumpspeed*1.25; %*.14;% L/min
Cc=((1349.*(D.^4))./L);       % m^3
Pi=((So)./Cc);             %
Tau=(V./So);               %min
Po2=Po;                   %Pa
L2=L;                     %m
D2=D;                     %m
V2=V.*0.001;              %m^3
So2=So.*0.001./60;         %
Cc2=(1349.*(D2.^4))./L2;    %
P_trans=So2/Cc2;           %
Pi2=((So2)./Cc2);          %
Tau2=(V2./So2);            %
PFinalA=Po.*exp(-TimeStep./(Tau2));     %exponential
PFinalB=(2.*Pi2.*Tau2)./i;             %inverseproportinal
if PFinalA>P_trans
   PresPa=PFinalA;
else
   PresPa=PFinalA;
end
   PresPa=PresPa; %+0.01; %0.0188;
end

%% Calculates Real Flow No Leaks  (SavePres 2)

PresPa=PresPai;
for i=1:TimeStep:TotalTime
   SavePres2(i)=PresPa;
   Pres=PresPa.*0.01; %mbar
   if Pres>=100
```

```
   pumpspeed=27;
   elseif Pres>=0.012
   pumpspeed=1761.*exp(-0.015.*((-
0.0000003).*(86.73.*log(Pres)+733.24).^3+0.0008.*(86.73.*log(Pres)+733.24).^2-
0.7406.*(86.73.*log(Pres)+733.24)+520.09));
   elseif Pres<0
   pumpspeed=0;
   else
   pumpspeed=1761.*exp(-0.015.*(0.0079.*(86.73.*log(Pres)+733.24).^2-
6.264.*(86.73.*log(Pres)+733.24)+1565.5));
   end
   if pumpspeed>25
      pumpspeed=25;
   end
   savepumpspeed2(i)=pumpspeed; %pumpspeed m^3/hr

Po=PresPa;                % Pa
So=(1000./60).*pumpspeed*1.25; %*.14;% L/min
Cc=((1349.*(D.^4))./L);       % m^3
Pi=((So)./Cc);              %
Tau=(V./So);                %min
Po2=Po;                    %Pa
L2=L;                     %m
D2=D;                      %m
V2=V.*0.001;                %m^3
So2=So.*0.001./60;          %
Cc2=(1349.*(D2.^4))./L2;    %
P_trans=So2/Cc2;
Pi2=((So2)./Cc2);           %
Tau2=(V2./So2);             %
PFinalA=Po.*exp(-TimeStep./(Tau2));     %exponential
PFinalB=(2.*Pi2.*Tau2)./i;
if PFinalA>P_trans
   PresPa=PFinalA;                  %exponential
else
   PresPa=PFinalB;                 %inverseproportinal
end
   PresPa=PresPa; %+0.01; %0.0188;
end

%% Calculates Real Flow With Leaks  (SavePres4)

PresPa=PresPai;
for i=1:TimeStep:TotalTime
   SavePres3(i)=PresPa;
   Pres=PresPa.*0.01; %mbar
   if Pres>=100
   pumpspeed=27;
   elseif Pres>=0.012
   pumpspeed=1761.*exp(-0.015.*((-
0.0000003).*(86.73.*log(Pres)+733.24).^3+0.0008.*(86.73.*log(Pres)+733.24).^2-
0.7406.*(86.73.*log(Pres)+733.24)+520.09));
   elseif Pres<0
   pumpspeed=0;
   else
```

```
    pumpspeed=1761.*exp(-0.015.*(0.0079.*(86.73.*log(Pres)+733.24).^2-
6.264.*(86.73.*log(Pres)+733.24)+1565.5));
    end
    if pumpspeed>25
        pumpspeed=25;
    end
    savepumpspeed3(i)=pumpspeed; %pumpspeed m^3/hr

Po=PresPa;                  % Pa
So=(1000./60).*pumpspeed*1.25; %*.14;% L/min
Cc=((1349.*(D.^4))./L);       % m^3
Pi=((So)./Cc);              %
Tau=(V./So);                %min
Po2=Po;                     %Pa
L2=L;                       %m
D2=D;                       %m
V2=V.*0.001;                %m^3
So2=So.*0.001./60;          %
Cc2=(1349.*(D2.^4))./L2;    %
P_trans=So2/Cc2;
Pi2=((So2)./Cc2);           %
Tau2=(V2./So2);             %
PFinalA=Po.*exp(-TimeStep./(Tau2));     %exponential
    PresPa=PFinalA;                     %exponential
    PresPa=PresPa+LeakRate;
end

%% Imports Data
% Rough Low Pressure
RTime=[1,27.285,39.085,48.552,60.819,72.819,87.552,101.485,117.119,132.485,149.066,166.019,186.585
,206.819,228.865,252.419,280.22,304.819,341.757,395.985,434.02,478.219,552.998,639.753,793.119,104
5.659];
RPres=[101300,84368.05,80981.66,77595.27,74208.88,70822.49,67436.1,64049.71,60663.32,57276.93,53
890.54,50504.15,47117.76,43731.37,40344.98,36958.59,33572.2,30185.81,26799.42,23413.03,20026.64,1
6640.25,13253.86,9867.47,6481.08,3094.69];
% Medium Low Pressure
RPreslow=[266.510678,259.977900,246.645700,239.979600,226.647400,219.981300,213.315200,207.982
320,199.983000,191.983680,183.984360,175.985040,173.318600,162.652840,155.986740,151.987080,14
7.987420,142.654540,137.321660,133.322000];
RTimelow=1800:10:(1790+10*(length(RPreslow)));
MRPreslowdata=tdfread('morevacdata.txt');
MRPreslow=MRPreslowdata.x1320x2E917042(:)';
MRTimelow=[1990.05:0.5:(1990.5+0.5*(length(MRPreslow)-1))];

%% Sorting Data Into Plottable Sections

% Defining Time
Time=1:TimeStep:TotalTime;

% Clipping The Molecular Flow Data
for i=1:length(SavePres2)
    if SavePres2(i)<P_trans
    SavePres2num(i)=1;
    else
    SavePres2num(i)=0;
    end
```

```
end
count=1;
for i=1:length(SavePres2num)
   if SavePres2num(i) == 1
      Timenew2(count)=Time(i);
      SavePres2new(count)=SavePres2(i);
      count=count+1;
   else
   end
end


% Clipping The Leak Limit Data
for i=1:length(SavePres2)
   if SavePres3(i)>SavePres2(i)
      if Time(i)>10^4
   SavePres3num(i)=1;
      end
   else
   SavePres3num(i)=0;
   end
end
count=1;
for i=1:length(SavePres3num)
   if SavePres3num(i) == 1
      Timenew3(count)=Time(i);
      SavePres3new(count)=SavePres3(i);
      count=count+1;
   else
   end
end


%% Plot Data for the System Pressure
fig=figure;
left_color = [0 0 0];
right_color = [0 0 0];
set(fig,'defaultAxesColorOrder',[left_color; right_color]);
subplot(2,1,1);

% This is the viscous flow solution
loglog(Time,SavePres1,'r','LineWidth',2);
hold on

% This is the molecular flow solution
loglog(Timenew2,SavePres2new,'g','LineWidth',2);

% This is just real flow solution
loglog(Timenew3,SavePres3new,'b','LineWidth',2);

% This is the transferring pressure
loglog([min(Time) max(Time)],[P_trans, P_trans],'Color',[0.5 0.5 0.5],'LineWidth',1);

% This is the experimental data
loglog(RTime,RPres,'sk','MarkerSize',6,'MarkerFaceColor','k');
loglog(RTimelow,RPreslow,'k.','MarkerSize',12);
```

```
loglog(MRTimelow,MRPreslow,'k.','MarkerSize',12);

% Formating
axis([1 10^5 10^-1 10^6])
grid on
set(gca,'FontSize',12,'FontName','Times');
set(gca,'XMinorTick','on','YMinorTick','on')
xlabel('Pumping Time (Sec)')
ylabel('Pressure (Pa)')
legend('Viscous Flow','Molecular Flow','Leak Limit','Transferring Pressure','High Pressure Data','Low
Pressure Data')
set(gca, 'YTick', [10.^0 10.^1 10.^2 10.^3 10.^4 10.^5 10.^6 10.^7 10.^8 10.^9 10.^10])

%Secondary Axis
yyaxis right
loglog(-1:-10,-1:-10)
yyaxis right
axis([1 10^5 (10^-1)*(0.00750062)*1000 (10^6)*(0.00750062)*1000])
set(gca, 'YScale', 'log')
ylabel('mTorr')

%% Plot Data for the Pumping Speed
subplot(2,1,2);

% This is the viscous flow solution
z4=loglog(Time,savepumpspeed1,'r','LineWidth',2);
hold on

% This is the molecular flow solution
z5=loglog(Time,savepumpspeed2,'g','LineWidth',2);

% This is just real flow solution
z6=loglog(Time,savepumpspeed3,'b','LineWidth',2);

% Formating
axis([1 10^5 0 30])
legend([z4 z5 z6],'Viscous Pump Speed','Molecular Pump Speed','Real Pump Speed','location','SouthWest')
box on
grid on
set(gca,'FontSize',12,'FontName','Times');
set(gca,'XMinorTick','on','YMinorTick','on')
xlabel('Pumping Time (Sec)')
ylabel('Effective Pumping Speed (m^3/hr)')
```

Appendix E: MATLAB Program for Light Gate Interpretation Single .csv file

Using the script included below users should be able to use light gate output data from a single oscilloscope .csv file to find projectile velocity and create a plot similar to Figure 2.44. It has been noted by the author that on some occasions oscilloscopes will output multiple csv files, one for each channel. Users will need to modify the script in this case.

```
%% Light Gate Velocity Calculator
%  Created by Nathaniel Helminiak (2015-2017)
%  Forward Complaints to ---> nathanielhelminiak@yahoo.com


%% The Setup
clc, clear all, close all
hold on

%% Input User Variables.
filename = '5_3_lg.csv';
delimiter = ',';
GapADist = 0.75; %inches
GapBDist = 0.75; %inches
GapCDist = 0.75; %inches

%% Read columns of data as strings:
% For more information, see the TEXTSCAN documentation.
formatSpec = '%q%q%q%q%q%q%[^\\n\r]';

%% Open the text file.
fileID = fopen(filename,'r');

%% Read columns of data according to format string.
% This call is based on the structure of the file used to generate this
% code. If an error occurs for a different file, try regenerating the code
% from the Import Tool.
dataArray = textscan(fileID, formatSpec, 'Delimiter', delimiter,  'ReturnOnError', false);

%% Close the text file.
fclose(fileID);

%% Convert the contents of columns containing numeric strings to numbers.
% Replace non-numeric strings with NaN.
raw = repmat({''},length(dataArray{1}),length(dataArray)-1);
for col=1:length(dataArray)-1
    raw(1:length(dataArray{col}),col) = dataArray{col};
end
numericData = NaN(size(dataArray{1},1),size(dataArray,2));

% Converts strings in the input cell array to numbers. Replaced non-numeric
```

```
% strings with NaN.
rawData = dataArray{1};
for row=1:size(rawData, 1);
    % Create a regular expression to detect and remove non-numeric prefixes and
    % suffixes.
    regexstr = '(?<prefix>.*?)(?<numbers>([-]*(\d+[\,]*)+[\.]{0,1}\d*[eEdD]{0,1}[-+]*\d*[i]{0,1})|([-
]*(\d+[\,]*)*[\.]{1,1}\d+[eEdD]{0,1}[-+]*\d*[i]{0,1}))(?<suffix>.*)';
    try
        result = regexp(rawData{row}, regexstr, 'names');
        numbers = result.numbers;

        % Detected commas in non-thousand locations.
        invalidThousandsSeparator = false;
        if any(numbers==',');
            thousandsRegExp = '^\d+?(\,\d{3})*\.{0,1}\d*$';
            if isempty(regexp(numbers, thousandsRegExp, 'once'));
                numbers = NaN;
                invalidThousandsSeparator = true;
            end
        end
        % Convert numeric strings to numbers.
        if ~invalidThousandsSeparator;
            numbers = textscan(strrep(numbers, ',', ''), '%f');
            numericData(row, 1) = numbers{1};
            raw{row, 1} = numbers{1};
        end
    catch me
    end
end


%% Split data into numeric and cell columns.
rawNumericColumns = raw(:, 1);
rawCellColumns = raw(:, [2,3,4,5]);


%% Replace non-numeric cells with NaN
R = cellfun(@(x) ~isnumeric(x) && ~islogical(x),rawNumericColumns); % Find non-numeric cells
rawNumericColumns(R) = {NaN}; % Replace non-numeric cells

%% Allocate imported array to column variable names
second1 = cell2mat(rawNumericColumns(:, 1));
Volt = rawCellColumns(:, 1);
Volt1 = rawCellColumns(:, 2);
Volt2 = rawCellColumns(:, 3);
Volt3 = rawCellColumns(:, 4);


%% Clear temporary variables
clearvars filename delimiter formatSpec fileID dataArray ans raw col numericData rawData row regexstr
result numbers invalidThousandsSeparator thousandsRegExp me rawNumericColumns rawCellColumns R;

%% Convert Data To Doubles
Volt(1,1)={''};
Volt(2,1)={''};
Volt1(1,1)={''};
```

```
Volt1(2,1)={''};
Volt2(1,1)={''};
Volt2(2,1)={''};
Volt3(1,1)={''};
Volt3(2,1)={''};
Time      = second1;
Volt1data = str2double(Volt);
Volt2data = str2double(Volt1);
Volt3data = str2double(Volt2);
Volt4data = str2double(Volt3);

%% Find when the Tip of the Projectile Arrives and Leaves

Thresholda=.9
Thresholdb=.1

Volt1Peak=max(Volt1data(1:2000));
Volt2Peak=max(Volt2data(1:2000));
Volt3Peak=max(Volt3data(1:2000));
Volt4Peak=max(Volt4data(1:2000));

SearchVolt1a=Volt1Peak*Thresholda;
SearchVolt2a=Volt2Peak*Thresholda;
SearchVolt3a=Volt3Peak*Thresholda;
SearchVolt4a=Volt4Peak*Thresholda;

SearchVolt1b=Volt1Peak*Thresholdb;
SearchVolt2b=Volt2Peak*Thresholdb;
SearchVolt3b=Volt3Peak*Thresholdb;
SearchVolt4b=Volt4Peak*Thresholdb;

% Voltage Drops
for i= 1:length(Volt1data)
   if Volt1data(i)<SearchVolt1a
      ArrivalTime1=Time(i);
      SaveDrop1=i;
      break
   end
end

for i= 1:length(Volt2data)
   if Volt2data(i)<SearchVolt2a
      ArrivalTime2=Time(i);
      SaveDrop2=i;
      break
   end
end

for i= 1:length(Volt3data)
   if Volt3data(i)<SearchVolt3a
      ArrivalTime3=Time(i);
      SaveDrop3=i;
      break
   end
end
```

```
for i= 1:length(Volt4data)
   if Volt4data(i)<SearchVolt4a
      ArrivalTime4=Time(i);
      SaveDrop4=i;
      break
   end
end

% Voltage Rises

V1Zero=SaveDrop1+(SaveDrop2-SaveDrop1);
for i= V1Zero:length(Volt1data)
   if Volt1data(i)>SearchVolt1b
      ExitTime1=Time(i);
      break
   end
end

V2Zero=SaveDrop2+(SaveDrop2-SaveDrop1);
for i= V2Zero:length(Volt2data)
   if Volt2data(i)>SearchVolt2b
      ExitTime2=Time(i);
      break
   end
end

V3Zero=SaveDrop3+(SaveDrop2-SaveDrop1);
for i= V3Zero:length(Volt3data)
   if Volt3data(i)>SearchVolt3b
      ExitTime3=Time(i);
      break
   end
end

V4Zero=SaveDrop4+(SaveDrop2-SaveDrop1);
for i= V4Zero:length(Volt4data)
   if Volt4data(i)>SearchVolt4b
      ExitTime4=Time(i);
      break
   end
end


%% Find the Start and End of Data

for i= 1:length(Volt1data)
   if Volt1data(i)>0
      StartTime1=Time(i);
      break
   end
end

for i= 1:length(Volt1data)
   j=length(Volt1data)-i;
   if Volt1data(j)>0
      EndTime1=Time(j);
```

```
        break
    end
end

%% Creates Plot Markers for Arrival Time

maxvoltage=int16(max([Volt1Peak,Volt2Peak,Volt3Peak,Volt4Peak]))+.99;
minvoltage=-int16(abs(min([Volt1Peak,Volt2Peak,Volt3Peak,Volt4Peak])))+.01;
%% Plots Data
plot(Time*10^6,Volt1data/Volt1Peak,'color',[1 0 0]);
hold on
plot(Time*10^6,Volt2data/Volt2Peak,'color',[0.996078 0.537255 0]);
plot(Time*10^6,Volt3data/Volt3Peak,'color',[0 0.392157 0.003922])
plot(Time*10^6,Volt4data/Volt4Peak,'b')
plot([ArrivalTime1*10^6,ArrivalTime1*10^6],[-.2,1.2],'k-');
plot([ExitTime1*10^6,ExitTime1*10^6],[-.2,1.2],'k--');
plot([ArrivalTime2*10^6,ArrivalTime2*10^6],[-.2,1.2],'k-');
plot([ExitTime2*10^6,ExitTime2*10^6],[-.2,1.2],'k--');
plot([ArrivalTime3*10^6,ArrivalTime3*10^6],[-.2,1.2],'k-');
plot([ExitTime3*10^6,ExitTime3*10^6],[-.2,1.2],'k--');
plot([ArrivalTime4*10^6,ArrivalTime4*10^6],[-.2,1.2],'k-');
plot([ExitTime4*10^6,ExitTime4*10^6],[-.2,1.2],'k--');

%% Add Some Labels and Personal Preferances
box on
grid on
set(gca,'FontSize',18,'FontName','Times');
set(gca,'XMinorTick','on','YMinorTick','on');
xlabel('Time (\mus)');
ylabel('Normalized Voltage (V/V_m_a_x)');
xmin=StartTime1*10^6;
xmax=double((int16(EndTime1*10^6)/(10^(numel(num2str(int16(EndTime1*10^6)))-
1)))*(10^(numel(num2str(int16(EndTime1*10^6)))-1)));
ymin=-.2;
ymax=1.2;
stuff=[xmin,xmax,ymin,ymax];
axis(stuff);
legend('Pin 1','Pin 2','Pin 3','Pin 4','Arrival','Exit');
%% Calculates the Velocity

GapATime=ArrivalTime2-ArrivalTime1; % sec
GapBTime=ArrivalTime3-ArrivalTime2; % sec
GapCTime=ArrivalTime4-ArrivalTime3; % sec

GapADistm = (GapADist*2.54)/100; %m
GapBDistm = (GapBDist*2.54)/100; %m
GapCDistm = (GapCDist*2.54)/100; %m

VelocityA = GapADistm/GapATime; %m/s
VelocityB = GapBDistm/GapBTime; %m/s
VelocityC = GapCDistm/GapCTime; %m/s

TimeLength1=ExitTime1-ArrivalTime1;
TimeLength2=ExitTime2-ArrivalTime2;
TimeLength3=ExitTime3-ArrivalTime3;
TimeLength4=ExitTime4-ArrivalTime4;
```

```
VeloAvg = (VelocityA+VelocityB+VelocityC)/3, %m/s
SabotLength1=VeloAvg*TimeLength1, %m
SabotLength2=VeloAvg*TimeLength2, %m
SabotLength3=VeloAvg*TimeLength3, %m
SabotLength4=VeloAvg*TimeLength4, %m
```

Appendix F: MATLAB Program for PDV Interpretation

The following is a simple sliding FFT PDV script which takes a beat frequency and sample frequency to create a graph similar to Figure 2.54. This is a raw output showcasing user selected percentages of data where the author has selected the top 0.5, 2.5, and 100 percent of sampled velocity data. While this script should allow users a quick method with which to process PDV data sets of filters and post processors will likely be needed to extract the desired velocity profiles from noise in the data set.

```
%% Sliding FFT PDV Calculator
%  Created by Nathaniel Helminiak (2015-2017)
%  Forward Complaints to ---> nathanielhelminiak@yahoo.com
%  Calculates the velocity based on the known beat frequency of a signal.
%  Will find the measured velocity as a function of time for PDV Data.
%  This Function chooses the highest likely velocity measurement.
%  A future update would be to include the range of likely velocities,
%  though this would take a longer calculation time.


%% The Setup
clc, close all

% This can save time when reanaylsing
clearvars -except PDV_Data


%% Inputs / Variables

% Imports the Shot Data
fprintf('Loading Data');
%May wish to comment the line below after first run
%PDV_Data = csvread('ConicalPDV_050317.csv');

% Beat Frequency
% Note the input "beat" frequency be time dependant
% over long duration experiments
Target_Wavelength = 1550.001*10^-9;

% Split the domain into x samples in time
Split_into_n_samples=2000;

% Choose the channel to anaylize
ChannelNumber=3;
% Sorts Data
Time     = PDV_Data(:,1);
Channel1 = PDV_Data(:,ChannelNumber);
```

```
% Choose a beat channel to sample
BeatChannelNumber=4;
% Split the beat domain into x samples in time
BeatSplit_into_n_samples=2000;
% Stop after the first x samples
StopBeat=10;
% Sorts Data
BeatChannel1 = PDV_Data(:,BeatChannelNumber);


% Plotting Selectiviness (High, Medium Low) Percent
HSelect=0.5;
MSelect=2.5;
LSelect=100;

%FFT Controls
% Number of Bins
n = 15;

% Sampling Frequency
Fs = (((Time(length(Time))-Time(1))/length(Time))^-1); %/ChannelsUsed
%Fs = 2.5*10^9;

%% Calculate the Beat Reprocusions from Choices

BeatNum=BeatSplit_into_n_samples;
BeatData = BeatChannel1;
BeatSectionedData=round(length(BeatChannel1)/BeatNum);

%% Beat FFT Stuff
for i=0:StopBeat
i,
%PercentComplete=((i/(Num-1))*100),
Tempsamples=BeatSectionedData*(i)+1:1:BeatSectionedData*(i+1)-1;
TempData=BeatData(Tempsamples,1);
% Bin Size Creator (Must be a power of 2)
N=2^n;
% Finds the residual of a linear fit
Y = detrend(TempData);
% Performs the FFT
Y_1 = fft(Y,N);
% Perform Data For Plots
P2 = abs(Y_1/N);        % Take absolute values to get rid of imaginary
P1 = P2(1:(N/2+1));
P1 = P1*2;
% Find Length/Set Frequency Vector
f = Fs*(0:(length(Y_1))/2)/length(Y_1);
[OrderedFreq ListHightoLow] = sort(P1,'descend');
SAVEHIGHESTBEAT(i+1)=f(ListHightoLow(1));
end

%% Calculate the Reprocusions from Choices

Num=Split_into_n_samples;
Data = Channel1;
```

```
SectionedData=round(length(Channel1)/Num);
Timeperstep=((Time(length(Time))-Time(1))/length(Time))*SectionedData;


%% FFT Stuff
for i=0:Num-1
i,
%PercentComplete=((i/(Num-1))*100),
Tempsamples=SectionedData*(i)+1:1:SectionedData*(i+1)-1;
TempData=Data(Tempsamples,1);
% Bin Size Creator (Must be a power of 2)
N=2^n;
% Finds the residual of a linear fit
Y = detrend(TempData);
% Performs the FFT
Y_1 = fft(Y,N);
% Perform Data For Plots
P2 = abs(Y_1/N);        % Take absolute values to get rid of imaginary
P1 = P2(1:(N/2+1));
P1 = P1*2;
% Find Length/Set Frequency Vector
f = Fs*(0:(length(Y_1))/2)/length(Y_1);
[OrderedFreq ListHightoLow] = sort(P1,'descend');
  for j=1:length(OrderedFreq)
  SAVEHIGHEST(i+1,j)=f(ListHightoLow(j));
  end
end

%% Plotting The Histogram Found
%Show Frequencies found
%plot(f,P1),

TimeTotal=Timeperstep*10^6:Timeperstep*10^6:(Num)*Timeperstep*10^6;
%Plot velocites found with respect to time

for i=1:int16(Split_into_n_samples*LSelect*0.01)
PDV_vel = (SAVEHIGHEST(:,i)-mean(SAVEHIGHESTBEAT)).*(Target_Wavelength./2);
z3=plot(TimeTotal,PDV_vel,'k.','MarkerSize',10);%,TimeTotal,PDV_vel2)
hold on
end
for i=1:int16(Split_into_n_samples*MSelect*0.01)
PDV_vel = (SAVEHIGHEST(:,i)-mean(SAVEHIGHESTBEAT)).*(Target_Wavelength./2);
z2=plot(TimeTotal,PDV_vel,'b.','MarkerSize',10);%,TimeTotal,PDV_vel2)
end
for i=1:int16(Split_into_n_samples*HSelect*0.01)
PDV_vel = (SAVEHIGHEST(:,i)-mean(SAVEHIGHESTBEAT)).*(Target_Wavelength./2);
z1=plot(TimeTotal,PDV_vel,'r.','MarkerSize',10);%,TimeTotal,PDV_vel2)
end
%PDV_vel = (SAVEHIGHEST-Input_Frequency).*(Input_Frequency./2);
%PDV_vel2 = (SAVE2ndHIGHEST-mean(SAVEHIGHESTBEAT)).*(Input_Frequency./2);



%% Add Some Labels and Personal Preferances
box on
```

```
grid on
set(gca,'FontSize',18,'FontName','Times');
set(gca,'XMinorTick','on','YMinorTick','on')
xlabel('Time ({\mu}s)');
ylabel('Velocity (m/s)');
legend([z1,z2,z3],sprintf('Top %2.2f Percent of Data',HSelect),sprintf('Top %2.2f Percent of
Data',MSelect),sprintf('Top %2.2f Percent of Data',LSelect),'location','NorthWest')

%% Output Results To User
fprintf('\nYou Analyzed Channel %4.0f\n',ChannelNumber);
fprintf('With a Beat Frequency of %4.2f nm\n',Target_Wavelength*10^9);
fprintf('Detected Steady Frequency of %4.2f nm \n',mean(SAVEHIGHESTBEAT)*10^-9);
fprintf('and a Sampling Frequency of %4.2f ns^-1 \n',Fs*10^-9);
```

Appendix G: MATLAB Program for Burst Disk Selection

The following script requires knowledge of upper and lower burst pressures for high and low pressure disks within a dual diaphragm system as well as a set of safety factors with which to treat these apparent burst pressures (three have been suggested by the author). With these parameters Figure 4.6 is created giving experiment designers a range of pressures at which a pair of burst disks can safely be controlled.

```
%% Burst Disk Calculator
%  Created by Nathaniel Helminiak (2015-2017)
%  Forward Complaints to ---> nathanielhelminiak@yahoo.com
%  Gives the safe operational use for given burst disk configurations

%% The Setup
clc, clear all, close all
hold on

%% Inputs / Variables

% Over Pressure FOS
O=0.2;
% Under Pressure FOS
U=0.8;
% Small Chamber FOS
SC=0.85;

% Low Pressure Burst Disk
% Minimum Burst Pressure
LPresBurstmin = 1297;
% Maximum Burst Pressure
LPresBurstmax = 1779;
% Average Burst Pressure
LPresBurstavg = (LPresBurstmin+LPresBurstmax)/2;

% Alternate Low Pressure Burst Disk
% Minimum Burst Pressure
APresBurstmin = 1000;
% Maximum Burst Pressure
APresBurstmax = 1000;
% Average Burst Pressure
APresBurstavg  = (APresBurstmin+APresBurstmax)/2;

% High Pressure Burst Disk
% Minimum Burst Pressure
HPresBurstmin = 1297;
% Maximum Burst Pressure
HPresBurstmax = 1779;
% Average Burst Pressure
HPresBurstavg  = (HPresBurstmin+HPresBurstmax)/2;
```

```
%% Calculate the Small Chamber Set Pressure
% Caclulates the  upper bound small chamber pressure
SmallChamberPresmax=SC*LPresBurstmin;

% Caclulates the  upper bound alternate small chamber pressure
ASmallChamberPresmax=SC*APresBurstmin;

%%  Calculate the Large Chamber Set Pressure
% Calculates the Lower Bound of the Large Chamber
LargeChamberPresmin=HPresBurstmax+O*(HPresBurstmin+HPresBurstmin-HPresBurstmax);

% Calculates the Upper Bound of the Large Chamber
LargeChamberPresmax=SmallChamberPresmax-
HPresBurstmin+LargeChamberPresmin+U*(HPresBurstmin+HPresBurstmin-LargeChamberPresmin);

%plot([0,1500],[LargeChamberPresmax,LargeChamberPresmax],'b')
%hold on

% Calculates the Alternate Upper Bound of the Large Chamber
ALargeChamberPresmax=ASmallChamberPresmax-
HPresBurstmin+LargeChamberPresmin+U*(LPresBurstmin+HPresBurstmin-LargeChamberPresmin);
%plot([0,1500],[ALargeChamberPresmax,ALargeChamberPresmax],'b')


%% Plot Disk Use Space
% The Maximum Theoretical Bounds
Maxminimumx=[0,LPresBurstmax];
Maxminimumy=[HPresBurstmax,HPresBurstmax];
plot(Maxminimumx,Maxminimumy,'r')
Maxmaximumx=0:1:LPresBurstmax;
Maxmaximumy=Maxmaximumx+HPresBurstmax;
z1=plot(Maxmaximumx,Maxmaximumy,'r')
plot([LPresBurstmax,LPresBurstmax],[HPresBurstmax,LPresBurstmax+HPresBurstmax],'r')

% The Nominal Theoretical Bounds
Avgminimumx=[0,LPresBurstavg];
Avgminimumy=[HPresBurstavg,HPresBurstavg];
Avgmaximumx=0:1:LPresBurstavg;
Avgmaximumy=Avgmaximumx+HPresBurstavg;

% The Minimum Theoretical Bounds
Minminimumx=[0,LPresBurstmin];
Minminimumy=[HPresBurstmin,HPresBurstmin];
plot(Minminimumx,Minminimumy,'r')
Minmaximumx=0:1:LPresBurstmin;
Minmaximumy=Minmaximumx+HPresBurstmin;
plot(Minmaximumx,Minmaximumy,'r')
plot([LPresBurstmin,LPresBurstmin],[HPresBurstmin,LPresBurstmin+HPresBurstmin],'r')

% Acceptable Bounds for Experimental Use
Expminimumx=[0,SmallChamberPresmax];
Expminimumy=[LargeChamberPresmin,LargeChamberPresmin];
Expmaximumx=0:1:SmallChamberPresmax;
```

```
Expmaximumy=Expmaximumx-
HPresBurstmin+LargeChamberPresmin+U*(LPresBurstmin+HPresBurstmin-LargeChamberPresmin);
 %fit linear polynomial
 p1 = polyfit(Expminimumx,Expminimumy,1);
 p2 = polyfit(Expmaximumx,Expmaximumy,1);
 r1=roots(p1);
 r2=roots(p2);
 %calculate intersection
 x_intersect = fzero(@(u) polyval(p1-p2,u),3);
 y_intersect = polyval(p1,x_intersect);
Expminimumx=[x_intersect,SmallChamberPresmax];
Expminimumy=[LargeChamberPresmin,LargeChamberPresmin];
Expmaximumx=x_intersect:1:SmallChamberPresmax;
Expmaximumy=Expmaximumx-
HPresBurstmin+LargeChamberPresmin+U*(LPresBurstmin+HPresBurstmin-LargeChamberPresmin);
z2=plot(Expminimumx,Expminimumy,'k')
plot(Expmaximumx,Expmaximumy,'k')
plot([SmallChamberPresmax,SmallChamberPresmax],[LargeChamberPresmin, max(Expmaximumy)],'k')

% Alternate Acceptable Bounds for Experimental Use
Expminimumx=[0,ASmallChamberPresmax];
Expminimumy=[LargeChamberPresmin,LargeChamberPresmin];
Expmaximumx=0:1:ASmallChamberPresmax;
Expmaximumy=Expmaximumx-
HPresBurstmin+LargeChamberPresmin+U*(LPresBurstmin+HPresBurstmin-LargeChamberPresmin);
 %fit linear polynomial
 p1 = polyfit(Expminimumx,Expminimumy,1);
 p2 = polyfit(Expmaximumx,Expmaximumy,1);
 r1=roots(p1);
 r2=roots(p2);
 %calculate intersection
 x_intersect = fzero(@(u) polyval(p1-p2,u),3);
 y_intersect = polyval(p1,x_intersect);
Expminimumx=[x_intersect,ASmallChamberPresmax];
Expminimumy=[LargeChamberPresmin,LargeChamberPresmin];
Expmaximumx=x_intersect:1:ASmallChamberPresmax;
Expmaximumy=Expmaximumx-
HPresBurstmin+LargeChamberPresmin+U*(LPresBurstmin+HPresBurstmin-LargeChamberPresmin);
z3=plot(Expminimumx,Expminimumy,'g')
plot(Expmaximumx,Expmaximumy,'g')
plot([ASmallChamberPresmax,ASmallChamberPresmax],[LargeChamberPresmin,
max(Expmaximumy)],'g')


%% Add Some Labels and Personal Preferances
box on
grid on
set(gca,'FontSize',18,'FontName','Times');
set(gca,'XMinorTick','on','YMinorTick','on')
ymin=double((int16(HPresBurstmin)/(10^(numel(num2str(int16(HPresBurstmin)))-
1)))*(10^(numel(num2str(int16(HPresBurstmin)))-1)));
ymax=double((int16(max(LPresBurstmax+HPresBurstmax))/(10^(numel(num2str(int16(max(LPresBurstm
ax+HPresBurstmax))))-1)))*(10^(numel(num2str(int16(max(LPresBurstmax+HPresBurstmax))))-1)));
axis([0 HPresBurstmax ymin ymax])
xlabel('Small Chamber Set Pressure (psi)')
ylabel('Large Chamber Set Pressure (psi)')
```

```
legend([z1,z2,z3],'Alum-Alum System Limits', 'Alum-Alum Disk', '9Mylar-Alum
Disk','location','northwest')



%% Nominal Figure
%Avgminimumx=[0,LPresBurstavg];
%Avgminimumy=[HPresBurstavg,HPresBurstavg];
%plot(Avgminimumx,Avgminimumy,'k')
%hold on
%Avgmaximumx=0:1:LPresBurstavg;
%Avgmaximumy=Avgmaximumx+HPresBurstavg;
%plot(Avgmaximumx,Avgmaximumy,'k')
%plot([LPresBurstavg,LPresBurstavg],[HPresBurstavg,LPresBurstavg+HPresBurstavg],'k')
%
%ymin=double((int16(HPresBurstmin)/(10^(numel(num2str(int16(HPresBurstmin)))-
1)))*(10^(numel(num2str(int16(HPresBurstmin)))-1)));
%ymax=double((int16(max(LPresBurstmax+HPresBurstmax))/(10^(numel(num2str(int16(max(LPresBurst
max+HPresBurstmax))))-1)))*(10^(numel(num2str(int16(max(LPresBurstmax+HPresBurstmax))))-1)));
%box on
%set(gca,'FontSize',18,'FontName','Times');
%set(gca,'XMinorTick','on','YMinorTick','on')
%axis([0 HPresBurstavg ymin ymax])
%xlabel('Small Chamber Set Pressure (psi)')
%ylabel('Large Chamber Set Pressure (psi)')
```

Appendix H: CTH Flyer Plate Simulation

The following is a sample annotated input deck for the impact of a copper flyer traveling at 600 m/s impacting an aluminum plate as shown in Figure 5.8. Including annotations highlights each of the relevant of a CTH input deck which are commonly included and gives early as well as experienced users a template with which to organize and verify input information.

```
*************************************************************************
*
*NATHANIEL HELMINIAK FLYER PLATE SIMULATION
*
*Created 4/5/2016
*
*set ff=unix <-- in vim if the file does not run right "^M" or sim
*
* CTH units cm, dynes, ev, sec <---- CGSeV units
*
*eor* cthin
*
* Title REQUIRED! (Do not add another non-comment line before control)
Aluminum-Copper Flyer Plate
*
*************************************************************************
*
*  Control REQUIRED!
*
*  Basic Rules for the Simulation
*
control
  mmp          * multiple material temp and pressure simulation
  tstop 100e-6   * specifies the simulated run time
  tbad 1e50      * acceptable number of temp discards (set high)
  print
endc
*
*************************************************************************
*
*  discard Not Required (but often are...)
*  Remove Problem Data, but does not replace with anything...
*
```

```
*
*discard
*
*mat -1 dens=1e99 densl=0 teml=100 temp=1000
*
*endd
*
*
**********************************************************************
*
*  mindt REQUIRED!
*  if the time step fall lower than this end the sim!
*
mindt
  time = 0  dt = 1.e-20
endm
*
*
**********************************************************************
*
*  edit REQUIRED!
*  shortest step, longest step, restart file dump time!
*
edit
*
 shortt
  time=0.0  dt=5.0e-6
 ends
*
 longt
  time=0.0  dt=25e-6
 endl
*
 restt
  time=0.0  dt=2.0e-5
 endr
endedit
*
*
**********************************************************************
*
*  mesh REQUIRED!
*  Creates the cells for the code to run
*
*  NOTE!: Just grade out area around the domain do not trust
*         boundries, they often lead to heartache and pain!
```

```
*
*  NOTE!: Good to have at least 12 cells through smallest
*        length scale to start with... Then rez up and check!
*
*  Recommended Format (Others Avalible)
*
*  x0 0
*  ^ Start
*     V Width  V First   V Last (units: cells/cm)
*  x1  w=12    dxf=       dxl=
*  ^ Grade into Area of Intrest
*  x2  w=12    dxf=       dxl=
*  ^ Area of Intrest
*  x3  w=12    dxf=       dxl=
*  ^ Grade out of Area of Intrest
*  endx
*  ^ end
*
*  OPTIONS:
*
*  1dr: 1D Rectilinear
*  1dc: 1D Cylindrical
*  1ds: 1D Spherical
*  2dr: 2D Rectangular
*  2dc: 2D Cylindrical
*  3dr: 3D Rectangular
*
*
*
mesh
*
 block 1 geom=2dc type=e
*
*
   x0  0.
    x1  n=128  dxf=.05 w=3.0
   endx
*
   y0  -2.25
    y1  n=256  dyf=.05 w=10.0
   endy
*
   xact =  0.0, 3.0
   yact = -4.0, 6.0
*
 endb
```

```
endm
*
*
**************************************************************************
*
*  edit REQUIRED!
*  Boundry conditions on the domain
*
*  OPTIONS:
*
*  0: Symmetry               BC - Reflecting Boundary
*  1: Transmitting           BC - Infinite Medium
*  2: Outflow                BC - Mass can leave the Domain
*  3: Inflow                 BC - Mass at boundry always to appears
*  4: Outflow with Pressure  BC - Mass out with pressure maintained
*  5: Symmetry w/ void inflow  BC - "Non-Sticky?"
*  6: Periodic               BC - Parrallel with Explicit Structure
*
* NOTE!: 2dc bxbot becomes 0!
*
*       y  <-symmetry
*       ^
*       l
*     ---l---
*    l  l  l
* <-----l-----> x  radial
*
*
boundary
  bhydro
      bxbot = 0 , bxtop = 2
      bybot = 0 , bytop = 0
  endh
endb
*
*
**************************************************************************
*
*  eos REQUIRED! (If you want to simulate something...)
*  Equations of State
*
*  jwl lx-14-0 <-- for explosive and heburn
*
eos
          mat1 mgr copper
          mat2 mgr 6061-T6_AL*UMINUM
```

```
endeos
*
*
**********************************************************************
*
*  epdata Highly Recommended!
*  Material Strength Information
*
epdata
  matep=1 ST copper
  matep=2 ST 6061-T6_ALUMINUM
*  matep1 eppvm user yield 3e8
*  matep3 SLIDE
  mix 3
endep
*
*
**********************************************************************
*
*  pfract/fracts Recommended
*  Material Faliure/Spall Information
*
*  Note!: Use the ultimate material strength if no published data!
*        convert to dynes/cm2 and slap a (-) sign in front
*
*  Note!: Super high for fluids (-1e30 ok)
*
 fracts
  pressure
  pfrac1 -2.6e10   *copper
  pfrac2 -4.0e10   *aluminum
  pfvoid -5.0e20
 endf
*
*
**********************************************************************
*
*  diatom REQUIRED! (If you want to simulate something...)
*  Places your materials with Initial Conditions
*
*  NOTE!: In addition to adding material can be replaced
*        can be of some use for tricky BCs
*  SAMPLE v
*  replace_package 'name'
*    on 0
*    off 1e99
```

```
*    mat 2
*    insert box
*    p1 0 1
*    p2 3 9
*    end i
*  endrep
*
*
diatoms
  package 'Copper Flyer'
    material 1
    yvel 0.6e5
    iter 3
    insert box
      p1 = 0.0,  0.0
      p2 = 3.0, -2.0
    endinsert
  endpackage
  package 'Alum Target'
    material 2
    iter 3
    insert box
      p1 = 0.0, 0.0
      p2 = 3.0, 2.0
    endinsert
  endpackage
enddiatom
*
*
*********************************************************************
*
*  tracer Not Required
*  Tracks cell information (can follow material or remain fixed)
*
*SAMPLE
*tracer
*  add 0.0 10.0 to 0.0 20.0 n=50 fix xy
*endtracer
*
tracer
 add 0 1.98
endtracer
*
*
*********************************************************************
*
```

```
*  convct  REQUIRED!
*  How does material move through the domain
*
convct
  convection = 1
  interface = high_resolution
endc
*
*
**********************************************************************
*
*  heat Not Required
*  Does heat conduction...
*
*heat
*  mat 5 K0=5e11
*endh
*
*
**********************************************************************
*
*  vadd Not Required
*  Adds velocity to materials within the sim
*  Useful for keeping some simulations within the domain
*
*vadd
*  mat 3
*  mat 7
*  tadd 2e-5
*  yvel -2e5
*endv
*
*
**********************************************************************
*
*  heburn Not Required
*  Adds velocity to materials within the sim
*  Useful for keeping some simulations within the domain
*
*heburn  *v detonation veolcity
*  mat 1  d 6.93e5
*  dp 0.0 10.0  r 1.0  time 0.0  *< -- at time = #
*            *^ burn radius
*endh
*
*
```

```
*************************************************************************
*
* SpyMaster <-- This plots the stuff Run by diff rules too
*
*  % <- Comments
*  must end all lines in ";" else errors!
*
*
spy
 SaveTime(0, 0.5e-6);
 PlotTime(0, 0.5e-6);
 Save("M,T,VOLM,VX,VY,P,TM+1,TK,Q1,Q2");
 ImageFormat(3500,4000);

% UserVariable("postveladd", Y velocity (km/s))
% define postveladd()
% {
% variable base_vel;
% base_vel=Get("VY");
% return (base_vel+210000)/100000;
% }
%
% DataOut("Temp_DATA","TM+1","TK");
%

 define main()
 {
   pprintf(" PLOT: Cycle=%d, Time=%e\n",CYCLE,TIME);
   XLimits(-8,8);
   YLimits(-4,6);

%   Image("Mats");
%    Window(0,0,0.75,1);
%    MatColors(GRAY,LIGHT_BLUE,RED,ORANGE);
%    Draw2DMesh;
%    Draw2DTracers;
%    Label(sprintf("Materials at %0.2e s.",TIME));
%    Plot2DMats;
%    %DrawBlockEdges;
%    MatNames("Steel","Air","Sabot","Flyer");
%    DrawMatLegend("",0.75,0.2,0.99,0.9);
%   EndImage;

   Image("Pressure",WHITE);
    Window(0.05,0.05,0.9,0.9);
    MatColors(ORANGE,LIGHT_GRAY);
```

```
    XBMirror(ON);
    Plot2DMats;
    ColorMapRange(1,5e11,LOG_MAP);
    ColorMapClipping(ON,OFF);
    Label(sprintf("Time=%5.1f ~m~s",1E6*TIME));
    Plot2D("P");
    Draw2DTracers(3);
    DrawColorMap("P (dyn/cm^2^)",0.85,0.4,1,0.8);
   EndImage;
UPlot("Plastic1","range:0,4","2d:Q1,int,leg");
UPlot("Velocity","range:1,60000","2d:VMAG,int,leg");

*   Image("Vmag");
*    Window(0,0,0.75,1);
*    ColorMapRange(1e2,1e6,LOG_MAP);
*    Label(sprintf("Velocity Magnitude at %0.2e s.",TIME));
*    Plot2D("VMAG");
*    Draw2DMatContour;
*    Draw2DTracers(3);
*    DrawColorMap("(cm/s)",0.75,0.4,0.9,0.9);
*   EndImage;

%  Image("Velo-Temp",WHITE,BLACK);
%    Window(0,0,0.75,1);
%    MatColors(GRAY,LIGHT_BLUE,RED,ORANGE);
%    Plot2DMats;
%    ColorMapRange(0.01,4000000);
%    ColorMapClippling(ON,OFF);
%    DrawColorMap("(cm/s)",0.85,0.4,0.99,0.8);
%    Label(sprintf("Velocity Temp Magnitude at %0.2f |c03BC|cs",TIME*1.E6"));
%
%    Right2D;
%    Plot2D("VMAG");
%    ColorMapRange(0,2000);
%    ColorMapClippling(ON,OFF);
%    DrawColorMap("(K)",0.005,0.4,0.19,0.8);
%    Left2D;
%    Plot2D("TK");
%    Draw2DMatContour;
%    ResetMirrors;
%    XBMirror(ON);
%  EndImage;


%  Image("1D Axial Velocity");
%   Fix1D(0.1,-20,0.1,60);
```

```
%   VLimits(0,350000);
%   Label(sprintf("Velocity Magnitude at %0.2f sec |c03BC|cs",TIME*1.E6"));
%   Plot1D("VY",ON);
%  EndImage;


% if (TIME> 500e-6)
%  {
%  Image("radiob");
%    XBMirror(ON);
%    ReverseGrayMap;
%    ColorMapRange(1e-2,100,LOG_MAP);
%    ColorMapClipping(ON,OFF);
%    DrawColorMap("Area Density",0.2,0.2,0.4,0.8);
%    Label(sprintf("Synthetic Radiograph at %0.2f sec |c03BC|cs",TIME*1.E6"));
%    Radiographic2dc(0,0,12,-20,60,500,100,1);
%  EndImage;
%  }

}

 HisTime(0,1e-6);
 SaveTracer(ALL);
 SaveHis("GLOBAL,POSITION,P,VX,VY,VY.1,Q1,PSR,YLD,DTIME");

 define spyhis_main()
 {
  HisLoad(1,"hscth");
  HisImageName("Target_Velocity_History")
  Label("Velocity at Tracer 1");
  TPlot("VY.1",1,AUTOSCALE);
 }

endspy
```